

# **Arbeitsbericht NAB 19-46**

**Interpretation of the First 5 Years  
of the FE Experiment:  
a THM Synthesis**

September 2020

B. Lanyon, B. Firat Lüthi & E. Manukyan

**National Cooperative  
for the Disposal of  
Radioactive Waste**

Hardstrasse 73  
P.O. Box 280  
5430 Wettingen  
Switzerland  
Tel. +41 56 437 11 11  
[www.nagra.ch](http://www.nagra.ch)



# Arbeitsbericht NAB 19-46

## Interpretation of the First 5 Years of the FE Experiment: a THM Synthesis

September 2020

B. Lanyon<sup>1</sup>, B. Firat Lüthi<sup>2</sup> & E. Manukyan<sup>2</sup>

<sup>1</sup>Fracture Systems  
<sup>2</sup>Nagra

### KEYWORDS

FE-Experiment, Full Scale Emplacement Experiment,  
FE assessment case, THM coupled processes,  
repository induced effects

**National Cooperative  
for the Disposal of  
Radioactive Waste**

Hardstrasse 73  
P.O. Box 280  
5430 Wettingen  
Switzerland  
Tel. +41 56 437 11 11  
[www.nagra.ch](http://www.nagra.ch)

Nagra Arbeitsberichte ("Working Reports") present the results of work in progress that have not necessarily been subject to a comprehensive review. They are intended to provide rapid dissemination of current information.

"Copyright © 2020 by Nagra, Wettingen (Switzerland) / All rights reserved.

All parts of this work are protected by copyright. Any utilisation outwith the remit of the copyright law is unlawful and liable to prosecution. This applies in particular to translations, storage and processing in electronic systems and programs, microfilms, reproductions, etc."

## Table of Contents

Table of Contents.....	I
List of Tables.....	III
List of Figures.....	V
<b>1 Introduction.....</b>	<b>1</b>
1.1 The Full-Scale (FE) Emplacement Experiment .....	1
1.2 Report objectives.....	2
1.3 Interpretation dataset .....	2
1.4 Report Organisation .....	3
<b>2 FE tunnel, excavation, emplacement and instrumentation.....</b>	<b>5</b>
2.1 Location and local geological setting.....	5
2.2 Excavation .....	7
2.2.1 Measured response to excavation.....	11
2.2.2 Open tunnel period.....	20
2.3 EBS emplacement and instrumentation.....	26
2.4 Schedule of events relevant to FE evolution.....	36
<b>3 System evolution after emplacement and start of heating .....</b>	<b>39</b>
3.1 Thermal data: Temperature and heater power .....	39
3.1.1 Heater power and surface temperature .....	39
3.1.2 Temperature .....	43
3.2 Hydraulic data: saturation and pore pressure.....	54
3.2.1 Saturation.....	54
3.3.2 Pore pressure.....	68
3.3.3 Packer pressure .....	79
3.3 Mechanical data: Deformation and stress.....	82
3.3.1 Displacements.....	82
3.3.2 Total pressure.....	95
3.4 Geophysical measurements .....	99
<b>4 Response to Ga18 excavation .....</b>	<b>111</b>
4.1 Ga18 excavation.....	111
4.2 Extensometer and LVDT measurements.....	114
4.3 Interval and packer pressures.....	118
4.4 Summary of response to Ga18 excavation .....	128
<b>5 Integrated THM interpretation .....</b>	<b>129</b>
5.1 Expected evolution of EBS and geosphere.....	129
5.1.1 HE-E.....	129
5.1.2 Modelling and scoping calculations.....	131

5.1.3	Evaluation at 18 months .....	134
5.2	Summary of observed response at FE .....	135
5.2.1	Geosphere response to FE tunnel excavation and ventilation.....	135
5.2.2	Response to EBS emplacement and heating.....	135
5.2.3	Saturation state of the EBS .....	143
5.2.4	Saturation of the shotcrete and rock.....	144
5.3	Significant THM Processes during early evolution .....	146
5.3.1	THM processes and couplings in the EBS.....	146
5.3.2	THM processes and couplings in the rock.....	148
5.4	Exchanges between EBS and geosphere .....	149
<b>6</b>	<b>Conclusions and recommendations.....</b>	<b>153</b>
6.1	FE first five years of heating.....	153
6.2	Early evolution of an emplacement drift .....	154
6.3	Open questions.....	156
6.4	Recommendations.....	156
<b>7</b>	<b>References.....</b>	<b>159</b>
<b>App. A:</b>	<b>Instrumentation.....</b>	<b>A-1</b>
<b>App. B:</b>	<b>Borehole instrumentation .....</b>	<b>B-1</b>
<b>App. C:</b>	<b>FE multi-packer system interval and packer systems.....</b>	<b>C-1</b>
<b>App. D:</b>	<b>Relationship between relative humidity and saturation/volumetric water content and thermal conductivity and saturation for GBM.....</b>	<b>D-1</b>
<b>App. E:</b>	<b>Water Content Measurements (non-engineering units).....</b>	<b>E-1</b>
<b>App. F:</b>	<b>Pressure change in response to Ga18 excavation .....</b>	<b>F-1</b>
<b>App. G:</b>	<b>Kirsch equations.....</b>	<b>G-1</b>
<b>App. H:</b>	<b>Pore pressure disturbances during excavation of Gallery 98 (New Gallery) .....</b>	<b>H-1</b>

## List of Tables

Tab. 1:	Support used in excavation of FE Gallery.....	8
Tab. 2:	BFEA boreholes drilled sub-parallel to FE Gallery from FE-A Niche .....	10
Tab. 3:	Convergence sections in FE Gallery .....	13
Tab. 4:	Measured convergences in FE Gallery approximately one month after excavation.....	16
Tab. 5:	Measured strain normalised to gallery radius .....	17
Tab. 6:	Extensometer sections in FE Gallery .....	17
Tab. 7:	Wet spot locations and related features .....	24
Tab. 8:	Instrumentation sections in the FE Gallery.....	27
Tab. 9:	Dedicated THM instrumentation sections in the FE Gallery.....	28
Tab. 10:	As-emplaced volume-mass properties of the GBM .....	32
Tab. 11:	Estimated pore volume (m <sup>3</sup> ) and water needed for saturation (m <sup>3</sup> ) per metre of tunnel for different tunnel radii and as-emplaced density.....	33
Tab. 12:	Main events relevant to FE Experiment .....	36
Tab. 13:	Simplified Ga18 Excavation schedule.....	38
Tab. 14:	Main heating events .....	39
Tab. 15:	Summary of thermal conductivity measurements.....	53
Tab. 16:	Mean measured relative humidity in the rock, GBM and heater pedestals over selected periods.....	64
Tab. 17:	Extensometer boreholes and sensors .....	82
Tab. 18:	LVDT sensors located between heater and shotcrete.....	87
Tab. 19:	Geophysical campaigns performed in the FE Gallery.....	99
Tab. 20:	Outputs from the different geophysical measurements .....	100
Tab. 21:	Geophysical measurement sensitivity .....	102
Tab. 22:	Ga18 excavation phases .....	111
Tab. 23:	Summary of Ga18 responses during Phase 2D.....	128
Tab. 24:	Predictions of FE response to heating from Garitte (2013) .....	132
Tab. 25:	Measurements related to state of buffer saturation as of 31.08.2019 .....	137
Tab. 26:	Summary of BFEA002 to A007 interval and packer response to heating .....	141
Tab. 27:	Summary of saturation related measurements for EBS.....	143
Tab. 28:	Summary of observations related to rock saturation .....	145
Tab. 29:	Estimated flow (ml/day) to 1m of low pressure zone around FE tunnel test section for hydraulic conductivity of $2 \times 10^{-13}$ and $2 \times 10^{-12}$ m/s for condition prior to heating and during heating .....	150
Tab. 30:	FE Sources of heterogeneity and anisotropy .....	154

Tab. A-1:	Number of sensors used in THM interpretation split by location .....	A-1
Tab. B-1:	BFEA boreholes drilled from FE-A Niche sub-parallel to FE Gallery .....	A-1
Tab. B-2:	BFEB boreholes drilled radially out from FE Gallery (except BFEB048).....	A-2
Tab. B-2:	Cont.....	A-3
Tab. B-3:	BFEC boreholes drilled radially out from FE Gallery (except BFEC054).....	A-4
Tab. B-4:	BFEE boreholes drilled radially out from FE Gallery.....	A-5
Tab. C-1:	Parameter ranges .....	C-1
Tab. C-2:	Multi-packer monitoring system interval locations.....	C-3
Tab. C-3:	Multi-packer monitoring system packer locations .....	C-4
Tab. D-1:	Granular bentonite properties and van Genuchten model parameters from Nagra (2019), Garitte (2013).....	D-2
Tab. F-1:	Pore pressure peak and change during Ga18 excavation Phase 2D. Change calculated as peak pressure minus average pressure from 02. – 07.05.2019.....	F-1
Tab. F-2:	Pore pressure change during excavation days Ga18 Phase 2D. Change calculated as maximum pressure after 06:00 minus average pressure from 00:00 – 06:00 .....	F-4
Tab. F-2:	Pore pressure change during excavation days Ga18 Phase 2D. Change calculated as maximum pressure after 06:00 minus average pressure from 00:00 – 06:00 .....	F-5

## List of Figures

Fig. 1:	FE experiment and reporting time line.....	3
Fig. 2:	Face mapping from FE Gallery at GM 26.5 (left) and at GM 43.5 (right).....	6
Fig. 3:	Conventions used to describe position around the tunnel (looking toward tunnel end).....	6
Fig. 4:	3D view of borehole array used to monitor the construction of the FE Gallery.....	7
Fig. 5:	Excavation of FE Gallery a) pneumatic hammer from FE-A Niche, b) profiling using road header.....	8
Fig. 6:	3D and plan view of FE tunnel showing boreholes, anchors, shotcrete and steel sets .....	9
Fig. 7:	Pore pressure response to FE Gallery excavation in monitoring borehole array .....	13
Fig. 8:	Geometry of FE Gallery convergence sections and extensometer sections .....	13
Fig. 9:	FE Gallery Convergence measurements versus distance behind excavation face for P1-P7.....	15
Fig. 10:	Geological mapping of excavation face of FE Gallery at approximate locations of convergence sections .....	16
Fig. 11:	Measured strains versus days after excavation for extensometers at E1 and E2 sections of FE Gallery .....	18
Fig. 12:	Strain profiles in tunnel wall at (a) E1 (GM 14.6 shotcrete only) and (b) E2 (GM 43.1 arches only) on 06.08.2012 .....	19
Fig. 13:	Comparison of convergence and extensometer response, parallel to bedding (left) and normal to bedding (right) for FE Gallery .....	20
Fig. 14:	Climate in the FE-A Niche from 01.01.2012 to 01.07.2015 covering period when FE Gallery was open and ventilated.....	20
Fig. 15:	BFEA multipacker system response during open tunnel period.....	22
Fig. 16:	Linear and log-linear plots of total convergence measured at FE Gallery .....	23
Fig. 17:	Examples of wetspots in the FE tunnel after excavation.....	24
Fig. 18:	Wetspots and associated boreholes where grouting tubes lead to observed wet spots .....	26
Fig. 19:	FE Gallery layout a) schematic, b) instrumentation section positions .....	27
Fig. 20:	Photograph of a bentonite block pedestal supporting a heavily instrumented heater in the FE tunnel.....	29
Fig. 21:	GBM produced for the FE Experiment .....	30
Fig. 22:	Longitudinal section of the backfilled FE tunnel indicating the position of the 3-D slope scans and the resulting bulk dry densities calculated for each of the sections.....	31

Fig. 23:	Swelling pressure versus initial dry density under constant volume conditions in compacted shot-clay and MX-80 bentonite samples .....	33
Fig. 24:	Layout of each instrumentation section.....	34
Fig. 25:	Gal8 excavation plan showing main excavation phases and direction of advance.....	37
Fig. 26:	Heater power a) overview b) detail response showing small variation in power.....	40
Fig. 27:	Heater surface temperature .....	41
Fig. 28:	Heater power and surface temperature from installation to 01.06.2015.....	42
Fig. 29:	Temperature data from sensors at the shotcrete or tunnel wall in Gap 2-3, H2 and Gap 0 (ISS) sections .....	43
Fig. 30:	Temperature data from radial boreholes in H2, H3 and Gap 0 (ISS) sections .....	44
Fig. 31:	Temperature data from longitudinal boreholes BFEA010 and BFEA011.....	45
Fig. 32:	Temperature contours of date (Y) versus metre along hole (mah) for the longitudinal boreholes BFEA010 and BFEA011 .....	45
Fig. 33:	Temperature distribution with radial distance from the tunnel axis.....	47
Fig. 34:	Measured temperature in geosphere versus radial distance from the FE Tunnel .....	48
Fig. 35:	Measured temperature in geosphere at 31.0.8.2019.....	48
Fig. 36:	Temperature distribution in the different sections of the FE tunnel.....	49
Fig. 37:	Temperature difference (°C) from 01.12.2014 (prior to heating) to 31.08.2019 (end of monitoring period) .....	51
Fig. 38:	Estimated thermal conductivity from periodic measurements in GBM and heater pedestals a), b), c), d), e) sensors in H2 pedestal.....	52
Fig. 39:	Relative humidity measurements at H1.....	56
Fig. 40:	Relative humidity measurements at H2.....	57
Fig. 41:	Relative humidity measurements at H3.....	58
Fig. 42:	Relative humidity measurements .....	59
Fig. 43:	Spatial distribution of relative humidity measurements as vertical cross-sections .....	61
Fig. 44:	Relative humidity versus radial distance from the tunnel axis at selected times.....	62
Fig. 45:	Relative humidity measurements near the shotcrete and rock.....	63
Fig. 46:	Spatial distribution of relative humidity (%) .....	65
Fig. 47:	Volumetric water content in buffer around H2 and H3.....	66
Fig. 48:	Volumetric water content in boreholes around H2 and H3 .....	67
Fig. 49:	Plan view of BFEA002-7 boreholes and monitoring intervals .....	69

Fig. 50:	Measured interval pressure in BFEA002 (parallel to bedding) and BFEA005 (normal to bedding) .....	70
Fig. 51:	Measured interval pressure in BFEA003 (parallel to bedding) and BFEA006 (normal to bedding) .....	71
Fig. 52:	Measured interval pressure in BFEA004 (parallel to bedding) and BFEA007 (normal to bedding) .....	71
Fig. 53:	Measured interval pressure in radial boreholes in a) H3 section and b) H2 section.....	72
Fig. 54:	Measured interval pressure in tunnel entrance section.....	73
Fig. 55:	Measured interval pressure in radial boreholes in a) Porous concrete section and b) end of the FE Tunnel.....	74
Fig. 56:	Measured interval pressure versus radial distance from the FE Tunnel .....	75
Fig. 57:	Spatial distribution of interval pore pressure (kPa abs) at 31.08.2019 (end of current monitoring period).....	77
Fig. 58:	Spatial distribution of change in interval pore pressure (kPa abs) from start of heating to 31.08.2019 (end of current monitoring period) .....	78
Fig. 59:	Plan view of packer locations BFEA002-7.....	79
Fig. 60:	Measured packer pressure in BFEA002 and BFEA005 .....	80
Fig. 61:	Measured packer pressure in BFEA003 and BFEA006 .....	80
Fig. 62:	Measured packer pressure in BFEA004 and BFEA007 .....	81
Fig. 63:	Measured packer pressure in BFEA008 and BFEA009 .....	81
Fig. 64:	Measured displacement a) BFEC001,2, b)BFEC003,4,5 .....	84
Fig. 65:	Measured displacements BFEB009 – 14, b) Measured temperature BFEB009-14.....	85
Fig. 66:	Heater and LVDT sensors (1,4 upwards to roof, 2,3 down to floor).....	86
Fig. 67:	LVDT measurements for heaters H1,H2 and H3.....	87
Fig. 68:	Inclinometer settlement (mm).....	89
Fig. 69:	Inclinometer settlement contours (mm).....	90
Fig. 70:	Inclinometer settlement in heater sections.....	91
Fig. 71:	Inclinometer settlement (mm) versus elapsed days (log) since installation BFEA010, b) BFEA011 .....	92
Fig. 72:	3D view of inclinometer settlement (mm) at end of monitoring period.....	93
Fig. 73:	Vertical section view of inclinometer settlement (mm) at end of monitoring period.....	94
Fig. 74:	Time history of total pressure cells at tunnel wall at the Plug and Gap GP sections.....	96
Fig. 75:	Time history of total pressure cells on tunnel wall at the H3 and Gap 2-3 sections.....	96
Fig. 76:	Time history of total pressure cells at tunnel wall at the H2 and Gap 1-2 sections.....	97

Fig. 77:	Time history of total pressure cells at tunnel wall at the H1 and Gap 0 (ISS) and BBW sections.....	97
Fig. 78:	Time history of total pressure cells on the heater surfaces and in the pedestals .....	98
Fig. 79:	Time history of total pressure cells at tunnel wall at the H3 and Gap 2-3 sections.....	98
Fig. 80:	Location of glass-fibre tubes GP1 and GP2 within FE Gallery .....	101
Fig. 81:	Location of (semi-)permanently installed seismic sensors .....	101
Fig. 82:	Singe-hole geophysical logs for GP1 (left) and GP2 (right) for the first 6 campaigns: a) gamma-gamma data, b) neutron data .....	103
Fig. 83:	Mala single-hole velocity logs for GP1 (left) and GP2 (right): a) GPR velocity, b) difference in velocity between campaigns. ....	103
Fig. 84:	Mala single-hole amplitude logs for GP1 (left) and GP2 (right): a) GPR amplitude, b) difference in amplitude between campaigns .....	104
Fig. 85:	GPR velocity and attenuation tomograms for the first eight campaigns .....	105
Fig. 86:	GPR tomograms for the first eight campaigns.....	106
Fig. 87:	Seismic and velocity tomograms for the first eight campaigns .....	107
Fig. 88:	Comparison of GPR single-hole log data for the first six campaigns with a) temperature measured by FE_TEM_031 and b) relative humidity measured by FE_HUM_031 .....	108
Fig. 89:	Comparison of GPR and seismic tomography results for the first six campaigns with a) temperature measured by FE_TEM_046 and b) relative humidity measured by FE_HUM_046.....	108
Fig. 90:	Stages of Ga18 excavation (from daily reports) .....	112
Fig. 91:	Vertical geological section and schematic showing FE Tunnel, Ga18 and Main Fault.....	113
Fig. 92:	LVDT response (relative to 31.1.19) at heaters .....	114
Fig. 93:	Inclinometer settlement response (relative to 31.01.2018).....	115
Fig. 94:	Inclinometer settlement response at heaters (relative to 31.01.2018) .....	116
Fig. 95:	Inclinometer settlement response (relative to 31.01.2018).....	117
Fig. 96:	Ga18 excavation on 23.05.2019 a) Ga18 progress, b) Ga18 face mapping at 294 GM.....	118
Fig. 97:	BFEA002, 5 response to Ga18 excavation.....	119
Fig. 98:	BFEA003, 6 response to Ga18 excavation.....	120
Fig. 99:	BFEA003, 6 response to Ga18 excavation .....	121
Fig. 100:	Radial borehole pressure response to Ga18 excavation .....	122
Fig. 101:	Interval and packer pressure and temperature responses to Ga18 excavation at the BMB-15, 16 near the FE-A Niche.....	123
Fig. 102:	3D View of Ga18 excavation Phase 2D and MT FE tunnel and selected boreholes .....	124

Fig. 103:	Interval and responses to Ga18 excavation on 07.05.2019 and 23.05.2019 for BFEA002 and BFEA005 .....	125
Fig. 104:	Interval and responses to Ga18 excavation on 07.05.2019 and 23.05.2019 for BFEA003 and BFEA006 .....	125
Fig. 105:	Interval responses to Ga18 excavation on 07.05.2019 and 23.05.2019 for BFEA003 and BFEA006 .....	126
Fig. 106:	Interval responses to Ga18 excavation on 23.05.2019 for a) BFEB001,2,3,4 b) BFEB005,6,7,8.....	126
Fig. 107:	3D view showing maximum pressure change during a) Ga18 excavation Phase 2D and b) during 23.05.2019.....	127
Fig. 108:	Plan view showing maximum pressure change during a) Ga18 excavation Phase 2D and b) during 23.05.2019.....	127
Fig. 109:	Geosphere instrumentation around the VE microtunnel at Mont Terri .....	130
Fig. 110:	EBS instrumentation in the VE micro tunnel at Mont Terri .....	131
Fig. 111:	HE-E H2 a) temperature and b) power.....	131
Fig. 112:	Predicted temperature a) temperature versus radial distance from the tunnel axis and b) influence of THM parameters on temperature at the heater and at the buffer rock interface.....	133
Fig. 113:	Illustration of THM processes occurring in the FE Experiment .....	134
Fig. 114:	Radial Distribution of temperature at varying times during heating for a) H1, b) H2.....	136
Fig. 115:	Distribution of temperature and temperature gradient in HE-E experiment after 2'350 days of heating.....	137
Fig. 116:	Relative humidity in H3 sections in rock, at shotcrete wall and around the heater .....	138
Fig. 117:	Relative humidity in HE-E experiment .....	139
Fig. 118:	Pressure change versus temperature change in packers and intervals.....	140
Fig. 119:	Maximum post-heating pore pressure .....	142
Fig. 120:	Distribution of measured pore pressure around VE micro-tunnel in HE-E experiment after 2'350 days of heating.....	145
Fig. 121:	Schematic of coupled processes associated with moisture redistribution and vapour transport in the buffer .....	146
Fig. 122:	Schematic of exchange processes in the EBS and rock.....	147
Fig. 123:	Schematic of relationships between THM processes in a porous medium.....	148
Fig. 124:	Radial pressure (log scale) from selected dates together with estimated gradients.....	150
Fig. 125:	Simple heat conduction model and computed and measured radial temperature distributions for the 3 heaters .....	152
Fig. 126:	Interactions between emplacement tunnels in a deep SF/HLW repository .....	156

Fig. C-1:	FEA multi-packer system interval layout (BFEA002-7).....	C-1
Fig. C-2:	FE multi-packer system schematic for BFE-A002 (BFE-A003-A007 are similarly equipped).....	C-2
Fig. D-1:	Relative humidity versus a) saturation and b) volumetric water content based on van Genuchten model with uncertainty given by factor of 0.1,10 in capillary pressure.....	D-2
Fig. D-2:	Thermal conductivity as a function of the saturation measured in the lab for MX-80 bentonite pellets (blue dots) and MX80 bentonite blocks (red dots).....	D-3
Fig. E-1:	Volumetric water content measurements (mV) from BFEC006-8.....	E-1
Fig. E-2:	Volumetric water content measurements (mV) from BFEB050,51.....	E-1
Fig. G-1:	Geometry and co-ordinate system for Kirsch solution.....	G-1
Fig. G-2:	Estimated change in vertical, horizontal and mean total stress as a function of horizontal distance ( $r/a$ ) in homogeneous elastic medium under plan strain conditions.....	G-2
Fig. H-1:	BOP-1 and BDI-1 interval pressures during New Gallery excavation.....	H-1

# 1 Introduction

## 1.1 The Full-Scale (FE) Emplacement Experiment

The 'Full-Scale Emplacement' (FE) Experiment simulates, as realistically as possible, the construction, waste emplacement, backfilling and early stage thermo-hydro-mechanical (THM) post-closure evolution of a spent fuel (SF)/vitrified high-level waste (HLW) disposal tunnel according to the current Swiss repository concept (Müller et al. 2017). Nagra (2019) presents a synthesis of the design, construction and preliminary results of the FE Experiment up to the first 18 months of heater operation.

The objectives of the FE Experiment are:

- to investigate SF/HLW repository-induced THM coupled effects on the host rock at full scale and to validate existing coupled THM models
- to verify the technical feasibility of constructing an emplacement tunnel using standard industrial equipment
- to optimise the bentonite buffer material design and production, in particular to produce bentonite blocks that are capable of resisting the ambient conditions during the emplacement and operation phases
- to investigate (horizontal) canister and buffer emplacement procedures for underground conditions

The latter three objectives have been largely addressed in Nagra (2019) and so the emphasis here is on the first objective.

Practical considerations regarding instrumentation and construction at the Mont Terri Underground Rock Laboratory (URL) limit the scope of the investigations possible. In particular the design of the plug is not fully airtight which may result in a different gas phase evolution from that expected in a repository. Further, the FE Experiment was not designed to address demonstration of retrievability. Transferability of observations and process understanding (Mazurek et al. 2008) derived from the FE Experiment needs to take account of the different lithologic, tectonic, temperature, stress and pore pressure conditions at the Mont Terri URL from those prevailing at candidate repository sites.

The FE Experiment was undertaken by Nagra in collaboration with a range of partners including ANDRA, BGR, US DOE, FANC, GRS, Posiva, SKB and NWMO. Not all partners have participated in each phase of FE. The construction of the FE experiment was part of the European Union (EU) Large Underground Concept Experiment (LUCOEX) Project, which focused on demonstration of the technical feasibility of safe and reliable disposal of radioactive waste in geological formations.

## 1.2 Report objectives

This report aims to present an integrated THM interpretation of the results from the FE Experiment for the period up to 31.08.2019, covering almost five years (1'720 days) of heating from 15.12.2014 and over 7 years since the start of excavation (2'680 days). The report concentrates on the evolution of temperature, water content/saturation, pore pressure, deformation and stress in the Engineered Barrier System (EBS) and nearfield. The evolution of gas phase composition is not considered here, but first results have already been reported (Giroud et al. 2018).

The interpretation is based on the monitoring dataset and aims to provide a first level interpretation by considering the most important processes occurring in the EBS and geosphere together with descriptions of the exchanges between the two. The report aims to integrate

- different measurements of related key THM parameters including both monitoring and geophysics data
- the geological framework of the site (bedding and structures)
- the influence of different support systems (shotcrete test section and arch-supported Interjacent Sealing Section or ISS)

The report also provides a limited comparison of the data with the expected evolution based on understanding from previous testing together with predictive modelling performed prior to the start of heating. Detailed THM modelling of the FE Experiment played an important part in the development of the experiment concept and design (see discussion in Chapters 2 and 7 of Nagra, 2019). The models were based on those developed from a series of heater experiments previously performed at Mont Terri: HE-B (Göbel et al. 2007), HE-D (Zhang et al. 2007) and HE-E (Gaus 2011, Teodori & Gaus 2011). Predictive modelling was also performed when the detailed design was finalised (see Nagra 2019 and Senger 2015). These models, together with the understanding developed from other testing at Mont Terri form the basis for the expected evolution of the experiment. A modelling "Task Force" has recently been initiated by Nagra (Alcolea et al. 2019).

The report does not present detailed modelling results but aims to support future modelling work by providing a consistent presentations and interpretations.

## 1.3 Interpretation dataset

Online monitoring data and supporting information for the FE Experiment is held in the FE Information System Database (FEISDB) database (<https://feisdb.org/>). This report is based on data extracted from the FEISDB for the seven-year period from 01.01.2012 to 31.08.2019. The bulk of the data has been extracted from FEISDB using 12 hr average sampling. Higher time resolution data from FEISDB has been used to consider detailed responses to particular events.

The online data for the period 01.01.2012 – 31.08.2018 has been presented in a first Data Trend Report by Firat Lüthi (2018). A second Data Trend Report covering the period from 01.09.2018 to 31.08.2019 was published in 2019 (Firat Lüthi, 2019) and the two Data Trend reports provide a more detailed parallel discussion of sensor responses to this report. The experiment and reporting timelines are shown in Fig. 1.

Additional data including the results of geophysical surveys have been provided by the FE Team.

Future updates of this report will consider an extended dataset including the fibre optic systems measuring temperature and strain at the tunnel wall.

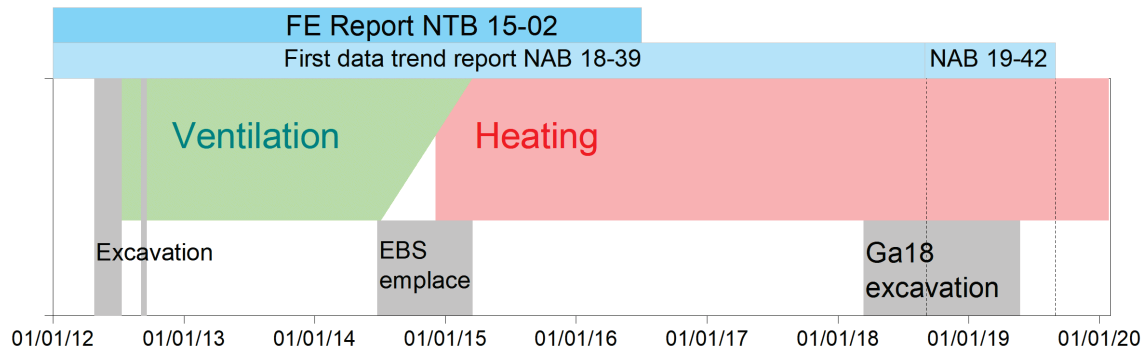


Fig. 1: FE experiment and reporting time line

## 1.4 Report Organisation

The report is organised as follows:

Chapter 2 presents the site geology, excavation, experimental layout, EBS emplacement and instrumentation. A chronology of the main events is also provided.

Chapter 3 presents the observed system response to emplacement and heating.

Chapter 4 presents the observed system response to excavation of Ga18.

Chapter 5 identifies the significant THM processes and couplings controlling the observed response.

Chapter 6 provides conclusions and recommendations, together with any significant open questions.



## 2 FE tunnel, excavation, emplacement and instrumentation

### 2.1 Location and local geological setting

The FE tunnel is located in an extension of the Mine-By Niche and was excavated towards  $244^\circ$  roughly parallel to bedding strike of about  $240^\circ$ . The FE Start Niche (Niche FE-A) was excavated in 2011 (Jaeggi et al. 2012) and the FE tunnel was excavated between 26.04.2012 and 10.07.2012. The tunnel lies within the shaly facies of the Opalinus Clay and passes through a bedding-parallel fault zone. Bedding dip was approximately  $35^\circ - 40^\circ$ , slightly greater than that observed in the Mine-By Niche. The bedding was tectonically affected showing visible sheared fractures (split/open bedding) with a normal separation of about 0.4 m. These features formed slip surfaces and slicken-sides. Low frequency secondary fracture sets were observed (Jaeggi et al. 2012).

A well-developed fault zone was identified from Gallery Meter (GM )14.5 to the end of the gallery. The fault shows three zones along the gallery (Jaeggi et al. 2012):

- GM 12-GM 14.5: The fault zone is located entirely below the invert at shallow depth. During the renovation of the tunnel invert, geological mapping identified destabilized rock at 5 o'clock due to the shallow fault zone.
- GM 14.5-GM 32.5: The fault zone is visible at the invert. The slight oblique orientation with respect to the tunnel axis results in an upward trend to the fault trace. The orientation of the zone is  $\sim 130^\circ$  with dip between  $40 - 50^\circ$ , somewhat steeper than the bedding.
- GM 32.5-GM 50: At GM 32.5 the lower boundary of the zone rises out of the invert and wanders upwards. At around GM 35 the orientation becomes parallel to the tunnel axis ( $\sim 150^\circ$ ) until the end of the gallery (see Fig. 2).

It is expected that the pre-excavation stress-state around the FE tunnel is similar to that around the MB Niche and is reasonably well described by the stress tensor suggested by Martin & Lanyon (2003). The maximum principal stress of 6.5 MPa is assumed to be roughly vertical and equivalent to an overburden of 250 – 300 m. The minimum horizontal stress is taken as 2.2 MPa and is approximately parallel to the tunnel. The maximum horizontal stress is 4 MPa and is oriented roughly parallel to Gallery 08. The presence of the faulted zone may indicate some local deviation from this stress field.

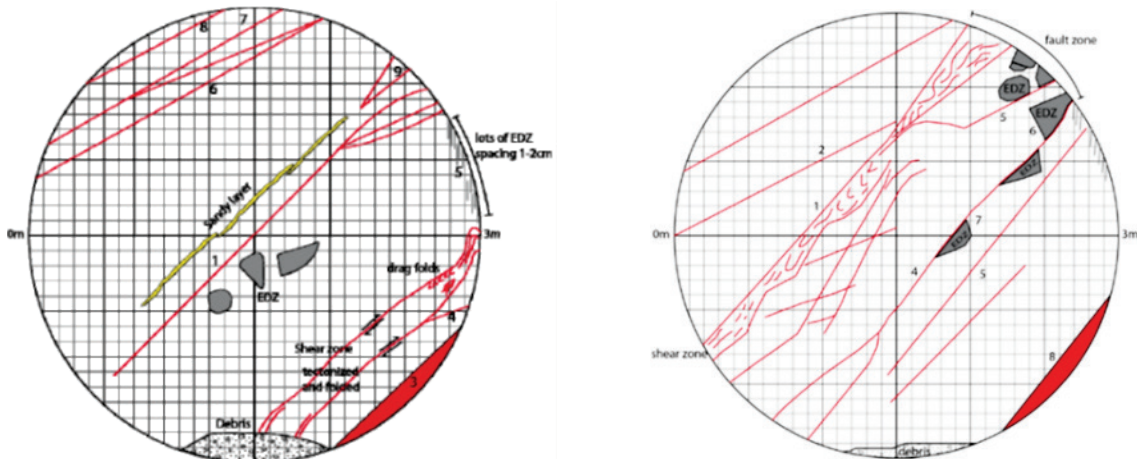


Fig. 2: Face mapping from FE Gallery at GM 26.5 (left) and at GM 43.5 (right)  
 Red features are pre-existing bedding-parallel tectonic structures – potentially reactivated by excavation.

**FE local coordinate system**

Position along the FE Tunnel is often given as gallery metres (GM ) but a local FE coordinate system was established based on the following coordinate axes:

- $X_{FE}$ : Horizontal normal to the tunnel axis towards NW 332°
- $Y_{FE}$ : Horizontal parallel to the tunnel axis towards SW at 242°.  $Y_{FE} = GM + 4.7$  m
- $Z_{FE}$ : vertically upward

The origin of the coordinate system in grid coordinates is (2579288.412, 1247619.968, 515.851). The origin corresponds to a fixed survey point within the FE-A Niche approximately 4.7 m from the start of the FE Tunnel. Within this report both GM and  $Y_{FE}$  coordinates are used. The radial distance from the  $Y_{FE}$  -axis is labelled as  $r$  and is used as an approximate measure of the distance from the tunnel axis. Positions around the tunnel have been described as clock positions and within this report by angle  $\theta$  relative to the  $X_{FE}$  and  $Z_{FE}$  axes as shown in Fig. 3.

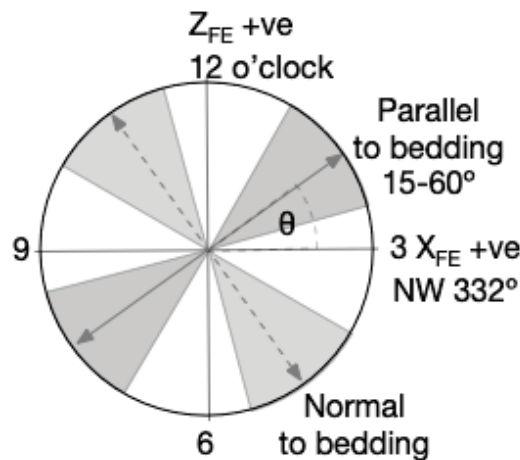


Fig. 3: Conventions used to describe position around the tunnel (looking toward tunnel end)  
 Mean bedding dip ~ 35° towards south-east ~ 150°

## 2.2 Excavation

The FE-A Niche was excavated from the end of the MB Niche in 2011 (Jaeggi et al. 2012). During excavation cracks in the shotcrete liner of the MB Niche were observed and fresh shotcrete and additional rock bolts were installed to minimize further displacements. Prior to excavation of the FE tunnel monitoring instruments were emplaced in a series of boreholes drilled from the FE-A Niche (see Fig. 4). The instrumentation included:

- six boreholes with multi-packer piezometer systems each with six intervals (BFEA002-7)
- two boreholes with single packer pressure, temperature monitoring systems (BFEA008-9)
- two boreholes above the tunnel (00:30 and 11:30 orientation) with 40-segment two-axis inclinometer chains and fibre-optic temperature measurements (BFEA010,11)

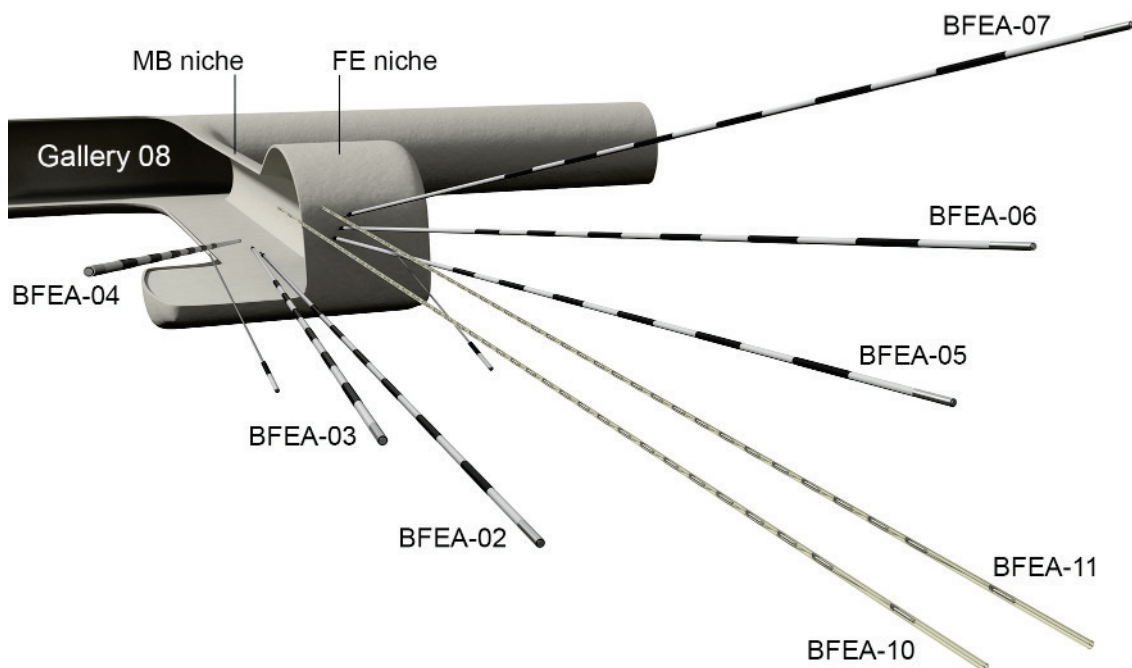


Fig. 4: 3D view of borehole array used to monitor the construction of the FE Gallery

The FE Tunnel was designed with a 3 m diameter circular cross-section and 50 m length. It was excavated with pneumatic hammer and roadheader. A pneumatic hammer was used to break out of the FE-A Niche (Fig. 5a). The tunnel was then excavated with the pneumatic hammer and subsequently, a roadheader was used to adjust the profile (Fig. 5b). The accuracy of the circular profile was low, and the invert was excavated as flat section rather than the original planned circular section. Support was varied along the gallery as listed in Tab. 1, with "shotcrete only" and an "arches only" ISS section.

Problems with cracks and large displacements in the shotcrete section led to the application of an additional 8 cm shotcrete layer from GM 9 – GM 18 together with steel rock bolts. The shotcrete showed some local deformations and ovality and the floor was subsequently replaced between GM 9 – GM 38. No significant problems were encountered in the ISS (steel arch only section). Breakout disturbance was observed at about 2 – 3 o'clock and persisted along the gallery. The overall excavation speed was about 1 m/day where steel arches were installed and about 1.5 m/day in regions without arches.

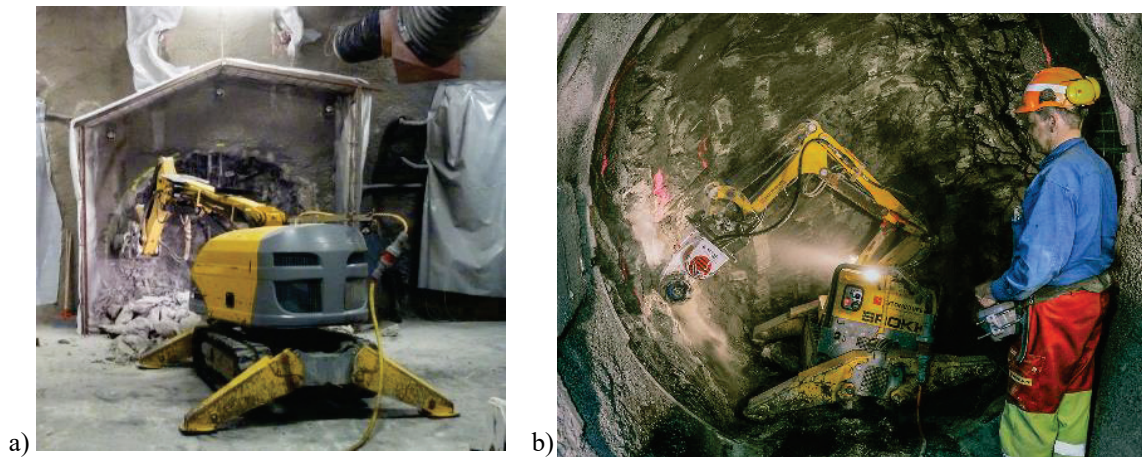


Fig. 5: Excavation of FE Gallery a) pneumatic hammer from FE-A Niche, b) profiling using road header

Note: Picture on the right: © Comet Photoshopping, Dieter Enz

Tab. 1: Support used in excavation of FE Gallery

Section	Support	Section	Anchors
GM 0-9 YFE 4.7-13.7	Shotcrete thickness 19 cm & steel arches (1 m spacing)		
GM 9-18 YFE 13.7-22.7	Shotcrete thickness 24 cm	GM 12.30-18.3 YFE 17-23	2.5 m GRP rock bolts, axial spacing 1.5 m
GM 18-38 YFE 22.7-42.7	Shotcrete thickness 16 cm	GM 19.8-37.8 YFE 24.5-42.5	7.5 m steel rock bolts, axial spacing 1.5 m
GM 38-50 YFE 42.7-54.7	No shotcrete only steel arches and mesh		

Once excavated additional instrumentation was emplaced either immediately after excavation or during the open tunnel period prior to EBS emplacement. Boreholes drilled from the tunnel were used for 4-point extensometers and mini-multi packer systems. Sensors included:

- continuous deformation monitoring using 60 reflectors in twelve 5-point sections
- two borehole extensometer arrays
- load cells within the shotcrete

### FE borehole array

There are 95 boreholes drilled around the FE site organised into the BFEA, BFEB, BFEC and BFEE borehole groups. Fig. 6 shows the complete array of boreholes. After excavation the 55 BFEB boreholes were drilled. All boreholes were drilled radially out from FE Gallery with the exception of BFEB048 (end of tunnel). A further 21 BFEC boreholes were also drilled, except for BFEC054, all these boreholes were also approximately radial to the gallery. Details of the BFEB, BFEC and BFEE boreholes are given in Appendix B.

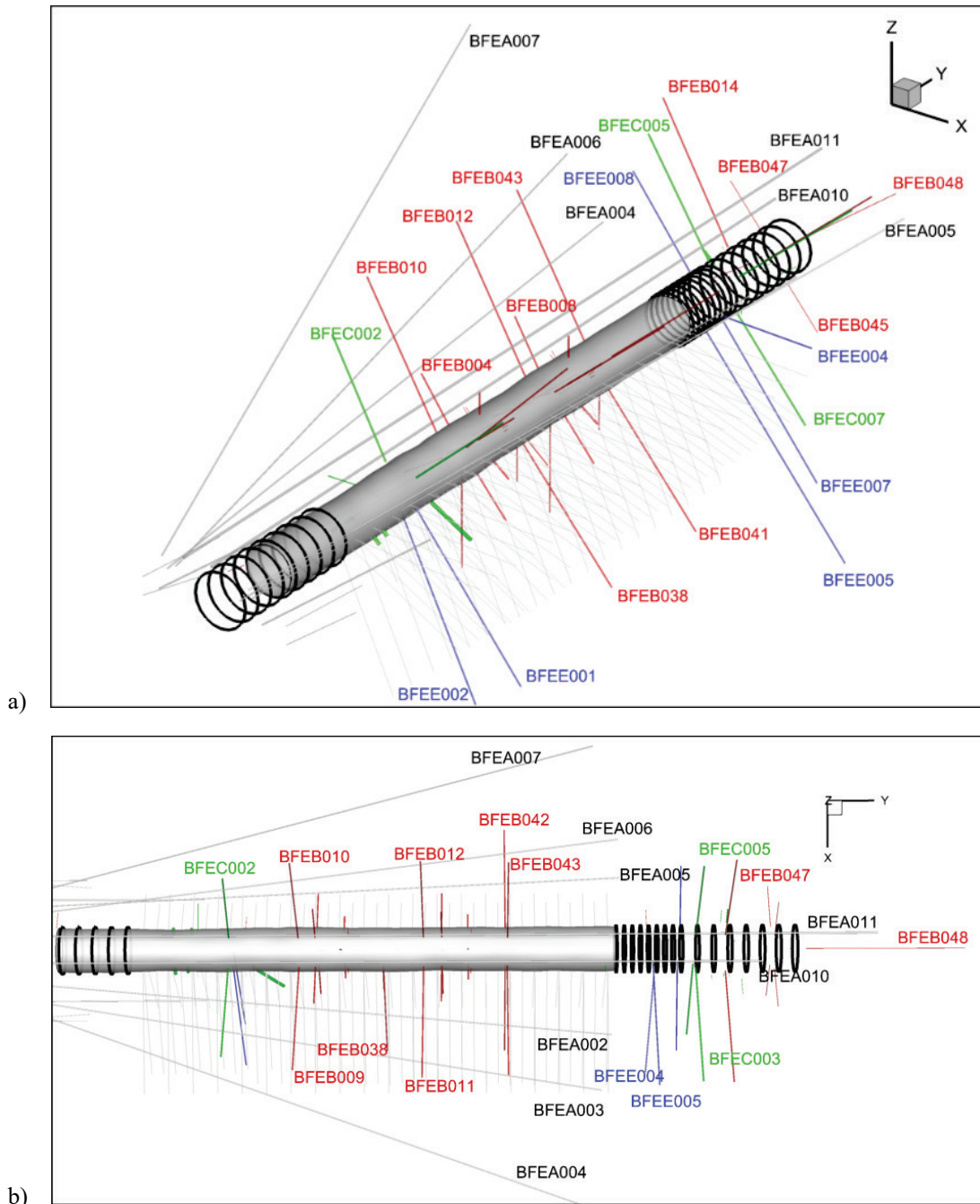


Fig. 6: 3D and plan view of FE tunnel showing boreholes, anchors, shotcrete and steel sets  
BFEA boreholes red, BFEB boreholes red, BFEC boreholes green, BFEE boreholes blue

Tab. 2 lists the BFEA boreholes drilled from the FE-A Niche (see Fig. 4). BFEA002-BFEA007 were equipped with multi-packer systems to monitor the response to excavation and subsequent evolution of the nearfield. Details of these borehole completions are given in Appendix C.

Tab. 2: BFEA boreholes drilled sub-parallel to FE Gallery from FE-A Niche

<b>Borehole</b>	<b><i>Start Section</i></b>	<b><i>End Section</i></b>	<b>Length (m)</b>	<b>Instrumentation</b>
BFEA002	<i>Niche</i>	<i>Gap 0 (ISS)</i>	38.4	6 intervals: temperature, pressure and packer pressure
BFEA003	<i>Niche</i>	<i>Heater 1</i>	38.2	6 intervals: temperature, pressure and packer pressure
BFEA004	<i>Niche</i>	<i>Heater 1</i>	40.2	6 intervals: temperature, pressure and packer pressure
BFEA005	<i>Niche</i>	<i>Gap 0 (ISS)</i>	38.8	6 intervals: temperature, pressure and packer pressure
BFEA006	<i>Niche</i>	<i>Gap 0 (ISS)</i>	39.5	6 intervals: temperature, pressure and packer pressure
BFEA007	<i>Niche</i>	<i>Heater 1</i>	40.1	6 intervals: temperature, pressure and packer pressure
BFEA008	<i>Niche</i>	<i>Plug</i>	13.5	1 interval: temperature, pressure and packer pressure
BFEA009	<i>Niche</i>	<i>Plug</i>	13.3	1 interval: temperature, pressure and packer pressure
BFEA010	<i>Niche</i>	<i>Porous Concrete Backfilling</i>	48.1	Inclination 80 sections, 40 temperature sensors
BFEA011	<i>Niche</i>	<i>Rock</i>	55.1	Inclination 80 sections, 40 temperature sensors
BFEA012	<i>Tunnel Entrance</i>		6.0	1 interval: temperature and pressure
BFEA013	<i>Tunnel Entrance</i>		6.1	1 interval: temperature and pressure
BFEA014	<i>Niche</i>	<i>Tunnel Entrance</i>	6.1	1 interval: temperature and pressure
BFEA015	<i>Niche</i>	<i>Tunnel Entrance</i>	6.0	1 interval: temperature and pressure

### 2.2.1 Measured response to excavation

Pore pressures were monitored in the six boreholes BFEA002-7 drilled from the FE-A Niche. Each borehole was equipped with a multi-packer system with six monitoring intervals (see Appendix C). Interval temperatures and the six packer pressures were also monitored.

The geometry of the boreholes (see Fig. 4) is such that the i6 intervals are closest to the FE Tunnel wall and the i1 intervals furthest from the gallery wall. The intervals are arranged roughly on vertical planes along the gallery such that intervals with the same number are within 1 m of the same distance along the gallery. BFEA002 (parallel to bedding) and BFEA005 (normal to bedding) intervals are within two diameters of the tunnel axis, while BFEA004 (parallel to bedding) and BFEA007 (normal to bedding) are beyond three diameters.

Fig. 7 shows the pore pressure response in the six boreholes. The influence of the open FE-A Niche can be seen in the data from intervals i4 - i6 which show a range of pre-excitation pressure. Intervals i1-i3 show undisturbed pore pressures  $\sim 2'000\text{kPa}$ . Almost all intervals show a pressure rise as the face approaches followed by a subsequent pressure fall and recovery. Pressure typically starts to rise 10 – 20 m ahead of the face and peaks about 2 m ahead of the face. The response to excavation is greatest in the boreholes closest to the excavation BFEA002 and BFEA005. Pore pressure in BFEA002 i6 drops to near atmospheric pressure but then recovers.

Such pore pressure responses can be expected in low-permeability rock where volumetric strain changes induced by excavation result in pore pressure change which is essentially undrained due to the very low hydraulic diffusivity of the intact rock (Wild et al. 2015). In addition to this poro-elastic response to excavation, any yield or micro-fracturing may result in dilation (and consequent pore pressure change) or in the case of macro-scale fracturing, possible connection and drainage to the excavation. To discriminate such responses, it is necessary to compare with the expected elastic response (Martin & Lanyon 2003).

The FE Gallery was equipped with both convergence arrays and extensometers installed in radial boreholes (arrangement shown in Fig. 8). There were nine total convergence sections (see Tab. 3) and two radial extensometer sections (Tab. 6). Each convergence section contained either five or seven targets located at standardized positions around the tunnel profiles. The radial extensometers included four measurement anchors at 1, 2, 3 and 6 m from the tunnel wall (Eiholzer 2012).

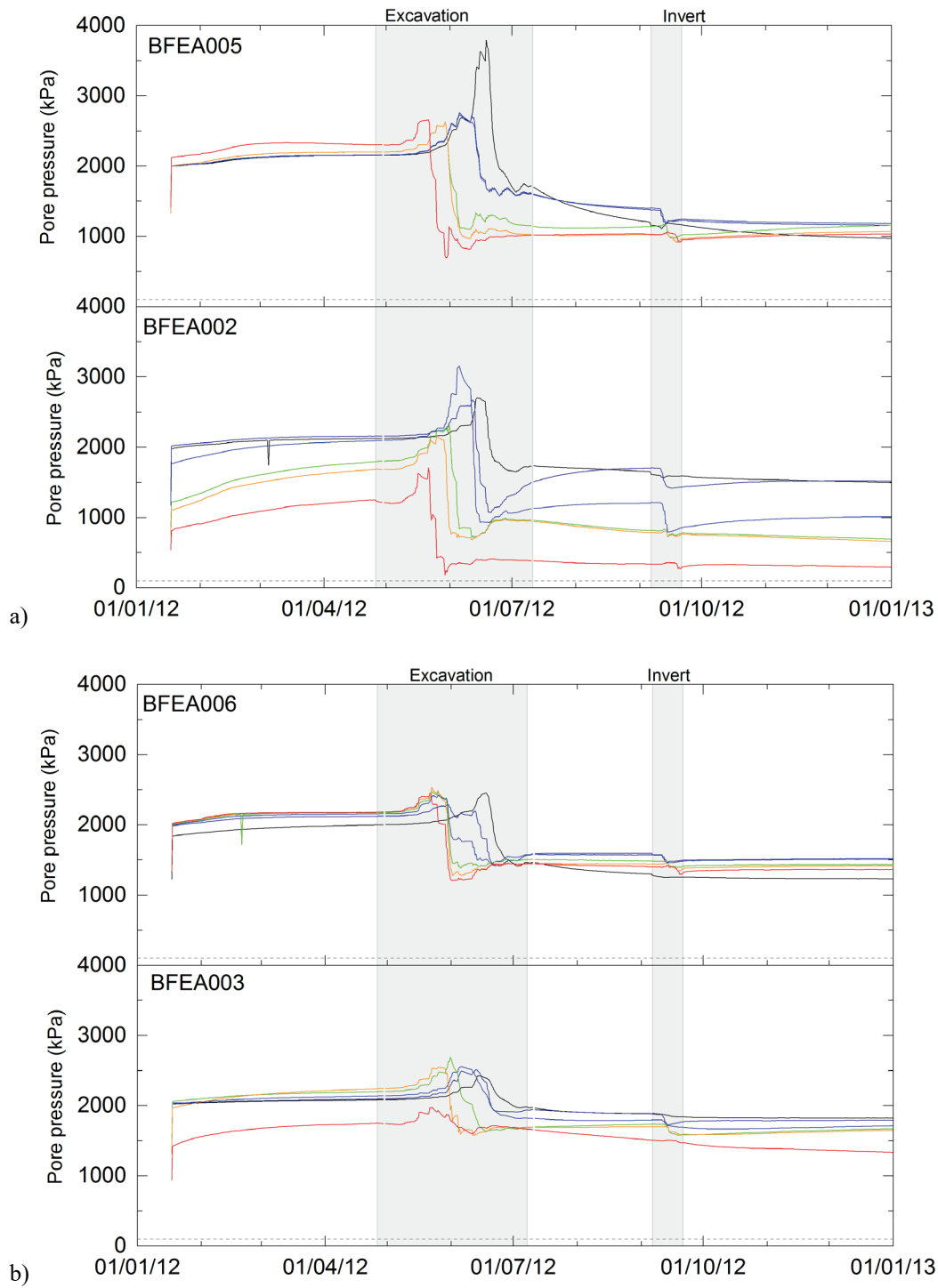
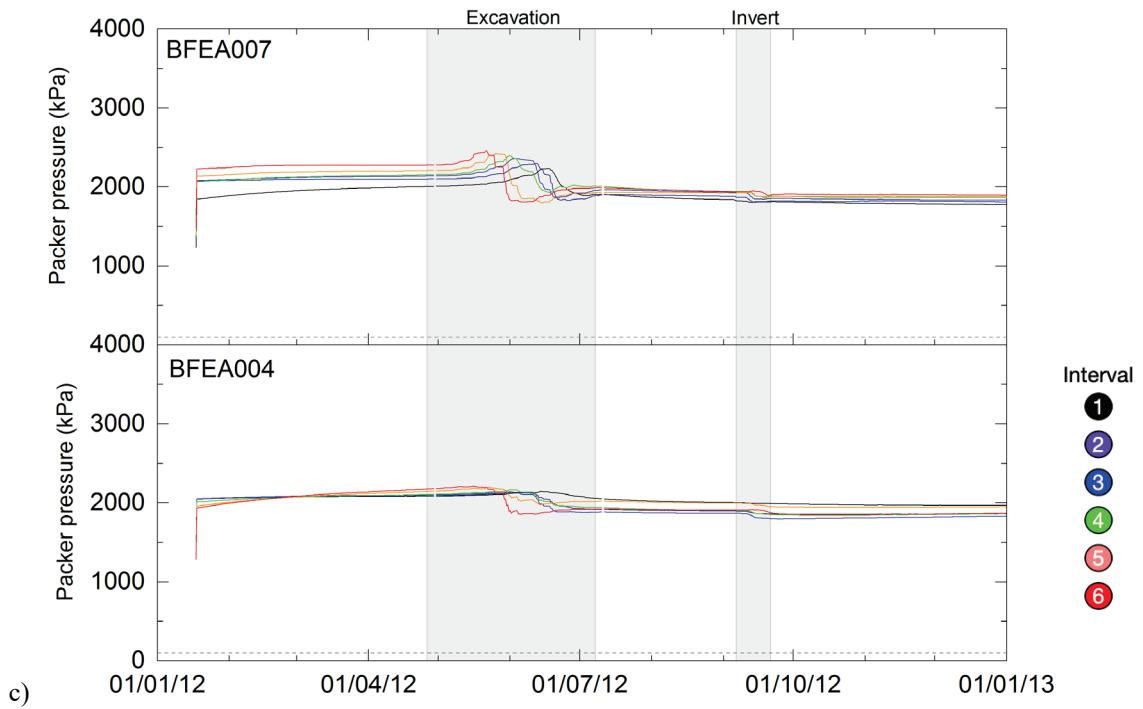


Fig. 7: Pore pressure response to FE Gallery excavation in monitoring borehole array



c) Fig. 7: Cont

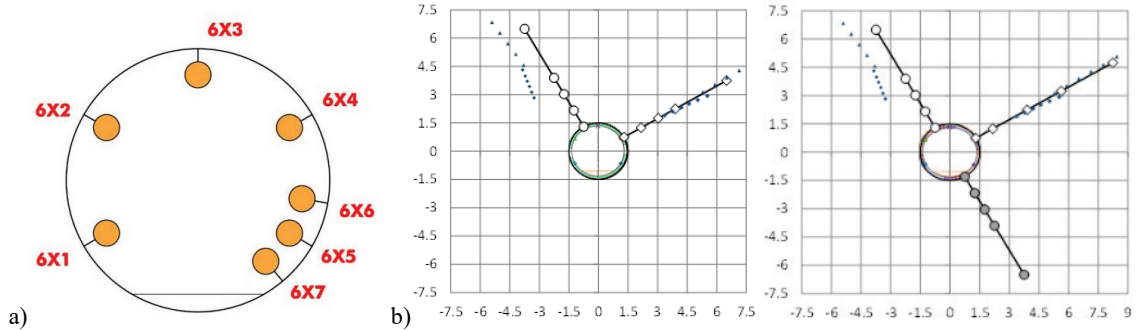


Fig. 8: Geometry of FE Gallery convergence sections and extensometer sections  
 a) convergence measurement numbering convention X = section number C0-9, for pin positions P1-7. b) vertical sections showing extensometer intervals at sections E1 (BFEC001,2) and E2 (BFEC003,4,5)

Tab. 3: Convergence sections in FE Gallery

Section	GM	Y <sub>FE</sub> (m)		Support	Pins	Install
C0	5.1	9.8	Tunnel Entrance	19 cm shotcrete + steel arches	601 – 605	09.05.2012 05:00
C1	10.6	15.3	Plug	24 cm shotcrete	611 – 615	15.05.2012 19:00
C2	14.3	19	Plug	24 cm shotcrete	621 – 625	22.05.2012 04:30
C3	21.8	26.5	Heater 3	16 cm shotcrete	631 – 635	31.05.2012 15:40
C4	27.6	32.3	Heater 2	16 cm shotcrete	641 – 645	11.06.2012 22:00
C5	34.3	39	Heater 1	16 cm shotcrete	651 – 657	18.06.2012 22:10
C6	43.6	48.3	Gap 0 (ISS)	Steel arches + mesh	661 – 667	29.06.2012 20:00
C7	44.2	48.9	Gap 0 (ISS)	Steel arches + mesh	671 – 677	28.06.2012 22:10
C8	48.5	53.2	Porous concrete backfilling	Steel arches + mesh	681 – 687	09.07.2012 22:10
C9	49.3	54	Porous concrete backfilling	Steel arches + mesh	691 – 697	09.07.2012 22:10

The measured radial convergence for each pin against distance behind the face is shown in Fig. 9. The largest convergence was measured at P5 in the "shotcrete only" section (C1-C5). It is also noticeable that convergences continued to develop after the face was beyond 15 m from the pin (5 diameters). The P5 pin is located near the invert at the base of the north-east wall in a region where disturbed tectonic fault planes were observed. These fault planes are associated with a fault zone present from 14.5 m onwards in the gallery. Convergences in the "arches only" section (C6-C9) were heterogeneous with displacements being focused between the arches (e.g. C7). The convergences one month after the end of excavation (08.08.2012) are presented in Tab. 4 and as normalised strains in Tab. 5. The high strains at P5 in the "shotcrete only" section range from 2.4 to 4 %. Tunnel face maps along the FE Gallery are shown in Fig. 10.

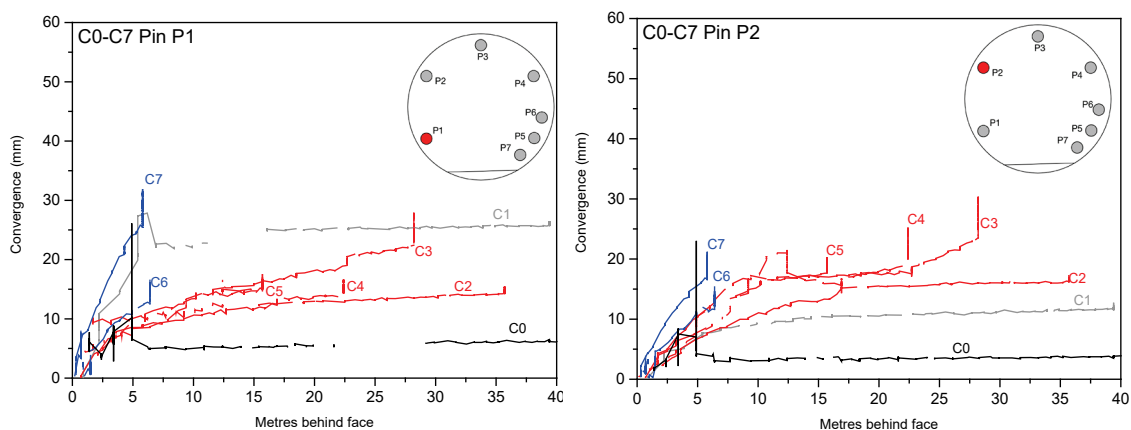


Fig. 9: FE Gallery Convergence measurements versus distance behind excavation face for P1-P7

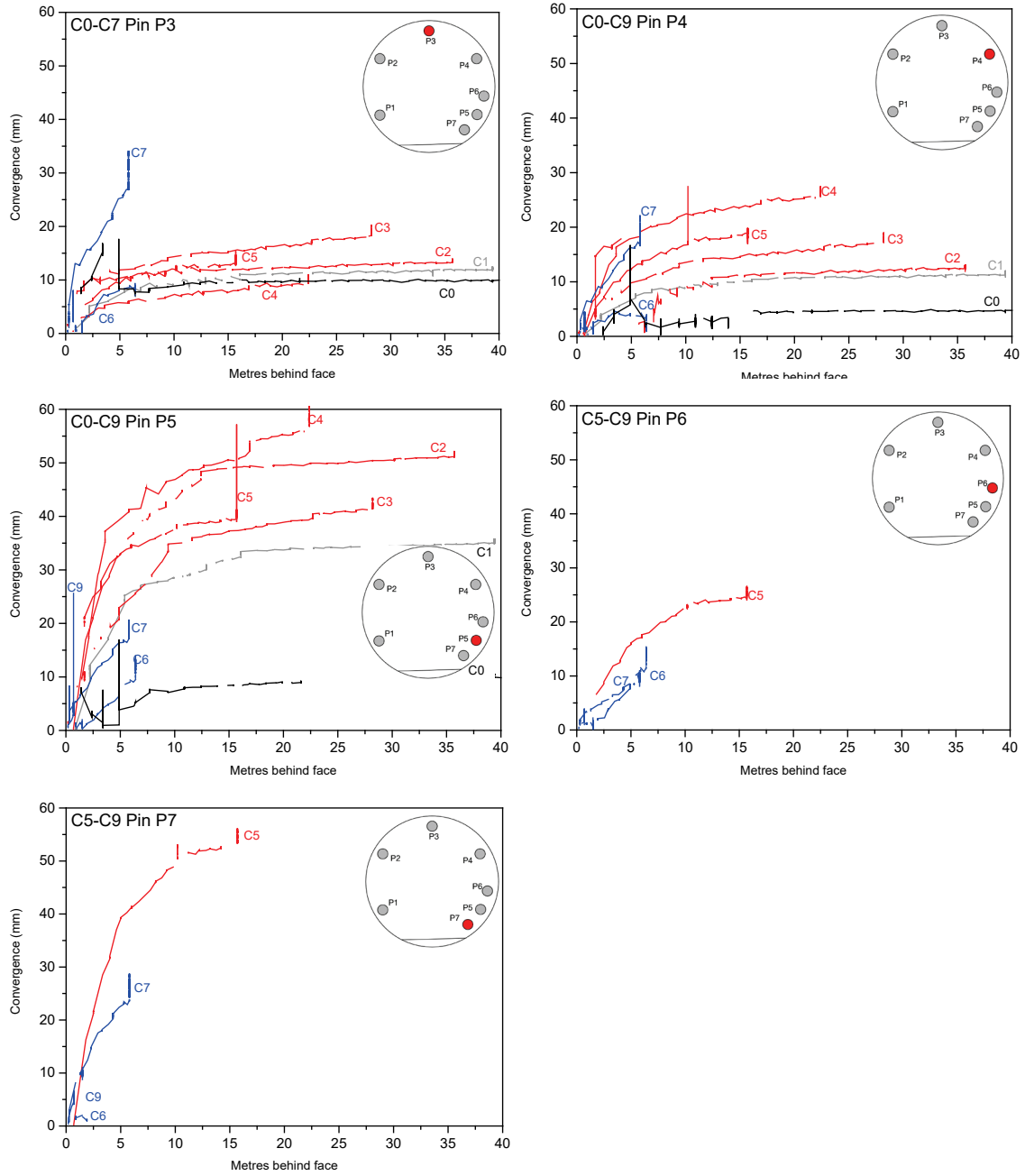


Fig. 9: Cont.

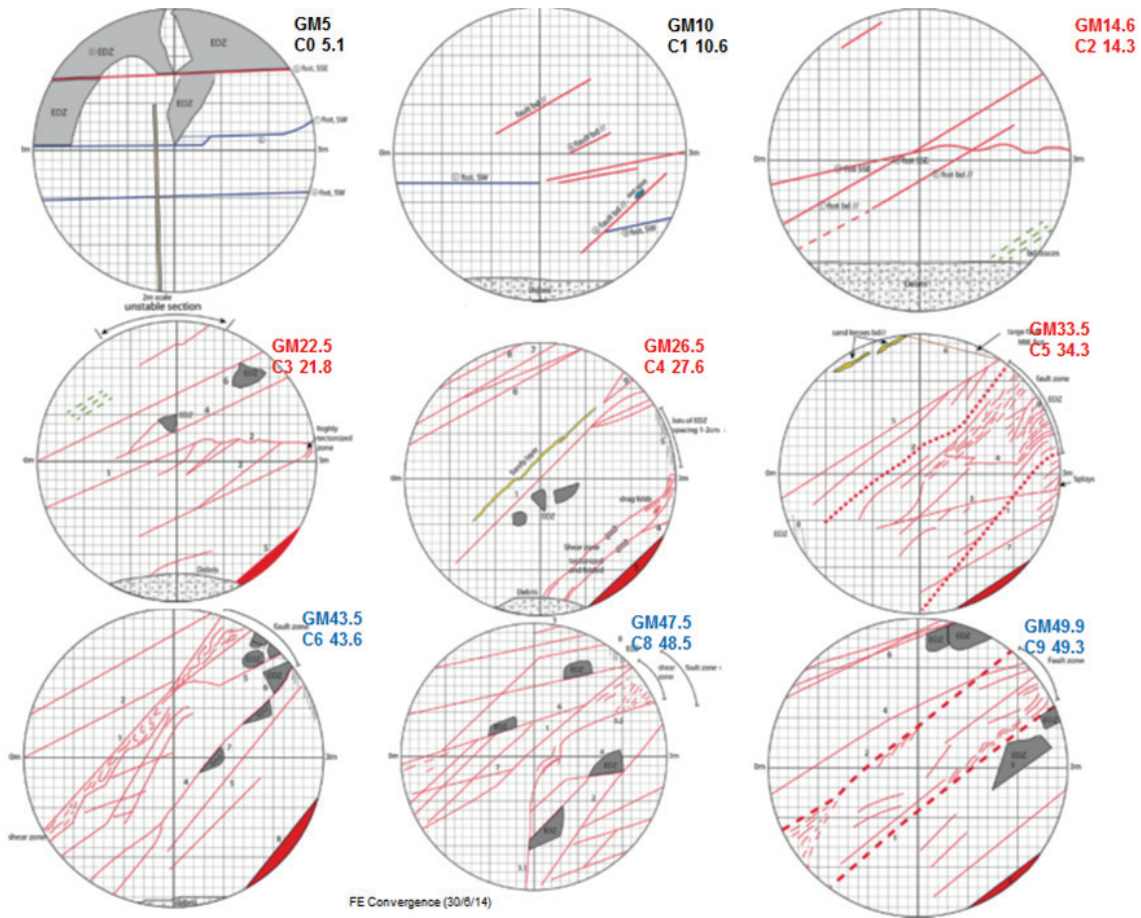


Fig. 10: Geological mapping of excavation face of FE Gallery at approximate locations of convergence sections

From Jaeggi et al. (2012)

Tab. 4: Measured convergences in FE Gallery approximately one month after excavation

Convergence section			Days after excavation	Behind face (m)	P1 (mm)	P2 (mm)	P3 (mm)	P4 (mm)	P5 (mm)	P6 (mm)	P7 (mm)
C0	C1	Date									
C0	5.1	08.08.2012	92.08	44.90	6.51	4.25	10.07	4.80	10.25		
C1	10.6	08.08.2012	85.17	39.40	11.79	26.23	12.30	11.89	35.56		
C2	14.3	08.08.2012	78.97	35.70	16.65	15.06	13.74	12.96	51.93		
C3	21.8	08.08.2012	68.97	28.20	29.25	26.64	19.83	18.55	42.90		
C4	27.6	08.08.2012	58.08	22.40	23.76	16.06	10.70	27.01	59.45		
C5	34.3	08.08.2012	51.10	15.70	18.98	16.41	14.53	18.64	40.68	25.98	55.09
C6	43.6	08.08.2012	41.29	6.40	13.59	14.95	7.64	1.50		14.36	
C7	44.2	08.08.2012	41.04	5.80	19.63	30.55	33.17	21.21	19.65	10.22	27.81
C8	48.5	08.08.2012	30.33	1.50	3.18	2.26	1.81	2.50	1.58	1.63	9.50
C9	49.3	08.08.2012	30.00	0.70	1.84	6.58	7.14	3.99	4.85	3.27	5.50

Tab. 5: Measured strain normalised to gallery radius

	Gallery support	P1	P2	P3	P4	P5	P6	P7
C0	Shotcrete + arches	0.4 %	0.3 %	0.7 %	0.3 %	0.7 %		
C1	Shotcrete only	0.8 %	1.7 %	0.8 %	0.8 %	2.4 %		
C2		1.1 %	1.0 %	0.9 %	0.9 %	3.5 %		
C3		1.9 %	1.8 %	1.3 %	1.2 %	2.9 %		
C4		1.6 %	1.1 %	0.7 %	1.8 %	4.0 %		
C5		1.3 %	1.1 %	1.0 %	1.2 %	2.7 %	1.7 %	3.7 %
C6	Arches only	0.9 %	1.0 %	0.5 %	0.1 %		1.0 %	
C7		1.3 %	2.0 %	2.2 %	1.4 %	1.3 %	0.7 %	1.9 %
C8		0.2 %	0.2 %	0.1 %	0.2 %	0.1 %	0.1 %	0.6 %
C9		0.1 %	0.4 %	0.5 %	0.3 %	0.3 %	0.2 %	0.4 %

Radial extensometers were installed in five boreholes located in two sections: E1 at GM 14.6 (BFEC001, 2) in the "shotcrete only" section and E2 at GM 43.1 (BFEC003, 4, 5) in the "arches only" section. Each extensometer was equipped with four sections and installed to 6 or 8 m into the rock. The calculated strains are plotted in Fig. 11.

Tab. 6: Extensometer sections in FE Gallery

Section	Boreholes			Pin	Interpretation
E1 GM 14.6 Y <sub>FE</sub> 19.3 Shotcrete only	BFEC001	6 m	⊥	C2P4	Significant displacement beyond 6 m
	BFEC002	6 m	∥	C2P3	Extensometer consistent with convergence. No significant displacement beyond 6 m
E2 GM 43.1 Y <sub>FE</sub> 47.8 Arches only	BFEC003	8 m	∥	C6P4	Significant displacement beyond 8 m
	BFEC004	6 m	⊥	C6P7	Significant displacement beyond 6 m
	BFEC005	6 m	⊥	C6P3	Significant displacement beyond 6 m

At E1 the largest strains were measured in BFEC002 (normal to bedding) between 1 – 3 m. Strains continued to increase during excavation. At E2 strains were largest in BFEC004 (normal to bedding) between 1-3 m into the floor.

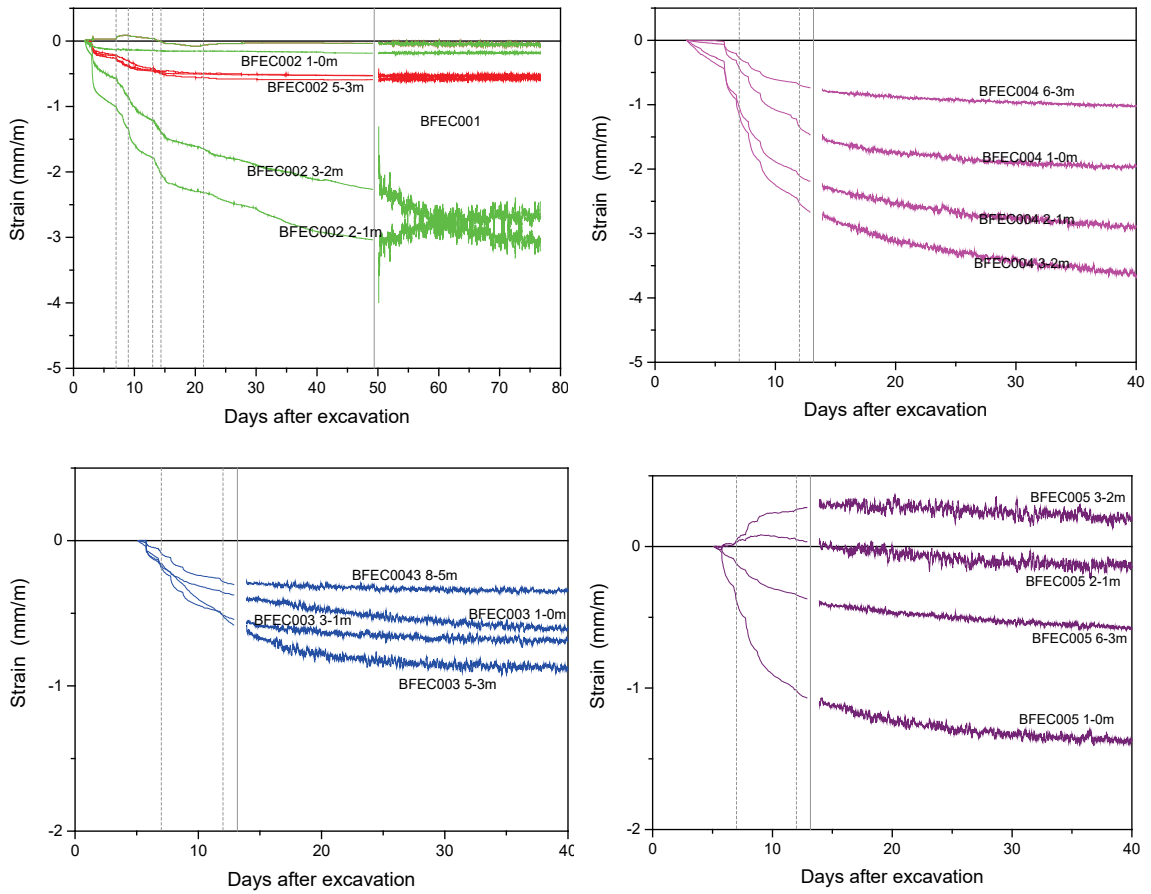


Fig. 11: Measured strains versus days after excavation for extensometers at E1 and E2 sections of FE Gallery

Strain profiles from the extensometer data (at 06.08.2012) show a significant difference between the normal to bedding direction (BFEC002, BFEC004, BFEC005) and the along bedding direction (BFEC001, BFEC003). The strain normal to bedding appears to be strongly localized in a high strain zone (0.2 – 0.4 %) close to the tunnel wall while strain along bedding shows a more uniform distribution (~ 0.05 – 0.1 %) potentially extending further from the tunnel wall. The profile for BFEC004, also normal to bedding, shows a rather different distribution (see Fig. 12) which may indicate significant heterogeneity in the strain profile.

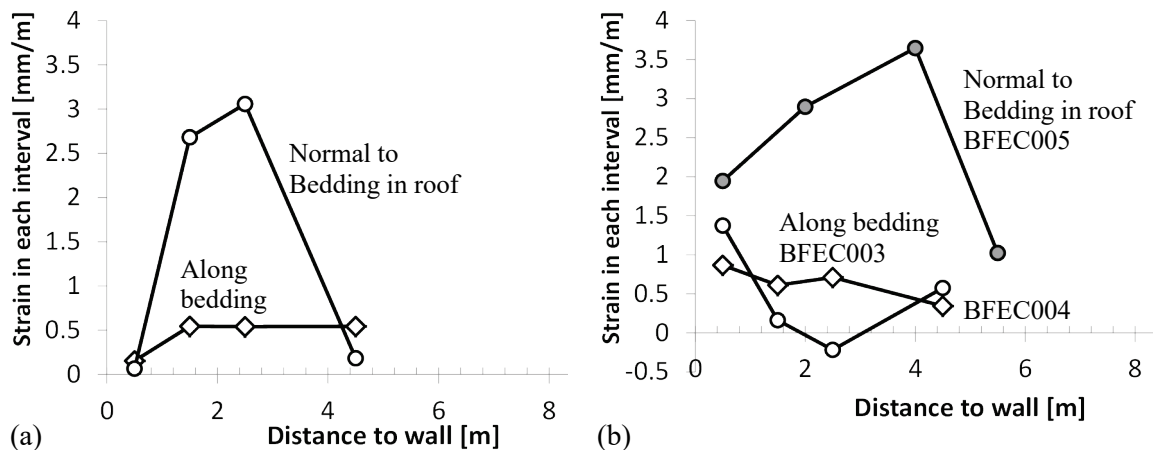


Fig. 12: Strain profiles in tunnel wall at (a) E1 (GM 14.6 shotcrete only) and (b) E2 (GM 43.1 arches only) on 06.08.2012

Differences between the response of the radial extensometers and convergence measurements can be due to:

- deformation beyond the end of the extensometer (E1, E2)
- differences in installation date (E1)
- localized greater convergence between arches (section E2)
- measurement of total rather than radial convergence

In the E1 section (shotcrete-only) comparison was straightforward indicating good agreement for the displacement parallel to bedding but significantly greater displacement in the convergence data than for the extensometer normal to bedding - suggesting displacement beyond the end of the extensometer (see Fig. 13).

In the E2 section (arches only) comparison is more difficult because displacements were typically small on the arches (section C6) but much greater between the arches (C7). How these heterogeneous displacements at the tunnel wall are redistributed within the rock is likely to be complex. Arches are placed at 1 m intervals and the extensometer section E2 is located 0.5 m from C6 (on the arch). If we compare the extensometer data with convergence data from C7 (between arches) then there appear to be significant displacements beyond the ends of the extensometers. If we compare with C6 data (on the arch) the two sets of displacements are comparable.

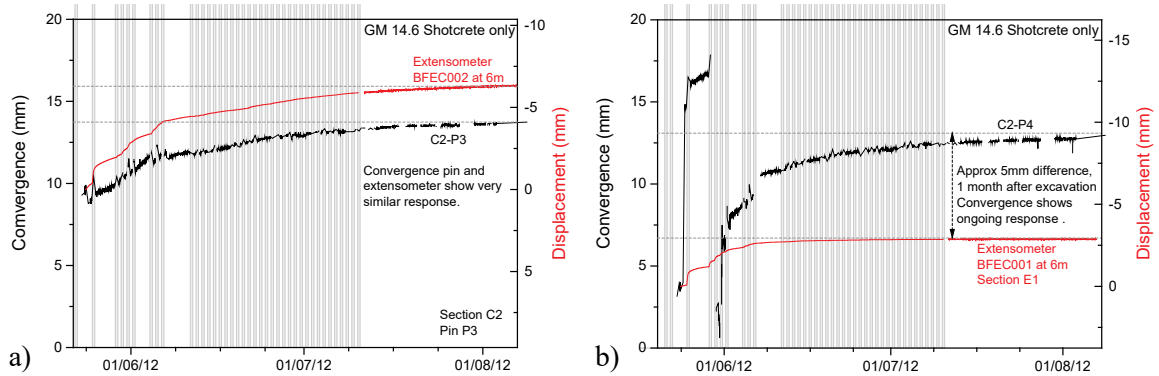


Fig. 13: Comparison of convergence and extensometer response, parallel to bedding (left) and normal to bedding (right) for FE Gallery

**2.2.2 Open tunnel period**

After excavation, the FE Tunnel remained open and ventilated until emplacement of the EBS started in July 2014. Fig. 14 shows the measured climate conditions in the FE-A Niche during this period. Temperature was maintained at 16 – 17 °C and the relative humidity varied between 50 and 80 % (although data during summer periods is not plotted). The ongoing ventilation will have dried the shotcrete and exposed Opalinus Clay in the ISS section. The extent to which the rock behind the shotcrete desaturated is uncertain and is likely to be heterogeneous and transient (Shao et al. 2016).

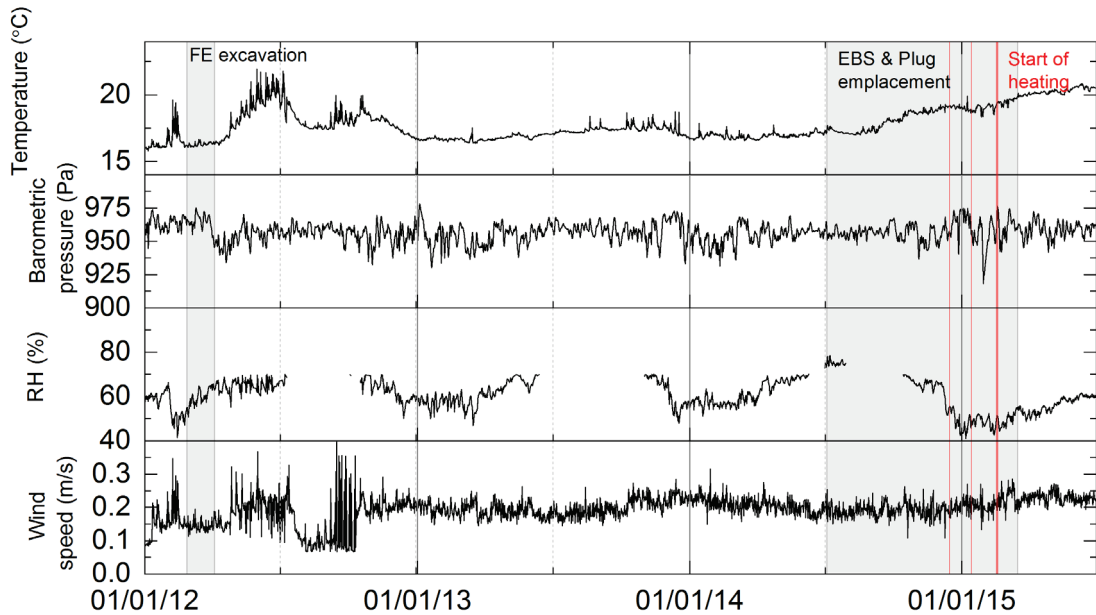


Fig. 14: Climate in the FE-A Niche from 01.01.2012 to 01.07.2015 covering period when FE Gallery was open and ventilated  
 Plug emplaced on 17.03.2015. Heating had started prior to plug emplacement.

## Pore pressure

Pore pressures around the tunnel during this period showed a strong response to replacement of the invert in September 2012 and then showed further responses in October 2013 with pressure responses seen in several of the intervals. On 09.10.2013 intervals i4,i5 and i6 of BFEA006 ( $Y_{FE}$  16.7-26.2) all dropped by  $\sim 200$  kPa and associated pressure drops were seen in interval i5 of BFEA005, interval i5 and i6 of BFEA007, intervals i2 and i3 of BFEA003. Small drops were also seen in BFEA002. Between 12.08 and 19.12.2013 several drilling and instrumentation activities took place which probably caused the observed pressure variations (Trick et al. 2014).

Hydraulic pulse tests were performed in several intervals of the multi-packer systems on 27.05.2014 and 26.06.2014. Hydraulic conductivity ranged from  $10^{-13}$  to  $7 \times 10^{-11}$  m/s with a geometric mean of  $10^{-12}$  m/s (see Appendix C). The results indicate higher permeability intervals may exist at greater radial distance in the direction normal to bedding. Hydraulic conductivity is less than  $10^{-12}$  m/s for the two parallel to bedding intervals beyond 5 m radius, while the two normal to bedding intervals are both above  $10^{-12}$  m/s. Rösli et al. (2016) comment that the transmissivities estimated from pulse tests are somewhat higher than those from the HI tests and that this may relate to the smaller radius of investigation of these tests.

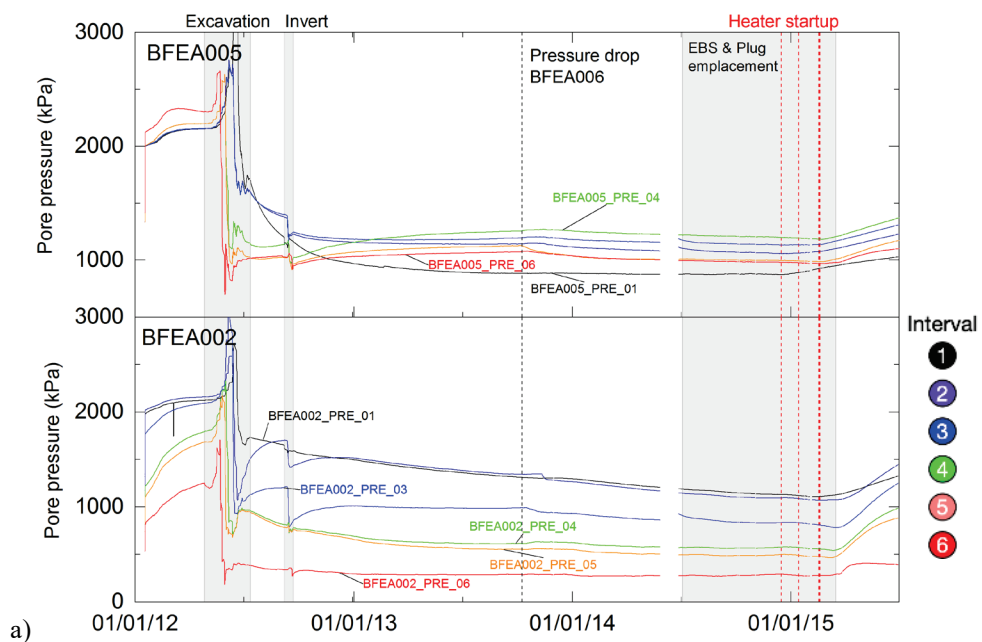


Fig. 15: BFEA multipacker system response during open tunnel period

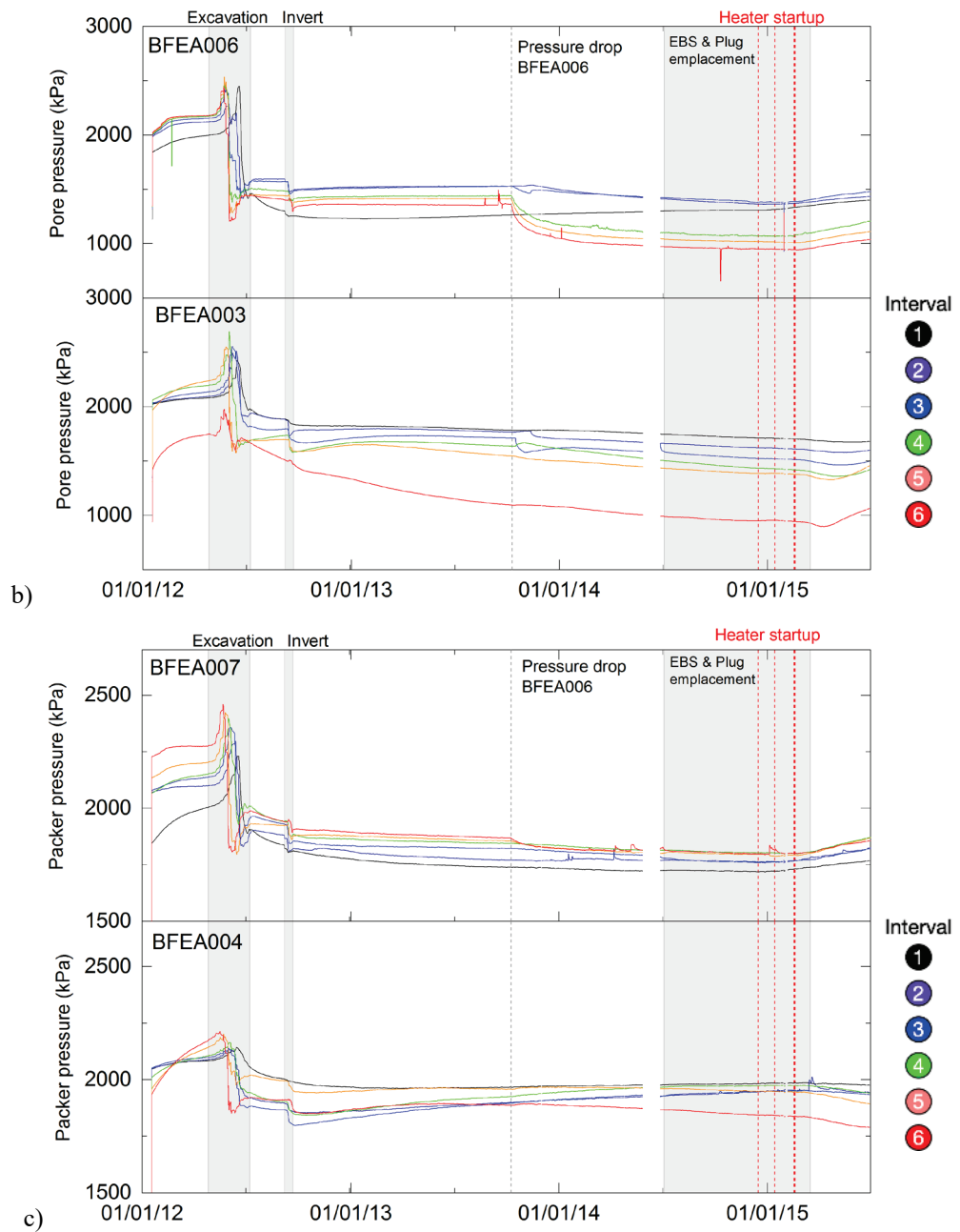


Fig. 15: Cont.

Hydraulic tests in the Excavation Damaged Zone (EDZ) were also performed in a mini-multi-packer system in BFEC019 (horizontal borehole at GM 13.9) between 04.07.2013 and 08.08.2013 (Trick et al. 2013). The short interval tests showed hydraulic conductivity between  $7 \times 10^{-13}$  (1.6 – 1.7 mah) to  $1.2 \times 10^{-10}$  m/s (0.81 – 0.92 mah). The initial pressure showed a strong decline from ~ 422 kPa to 67 kPa (gauge heights were not recorded).

**Deformation**

Fig. 16 shows linear and log-linear plots of the measured convergences at C4 and C7. Convergences were in the range 10-40 mm up to about day 100 in both sections for all but P5 at C4. After concreting of the invert, convergence increased sharply at C4 (shotcrete only) and then

quickly stabilized with almost stable deformations after this. At C7 (steel arches only) deformations continued with a roughly log-linear increase.

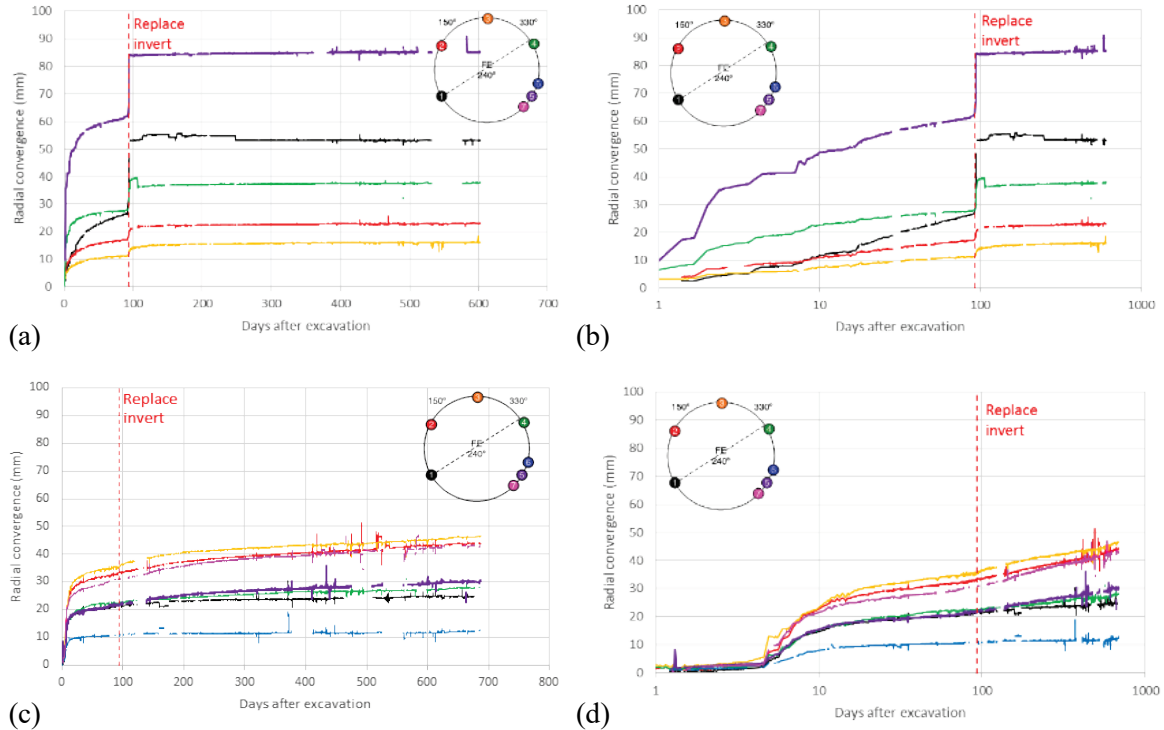


Fig. 16: Linear and log-linear plots of total convergence measured at FE Gallery  
(a), (b) C4 (GM 27.6 shotcrete only) and (c), (d) C7 (GM 44.2 – steel arches only) sections

### Wet spot observations

During excavation a series of transient wet spots were observed at the excavation face. These were located at the start of the tunnel at GM 2.7, 5, 5.1 and 10.2. These features ceased to flow as excavation progressed.

Subsequently additional wet spots were identified during the open tunnel period in 2013 and 2014. Many of the wet spots in the FE tunnel were associated with rock bolts or grouting tubes that perforated the shotcrete. A moist area was also observed around a small crack in the shotcrete. The wettest features were associated with grouting tubes. The wet spots are listed in Tab. 7 and shown in Fig. 18. Approximately 25 % of the 128 rock bolts were associated with wet spots and only two of the extensometer boreholes in the shotcrete section (BFEB038 and BFEB041) are not associated with a grouting tube wet spot.

No similar wet spot features were identified in the ISS section, despite their occurrence close to the end of the shotcrete at GM 38. It is likely that the rock bolts and grouting tubes provided a focus for flow from the rock such that the local flux (flow per unit area) was sufficient to overcome drying by the ventilation<sup>1</sup>. Fig. 17 shows example wet spots. For further discussions of wet spot occurrence at Mont Terri and relationship to ventilation see Becker & Vogt (2019) and Lanyon (2019b).

<sup>1</sup> There may also have been some water/moisture associated with the grout injection.

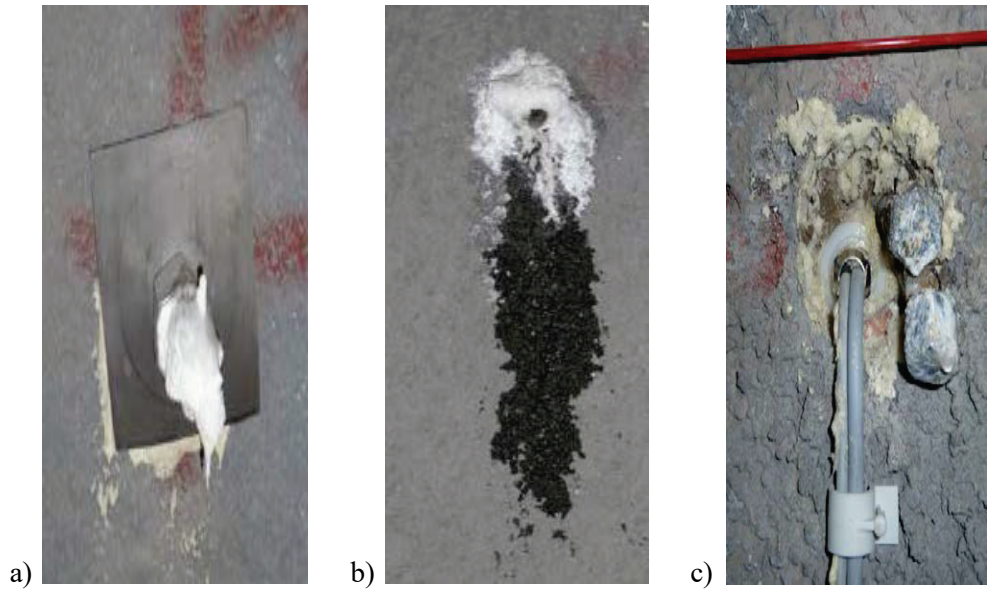


Fig. 17: Examples of wetspots in the FE tunnel after excavation  
 a) rock bolt head at GM 16.9, b) small crack in shotcrete at GM 36.5, c) extensometer grouting tubes in BFEB009

Tab. 7: Wet spot locations and related features  
 From Firat Lüthi (2018)

GM	Position	Related to	Comment	
9.4	05:30	Rock bolt	Moist	2014
12.5	03:00	Rock bolt	Moist	2014
12.5	03:30	Rock bolt	Moist	2014
13.9	03:00	Rock bolt	Moist	2014
14.2	05:30	Rock bolt	Moist	2013 post excavation
14.8	11:00	BFEC002, grout tubes	Wet	2013 post excavation
15.7	05:30	Rock bolt	Moist	2013 post excavation
16.2	03:30	Rock bolt	Moist	2014
16.9	03:00	Rock bolt	Moist	2013 post excavation
17.2	05:30	Rock bolt	Moist	2013 post excavation
17.7	03:30	Rock bolt	Dry but dark coloured	2014

Tab. 7: Cont.

GM	Position	Related to	Comment	
19.0	02:00	BFEB009, grout tubes	Wet	2014
19.0	11:00	BFEB010, grout tubes	Wet	2014
20.0	03:30	Rock bolt	Moist	2013 post excavation
20.0	11:00	BFEB004, grout tubes	Moist	2014
21.4	03:00	Rock bolt	Moist	2014
23.0	03:00	Rock bolt	Moist	2014
24.6	03:00	Rock bolt	Moist	2014
26.6	02:00	BFEB011, grout tubes	Wet	2014
26.6	03:30	Rock bolt	Moist	2014
26.6	11:00	BFEB012, grout tubes	Wet	2014
27.5	03:00	Rock bolt	Moist	2014
27.5	03:30	Rock bolt	Moist	2014
28.3	03:30	Rock bolt	Moist	2014
29.0	03:30	Rock bolt	Moist	2013 post excavation
29.7	03:30	Rock bolt	Moist	2014
30.4	03:00	Rock bolt	Moist	2014
30.4	05:30	Rock bolt	Moist	2014
31.6	02:00	BFEB040, grout tubes	Wet	2014
31.6	07:00	BFEB042, grout tubes	Very wet	2014
31.6	11:00	BFEB043, grout tubes	Moist	2014
32.0	03:00	Rock bolt	Moist	2013 post excavation
32.7	03:30	Rock bolt	Moist	2014
33.4	03:00	Rock bolt	Moist	2014
33.4	05:30	Rock bolt	Moist	2014
34.2	03:30	Rock bolt	Moist	2014
34.9	03:00	Rock bolt	Moist	2014
34.9	03:30	Rock bolt	Moist	2014
34.9	05:30	Rock bolt	Moist	2013 post excavation
36.5	03:00	Rock bolt	Moist	2014
36.5	03:30	Small crack	Moist	2013 post excavation
38.0	03:00	Rock bolt	Moist	2013 post excavation
38.0	05:30	Rock bolt	Moist	2014
<b>Associated feature</b>		<b>Count</b>	<b>Degree of moisture</b>	
Rock bolts		33	Moist (or dry with staining)	
Grouting tubes		9	Wet to very wet	
Small crack		1	Moist	

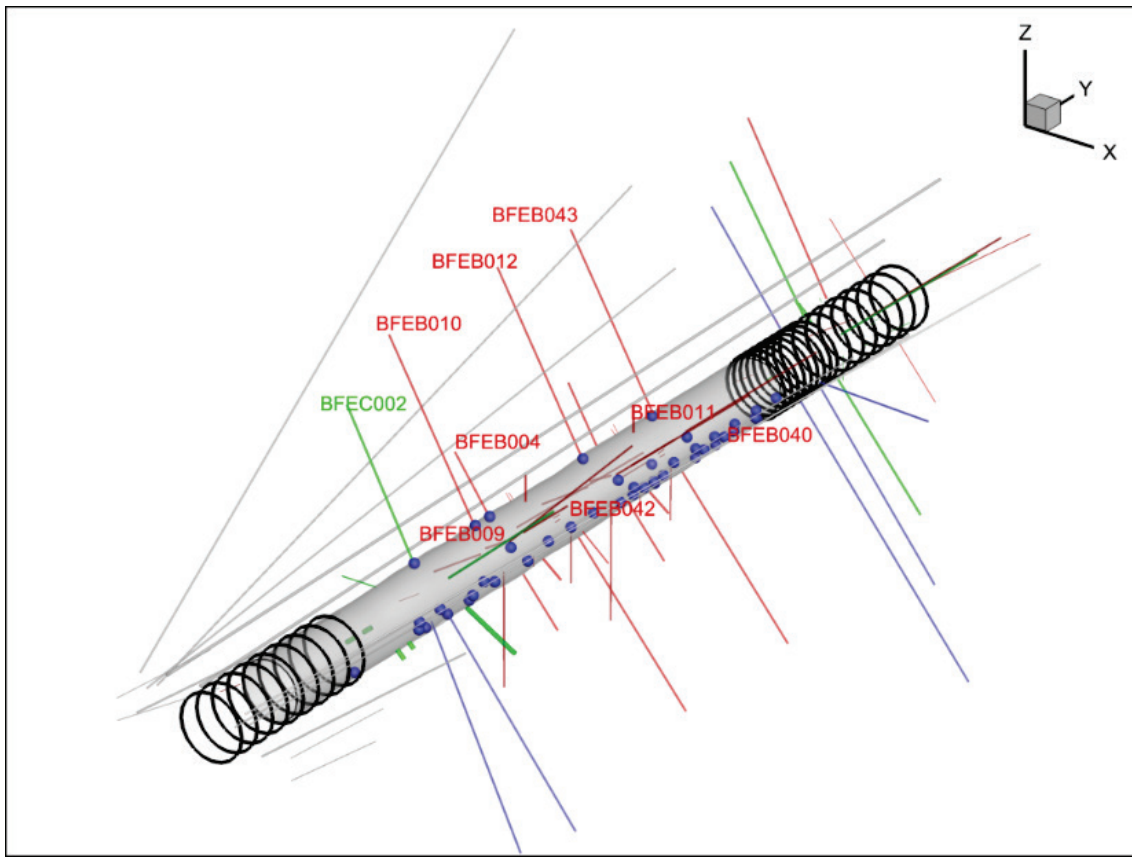


Fig. 18: Wetspots and associated boreholes where grouting tubes lead to observed wet spots

### 2.3 EBS emplacement and instrumentation

The overall layout of the FE Gallery is shown in Fig. 19. The gallery can be divided into a series of instrumentation sections as shown in Fig. 19b and listed in Tab. 8. The sections correspond to the heaters and backfill sections. The different sections and associated instrumentation are described below. In addition to the instrumentation sections a set of specific THM monitoring sections were also defined and are listed in Tab. 9.

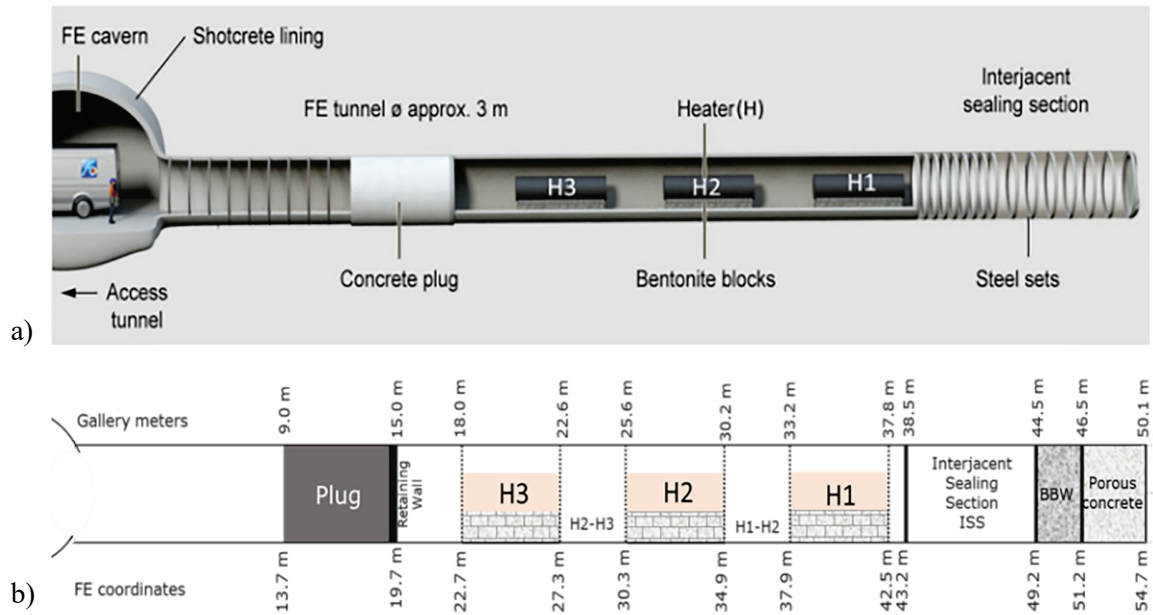


Fig. 19: FE Gallery layout a) schematic, b) instrumentation section positions

Tab. 8: Instrumentation sections in the FE Gallery

Section		$Y_{FE}$ (m)	FE GM	Length (m)
Tunnel Entrance		4.70	0.00	9.00
Plug		13.70	9.00	5.80
Retaining wall		19.70	14.80	0.2
Test Section	Gap GP	19.70	15.00	3.00
	Heater 3	22.70	18.00	4.60
	Gap 2-3	27.30	22.60	3.00
	Heater 2	30.30	25.60	4.60
	Gap 1-2	34.89	30.19	2.96
	Heater 1	37.85	33.15	4.60
	Gap 0	42.44	37.74	0.76
Gap 0 (ISS)		43.20	38.50	6.00
Bentonite Block Wall		49.20	44.50	2.00
Porous Concrete Backfilling		51.20	46.50	3.60
End of FE Gallery		54.80	50.1	

Tab. 9: Dedicated THM instrumentation sections in the FE Gallery

Section	THM Section	FE GM	Y <sub>FE</sub>
Plug	Plug	15	19.7
Gap GP	GP	16.4	21.1
Heater 3	H3-1	19	23.7
	H3-2	20.3	25
	H3-3	21.3	26
Gap 2-3	G2-3	24.1	28.8
Heater 2	H2-1	26.6	31.3
	H2-2	27.9	32.6
	H2-3	28.9	33.6
Gap 1-2	G1-2	31.7	36.4
Heater 1	H1-1	35.5	40.2
Gap 0 (ISS)	G1-1	41	45.7
	G0	43	47.7
Bentonite Block Wall	Block Wall	45	49.7
Porous Concrete Backfilling	Porous concrete	48	52.7

### Plug & Retaining wall (GM 9 – GM 15)

The Plug Section consists of a 5-m-long low-pH shotcrete plug that was used to seal off the experiment (from the FE-A Niche) holding the bentonite buffer in place and reducing air and water fluxes. The plug was constructed against a 20 cm thick concrete retaining wall sealed with resin.

The retaining wall was built in February 2015 from five specially constructed segments using bespoke formwork including openings for routing sensor cables. The segments were emplaced at the same time as the last of the granular bentonite mixture (GBM) was emplaced. The number of augurs were reduced as the height of the wall increased and the final section included a gap to allow emplacement of the last of the GBM using a single augur. The gap was then closed with concrete bricks and the retaining wall was sealed with two layers of resin in order to reduce vapour and gas transport.

On 17.03.2015, 31 m<sup>3</sup> of self-compacting concrete was pumped into the space between the retaining wall at GM 14.8 and formwork placed at GM 9.8. Forty days after pouring the gap (< 1 mm) between the shotcrete and the plug was sealed with 74.5 kg of resin (Sika®Injection-201).

In this section, the rock is supported by mesh-reinforced low-pH shotcrete.

### Test Section: GM 15 – GM 37.7

This section contains the 3 heaters (4.595 m long and 1.05 m in diameter) with 3 m gaps between them. The heaters were emplaced on bentonite block pedestals that sat on concrete bases (Fig. 20). The bases were emplaced on 04.09.2014 and were approximately 4.4 m long, 0.8 m wide and 115 mm high. The bentonite block pedestals were manually constructed directly on the concrete base. Each pedestal consisted of 132 rectangular blocks and 88 curved top layer blocks.

After the completion of each bentonite block pedestal, the corresponding heater was driven into the FE tunnel with a specially designed emplacement wagon. The 5'000 kg heaters were then carefully lowered onto the pedestal. Heater H1 was emplaced in October 2014, heater H2 in November 2014 and heater H3 in January 2015. The emplacement of each heater including construction and instrumentation of the pedestal took between 8 and 13 days.

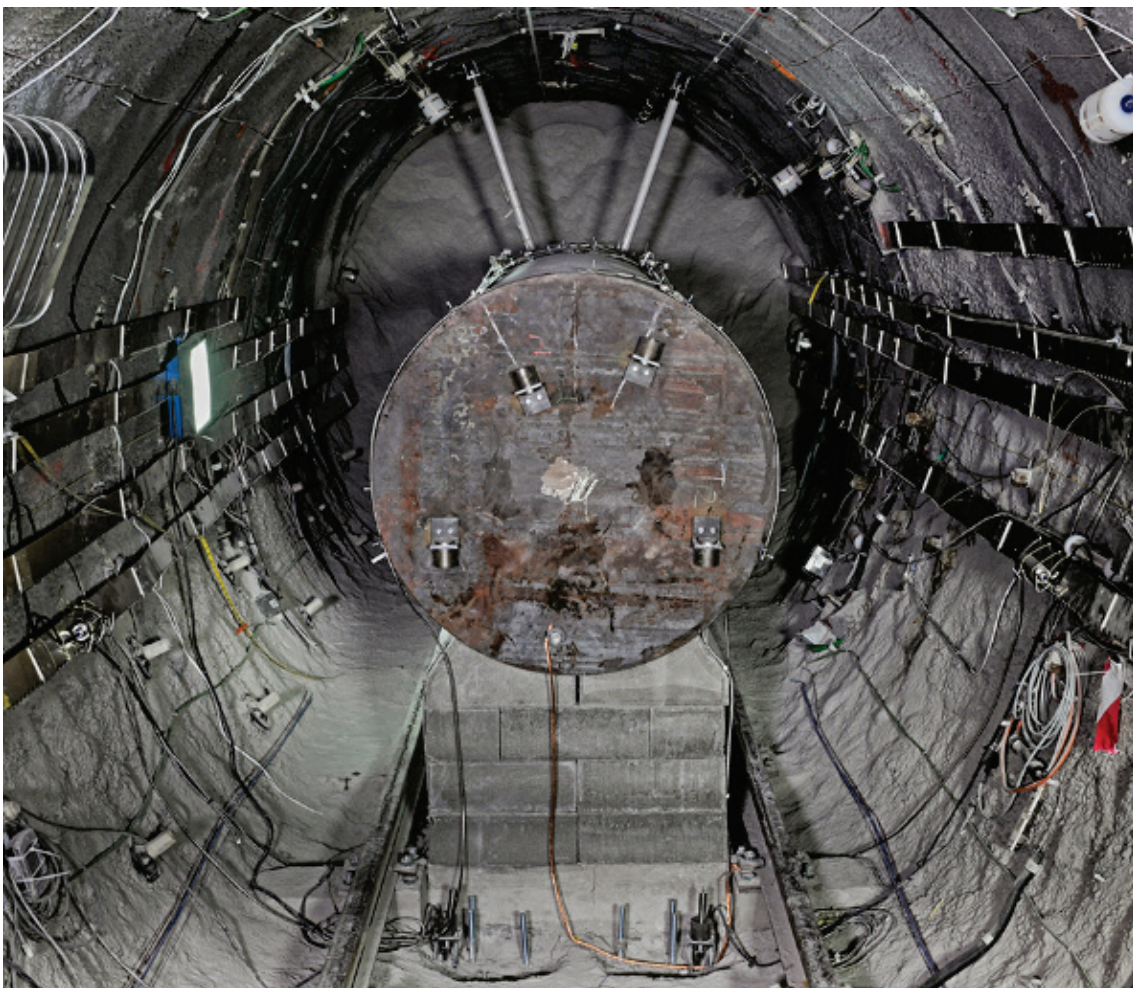


Fig. 20: Photograph of a bentonite block pedestal supporting a heavily instrumented heater in the FE tunnel

© Comet Photoshopping, Dieter Enz

The greyish mass in the background is a slope of GBM backfilled prior to the construction of the bentonite block pedestal. The cable routing channels made from stainless steel can be seen on the tunnel wall.

Müller et. al. (2017)

The volume around the heaters and in the gaps between heaters was filled with GBM emplaced by a specially designed back-filling augur machine. The GBM had been specially prepared with a water content in the range of 4 – 6 % and a controlled particle size distribution optimised for emplacement (Fig. 21).

Despite the influence of sensors and cables an average dry density of approximately  $1.49 \text{ g/cm}^3$  was achieved. The target dry density of  $1.45 \text{ g/cm}^3$  was not reached in two sections (see Fig. 22):

- In the section between Scan 9 and Scan 10, the average dry density was  $1.444 \text{ g/cm}^3$ . The bentonite in this section had been re-used from previous testing, and the lower density is believed to result from alterations to the particle size distribution.
- In the section between Scan 11 and the retaining wall for the concrete plug, the dry density was  $1.403 \text{ g/cm}^3$ . The low density in this area is thought to be the result of the challenges of emplacing the GBM at the same time as building the retaining wall.



Fig. 21: GBM produced for the FE Experiment  
Müller et. al. (2017)

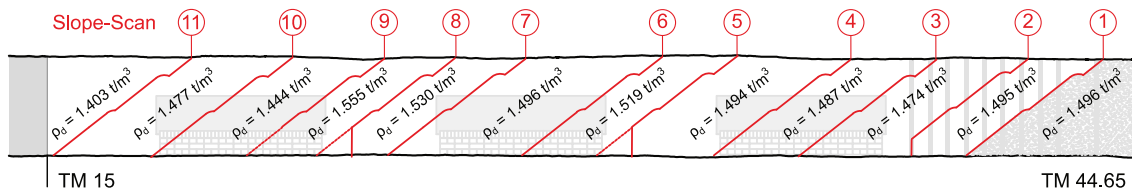


Fig. 22: Longitudinal section of the backfilled FE tunnel indicating the position of the 3-D slope scans and the resulting bulk dry densities calculated for each of the sections  
Müller et. al. (2017)

The Test Section is further split into the following instrumentation sections.

- Gap GP: GM 15-GM 18
- Heater 3: GM 18-GM 22.6
- Gap 2-3: GM 22.6-GM 25.6
- Heater 2: GM 25.6-GM 30.2
- Gap 1-2: GM 30.2-GM 33.2
- Heater 1: GM 33.2-GM 37.7

### Gap 0 (ISS): GM 37.7 – GM 38.5

At the far end of the FE tunnel, an Interjacent sealing Section (ISS) was simulated using only steel sets (and reinforcement mesh) but without shotcrete or bolts for rock support. The steel sets were placed with a spacing of 0.5m (close to the shotcrete section) or 1m. Each steel set was composed of several pieces with sliding connections that were tightened by bolts. The steel sets were bedded on grout-injected hoses in order to allow early load transfer (after hardening of the grout) and even load distribution from the rock onto the support element. The ISS was backfilled with GBM buffer using the augur system.

### Bentonite Block Wall: GM 44.5 – GM 46.5

A two-metre-thick bentonite block wall of highly compacted bentonite blocks were manually emplaced adjacent to the porous concrete wall. In total, about 14 m<sup>3</sup> of bentonite blocks were emplaced manually in nine working days during September 2014. The average dry density of each block was 1.78 g/cm<sup>3</sup> and the average water content was 18 %. One hundred and thirty kilograms of GBM, was emplaced in the gap between the bentonite blocks and the tunnel ceiling using a single auger system. An average bulk dry density of 1.69 ± 0.05 g/cm<sup>3</sup> was estimated for the bentonite block wall structure.

This section is supported by steel sets.

### Porous Concrete Backfilling: GM 46.5 – GM 50.1

The end of the gallery was backfilled with porous concrete on 04.07.2014. Samples of the emplaced concrete gave an interconnected porosity of 28 %, total porosity 42 % and permeability  $10^{-10} \text{ m}^2$ . A total of  $27 \text{ m}^3$  of concrete was emplaced.

This section is supported by steel sets.

### Properties of the GBM and compacted bentonite blocks

Volume-mass properties of the GBM for a range of as-emplaced densities are listed in Tab. 10. Porosity ranges from 42 – 48 % and initial saturation from 15 – 18 %. The pore water volumes and water volume needed for saturation per metre of tunnel are given in Tab. 11. The lowest water volume needed per metre of tunnel for saturation (high density small diameter in a heater section) is  $\sim 1.4 \text{ m}^3/\text{m}$  while for the ISS (average density)  $2.6 \text{ m}^3/\text{m}$  are needed<sup>2</sup>.

The GBM will swell on saturation and in confined conditions will develop significant swelling pressures. Under constant volume conditions the swelling pressure is largely controlled by the dry density if water salinity is low. Seiphoori (2015) provides a regression for the swelling pressure under constant volume condition of MX-80 bentonite versus dry density as shown in Fig. 23. The range of expected swelling pressure is between 2.4 and 4.3 MPa for the measured range of emplacement dry density.

For comparison the bentonite blocks in the bentonite block wall (BBW) had an average dry density of  $1.78 \text{ g/cm}^3$  and average water content of 18 %. After accounting for the gaps between the blocks a global average dry density of  $1.69 \pm 0.05 \text{ g/cm}^3$  was calculated. The blocks used to create the heater pedestals had an average dry density of  $1.78 \text{ g/cm}^3$  (Nagra, 2019). Significantly higher swelling pressures (5 – 10MPa) could therefore develop in these materials under confined conditions. However, it is likely that swelling of this material would result in further compaction of the GBM and so such high swelling pressures are unlikely to develop.

Tab. 10: As-emplaced volume-mass properties of the GBM

Assuming a grain density of  $2.7 \text{ g/cm}^3$

	Dry density $\rho_{dry}$ ( $\text{g/cm}^3$ )	Porosity $\phi$ (-)	Void ratio $e$ (-)	Gravimetric water content $w$	Volumetric water content $\theta$	Saturation $S$	Swelling pressure (MPa)
Low density	1.403	48 %	0.92	5 %	7.0 %	15 %	2.4
Average density	1.49	45 %	0.81	5 %	7.5 %	17 %	3.4
High density	1.555	42 %	0.74	5 %	7.8 %	18 %	4.3

<sup>2</sup> It is possible that the density of adsorbed water in the bentonite may be greater than that of free water but this has not been considered here.

Tab. 11: Estimated pore volume (m<sup>3</sup>) and water needed for saturation (m<sup>3</sup>) per metre of tunnel for different tunnel radii and as-emplaced density

No account taken of higher density and saturation of heater pedestal bentonite blocks.

	Heater section: radius 1.25 m		Gap: radius 1.25 m		Gap: radius 1.35 m		ISS: radius 1.5 m	
	Pore volume	Water needed	Pore volume	Water needed	Pore volume	Water needed	Pore volume	Water needed
Low density	1.94	1.66	2.36	2.01	2.75	2.35	3.40	2.90
Average density	1.81	1.51	2.20	1.83	2.57	2.14	3.17	2.64
High density	1.71	1.40	2.08	1.70	2.43	1.98	3.00	2.45

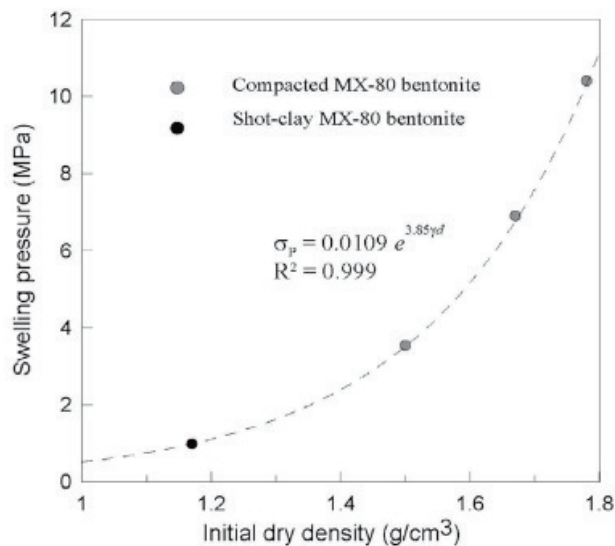


Fig. 23: Swelling pressure versus initial dry density under constant volume conditions in compacted shot-clay and MX-80 bentonite samples

From Seiphoori (2015)

## Instrumentation

The FE Gallery is highly instrumented in both the EBS and surrounding rock mass with a range of sensors measuring:

- Temperature at the heaters, in the EBS and in borehole intervals. Many of the temperature sensors are associated with other measurements (e.g. total pressure or relative humidity).
- saturation state as relative humidity, suction, gravimetric or volumetric water content
- pore pressure in the geosphere
- total pressure in the EBS
- deformation as convergence (prior to EBS emplacement), displacement or inclination (in the geosphere)



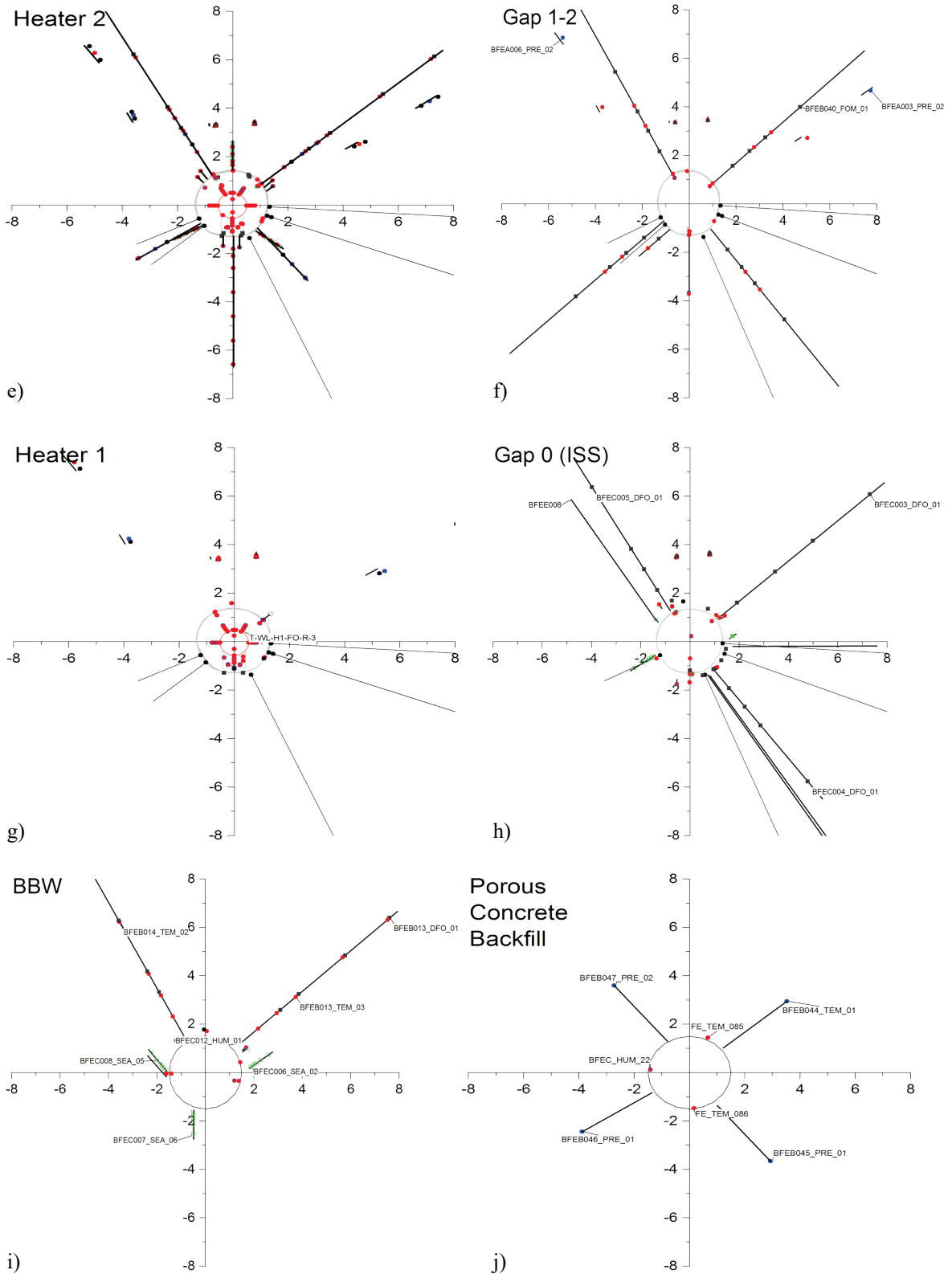


Fig. 24: Cont.

## 2.4 Schedule of events relevant to FE evolution

Tab. 12 provides a brief chronology of the main events relevant to the FE Experiment.

Tab. 12: Main events relevant to FE Experiment

26.04.2012	Start of excavation
22.05.2012	Excavation up to GM 16: E1 section
28.06.2012	Excavation up to GM 44.5: E2 section
11.07.2012	End of excavation
06.09.2012	Removal and renovation of invert GM 8.6-GM 38.3 (to 21.09.12)
04.07.2014	Emplacement of porous concrete
04.09.2014	Emplacement of BBW
22.09.2014	GBM emplacement ISS
09.10.2014	Heater H1 emplacement
23.10.2014	Backfill H1
10.11.2014	Heater H2 emplacement
20.11.2014	Backfill H2
12.01.2015	Heater H3 emplacement
21.01.2015	Backfill H3
26.01.2015	Retaining wall
17.03.2015	Plug emplacement
15.12.2014	Heater 1 start-up 500W
13.01.2015	Heater 1 power 1000W
16.02.2015	Heater 1 power 1350W
17.02.2015	Heater 2 start up 1350W
18.02.2015	Heater 3 start up 1350W
31.08.2019	End of monitoring data period for this report

From February 2018 to May 2019 significant excavation works were performed at the Mont Terri URL in the development of Gallery 18 (Ga18) as shown in Fig. 25. Phase 1 of the excavation started at the TT Niche (Ga314) and was followed by excavation of Niche 7 and 8 (approximately 60 m from the FE-A Niche) but then excavation switched to the DR Niche and excavation of Niche 1 from the Security Gallery and the start of Phase 2 of Ga18 and Niches 2, 3, 4, 5 and 6. Excavation of Ga18 was completed with cutting through from GM 297 to Niche 7 and 8 on 27.5.2019. A summary of the excavation timetable is given in Tab. 13. A more detailed excavation schedule and further discussion of the observed responses to Ga18 excavation are given in Chapter 4.



Tab. 13: Simplified Ga18 Excavation schedule

<b>Start</b>	<b>Excavation</b>	<b>Gallery 18 meters</b>
26.02.2018 08:00	Installation of dust doors	
12.03.2018 08:00	Opening ceremony	
14.03.2018 08:00	Ga18 Phase 1	314.4
04.04.2018 15:00	Niche 7	
24.04.2018 15:00	Niche 8	
04.06.2018 21:00	Niche DR	
14.06.2018 08:00	Niche 1	
03.07.2018 11:30	Ga18 Phase 2 A	11
13.09.2018 10:00	Niche 2 South	
12.02.2019 14:00	Ga18 Phase 2 C	182
12.04.2019 06:00	Niche 5	
07.05.2019 06:00	Ga18 Phase 2D	269.7
27.05.2019 17:00	Cutting through	297

### 3 System evolution after emplacement and start of heating

#### 3.1 Thermal data: Temperature and heater power

##### 3.1.1 Heater power and surface temperature

The three heaters H1-H3 were tested and powered on in late December 2014 and early January 2015. The main events are listed in Tab. 14. The power to the heaters is protected by an Uninterruptable Power Supply (UPS) and has remained steady between 1340 - 1360 W from late February 2015 onwards (see Fig. 26).

Tab. 14: Main heating events  
From Nagra (2015)

Start	Heater	Remark
20.10.2014	H1	Installation
14.11.2014	H2	Installation
15.12.2014 17:25	H1	Power to 500 W
14.01.2015	H1	Power to 1'000 W
16.01.2015	H3	Installation
20.01.2015	H3	Tested at 760 W
12.02.2015	H3	Tested at 670 W
12.02.2015	H2	Power test at 780 W
13.02.2015	H1	Power reduced to 900 W
16.02.2015	H1	Power to 1'350 W
17.02.2015	H2	Power to 1'350 W
18.02.2015	H3	Power to 1'350 W

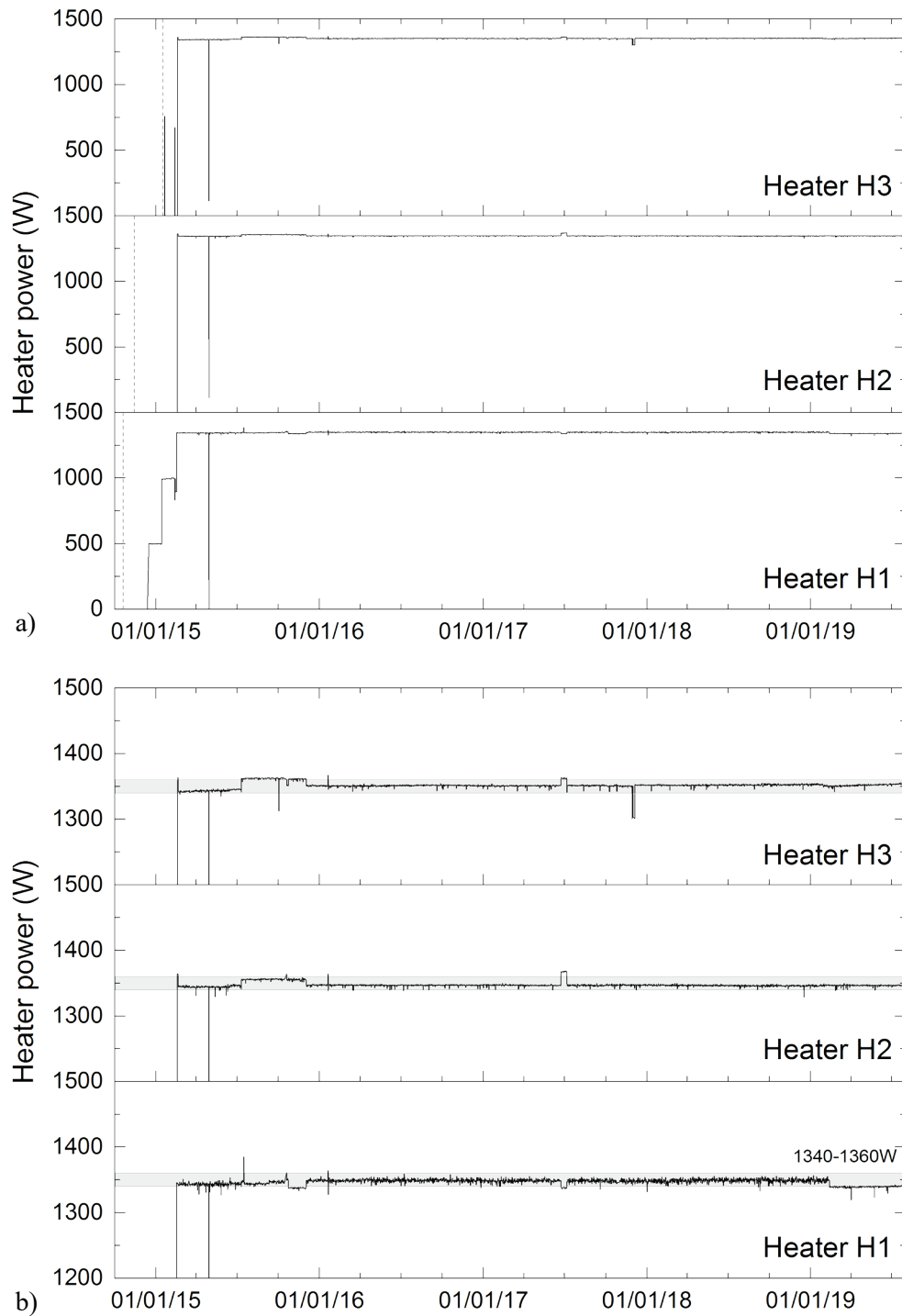


Fig. 26: Heater power a) overview b) detail response showing small variation in power

The H1 heater was powered up in stages but once it was set at 1350W on 16.02.2015, the H2 and H3 heaters were then powered up to 1350 W on the next two days. Heating at H1 had started at 550 W approximately 65 days prior to H3. The data considered in this report (to 31.08.2019) covers the response to heating at H1, H2 and H3 for 1720, 1656 and 1655 days respectively (for H1 a period of 4.7 years).

Heater surface temperature has been steady since the end of 2016 (see Fig. 27). Temperature varies over the surface of the heaters with the highest temperature at the top part of the heaters as the compacted bentonite blocks in the pedestal have a higher thermal conductivity. Steady temperatures range between 135 °C (top) and 120 °C (base).

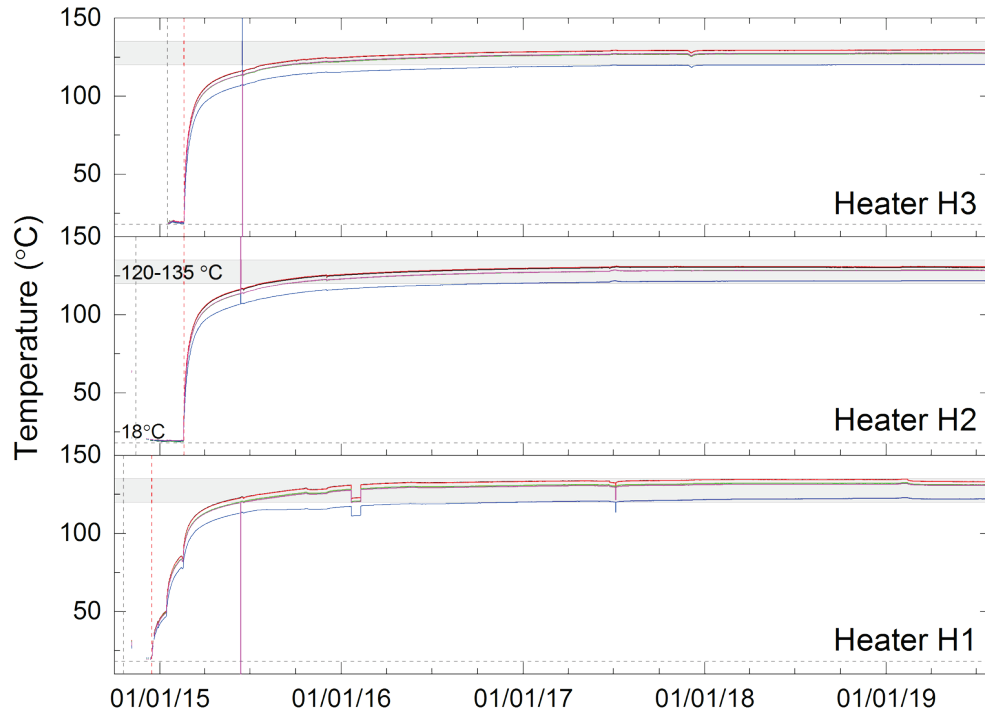


Fig. 27: Heater surface temperature

The early evolution of heater power and surface temperature are shown in Fig. 28, with a clear relationship between the steps in heater power and surface temperature changes.

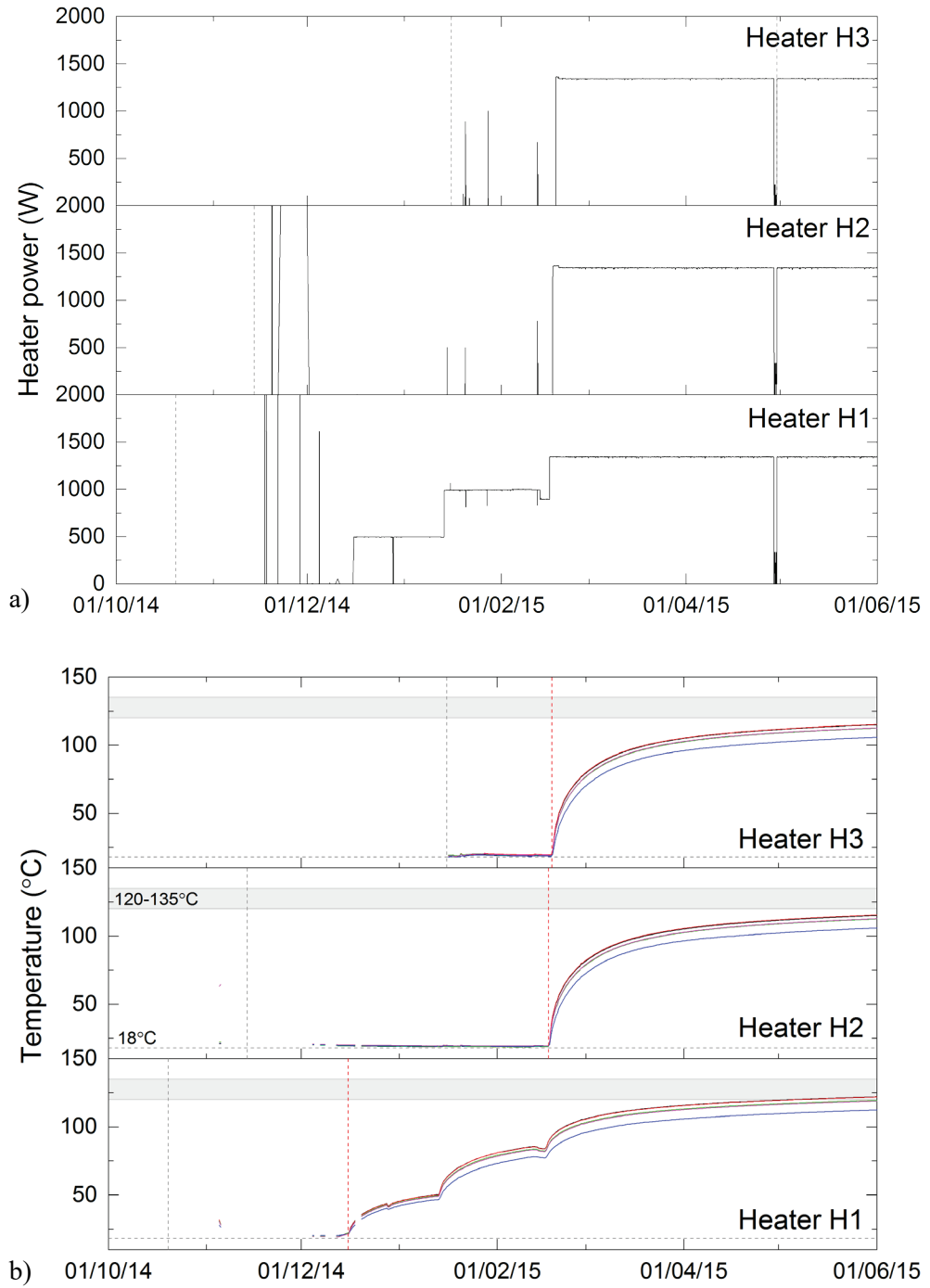


Fig. 28: Heater power and surface temperature from installation to 01.06.2015

Grey dashed vertical lines show the date of heater emplacement.

### 3.1.2 Temperature

#### Temperature evolution in the EBS

Prior to the start of heating the measured temperature in the bentonite was about 18 °C. Following the start of heating, temperature is largely controlled by the distance from the heater. Around each heater a radial temperature distribution develops over time with the thermal front reaching out beyond 10m radial distance towards the end of the monitoring period.

The maximum temperatures occur in the heater sections with temperature at the shotcrete in the H2 section reaching over 60 °C by the end of the data monitoring period. Temperatures in the gaps between the heaters and in the ISS section are considerably lower > 25 °C (Fig. 29).

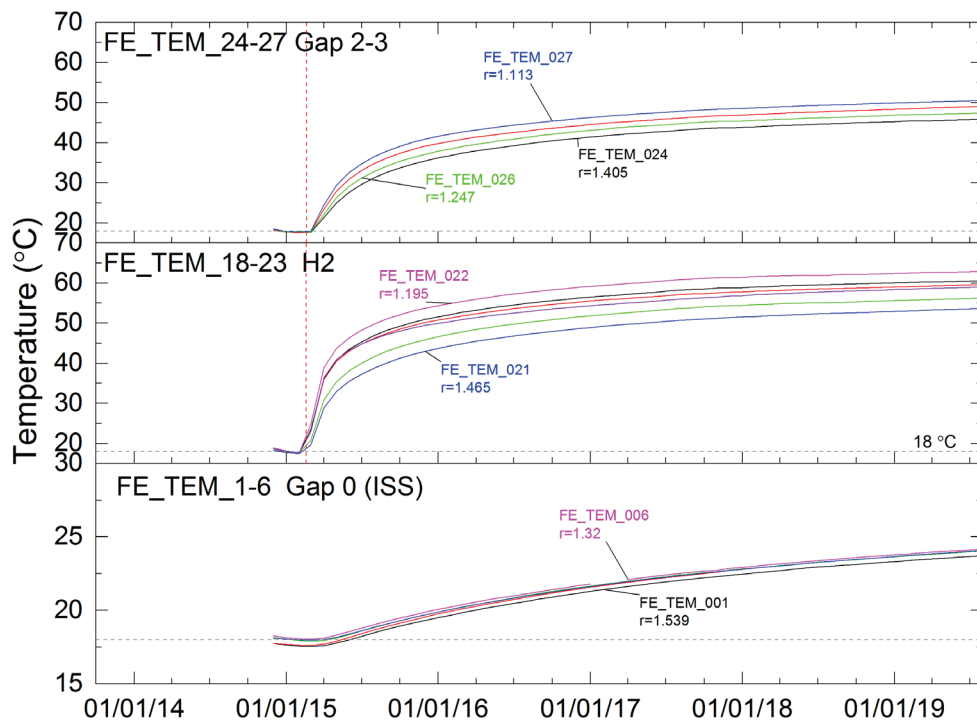


Fig. 29: Temperature data from sensors at the shotcrete or tunnel wall in Gap 2-3, H2 and Gap 0 (ISS) sections

Sensor name and radial distance  $r$  shown for selected sensors.

**Temperature evolution in the geosphere**

Fig. 30 shows temperature data from radial boreholes drilled at the H2, H3 and Gap 0 (ISS) sections. The highest temperatures occur closest to the tunnel wall (radial distance  $r \sim 2.5$  m) and reach over  $45\text{ }^\circ\text{C}$  by the end of the monitoring period. Temperature gradients are higher around the heaters than in the Gap 0 (ISS) section. Temperatures rise most quickly in boreholes parallel to bedding.

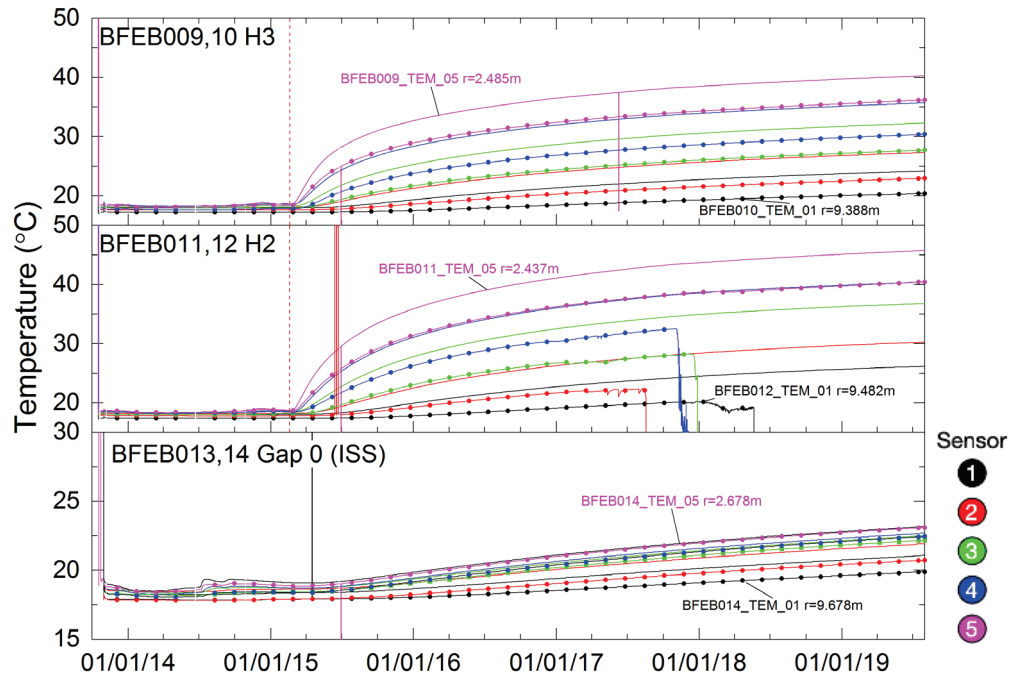


Fig. 30: Temperature data from radial boreholes in H2, H3 and Gap 0 (ISS) sections  
Data plotted with symbols are for boreholes normal to bedding (see Fig. 3).

Fig. 31 shows temperature data from the two longitudinal inclinometer boreholes above the FE Tunnel (radial distance  $r \sim 3.5$  m) BFEA010 and BFEA011. The highest temperatures ( $\sim 35\text{ }^\circ\text{C}$ ) occur in the H2 section. Seasonal variations in temperature can be seen in all intervals prior to heating and in the data from the section nearest the FE-A Niche throughout the monitoring period. The same data is also shown as contours along the boreholes in Fig. 32. The overall temperature distribution can be seen as roughly symmetric around H2 (centre  $Y_{FE}$  32.59 m) with slightly higher maximum temperatures at the end of the monitoring period (max  $36.4\text{ }^\circ\text{C}$  at  $Y_{FE}$  31.7 m) in BFEA010 than in BFEA011 (max  $34.9\text{ }^\circ\text{C}$  at  $Y_{FE}$  32.8m).

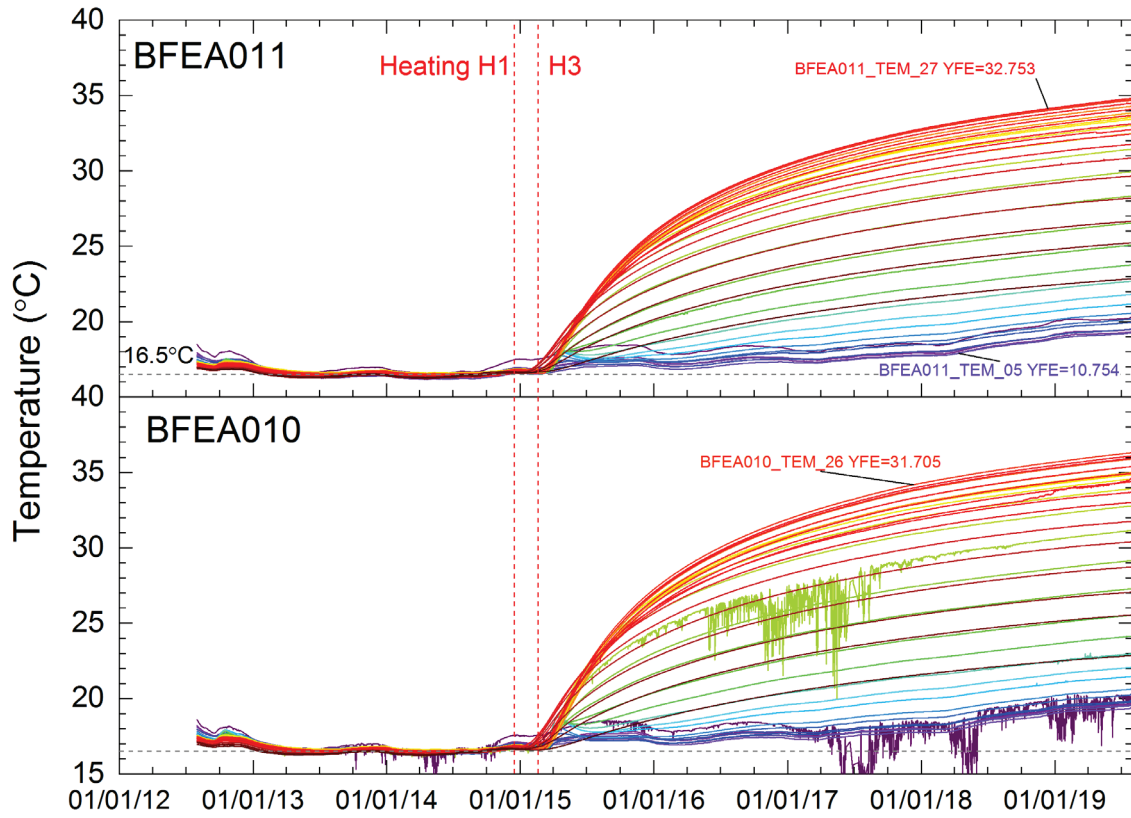


Fig. 31: Temperature data from longitudinal boreholes BFEA010 and BFEA011  
 Lines coloured by position from  $Y_{FE}=5.7$  m (purple) to  $Y_{FE}=46.7$  m (dark red)

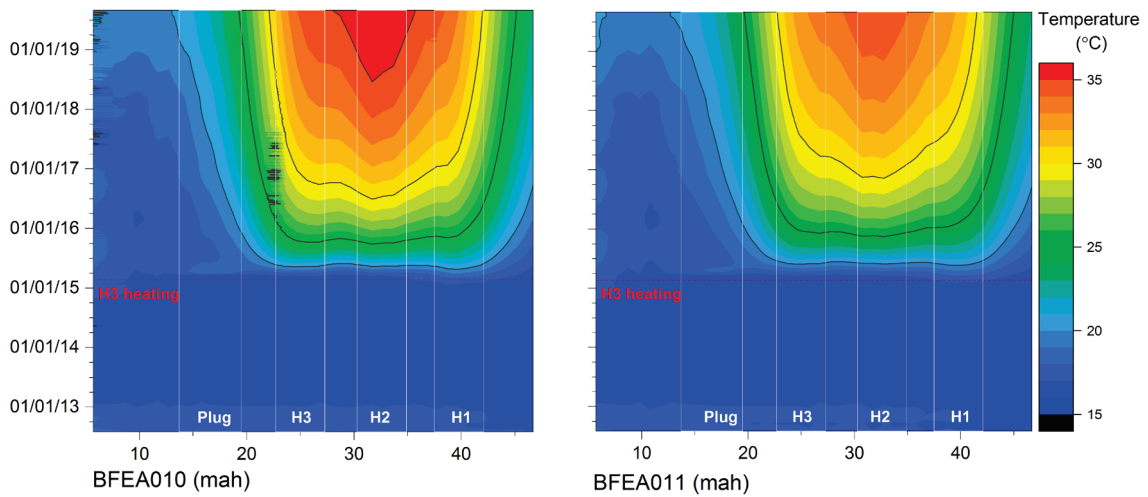


Fig. 32: Temperature contours of date (Y) versus metre along hole (mah) for the longitudinal boreholes BFEA010 and BFEA011

### **Temperature distribution within and around the FE Tunnel**

The temperature distribution with radial distance from the tunnel axis in the Heater H1, H2 and H3 sections at 01.12.2014 (prior to heating), 01.03.2015 (10 – 12 days from heating at 1'350 W), 01.06.2015 (~ 100 days from heating at 1350 W) and 31.08.2019 (~ 1'650 days from heating at 1'350 W) are shown in Fig. 33. There is a relatively rapid evolution of the temperature distribution immediately after the start of heating and only a gradual increase in temperature after that as the temperature front expands into the rock. The spread in temperature with radial distance is partly explained by the inhomogeneous temperature distribution on the heater surface but also may reflect local variations in bentonite properties and other features of the instrumentation (some of the sensors are placed on "stand-offs" from the heaters). While the overall trend is clear, individual sensors also show some anomalous values.

The evolution of the temperature distribution with radial distance in the geosphere around the heaters is shown in Fig. 34. The strong radial dependence and influence of relationship to bedding is clearly seen. The temperature around the FE tunnel at 31.08.2019 is shown in Fig. 35.

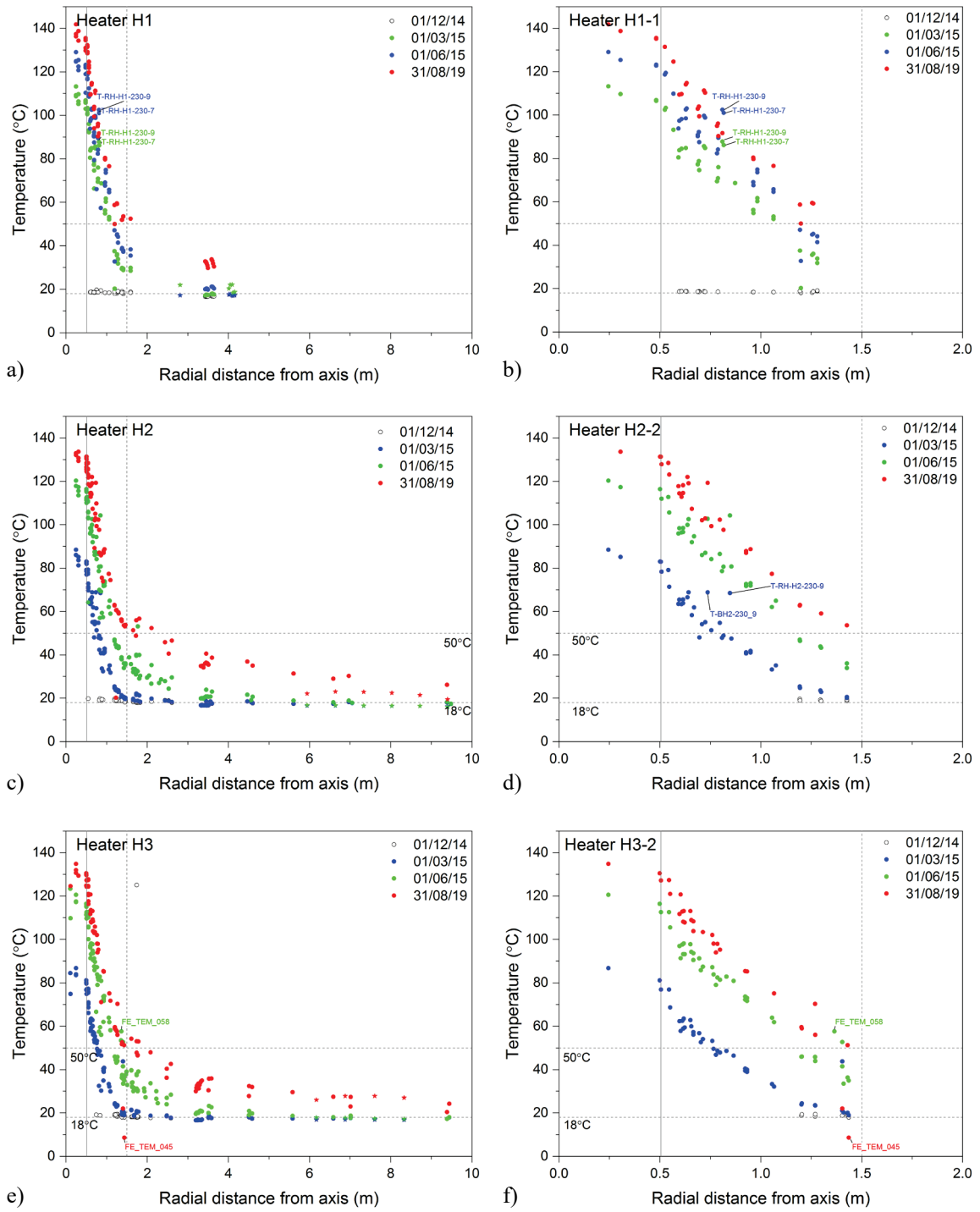


Fig. 33: Temperature distribution with radial distance from the tunnel axis  
 For a) Heater H1, b) THM section H1-1, c) Heater H2, d) THM section H2-2, e) Heater H3, f) THM section H3-2

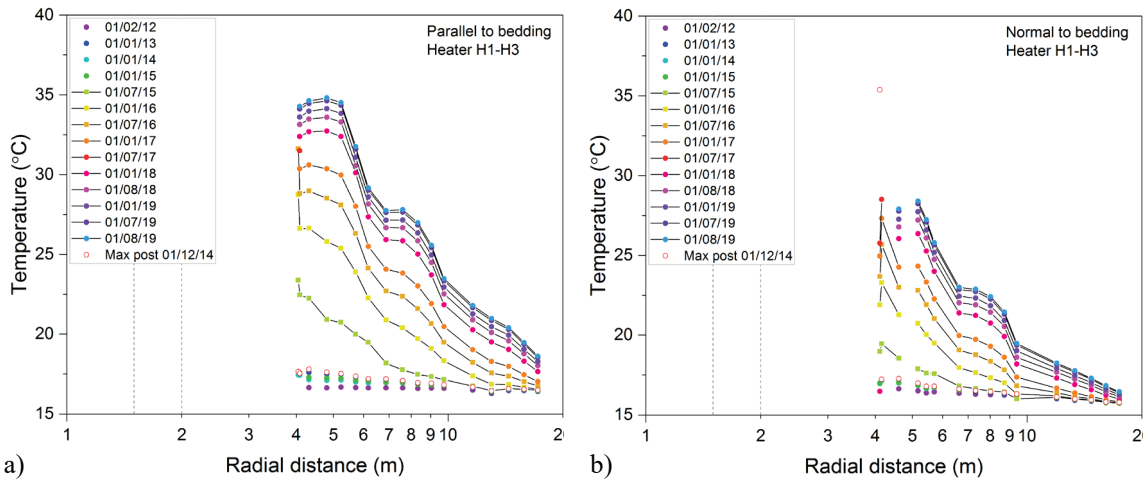


Fig. 34: Measured temperature in geosphere versus radial distance from the FE Tunnel  
a) along bedding, b) normal to bedding

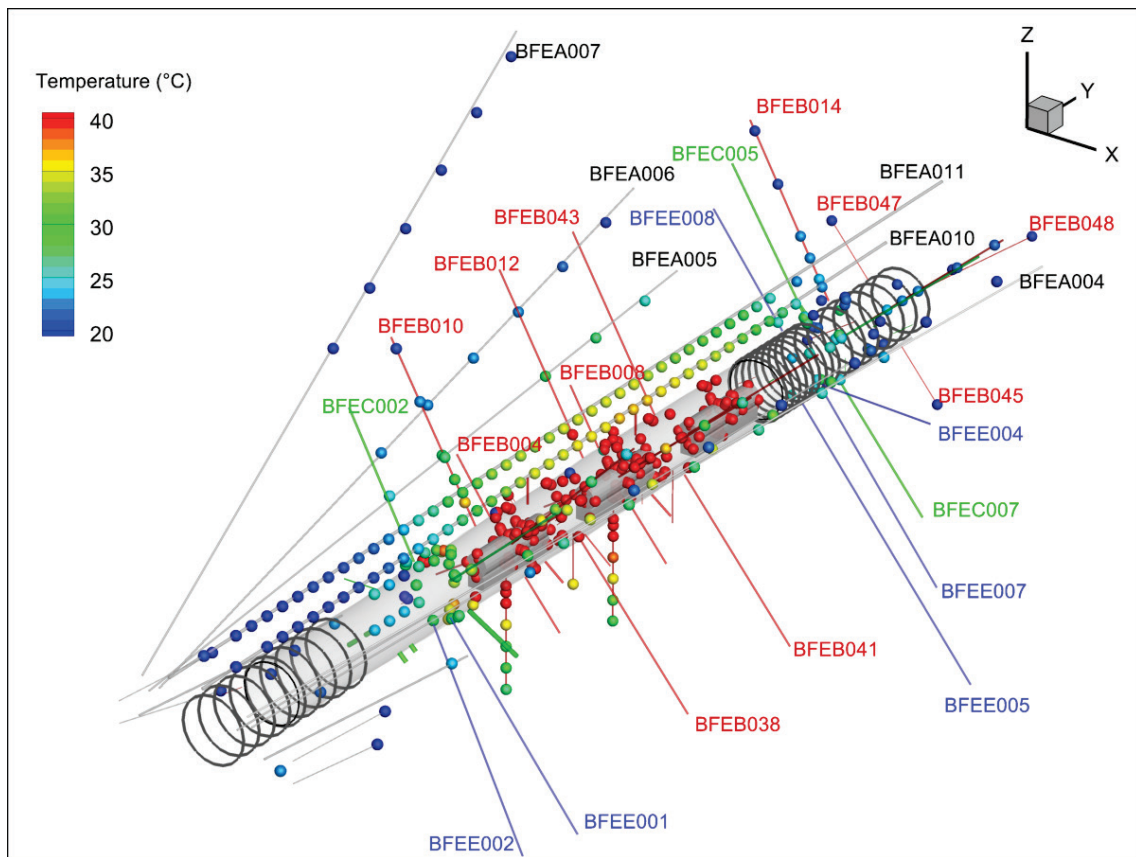


Fig. 35: Measured temperature in geosphere at 31.0.8.2019

Fig. 36 shows the temperature distribution at 31.08.2019 as measured by sensors in the EBS and rock in each of the instrumentation sections. The strong radial dependence is clearly seen in the heater sections. In the rock, temperature increases are typically larger along bedding than normal to bedding (for similar radial distance from the tunnel axis).

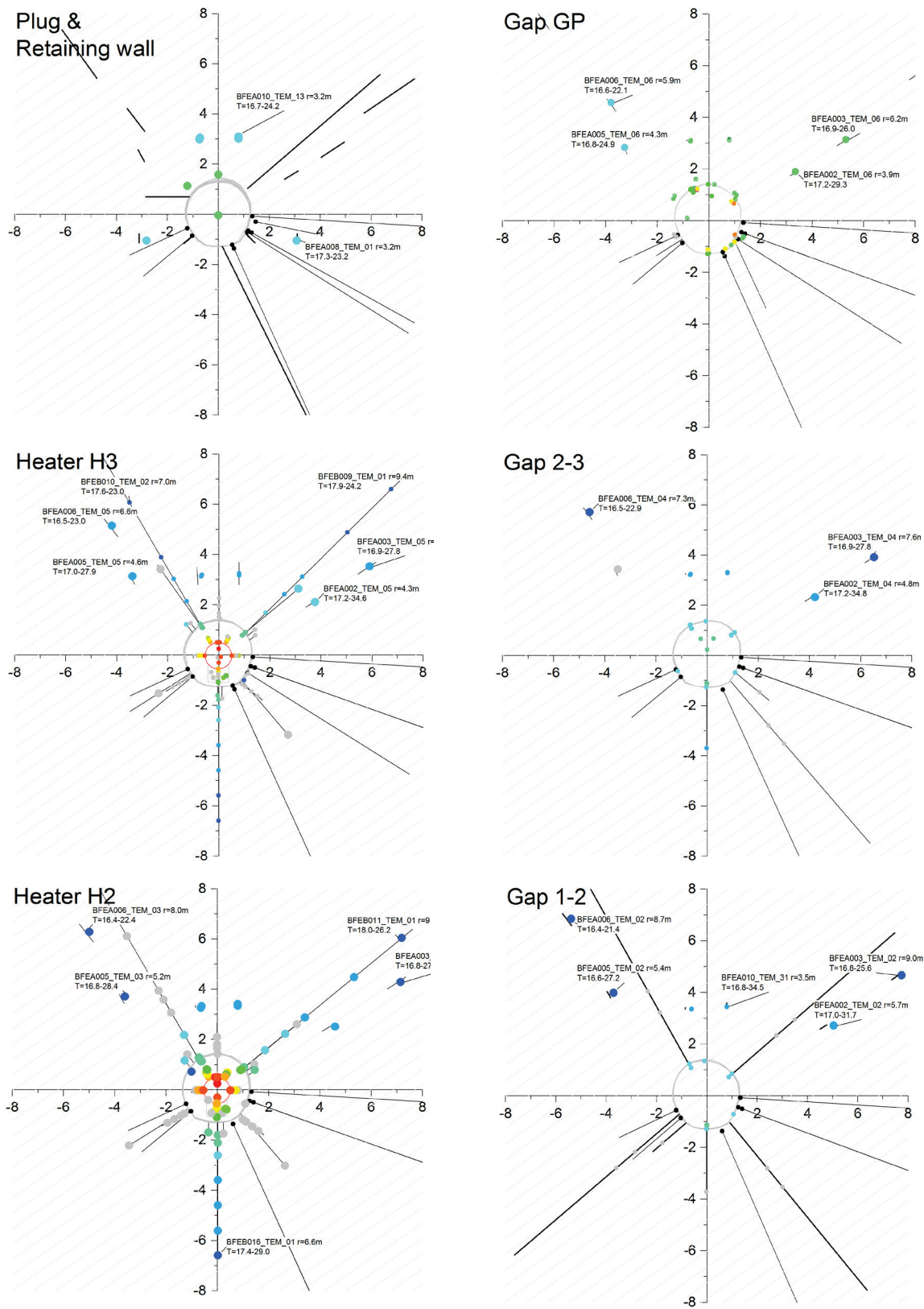


Fig. 36: Temperature distribution in the different sections of the FE tunnel  
 Labels give 12 hr average at 01.12.2014 (prior to heating) and 31.08.2019 for selected sensors.

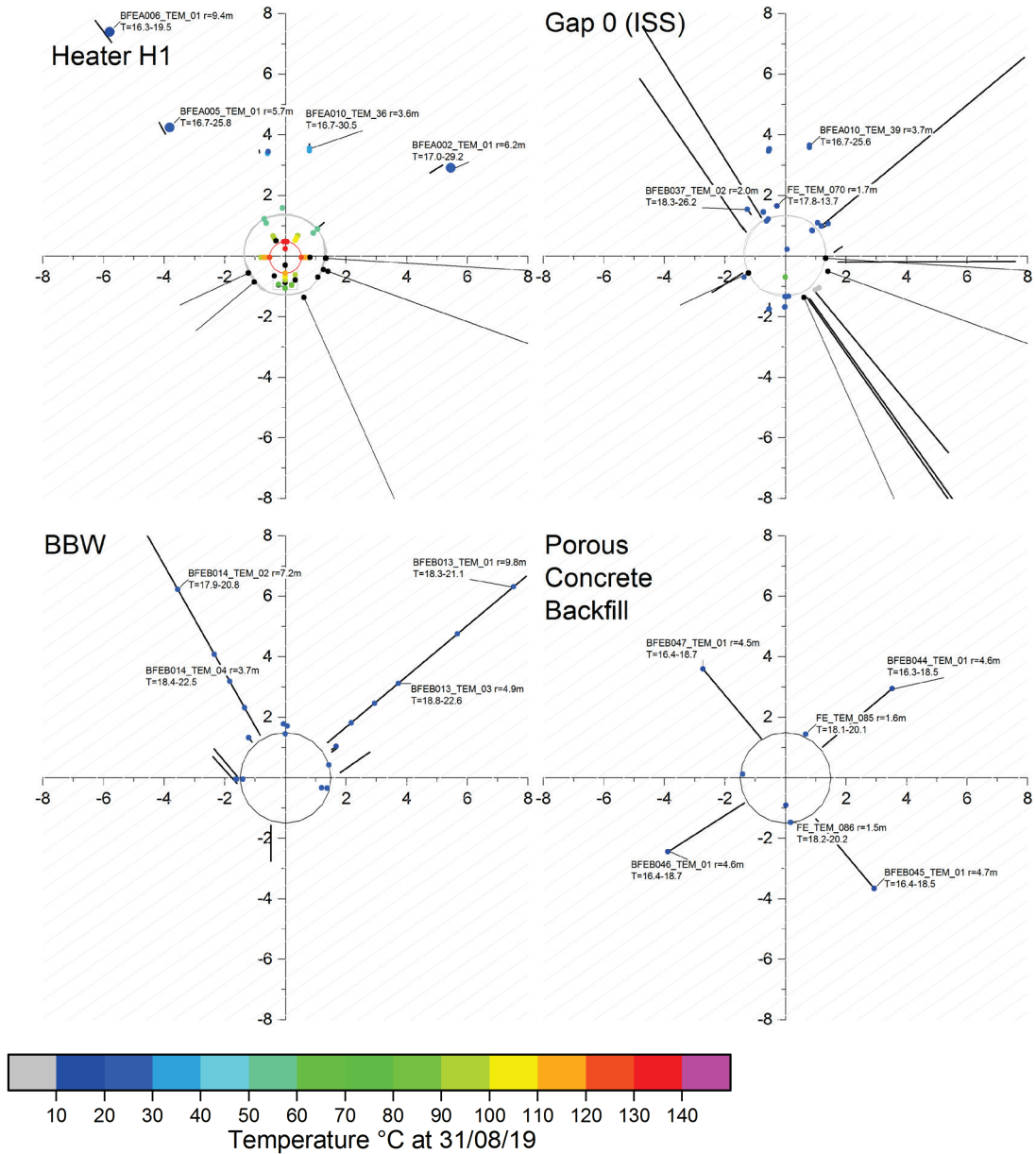


Fig. 36: Cont.

The observed change in temperature from prior to the start of heating (01.12.2014) to the end of the monitoring period (31.08.2019) is shown in Fig. 37. Only sensors with good measurements on both these dates are shown.

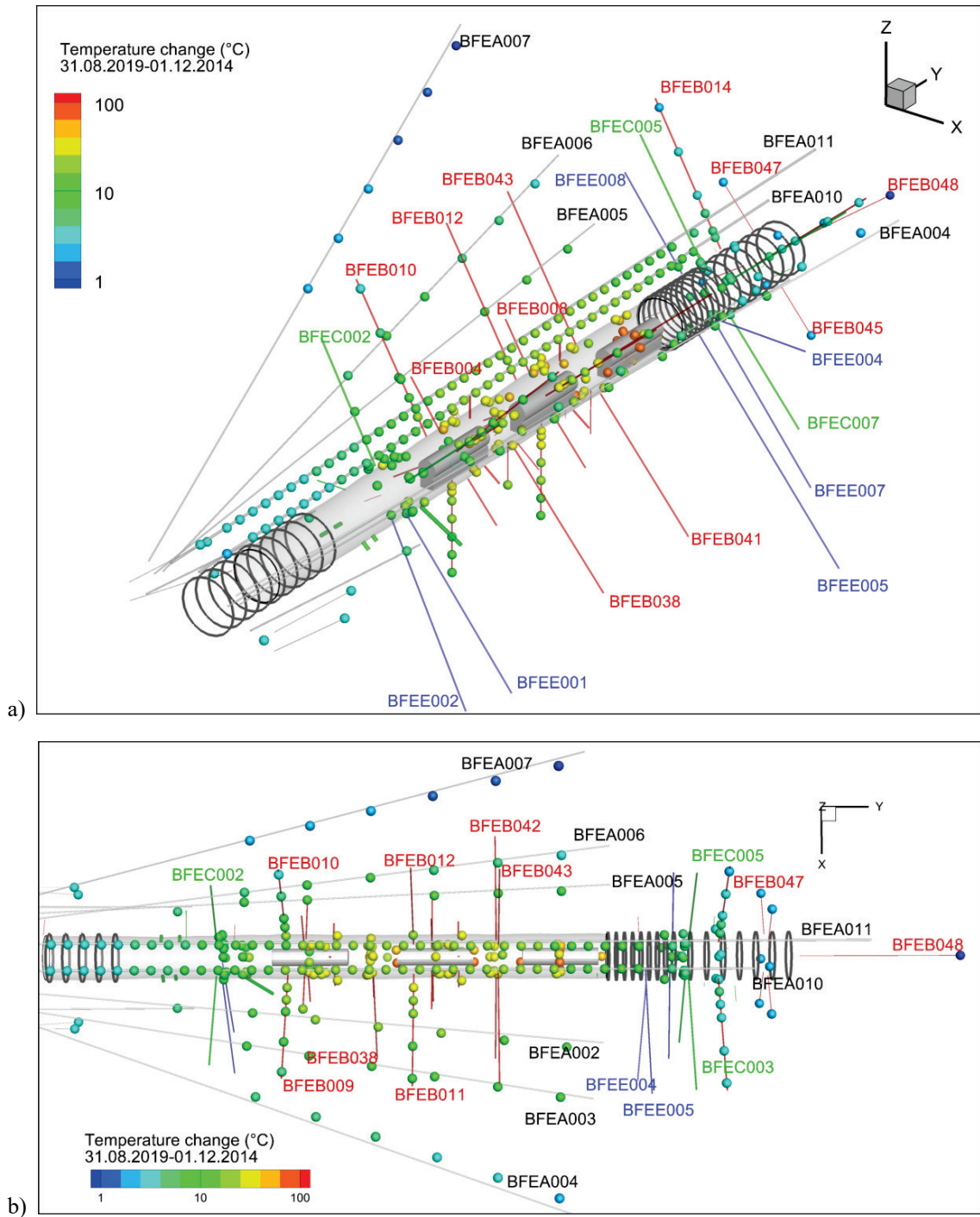


Fig. 37: Temperature difference (°C) from 01.12.2014 (prior to heating) to 31.08.2019 (end of monitoring period)

a) 0 3D view. b) Plan view. Temperature difference coloured in log scale from 1 – 100 °C

Temperature change in the geosphere is anisotropic with greater changes in the parallel to bedding direction and is less than 40 °C.

### Thermal conductivity

Thermal conductivity is measured in a set of 15 sensors (TR-1, heat-pulse probe with a 10 cm long needle) located in the H2, Gap 2-3 and H3 sections. While changes in GBM dry density may affect the measured thermal conductivity, it is expected that saturation will be the main influence and increases in thermal conductivity reflect increasing saturation. Measurements are made periodically with a 10-minute reading at high power to minimise measurement error. The thermal conductivity and associated error are estimated at each measurement from the response to heating. Fig. 38 shows the "good" measurements (estimate of thermal conductivity in expected range with small error) from the 15 sensors and the values are summarised in Tab. 15.

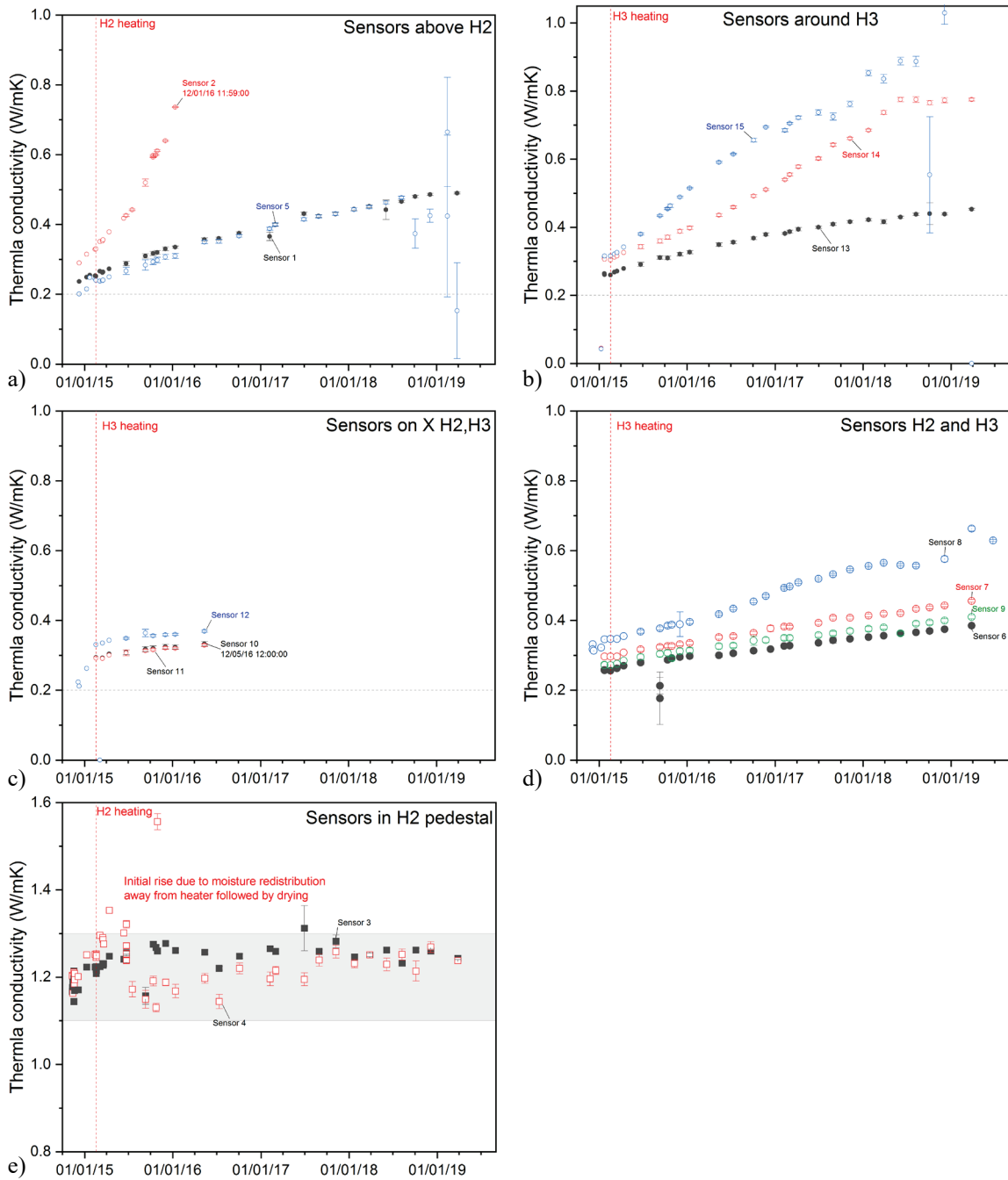


Fig. 38: Estimated thermal conductivity from periodic measurements in GBM and heater pedestals a), b), c), d), e) sensors in H2 pedestal

Sensor 2 shows a particularly swift rise in conductivity from  $\sim 0.3$  to  $0.8$  W/mK in about 1 year indicating more rapid local saturation. The sensor is located close to the wet spot associated with the BFE004 grout tubes at GM 26.6. Other sensors at the shotcrete wall show a slower long-term increase to between  $0.4$  and  $0.9$  (equivalent to GBM saturation 24-91 % based on the regression presented in Appendix D). Sensor 15 reaches over  $1.0$  W/mK (close to fully saturated) and is about  $0.5$ m from the wet spot associated with a rock bolt at GM 20.

The three sensors on the X section in the GBM between H2 and H3 show an initial small rise followed by stabilisation at below  $0.4$  W/mK before failing in mid-2017. The upper sensor (4) in the H2 pedestal shows an initial rise in conductivity due to increased saturation followed by drying and stabilisation at  $\sim 1.2$  (W/mK) while the lower sensor shows an initial small rise followed by a plateau at a similar value.

Tab. 15: Summary of thermal conductivity measurements

Saturation  $S$  has been estimated from the most recent values using the regression given in Appendix D.

ID/location	GM		First	Value	Error	Most recent	Value	Error	S	
1	H2	26.3	GBM	09.12.2014 12:12	0.24	0.00	27.03.2019 09:10	0.49	0.00	0.4
2	H2	26.3	GBM	09.12.2014 12:12	0.29	0.00	12.01.2016 11:59	0.74	0.00	0.7
5	H2	26.3	GBM	09.12.2014 12:12	0.20	0.00	15.02.2019 12:10	0.67	0.16	0.7
6	Gap	24.5	GBM	22.01.2015 17:58	0.26	0.00	27.03.2019 09:10	0.39	0.00	0.2
7	Gap	24.5	GBM	23.01.2015 11:35	0.30	0.00	27.03.2019 09:10	0.46	0.00	0.3
8	Gap	24.5	GBM	05.12.2014 12:13	0.33	0.00	24.06.2019 12:26	0.63	0.00	0.6
9	Gap	24.5	GBM	22.01.2015 17:58	0.27	0.00	27.03.2019 09:10	0.41	0.01	0.3
10	Gap X	24.1	GBM	17.02.2015 09:27	0.29	0.00	12.05.2016 12:00	0.33	0.01	0.1
11	Gap X	24.1	GBM	17.02.2015 09:27	0.29	0.00	12.05.2016 12:00	0.33	0.00	0.1
12	Gap X	24.1	GBM	05.12.2014 11:59	0.22	0.00	12.05.2016 12:00	0.37	0.00	0.2
13	H3	22.5	GBM	22.01.2015 17:58	0.26	0.00	27.03.2019 09:10	0.45	0.00	0.3
14	H3	22.5	GBM	22.01.15 17:58	0.26	0.00	27.03.19 09:10	0.78	0.00	0.8
15	H3	22.5	GBM	22.01.15 17:58	0.31	0.00	05.12.18 09:20	1.03	0.03	1.0
Minimum					0.20			0.33		0.08
Average					0.28			0.54		0.44
Maximum					0.33			1.03		1.02
ID/location			First	Value	Error	Most recent	Value	Error	S	
3	H2 Pedestal		11.11.14 00:00	1.18	0.00	27.03.19 09:10	1.24	0.00	-	
4	H2 Pedestal		11.11.14 00:00	1.20	0.00	27.03.19 09:10	1.24	0.01	-	

### 3.2 Hydraulic data: saturation and pore pressure

Saturation of the buffer and host rock is characterised using a variety of different measurements:

- relative humidity (RH)
- volumetric water content in %
- gravimetric water content in wt.-%
- suction in kPa

In this section the measured data is presented and no conversion to saturation is made. In addition, thermal conductivity of the buffer can be used here as a proxy for saturation (see previous section). Total pressure measurements in the GBM may also indicate saturation induced swelling. Saturation in the EBS is expected to be heterogeneous and the spatial distribution will be influenced by:

- redistribution of moisture due to drying near the heaters
- water (and water vapour) flowing from the rock (through the shotcrete or directly) to the buffer. Flow has been observed to be heterogeneous during the open tunnel period with a small number of wet spots all associated with perforations in the shotcrete.
- initial differences in dry density and buffer properties (GBM and bentonite blocks)

Pore pressures are measured in geosphere borehole intervals. Significant pore pressures are unlikely to build up within the EBS for some time. Pore pressure in the geosphere is influenced by:

- initial equilibration after installation
- poro-elastic effects related to excavation and ongoing deformation
- thermo-pore-elastic effects associated with heating (Ghabezloo & Sulem 2009)
- ventilation or drying of the rock wall or shotcrete
- advective flow of water and water vapour (partially saturated conditions)

#### 3.2.1 Saturation

##### Relative humidity sensors

Relative humidity (RH) is measured by 3 types of sensor in the GBM and in the rock. RH can theoretically be converted to suction (via Kelvin's equation) and then, via a material-specific water retention curve, to saturation. In view of the uncertainties associated with such a conversion, the RH data is presented. It must be remembered that any conversion to saturation is likely to be highly non-linear (see Appendix D).

Fig. 39, Fig. 40 and Fig. 41 show the RH data for the sensors in the Heater 1 (H1), Heater 2 (H2) and Heater 3 (H3) sections. All three heater sections show a similar pattern:

- Borehole sensors in the rock show an initial high RH (90 – 100 %) that declines slightly post-heating for a few sensors.
- RH measured by sensors near the shotcrete increases over the first year to between 60 – 100 % indicating increased saturation. This may be due to moisture from the rock (in some places via rock-bolts and other identified wet spots) and moisture redistributed from near the heater (where drying occurs and moisture is then transported as water vapour to the outer parts of the buffer).
- RH initially increased and then reduces over the first year at sensors in the GBM 10 or 20 cm from the heater due to drying of the bentonite. The initial rise occurs as the bentonite immediately around the heater dries. Sensors close to the heater often show erratic data indicating failure after 18 months to two years. There is no consistent evidence of any increases in saturation after the first response to heating and subsequent drying.
- RH initially increased and then reduces over the first year at sensors in the compacted bentonite block pedestals. Sensors 10 cm from the heater react quickly with an early rise in RH followed by drying over the next one to two years. At 20 cm a more prolonged rise and slower fall occurs.
- Sensors within 20 cm of the heater surface in the GBM show long term RH values below 25 %. At sensors in the pedestals RH is reduced to ~ 30 % but several sensors failed prior to stabilisation.

Fig. 42 shows the RH data for the GBM filled gaps between heaters and at the tunnel entrance and within the FE-A Niche. Again, a consistent response is seen in the different sections where:

- RH sensors in the centre of the tunnel show a slight increase over time but typically remain below 45 %
- RH sensors at the edges of the GBM near the shotcrete or tunnel wall slowly increase over time to a maximum of ~ 70 % at the end of the monitoring period
- RH sensors in boreholes at the tunnel entrance show near ~ 100 % with some deviations to values below 100 %
- RH sensors in the ventilated FE-A Niche show a clear annual seasonal pattern varying between 50 and 80 % with high RH in the summer

The spatial distribution of RH measurements at 31.08.2019 is shown in Fig. 43.

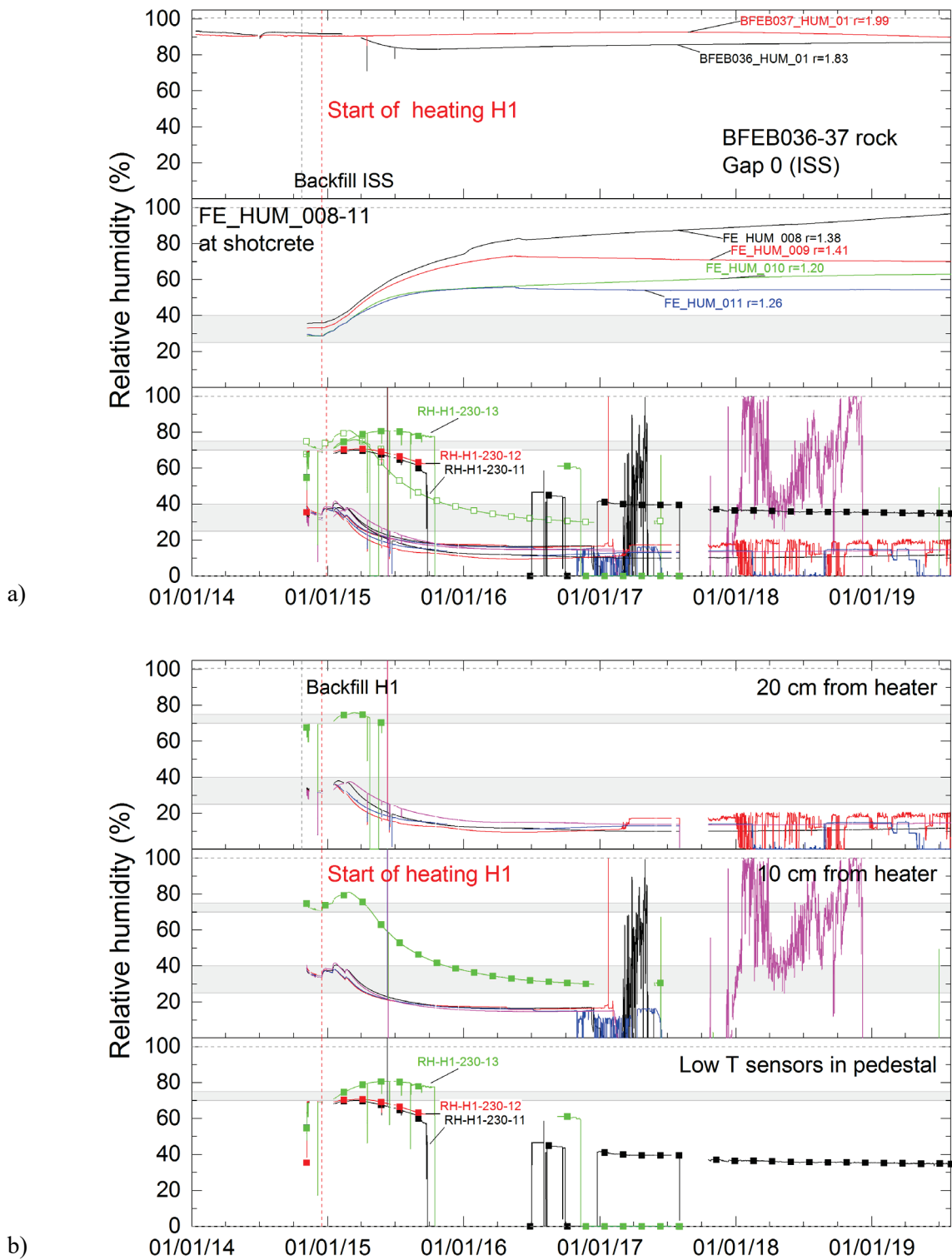


Fig. 39: Relative humidity measurements at H1

a) Overview of sensors in the rock, at the shotcrete and in the bentonite. b) Detail of measurements in the bentonite

Lines with symbols indicate sensors in the compacted bentonite block heater pedestals. Grey shaded regions indicate an approximate range of the as-emplaced relative humidity for sensors in the bentonite (GBM and blocks).

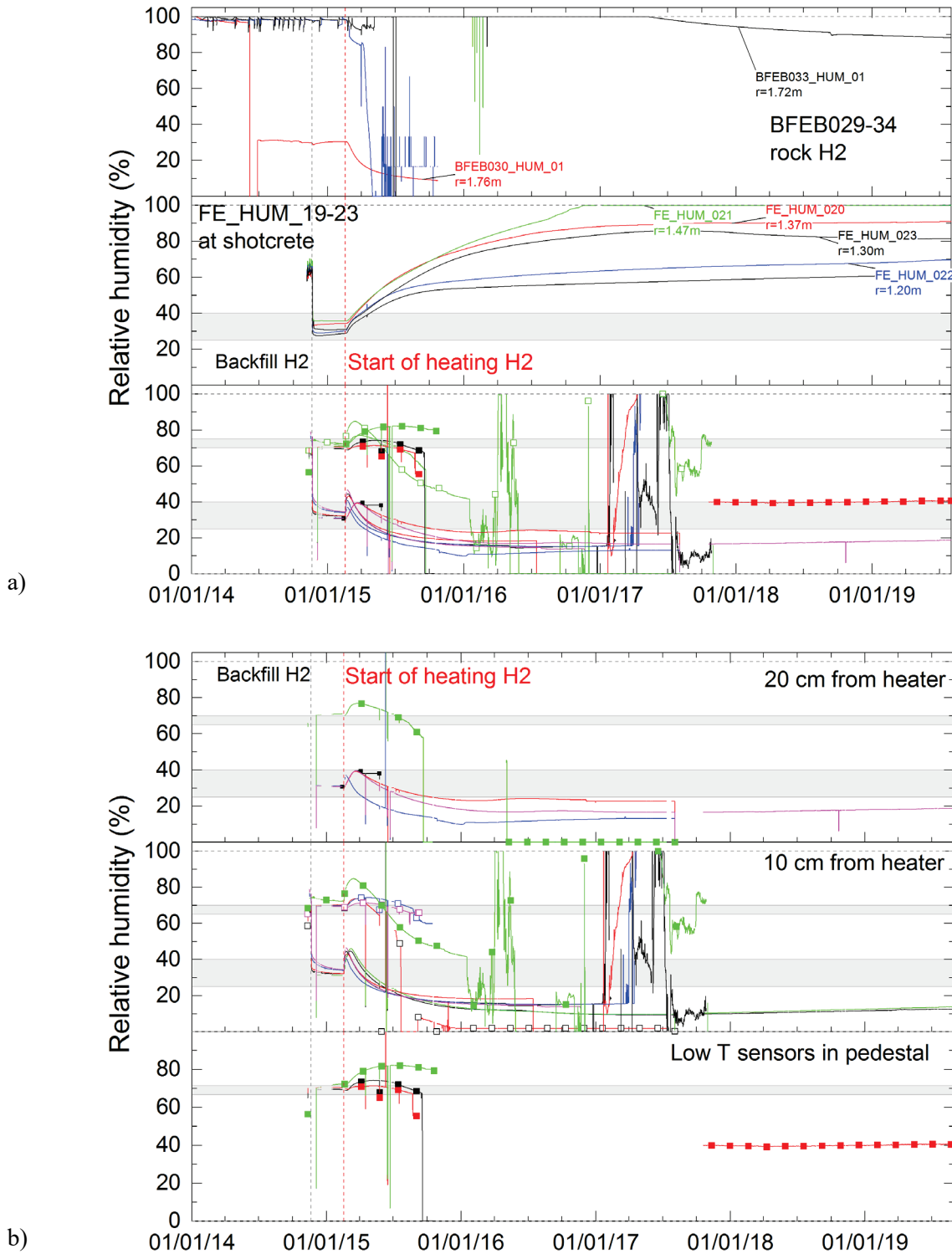


Fig. 40:

Relative humidity measurements at H2

a) Overview of sensors in the rock, at the shotcrete and in the bentonite. b) Detail of measurements in bentonite

Lines with symbols indicate sensors in the compacted bentonite block heater pedestals. Grey shaded regions indicate an approximate range of the as-emplaced relative humidity for sensors in the bentonite (GBM and blocks).

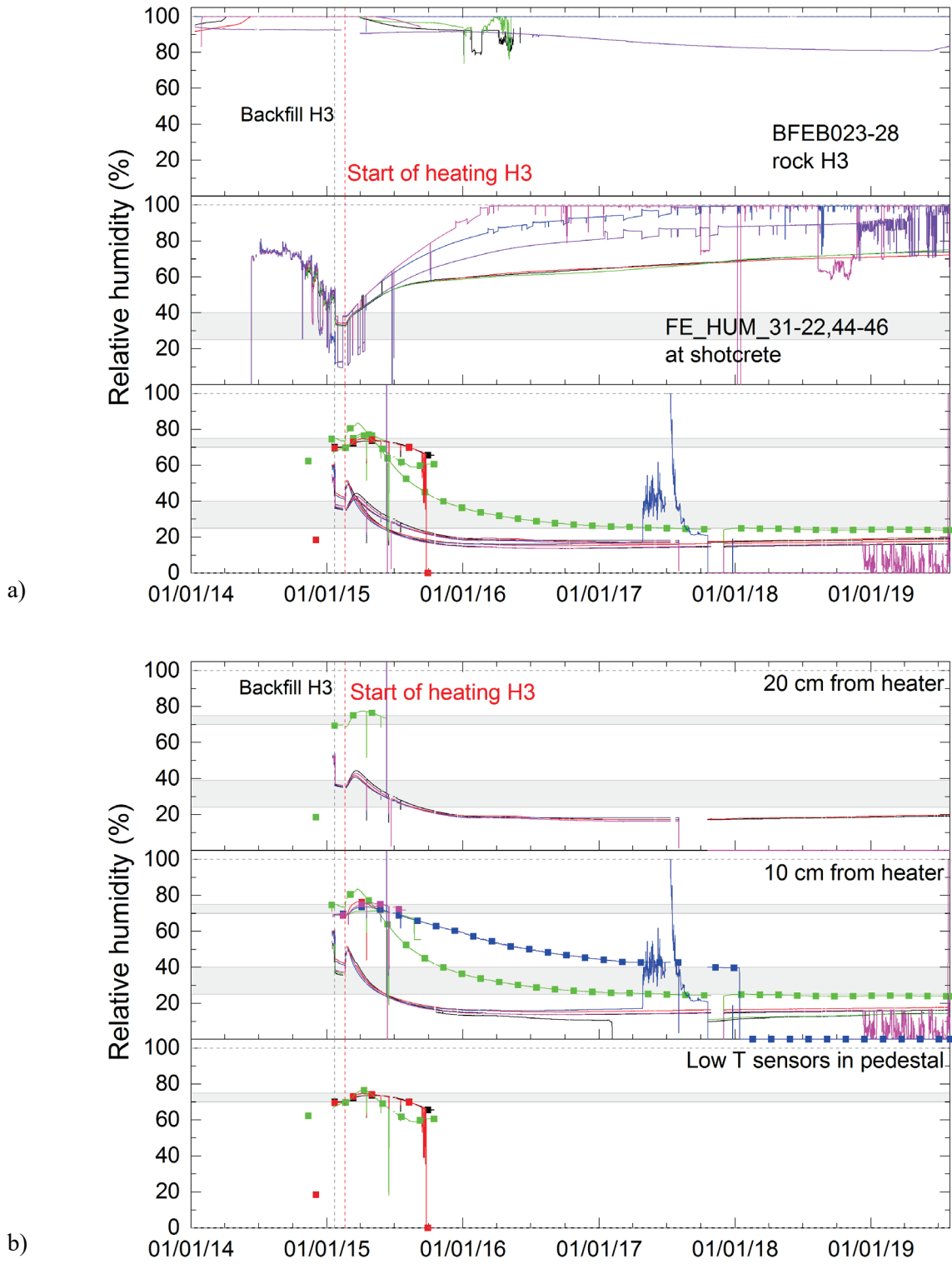


Fig. 41: Relative humidity measurements at H3

a) Overview of sensors in the rock, at the shotcrete and in the bentonite. b) Detail of measurements in bentonite

Lines with symbols indicate sensors in the compacted bentonite block heater pedestals. Grey shaded regions indicate an approximate range of the as-emplaced relative humidity for sensors in the bentonite (GBM and blocks).

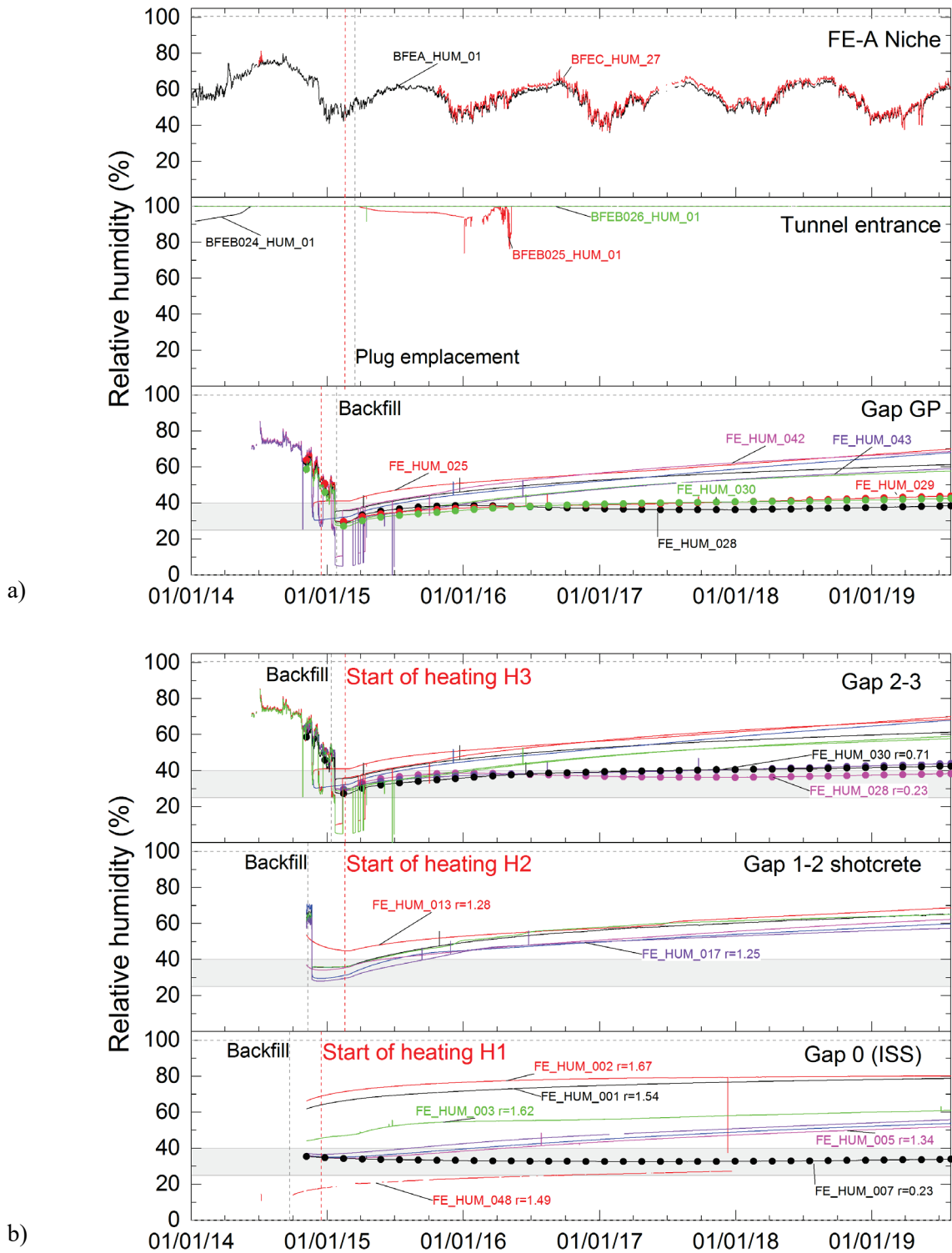


Fig. 42: Relative humidity measurements

a) In the ISS and gaps between heaters. b) The gap between H3 and the plug, in boreholes the tunnel entrance and in FE-A Niche (ventilated tunnel environment)

Lines with symbols indicate sensors in the compacted bentonite block heater pedestals. Grey shaded regions indicate an approximate range of the as-emplaced relative humidity for sensors in the bentonite (GBM and blocks).

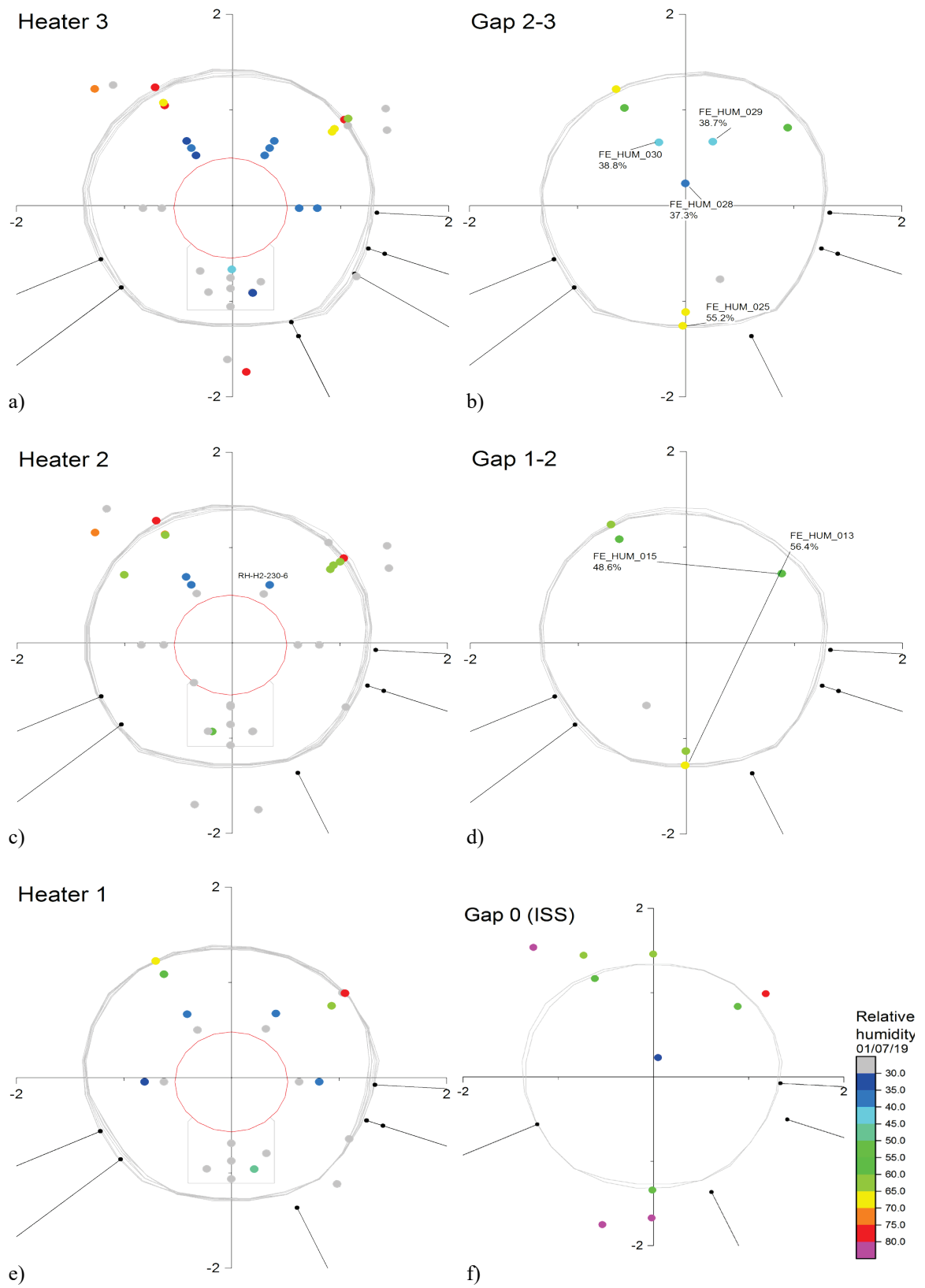


Fig. 43: Spatial distribution of relative humidity measurements as vertical cross-sections

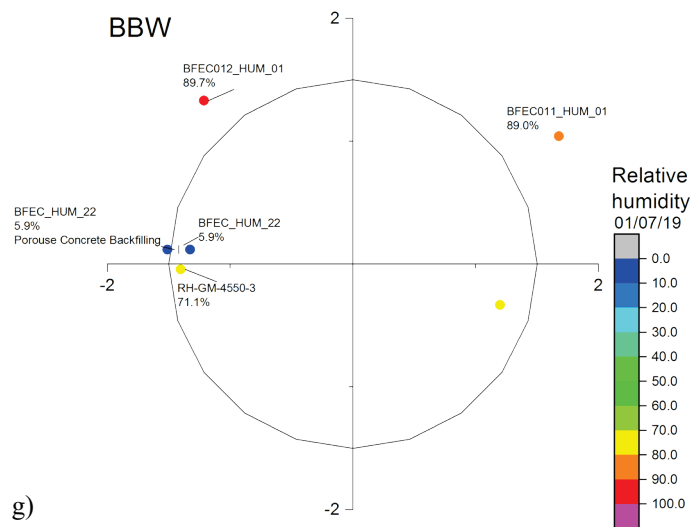


Fig. 43: Cont.

Fig. 44 shows the distribution of relative humidity with radial distance from the tunnel axis at selected times. In the heater sections relative humidity in the GBM increases with time from about 1m outwards and typically decreases within 1m of the tunnel axis. In the gap sections changes in relative humidity are typically smaller with minor changes in the centre of the GBM and relatively larger increases towards the shotcrete. In the rock several sensors show a reduction in relative humidity indicating possible desaturation.

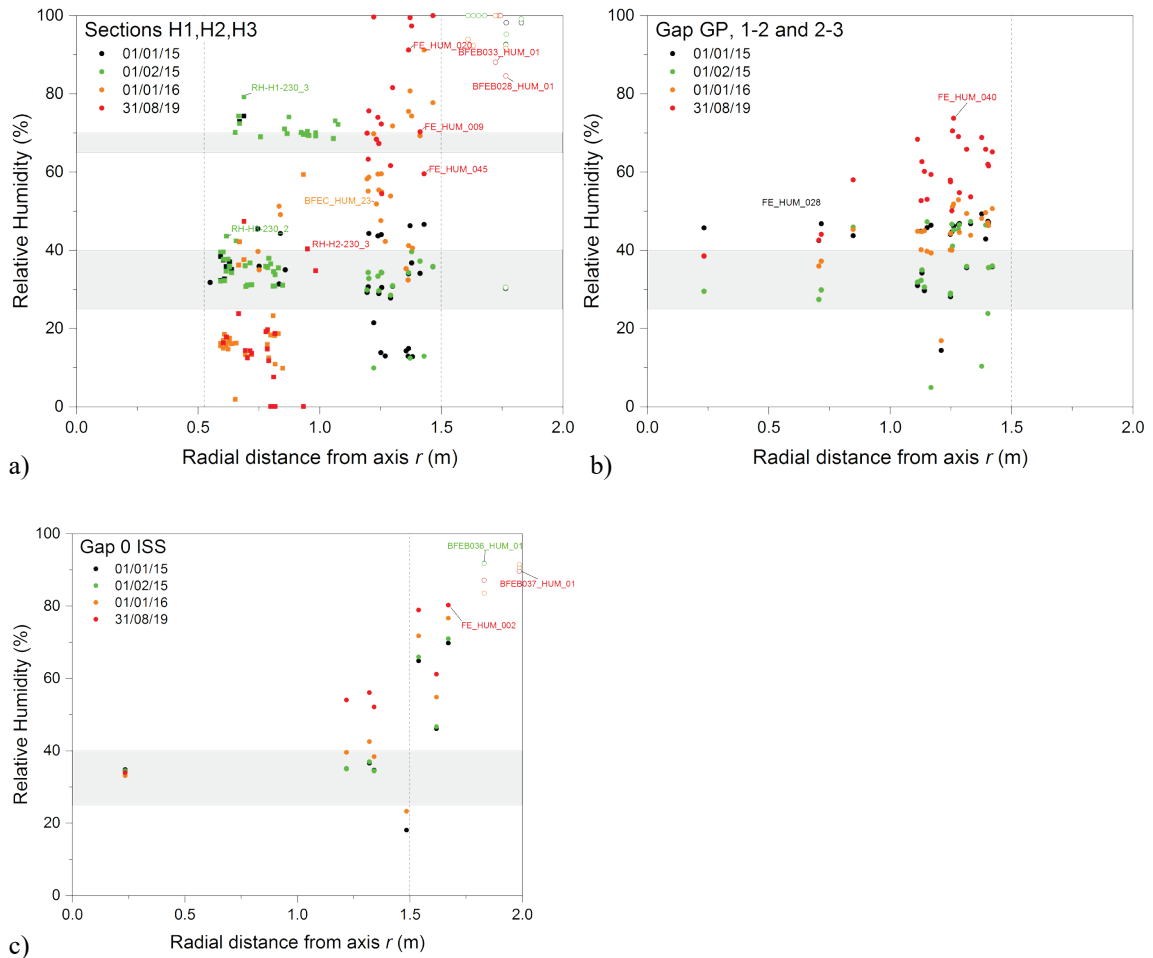


Fig. 44: Relative humidity versus radial distance from the tunnel axis at selected times  
 a) Heater sections. b) Gap GP, 1-2 and 2-3. c) Gap 0 (ISS). Borehole sensors shown as hollow symbols, sensors in the Heater pedestals are shown as solid squares

The RH evolution over time near the tunnel wall ( $r > 1.2\text{m}$ ) is shown in Fig. 45, together with the wet spot locations. Over the first year of heating (01.01.2016) the main increase in RH occurs in the heater sections, while by 31.08.19 a more general wetting pattern has evolved throughout the shotcrete section. In the ISS section there is a lower density of sensors, but wetting appears to increase more slowly than in the sections near the heaters. There is no obvious strong correlation with proximity to wet spots.

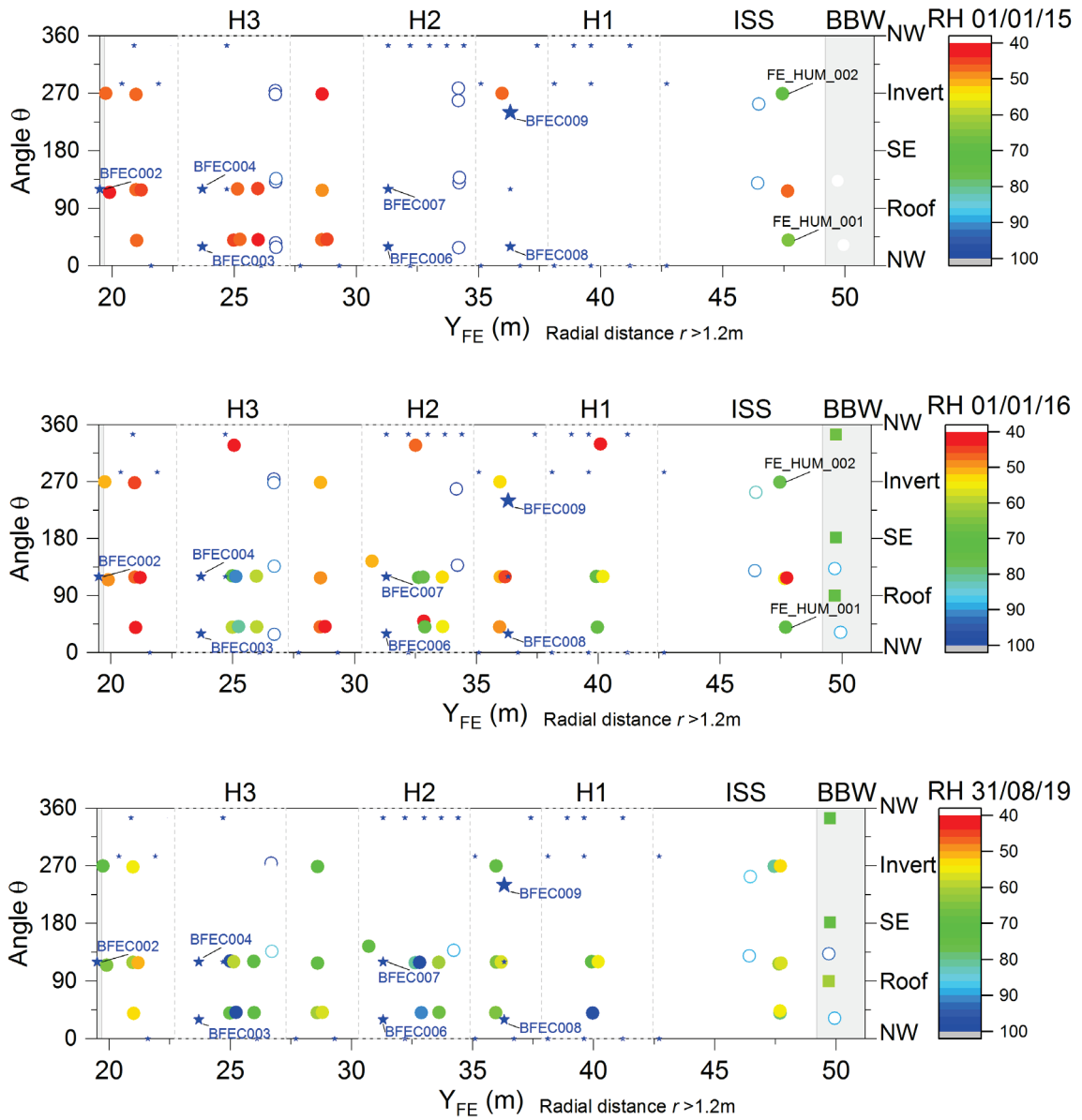


Fig. 45: Relative humidity measurements near the shotcrete and rock  
 a) 01.01.2015 prior to start of heating in H2,H3. b) 01.01.2016 after approximately 1 year of heating. c) 31.08.2019 at the end of the current monitoring period  
 Approximate wet spot locations shown as blue stars.

Tab. 16: Mean measured relative humidity in the rock, GBM and heater pedestals over selected periods

Pre startup of H2,3, after 1 year of heating and at the end of the current monitoring period

Values are calculated from the mean sensor measurement over the time period and reported as minimum, mean, maximum and number of sensors.

			Pre startup H2,3 01.01. – 14.01.2015				~ 1 year heating 01.01. – 01.02.2016				End monitoring period 01.08. – 31.08.2019				
	Heater		Min/Mean/Max/#				Min/Mean/Max#				Min/Mean/Max/#				
Rock	H2		30	88	100	6	97	99	100	2	88	88	88	1	
Rock	H3		93	99	100	6	89	93	100	4	84	92	100	2	
GBM	H1		31	35	38	8	11	33	76	11	1	47	100	9	
GBM	H2		28	32	36	10	11	37	79	16	12	58	100	10	
GBM	H3		34	44	49	6	13	40	92	14	0	45	100	13	
Pedestal	H1		75	75	75	1	37	37	37	1	35	35	35	1	
Pedestal	H2		73	73	73	1	2	17	32	2	41	41	41	1	
Pedestal	H3		73	73	73	1	19	38	58	3	0	14	24	3	
		$\Gamma_{\min}$	$\Gamma_{\max}$	Min/Mean/Max/#				Min/Mean/Max#				Min/Mean/Max/#			
GBM	H1	0.55	1	37	37	38	4	11	15	17	7	1	27	100	5
GBM	H2	0.55	1	32	34	36	4	11	16	23	9	12	15	19	3
GBM	H3	0.55	1					13	16	19	8	0	16	30	7
GBM	H1	1	1.5	31	34	37	4	55	64	76	4	54	71	97	4
GBM	H2	1	1.5	28	31	36	6	52	64	79	7	62	77	100	7
GBM	H3	1	1.5	34	44	49	6	59	70	92	6	59	79	100	6

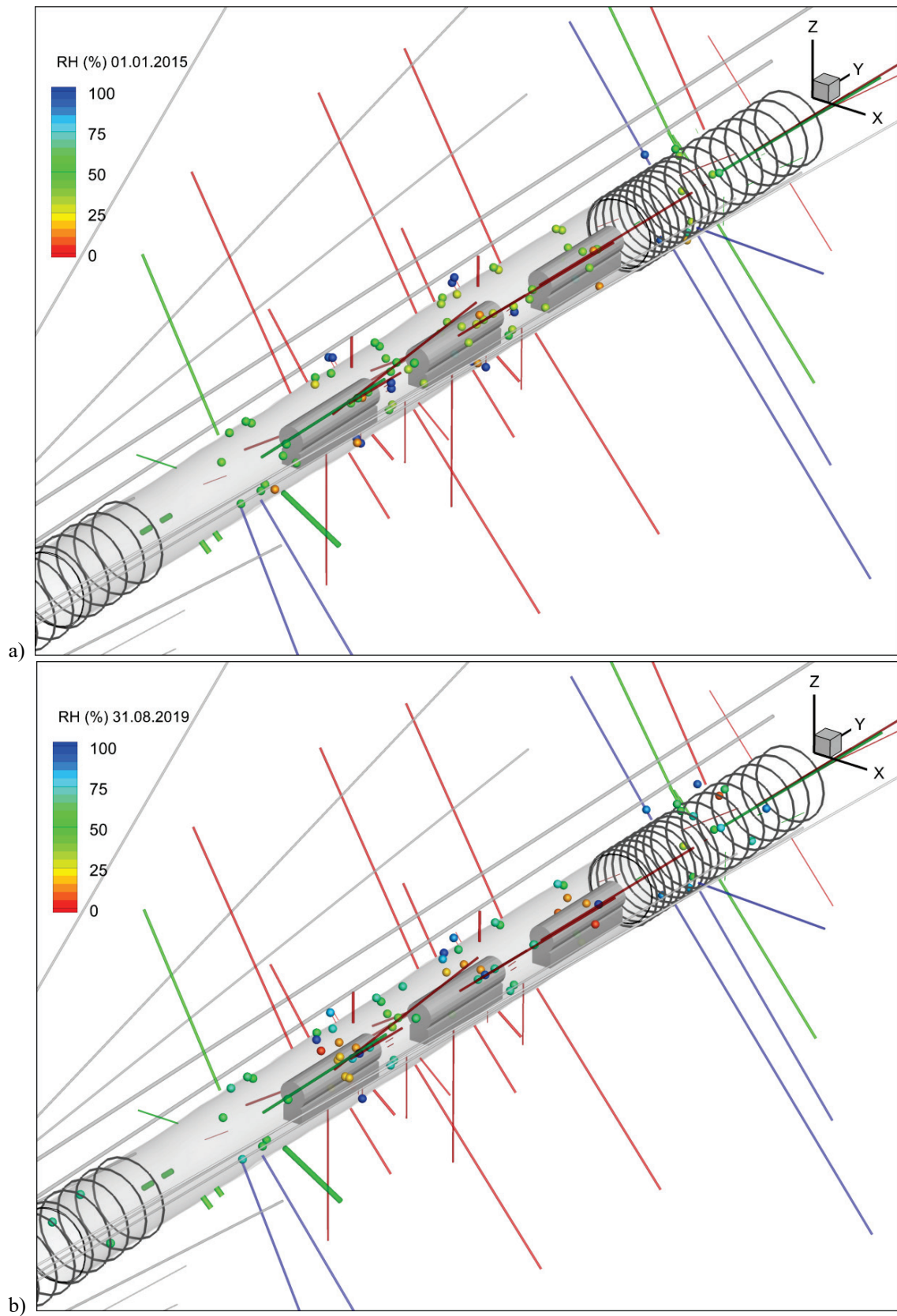


Fig. 46: Spatial distribution of relative humidity (%)  
a) Prior to heating H2 and H3 on 01.01.2015. b) End of monitoring 31.08.2019

**Volumetric water content in the buffer**

Volumetric water content was measured with 6 TDRs installed in the H2, Gap 2-3 and H2 and H3 sections on 03.06.2014. Data is available from March 2015 when the TDR DAS became operational. All 6 sensors show a common trend with first measurements between 5 and 10 % followed by a steady rise to between 14 and 17 %. The estimated water content from as emplaced values ranges from 7 to 8 % while the first measured values range between 6 and 10 %.

The overall trend is consistent with increased saturation of the GBM close to the shotcrete due to either flow from the rock through the shotcrete or redistribution of moisture from drying of the bentonite around the heaters. TDR FE\_SEA\_004s in the gap between the heaters shows slightly lower water content and a generally slower initial rise in water content. A volumetric water content of 20 % would correspond to a saturation of 40-50 % for the expected GBM porosity.

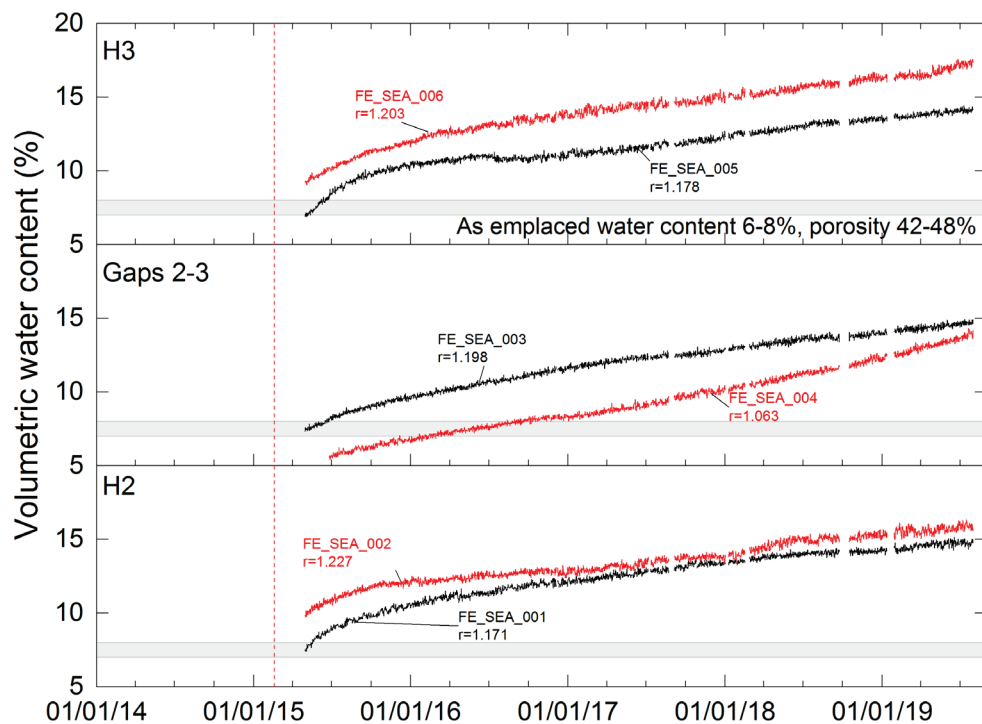


Fig. 47: Volumetric water content in buffer around H2 and H3

a) BFEB0017,18,19. b) BFEB020,21,22

**Volumetric water content in the rock**

Volumetric water content in the rock is monitored in 6 boreholes equipped with TDR and temperature sensors around H2 and H3. Boreholes were drilled and instrumented 17. – 21.02.2014. BFEB017 and BFEB02 were drilled into the roof, while the remaining were drilled downwards. Data is available for a few months after installation and from June 2015 on after installation of a new DAS. The sensors show a common trend with volumetric water content initially in the range 17 – 19 %. This probably represents saturated or nearly saturated conditions.

The response of the different sensors to heating is shown in Fig. 48.

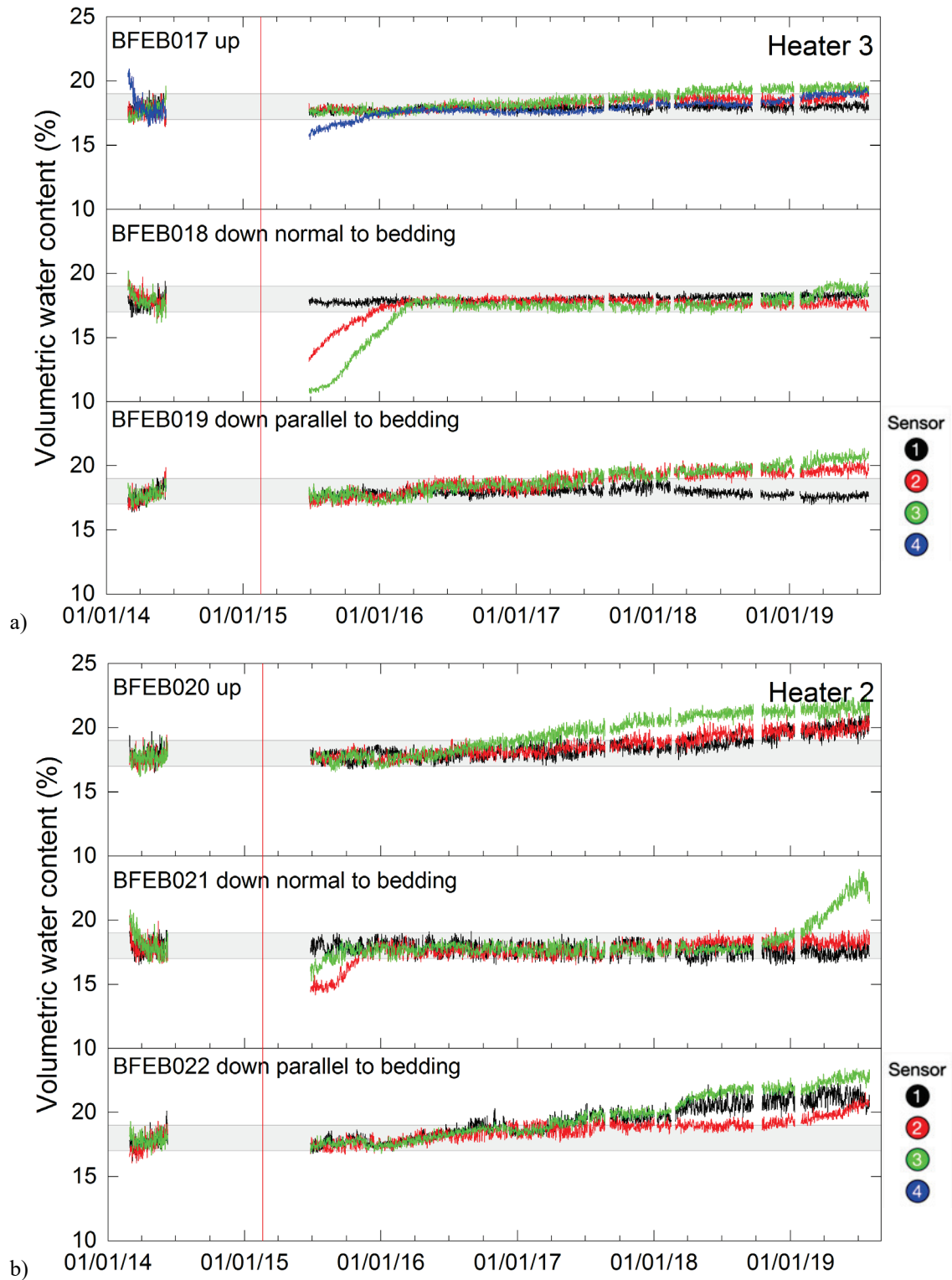


Fig. 48: Volumetric water content in boreholes around H2 and H3  
 a) BFEB0017, 18, 19. b) BFEB020, 21, 22

Fig. 48 shows the following responses:

- BFEB017 water content increases slowly after heating with no strong trend along the borehole.
- BFEB018 water content recovers in the first year after heating and then is stable.
- BFEB019 water content increases slowly after heating with lower water content at sensor 1.
- BFEB020 water content increases slowly after heating with a slight trend for higher values near the tunnel wall.
- BFEB021 water content at sensor 2 and 3 recovers in the first six months after heating. Sensor 3 (nearest the tunnel wall) shows a strong increase in 2019.
- BFEB022 water content increases slowly after heating with no particular trend with depth.

The low water content observed in the boreholes drilled normal to bedding (BFEB018, BFEB020) may indicate some local desaturation that occurred during the end of ventilation and the emplacement and initial heating periods. Water content in BFEB018 is lowest close to the tunnel (sensor 3). However, water content recovers in all 3 sensors at both boreholes by April 2016.

The overall steady rise in calculated water content seen at most sensors (Fig. 48) is probably due to calibration sensitivity to increasing temperature rather than a real increase in water content. The cause of the somewhat larger rise observed in BEFEB021 sensor 3 is unknown.

Data from FDR sensors in BFEC006, 7, 8 and BFEB050, 51 are given in Appendix E.

### **3.3.2 Pore pressure**

Pore pressures in the rock around the FE Gallery are monitored using:

- multi-packer systems in long boreholes drilled from the FE-A Niche prior to excavation of the FE Tunnel (BFEA002-7)
- short boreholes drilled from the FE-A Niche (BFEA008, 9, 12, 13, 14, 15)
- double packer systems in short radial boreholes drilled from the FE Tunnel (BFEB001-8, BFEB044-48, 54, 55)

Pore pressures are not measured in the EBS as the expected saturation period is long so that no significant pressure build-up within the EBS is expected.

### Multi-packer systems drilled from FE-A Niche

The multi-packer systems are equipped with interval and packer pressure sensors for each of the 6 monitoring intervals and packers, together with temperature sensors. This report concentrates on the response to heating, previous work (e.g. Lanyon et al. 2014) provide detailed analysis of the response to excavation and invert replacement.

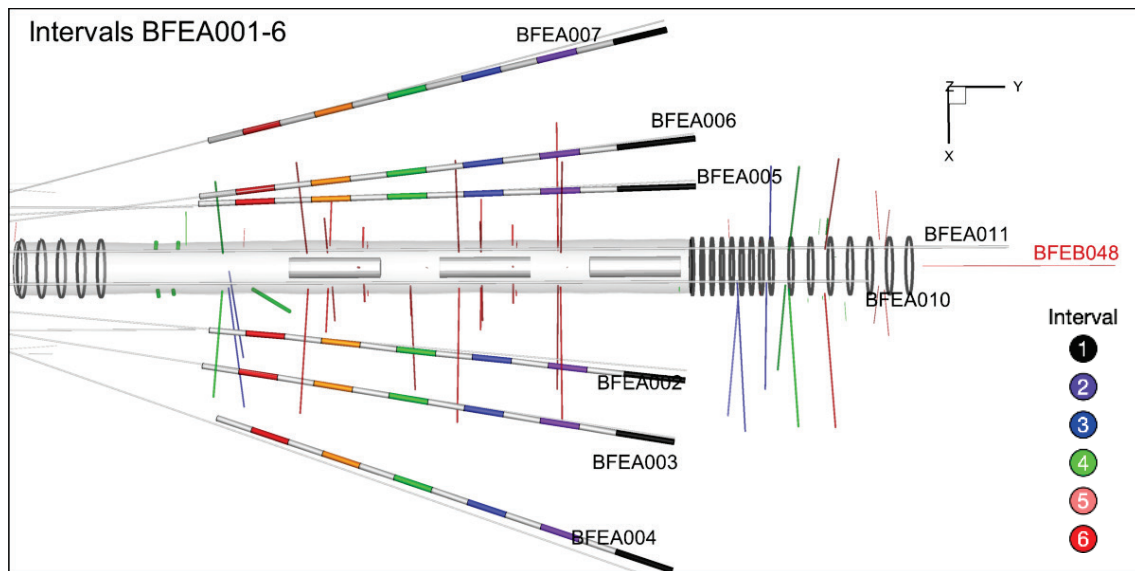


Fig. 49: Plan view of BFEA002-7 boreholes and monitoring intervals

Interval pressures for the six boreholes are shown in Fig. 50, Fig. 51 and Fig. 52. All the intervals show:

- initial equilibration period after saturation with synthetic pore water
- pressure response to excavation
- pressure response to replacement of the concrete invert
- post excavation equilibration to open tunnel conditions (hydrotesting in some intervals)
- response to heating

Maximum post-heating pressures are marked in Fig. 50, Fig. 51 and Fig. 52. Close to the tunnel there is a clear difference between the response parallel to bedding (BFEA002) and normal to bedding (BFEA005) with pressures peaking in BFEA002 by mid-2017 while pressures are typically still increasing (or show a very broad late peak) in BFEA005. Further from the tunnel in BFEA003 and BFEA006 pressures still reach a maximum earlier (parallel to bedding direction) than BFEA004 and BFEA007 (in the normal to bedding direction). In BFEA004 and BFEA007 pressures are still rising at the end of the monitoring period.

While the overall trends in pressure are very smooth some small disturbances can be seen e.g. BFEA005 intervals i1, i2, i3 in late 2015 and mid-2016. These are believed to relate to local deformations around the boreholes. They principally occur in the normal to bedding direction where the EDZ is believed to be of greater extent.

Small jumps in pressure in mid-2019 are seen in many of the intervals and are believed to relate to poro-elastic responses to the excavation of Ga18 (in particular excavation Phase 2D see next chapter for discussion).

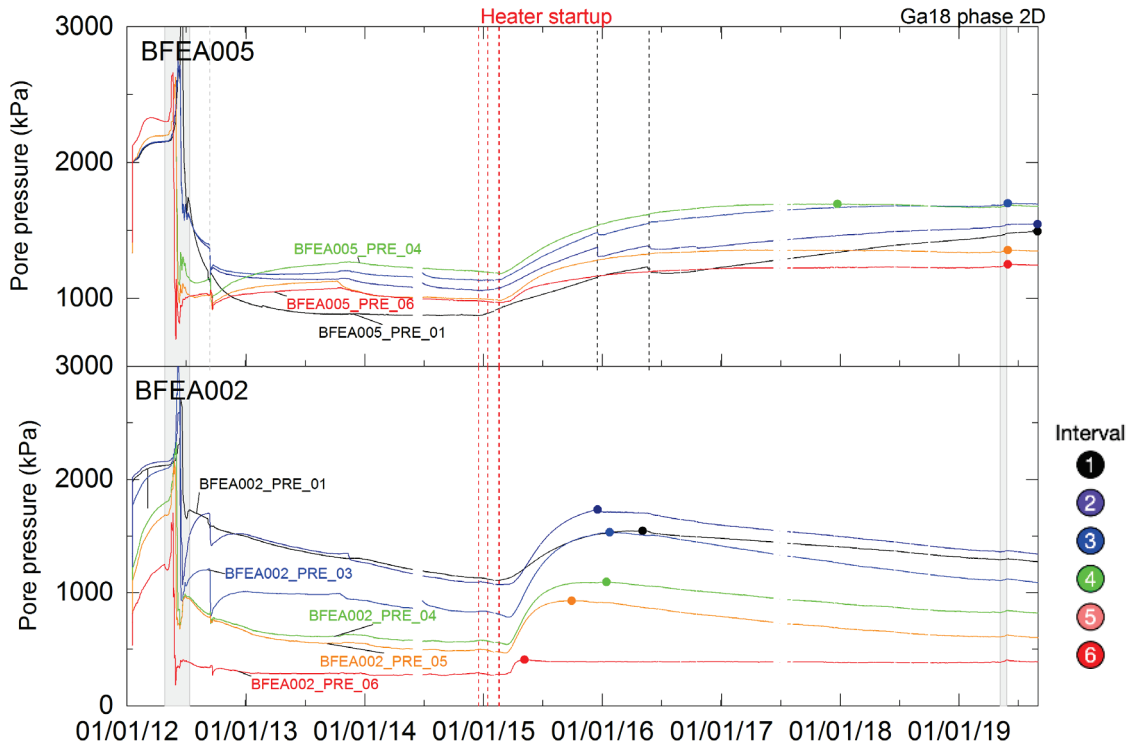


Fig. 50: Measured interval pressure in BFEA002 (parallel to bedding) and BFEA005 (normal to bedding)  
Symbols on lines indicate peak post-heating pressure.

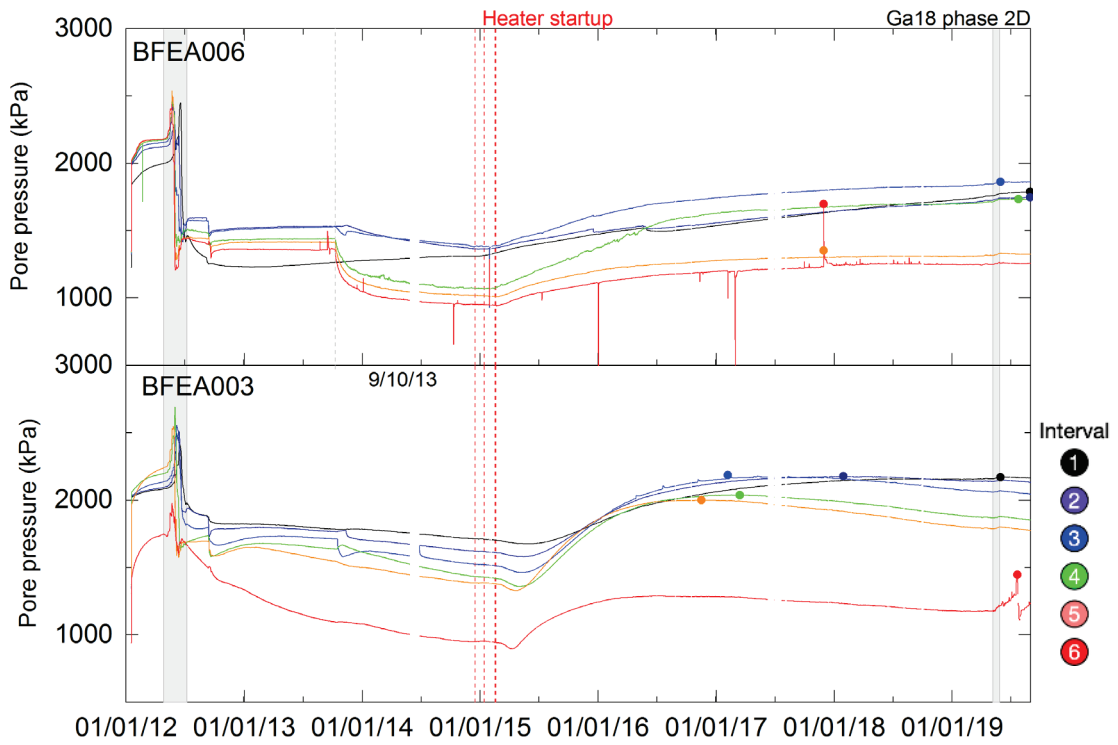


Fig. 51: Measured interval pressure in BFEA003 (parallel to bedding) and BFEA006 (normal to bedding)

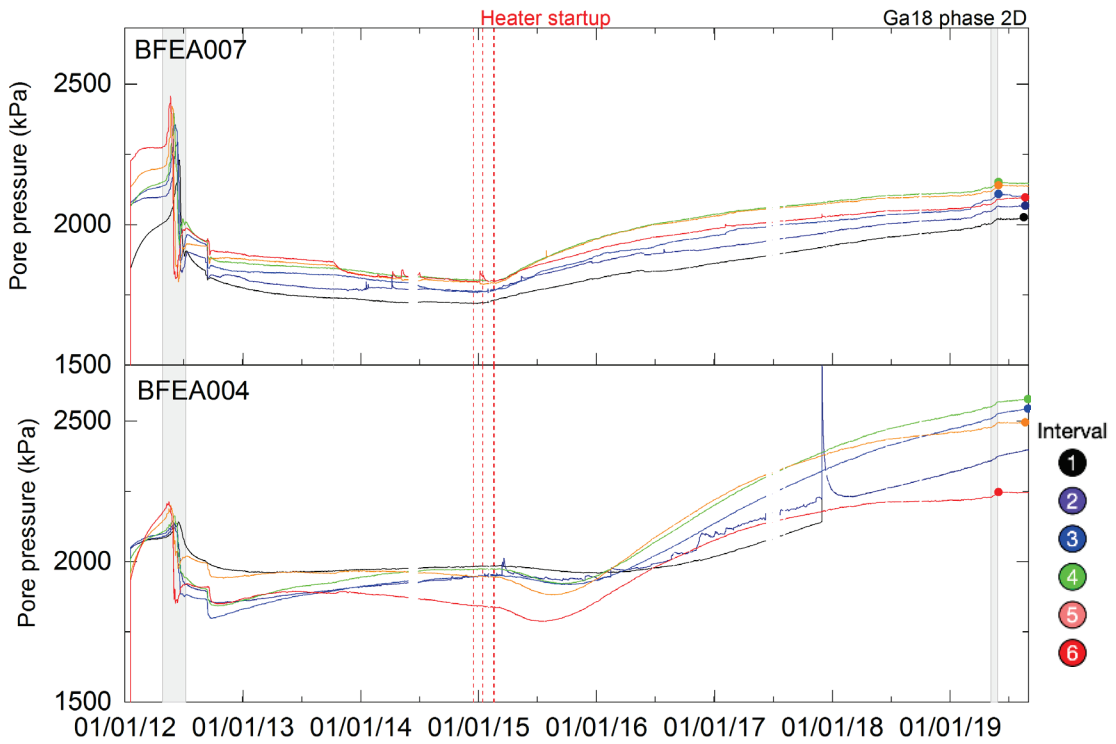


Fig. 52: Measured interval pressure in BFEA004 (parallel to bedding) and BFEA007 (normal to bedding)

**Radial boreholes drilled from FE tunnel in H2 and H3 sections**

A similar pattern of response is seen in the radial boreholes drilled from the H3 and H2 sections. Again, there is a clear difference between boreholes drilled parallel and normal to bedding. In the boreholes drilling parallel to bedding interval pressures show clear early peaks post heating (e.g. BFEB003 in Fig. 53), while normal to bedding a broader peak or slow rise occurs (e.g. BFEB004 in Fig. 53). Again, the normal to bedding intervals show a less smooth evolution than those parallel to bedding.

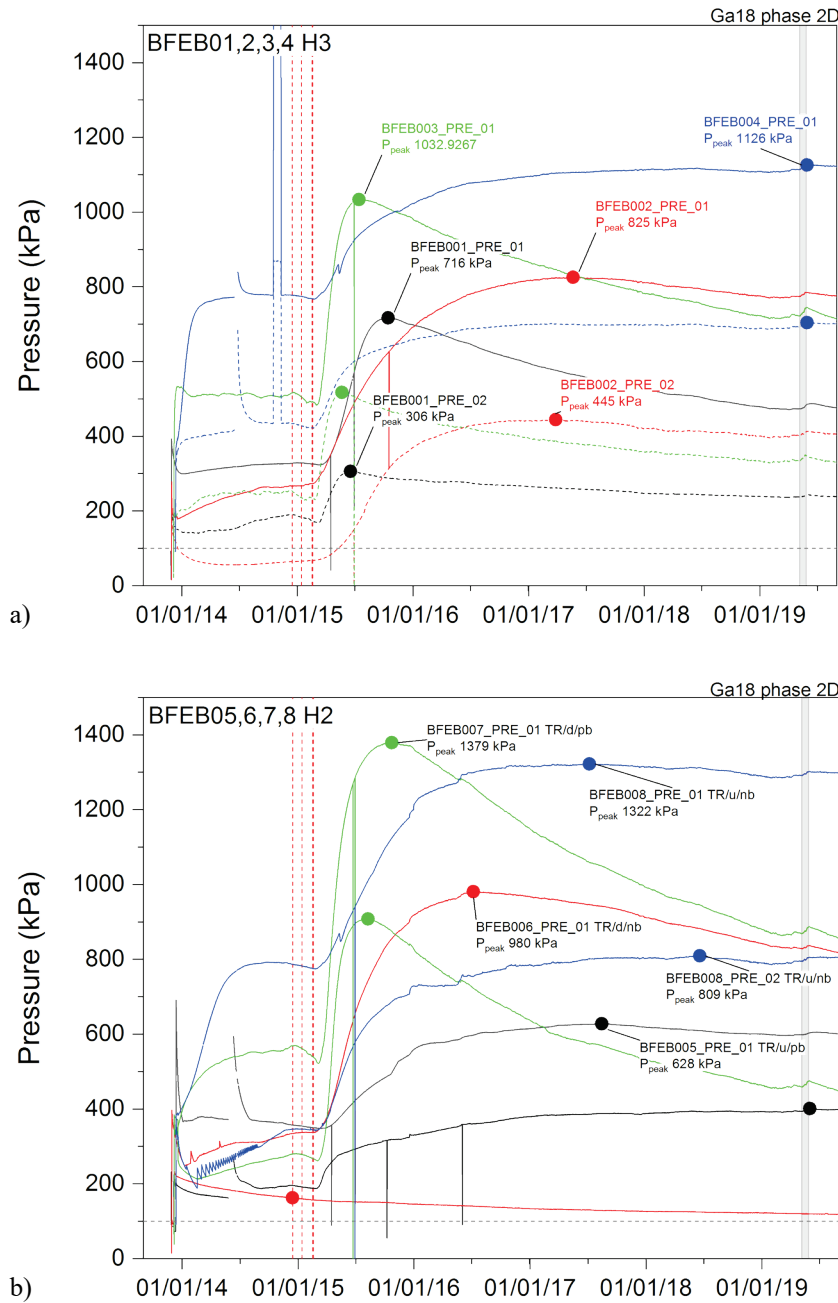


Fig. 53: Measured interval pressure in radial boreholes in a) H3 section and b) H2 section  
 Symbols on lines indicate peak post-heating pressure. Borehole direction: TR=radial, u/d up/down and relation to bedding pb/nb parallel and normal to bedding.

### Boreholes drilled from FE tunnel entrance

In the boreholes drilled from the tunnel entrance section a slow decline in pressure occurs until mid-2017 when pressures start to rise again. There is some influence of seasonal variations and of the Ga18 excavation.

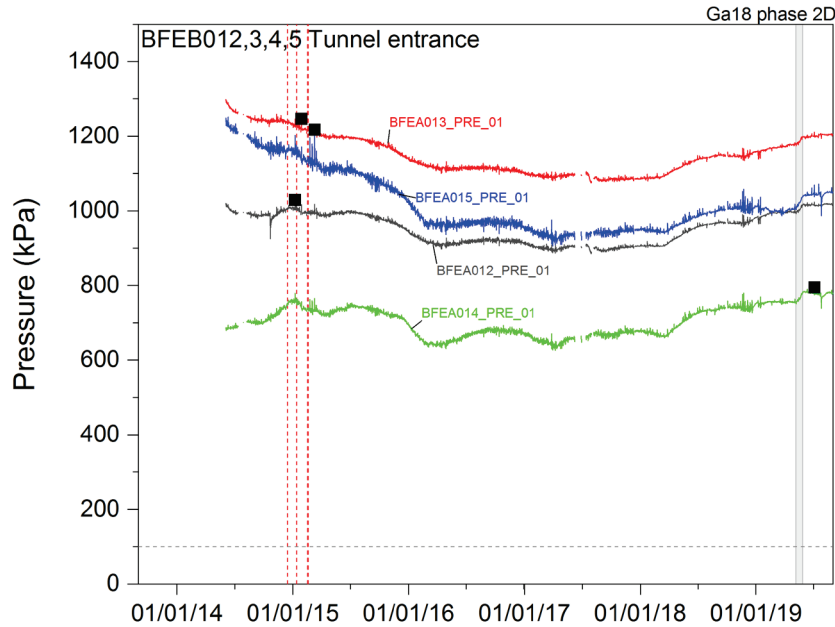


Fig. 54: Measured interval pressure in tunnel entrance section  
Symbols on lines indicate peak post-heating pressure

Pressure in borehole intervals around the porous concrete section (Fig. 55 a) show a complex response to heating which may indicate a lack of equilibration period prior to emplacement. BFEB005 pressures rise strongly prior to heating and then more steadily after the start of heating. Several small pressure drops occur in late 2018. Measured pressures in BFEB0044, 46 and 47 are lower and show no clear response to heating.

BFEB048 at the end of the FE tunnel shows relatively high pressure over 2000 kPa (comparable to pressure measured prior to excavation) that slowly declines during the monitoring period to ~1800 kPa. The two intervals (i1 and i2) initially show very similar pressures but interval i1 (0.9m mah) shows a drop in pressure after the start of heating that then recovers to nearly the same value as interval i2. The data from interval i1 stops after the end of July 2108 and it is assumed that the sensor has failed.

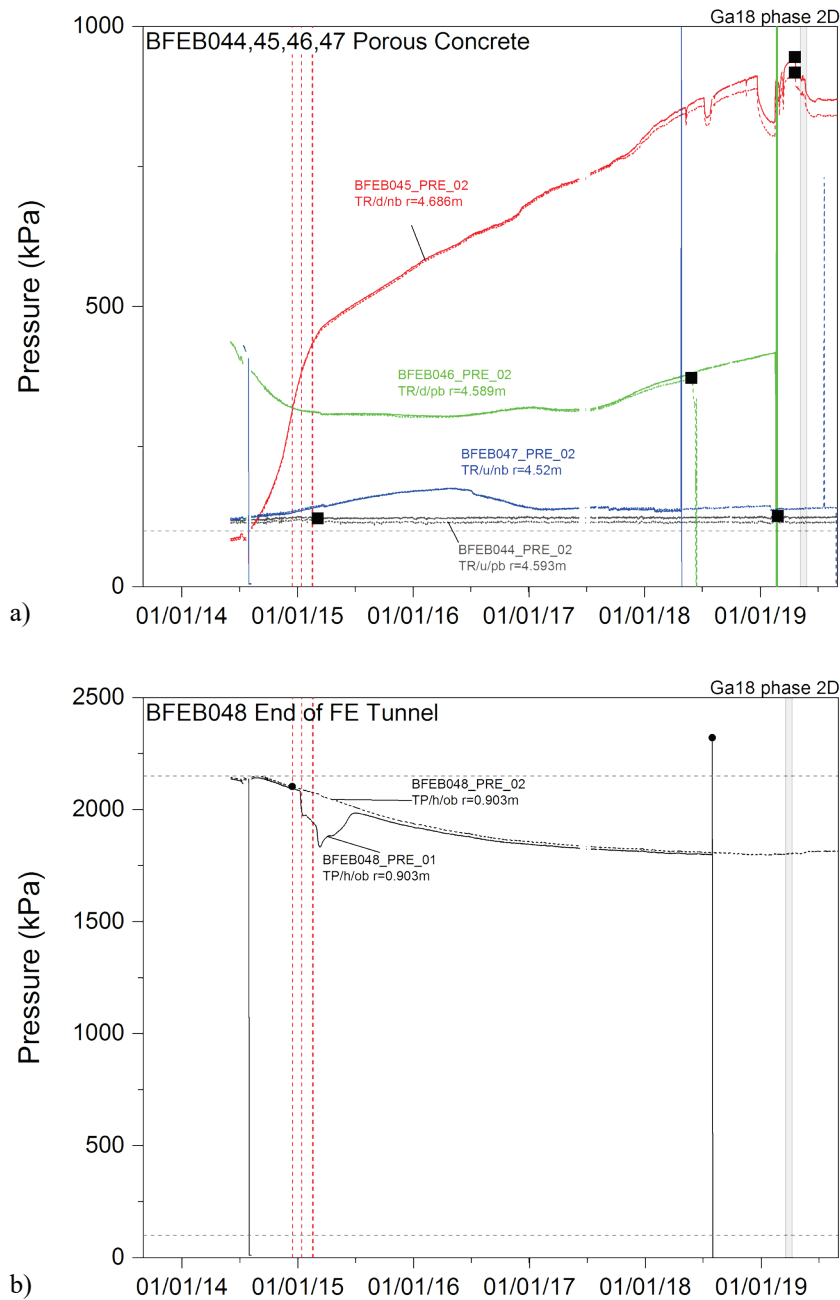


Fig. 55: Measured interval pressure in radial boreholes in a) Porous concrete section and b) end of the FE Tunnel

Symbols on lines indicate peak post-heating pressure. Borehole direction: TR = radial, u/d up/down and relation to bedding pb/nb parallel and normal to bedding.

**Pore pressure distribution around the FE Tunnel**

The measured pore pressure distribution around the FE Tunnel has evolved over time with periods of:

- initial equilibration to installation
- short-term response to excavation

- post -excavation pressure equilibration and response to flow to the open ventilated tunnel
- poro-elastic response to long term convergence of the rock
- thermo-pore-elastic response to heating
- limited response to Ga18 excavation

The overall pattern of pressure is illustrated in Fig. 56 which shows snapshots of measured pressure versus radial distance from the tunnel axis. Immediately prior to excavation for all but the closest interval to the FE-A Niche, measured pressures were ~ 2'000 kPa. Post excavation pressures dropped and equilibrated forming a "cone of depression" extending to about 10 m from the tunnel axis. The pressure distribution in the normal to bedding intervals is more uneven than that parallel to bedding, perhaps indicating greater response to excavation or a larger EDZ.

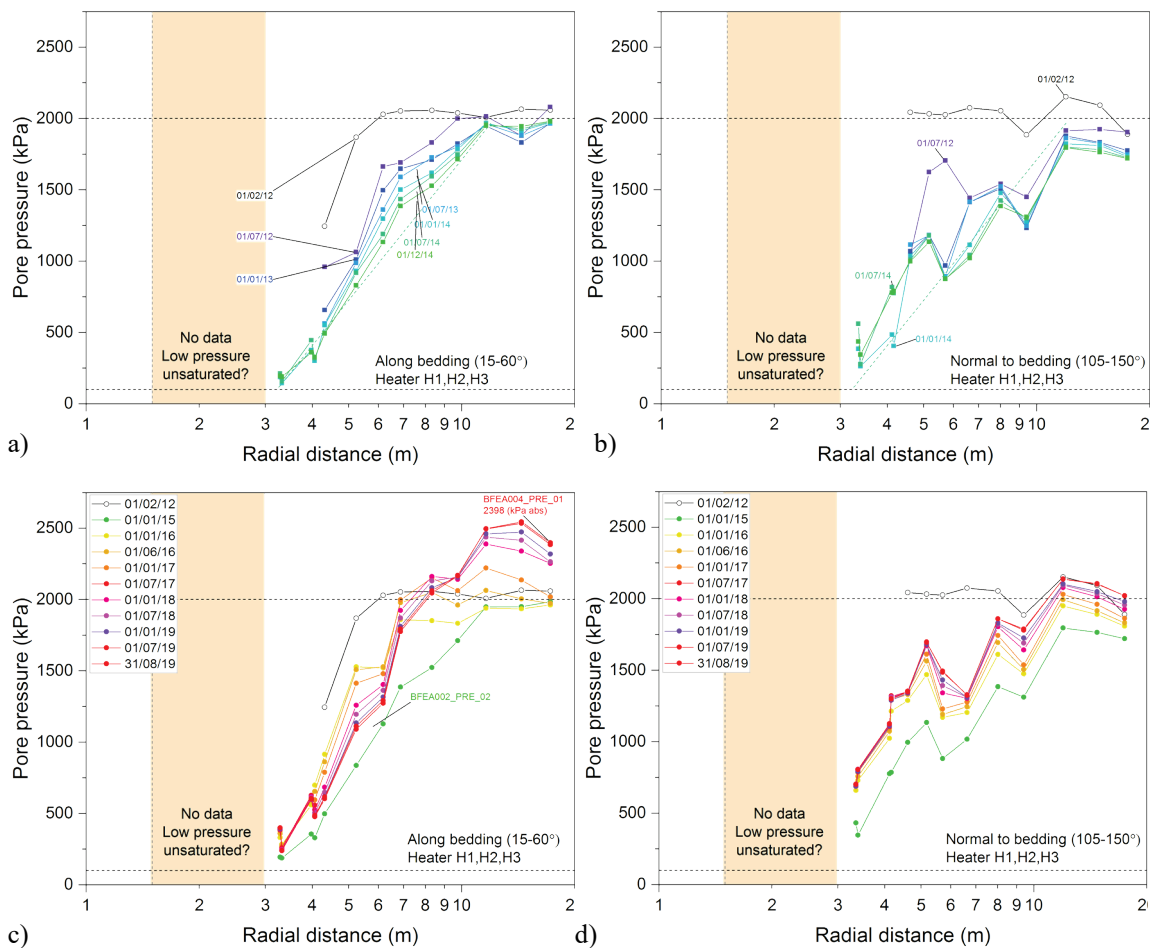


Fig. 56: Measured interval pressure versus radial distance from the FE Tunnel  
 a) Along bedding prior to heating. b) Normal to bedding prior to heating. c) Along bedding post heating. d) Normal to bedding post heating

Following heating, pressures rose due to thermo-poroelastic effects. The thermally induced front migrates more quickly parallel to bedding (higher thermal diffusivity) and extends to ~ 20 m. The thermal response is also more distinct parallel to bedding while normal to bedding a more general rise in pressure is seen. Parallel to bedding, peak thermally induced pressures occurred prior to 01.01.2017 within 6m of the tunnel axis (see Fig. 50).

The more distinct response parallel to bedding is likely to be influenced by:

- higher thermal diffusivity parallel to bedding
- the greater extent of EDZ and potentially higher hydraulic conductivity in the normal to bedding direction
- the anisotropy in elastic properties of the rock
- ongoing convergence normal to bedding resulting in volumetric strains and pore pressure reduction

Fig. 57 shows the spatial distribution of measured pore pressure at 31.08.2019. Fig. 58 shows the spatial distribution of maximum pore pressure increase (to 31.08.2019) from the start of heating.

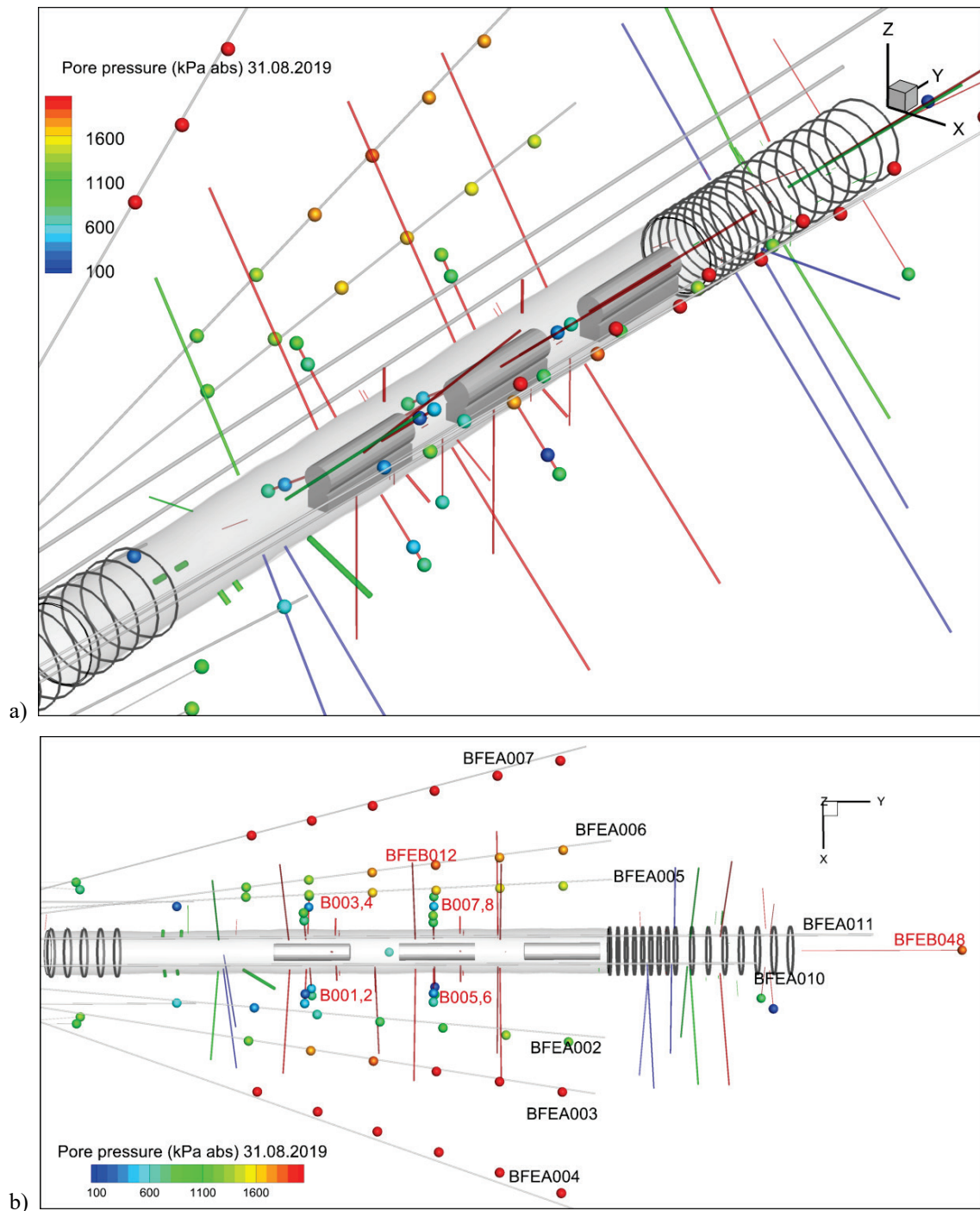


Fig. 57: Spatial distribution of interval pore pressure (kPa abs) at 31.08.2019 (end of current monitoring period)

a) 3D view. b) Plan view

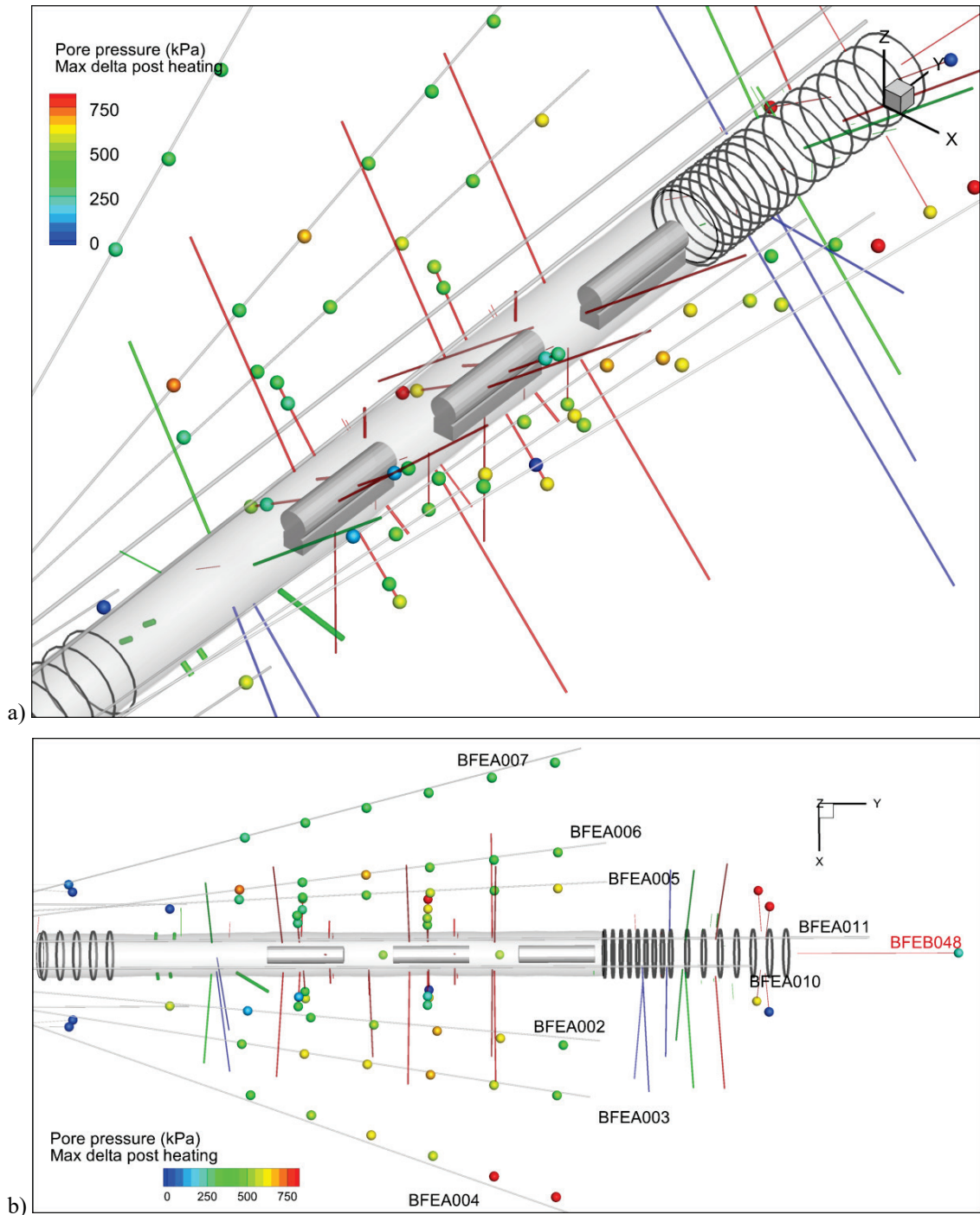


Fig. 58: Spatial distribution of change in interval pore pressure (kPa abs) from start of heating to 31.08.2019 (end of current monitoring period)

a) 3D view. b) Plan view

There are no pressure measurements close to the tunnel wall ( $r < 3$  m) due to practical limits on borehole completions but the trends shown in Fig. 56 and Fig. 57 suggest low pressures close to atmospheric in this region, which may indicate either partially saturated conditions, water in tension or a high conductivity zone close to the tunnel wall (EDZ).

### 3.3.3 Packer pressure

Packer pressures are monitored in the multi-packer systems installed in boreholes BFEA002, 3, 4, 5, 6, 7 and in the short boreholes BFEA008, 9. Packer pressures respond to:

- changes in stress around the borehole
- changes in pore pressure within neighbouring intervals
- heating due to expansion/contraction of the fluid and material of the packer system

Changes in packer pressures are likely to be indicative of deformation/ stress change rather than hydraulic processes but are reported in this section because they are measured in the same boreholes as the interval pressures. The layout of the packers is shown in Fig. 59. Fig. 60 to Fig. 63 show the packer pressures in the BFEA boreholes. The packer pressures show a period of stabilisation after excavation and then a clear response to heating with packer pressures rising strongly. Pressures rise most quickly in the boreholes parallel to bedding (BFEA002, 4, 6) influenced by greater thermal diffusivity in this direction and perhaps higher stiffness. For example, packer pressures have stabilised in BFEA002 while they are still rising in BFEA005 which are at comparable positions relative to the tunnel.

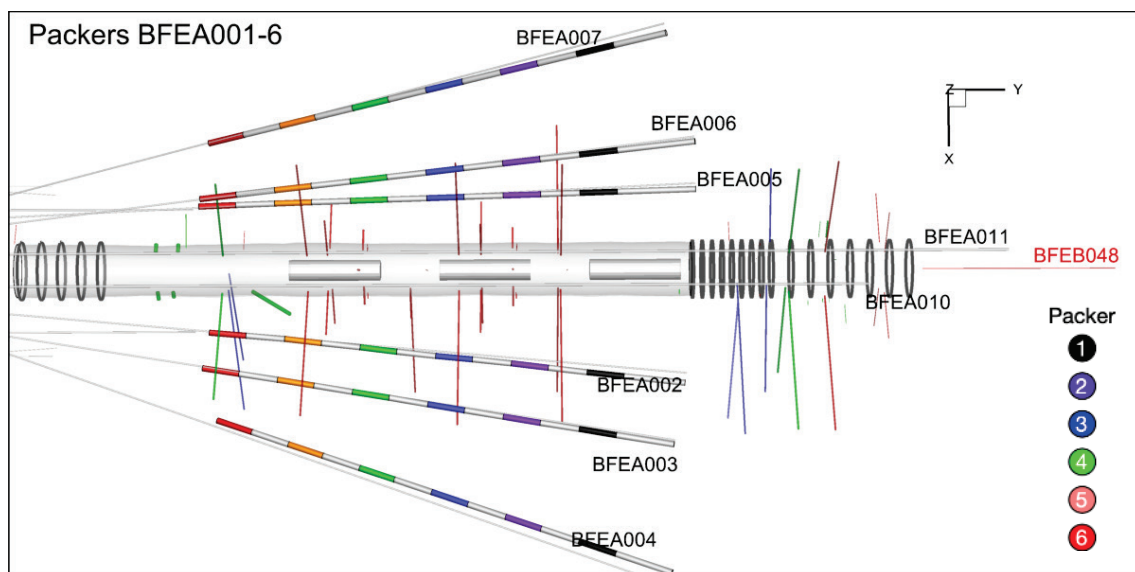


Fig. 59: Plan view of packer locations BFEA002-7

Some packer pressures also show minor jumps that are believed to be due to local deformation. Three packers show particularly irregular pressures: BFEA003 packer 2, BFA004 packer 1 and BFEA006 packer 5. This may indicate possible failure of the packer or of the rock around the packer seat.

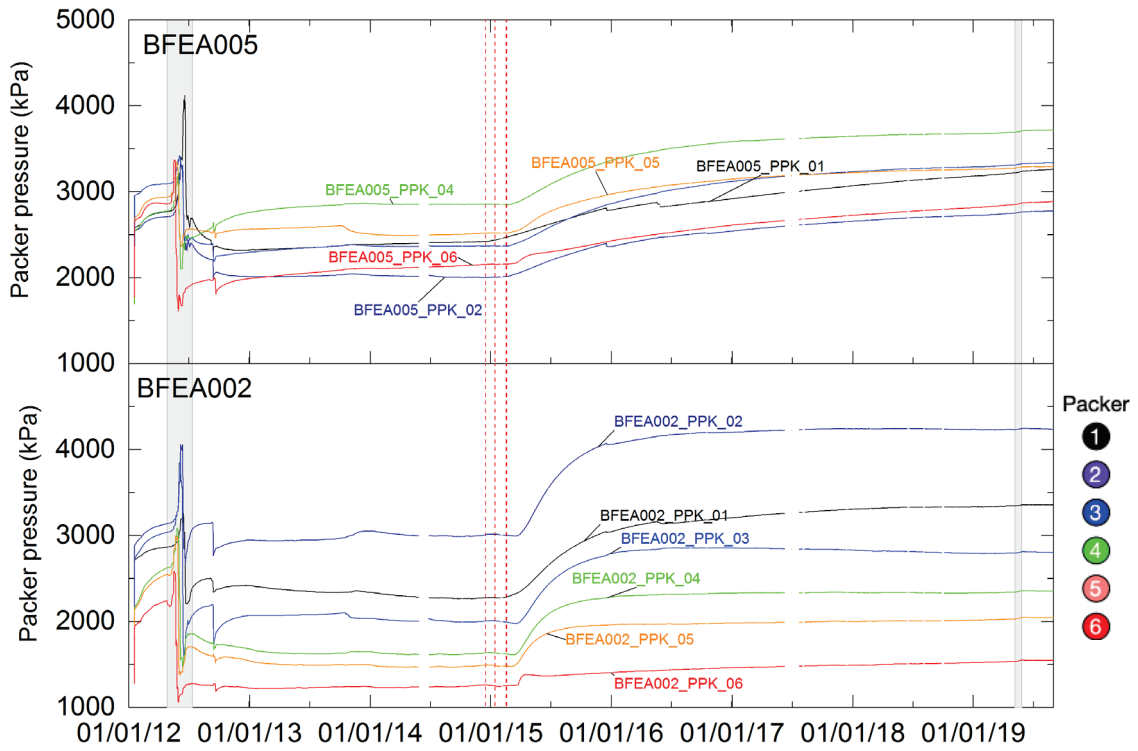


Fig. 60: Measured packer pressure in BFEA002 and BFEA005

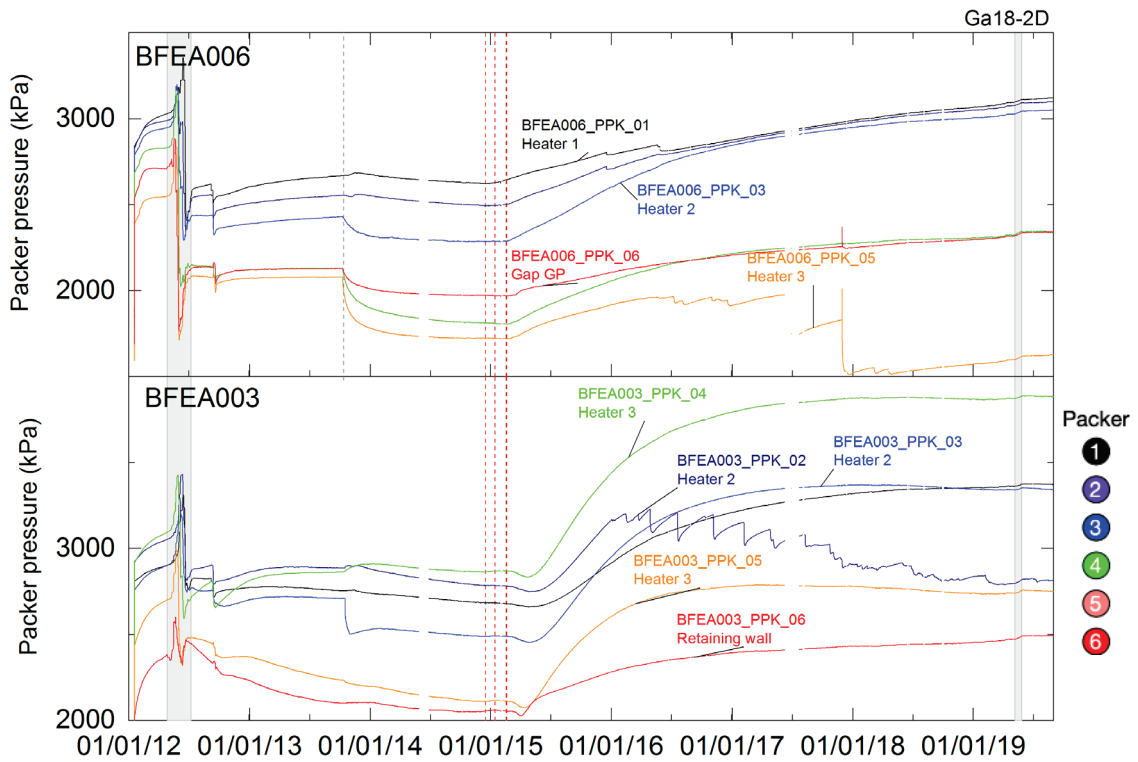


Fig. 61: Measured packer pressure in BFEA003 and BFEA006

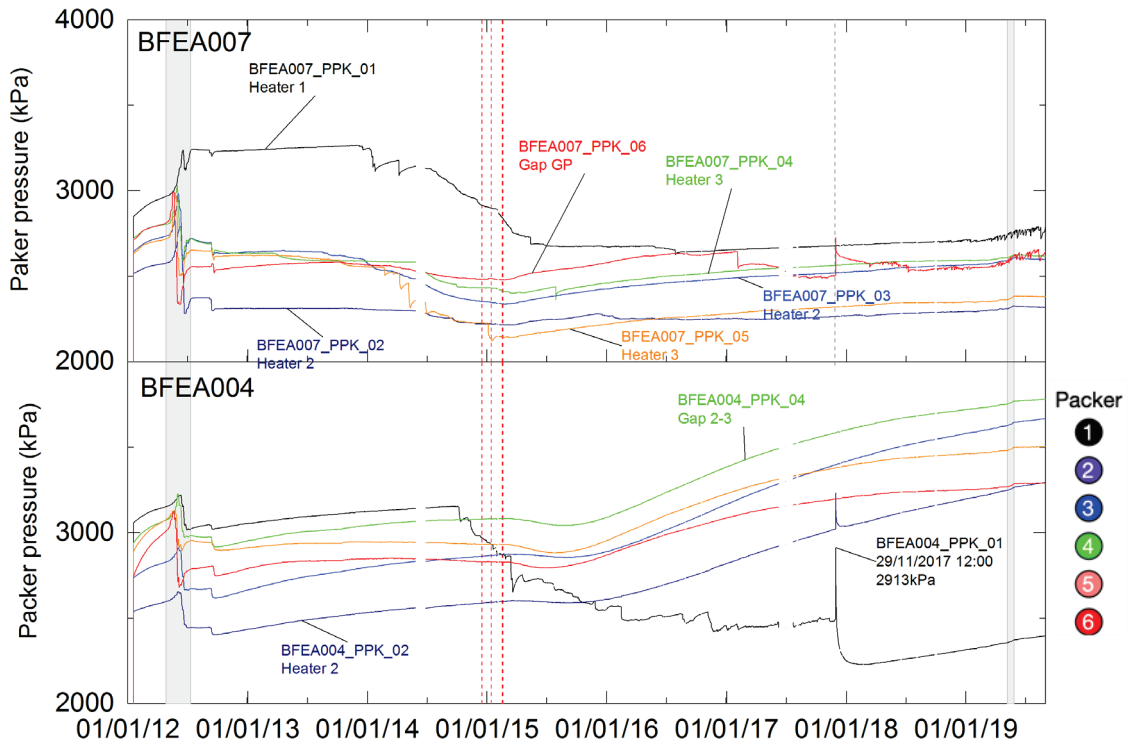


Fig. 62: Measured packer pressure in BFEA004 and BFEA007

Packer pressures in BFEA0008 and BFEA009 near the plug show an overall decline over time with some seasonal component and a response to Ga18 excavation in BFEA008 (Fig. 63).

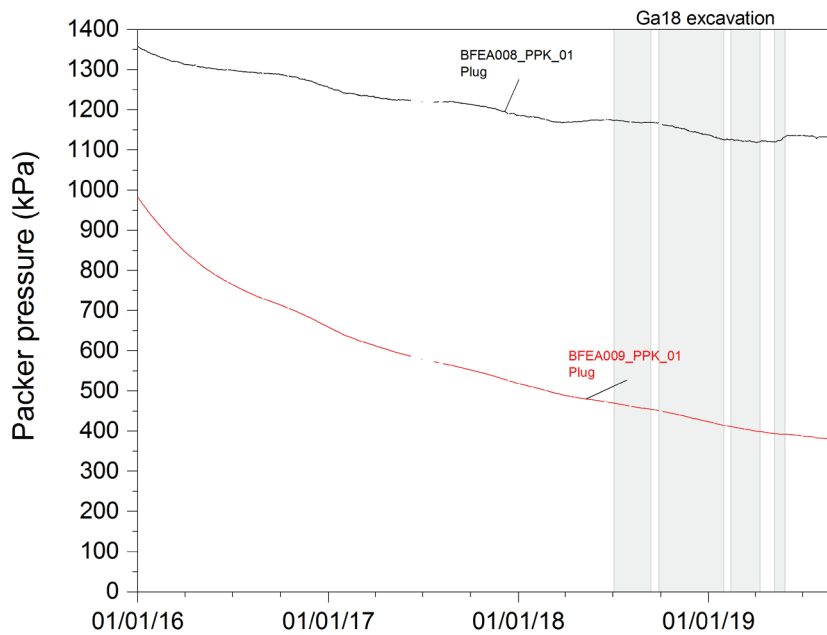


Fig. 63: Measured packer pressure in BFEA008 and BFEA009

While most packer pressures show a relatively smooth response to heating, several packers show a very irregular (or sawtooth) evolution these include:

- BFEA003: PPK\_02 where after an initial increase (response to heating) shows a sawtooth pattern from early 2016 to mid-2017 followed by an irregular decline.
- BFEA004: PPK\_01 where pressure drops in late 2014 and continue an irregular decline until 29.11.17 when pressure rise swiftly (packer inflation?) and then declines again. The response to inflation can be seen in several other packers.
- BFEA006: PPK\_05 pressure becomes irregular after mid-2017 and then shows some significant pressure drops followed by slow recovery.
- BFEA007: PPK\_01 where pressure drops in early 2014 and continues in an irregular decline until mid-2015. The packer pressure becomes very irregular in 2019.
- BFEA007: PPK\_06 where pressure drops in early 2017 and then becomes increasingly noisy in late 2018 and 2019.

Several packers show minor pressure changes  $\sim 10$  kPa which may indicate small deformations local to the boreholes.

### 3.3 Mechanical data: Deformation and stress

The mechanical processes in the EBS and geosphere are monitored using

- convergence arrays during the open tunnel period (see Chapter 2)
- total pressure cells at the tunnel wall, the heater pedestals and on the heater surfaces
- inclinometers in two boreholes above the FE Tunnel
- extensometers located in radial boreholes drilled from the FE Tunnel
- LVDT gauges located between the heater surface and the shotcrete wall

#### 3.3.1 Displacements

Four-point extensometers have been installed in boreholes drilled from the FE Tunnel. The boreholes are listed in Tab. 17. Shortening of the interval is positive and elongation negative.

Tab. 17: Extensometer boreholes and sensors

Boreholes	Section	Install	Reset	Sensor
BFEC001,2	Plug	23.05.2012	08.02.2015	4 point extensometers range of 100 mm and an accuracy of $\pm 0.02$ mm and associated temperature sensors.
BFEC003,4,5	ISS	29.06.2012	01.08.2012	
BFEB013,14	H1	30.10.2013	15.02.2015	
BFEB011,12	H2	17.10.2013	17.02.2015	
BFEB009,10	H3	16.10.2013	18.02.2015	
BFEB040,41,42,43,53	Gap H1-H2	14.11.2013	15.02.2015	4-point fiber optic extensometers (SOFO), 2 % accuracy, $2\mu$ resolution. BFEB052,53 single measurement points
BFEB038,52	Gap H2-H3	14.11.2013	17.02.2015	

**BFEC001,2,3,4,5 (no temperature measurements)**

BFEC001, 2 (Fig. 64a) show relatively small ongoing displacements. BFEC002\_DFO\_4 shows a drop from mid-2016 onwards. There is a small response to plug emplacement but no strong response to heating.

The extensometers in BFEC003, 4, 5 (Fig. 64b) show a significant difference between parallel and normal to bedding. Displacements stabilise during emplacement of the BBW and backfilling but then start to increase after the start of heating.

**BFEB009-14 (with temperature)**

Fig. 65 shows the displacements and temperatures measured in the BFEB009 – 14 boreholes around H2, H3 and Gap 0 (ISS). Around the heaters in boreholes drilled normal to bedding there is a strong response to heating in the intervals nearest the tunnel wall with increasing extension ~ 1 mm.

While in the boreholes parallel to bedding, ongoing slow contraction continues with only a very small increased response at the start of heating.

In the boreholes normal to bedding in the heater sections, initial slow roughly linear contraction changes to extension as heating progresses.

In the Gap 0 (ISS) borehole normal to bedding there are much larger extensions (up to 8 mm) but these are ongoing since installation. These sensors show no strong influence of heating, probably due to the smaller temperature rise at these boreholes. These results are comparable to those from BFEC003, 4, 5 in the same section (sensors were installed earlier and therefore show greater displacement).

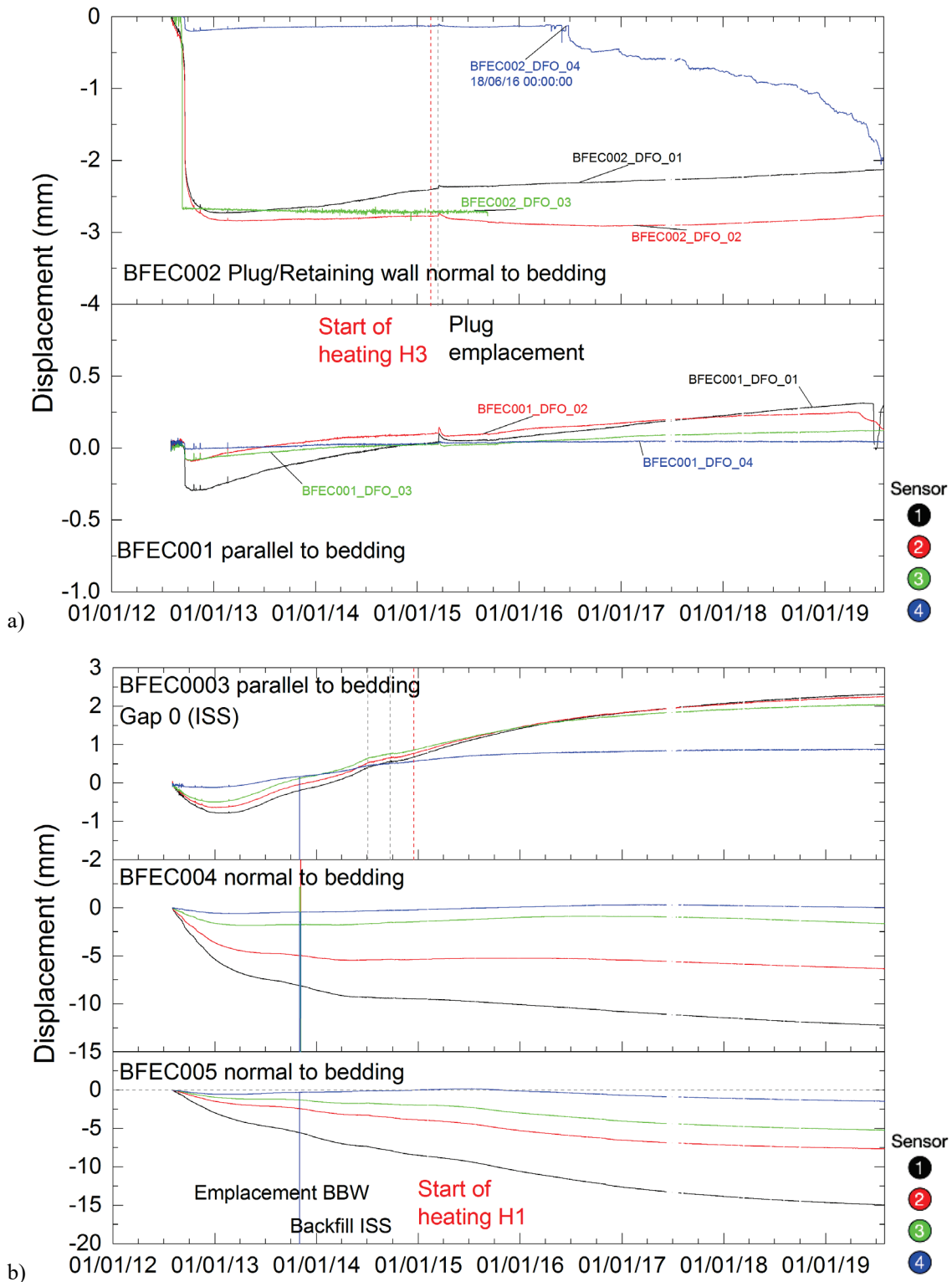


Fig. 64: Measured displacement a) BFEC001,2, b)BFEC003,4,5  
Displacements zeroed see Appendix C.

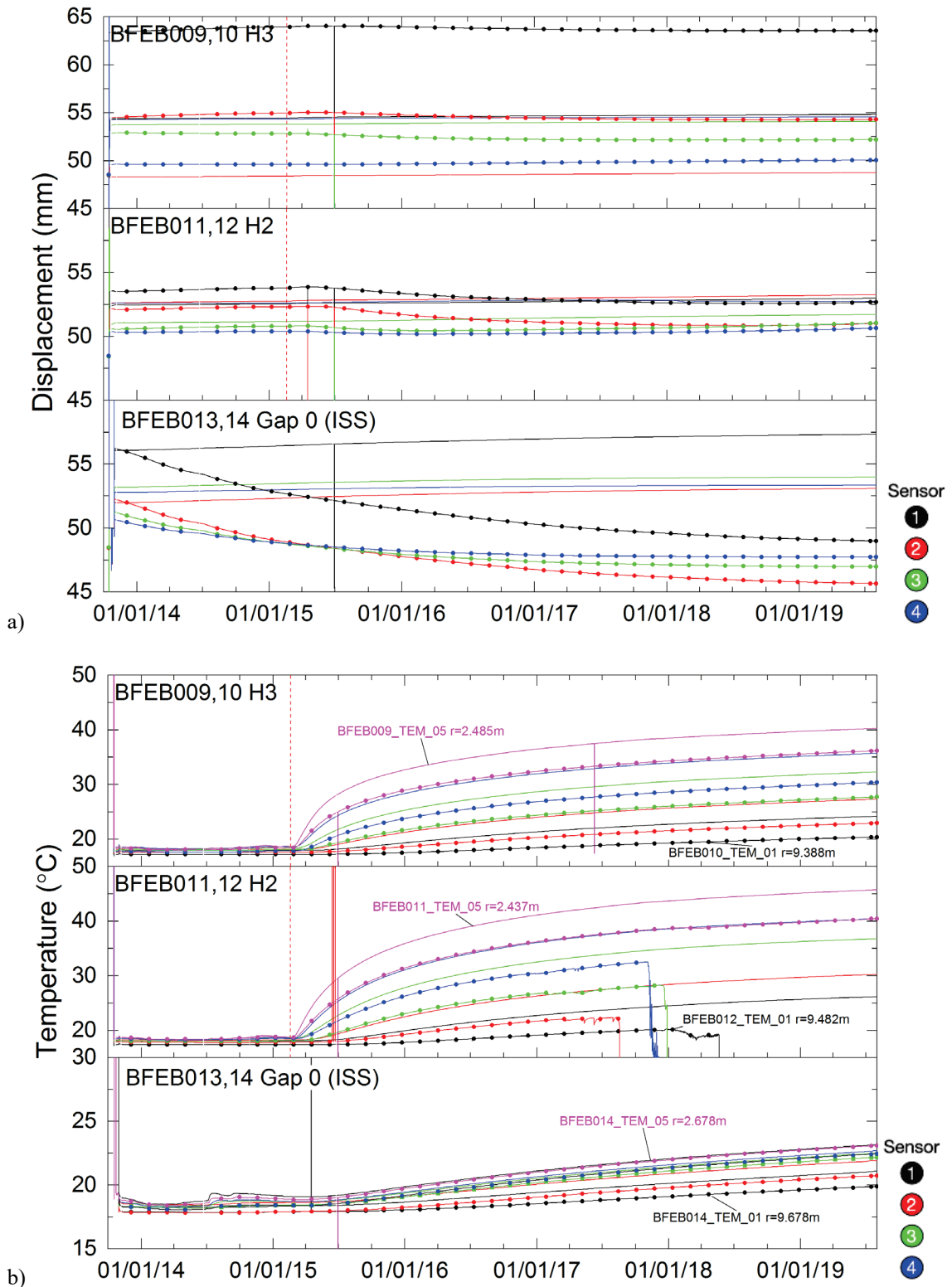


Fig. 65: Measured displacements BFEB009 – 14, b) Measured temperature BFEB009-14  
 Displacements zeroed see Appendix C.  
 Dotted lines show sensors in boreholes drilled normal to bedding (BFEB010, 012 and 014).

### D-Hx LVDT sensors

The LVDT sensors only measure a range of  $\pm 12.5$  mm. Deformation outside this range is not detected. In addition, data were zeroed when the corresponding heater was installed, so that the data range limits differ between the sensors. Firat Lüthi (2018) suggests that a "sudden kink-and stabilization in the plots can show out of range measurements." Sensors 1 and 4 connect the heater to the roof of the tunnel, while sensors 2 and 3 connect to the floor. The convention is that positive readings indicate extension (increase in length) and negative values contraction.

The measurements are shown in Fig. 67, the data for H2 and H3 show a similar trend with a small decrease (contraction) at sensors 1 and 4 and increase (extension) at sensors 2 and 3 immediately after the start of heating, followed by a reversal after about 20 days with increasing displacement at 1 and 4 and decreasing displacement at 2 and 3 which continues until the sensors fail or reach their limit at the end of the monitoring period.

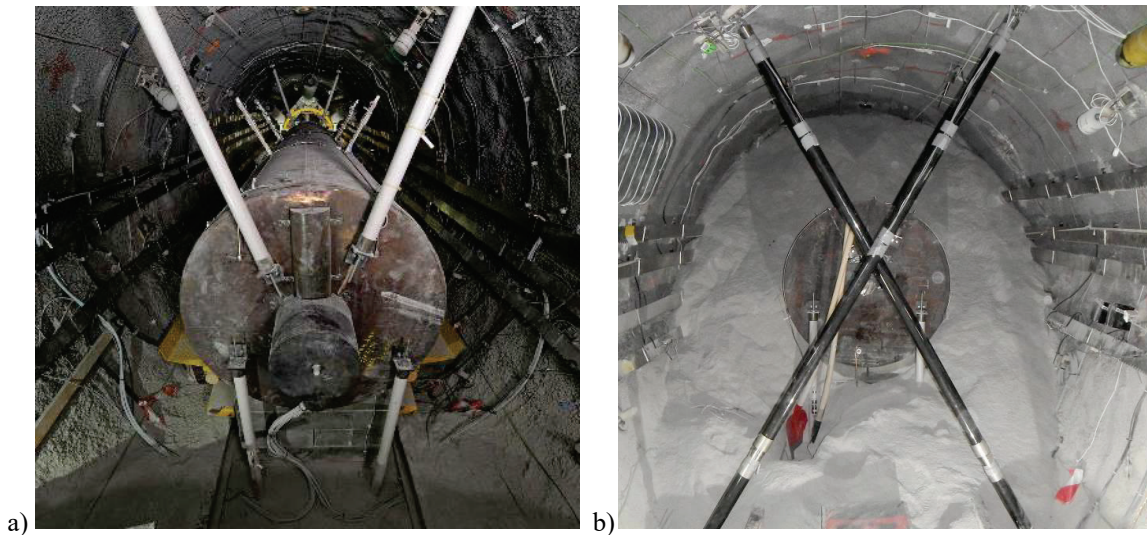


Fig. 66: Heater and LVDT sensors (1,4 upwards to roof, 2,3 down to floor)

Sensor 2 (H1, H2 at 000 and 460) displacements reduced by  $\sim 8 - 10$ mm (2 sensors probably failed).

In general displacement change smoothly although some minor jumps  $\sim 1$ mm can be seen to occur at some sensors (e.g. D-H2-460\_1).

Tab. 18: LVDT sensors located between heater and shotcrete  
 Comments from Firat Lüthi (2018)

Sensors	Heater	Comment
D-H1-000_1,2	H1	_1 Possibly reached limit Oct.2016. _2 No early data
D-H1-460_1	H1	Fixed at ~ 8 mm distance
D-H2-000_1,2,3,4	H2	_2 Possibly reached limit March 2017
D-H2-460_1,2,3,4	H2	_3 and _4 might be approaching limits
D-H3-000_1,2,3,4		Sensors 1 was fixed at ~ 10 mm distance from the center. Sensor 3 might be broken, sensor 2 might have reached its limit in Nov. 2016
D-H3-460_1,2,3,4		_3 might be broken

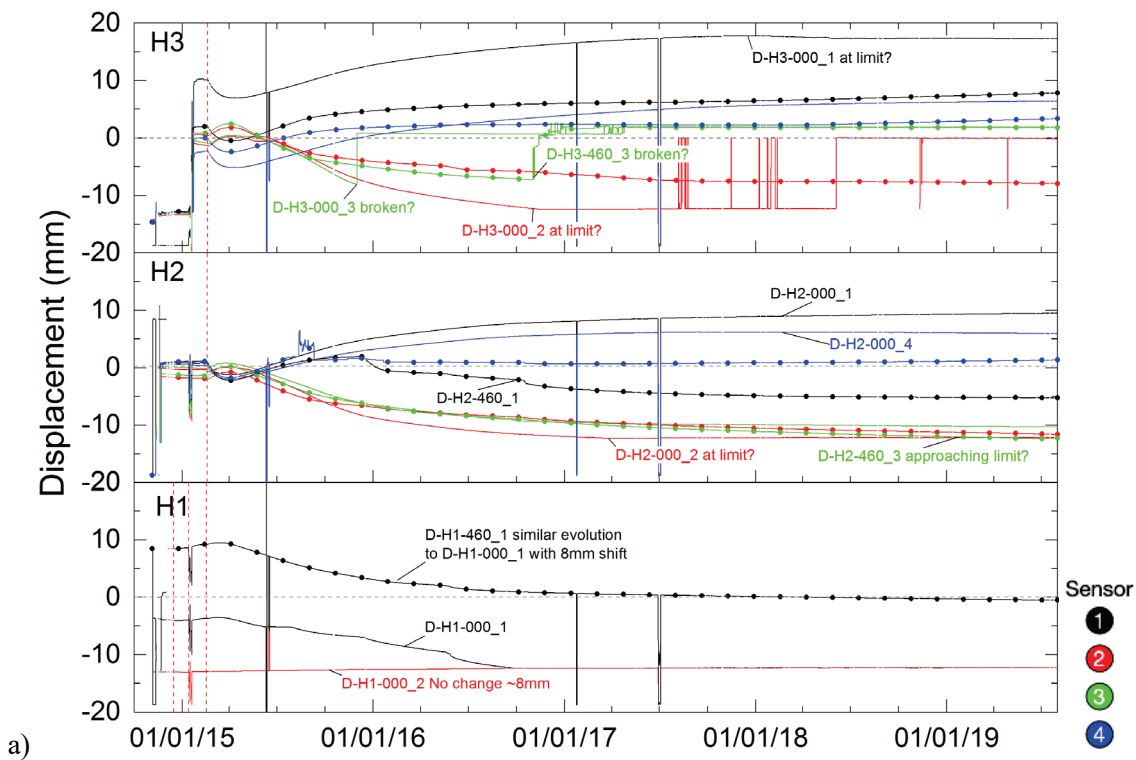


Fig. 67: LVDT measurements for heaters H1,H2 and H3

The overall pattern is of a small rise of the heaters at the start of heating followed by settling perhaps related to drying and shrinkage of the pedestals.

### **Inclinometers**

Two inclinometer chains were installed on 14.03.2012 in boreholes BFEA010 and BFEA011 about 3.0 – 3.7 m above the FE tunnel axis. BFEA010 is located in 00:30 (NW) and BFEA011 11:30 (SE) of the tunnel so that BFEA011 is closer to the normal to bedding direction.

The integrated settlement measurements are shown in Fig. 68 and against time from emplacement ( $\log_{10}$  scale) in Fig. 71. The spatial pattern of settlement is shown in the contour plots (Fig. 69). The plots show:

- the stabilisation of settlement in the shotcrete section after replacement of the invert
- decreasing settlement in the shotcrete section of BFE011 after replacement of the invert
- ongoing displacement in the ISS section of BFE010 and BFEA011 until emplacement and heating starts in early 2015
- settlements decrease after the start of heating in BFEA010 in both the heater section (shotcrete) and ISS section.
- distinct periods of changes in settlement in autumn 2018 to early 2019

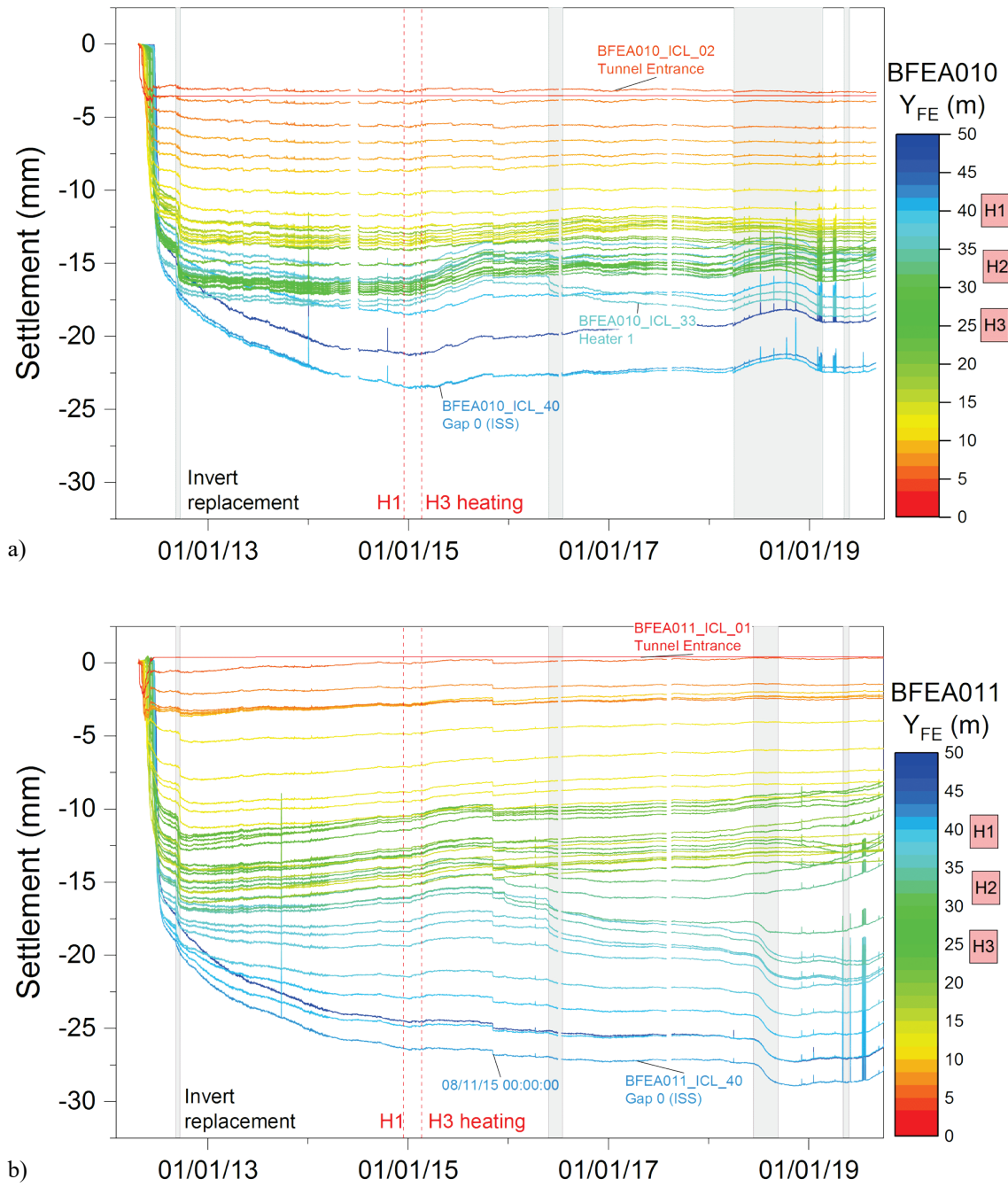


Fig. 68: Inclinerometer settlement (mm)  
a) BFEA010. b) BFEA01

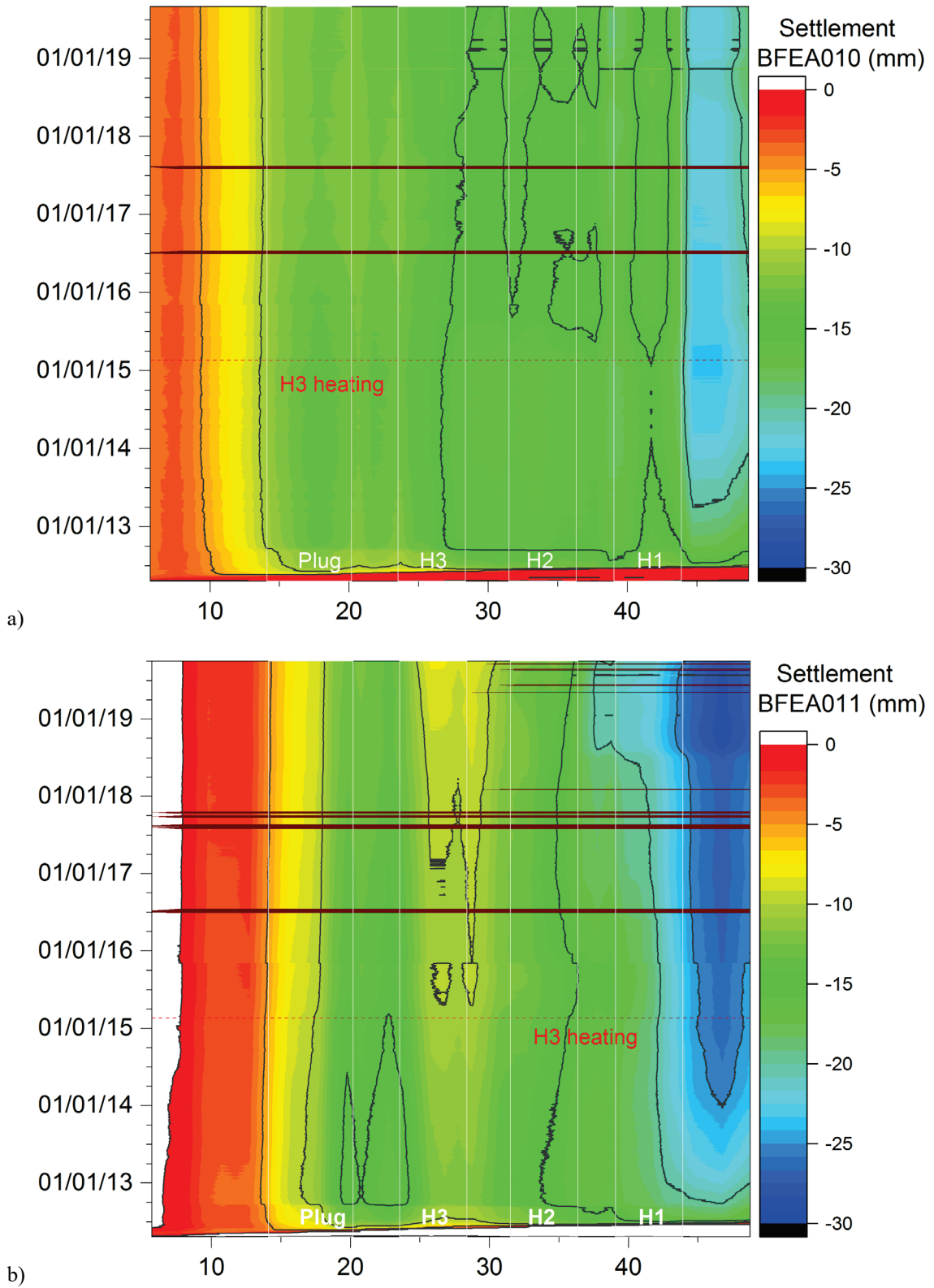


Fig. 69: Inclinator settlement contours (mm)  
a) BFEA010. b) BFEA011

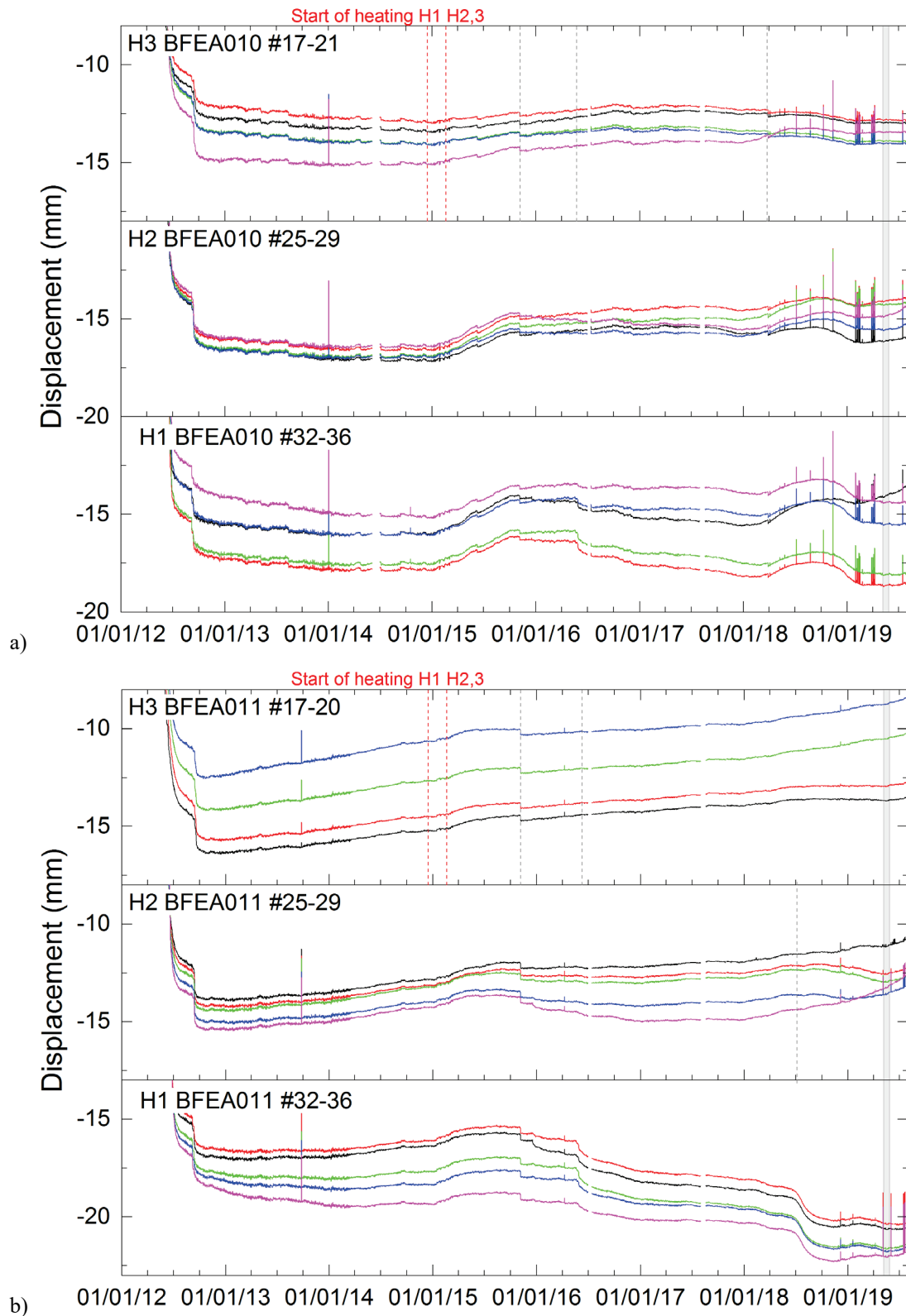


Fig. 70: Inclinometer settlement in heater sections

a) BFEA010. b) BFEA011

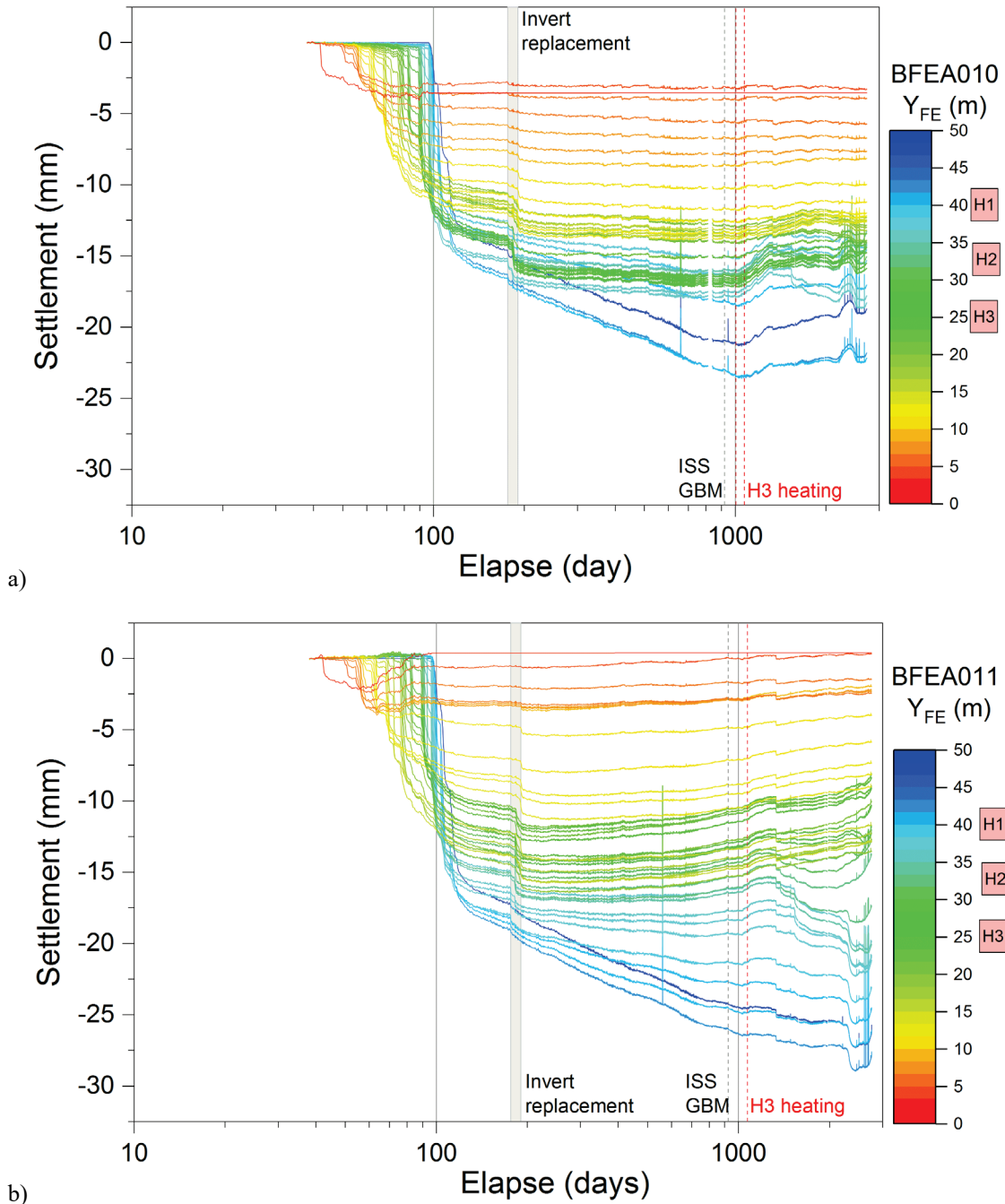


Fig. 71: Incliner settlement (mm) versus elapsed days (log) since installation BFEA010, b) BFEA011

The estimated settlements at the end of the monitoring period are shown in Fig. 73 and Fig. 73. Settlements clearly increase to over 20mm in BFEA011 as the borehole reaches H1 ( $Y_{FE} > 37$  m, see tunnel face map in Fig. 10 for convergence sections C5-C9) while larger settlements in BFEA010 only occur above the ISS section.



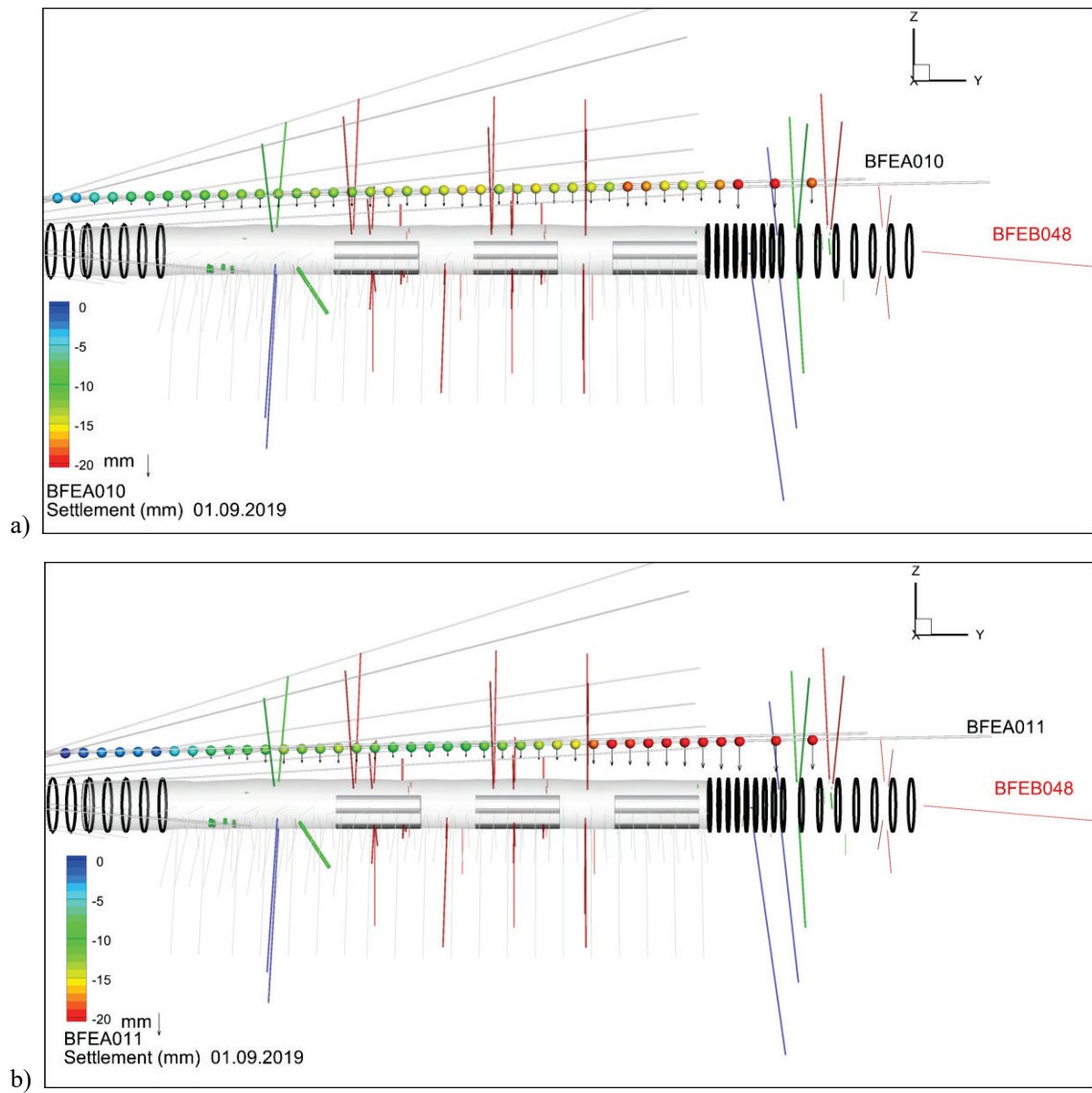


Fig. 73: Vertical section view of inclinometer settlement (mm) at end of monitoring period  
 a) BFEA010. b) BFEA011  
 Settlement shown as coloured symbol and scaled vertical arrow.

### 3.3.2 Total pressure

Four different types of total pressure cells have been installed:

- Stainless steel cells (Geokon 4810) installed on the tunnel wall with screws and cement. Sensors are FE\_PRE\_XXX with associated temperature sensors FE\_TEM\_XXX.
- Titanium cells (Geokon custom-built) fixed to the wall with a special mortar. Sensors are FE\_PRE\_XXX with associated temperature sensors FE\_TEM\_XXX.
- Standard thick-back pancake or low T TP cells (Standard 3500 Earth Pressure Cell) in the compacted bentonite block pedestals. Sensors are TP-Hx-230\_3. The sensors are 230 mm in diameter and 20 mm in thickness.
- Custom-built high temperature cells (Custom 3500 Earth Pressure Cell or high T TP) on the heater surface. This cell does not include a temperature sensor. Sensors are TP-Hx-230\_1,2. The sensors are 170 mm in diameter and 16 mm in thickness.

The first three types of cell are equipped with a temperature sensor. The sensors have a range of 0 – 5 MPa. The expected range of swelling pressure for the GBM is 2.4 – 4.3 MPa while higher swelling pressures may be generated by the compacted blocks in the pedestals or the blocks in the bentonite wall. Problems were encountered with the temperature sensors for FE\_TEM\_071, 073, 074, 076 and 079 which may result in erroneous data (Firat Lüthi 2018).

The total pressure data is shown in Fig. 74, Fig. 75, Fig. 76 and Fig. 77. Most operating sensors show a slow roughly linear increase since installation (some sensors showed an initial negative total pressure). The total pressure at the end of the monitoring period is typically less than 0.2 MPa. The highest reliable pressures are measured at the BBW section and at FE\_PRE\_84 at the roof in Gap 1-2 where pressures are approaching 0.5 MPa (again highest in the roof).

Sensor FE\_PRE\_075 measured total pressures in excess of 5 MPa which is both outside the expected range of swelling of the GBM and of the sensor. These high values are therefore thought to be anomalous and due to some error in the sensor or calibration.

The increase in total pressure at the tunnel wall could relate to:

- swelling of the bentonite
- ongoing loading of the liner (in shotcrete section) and convergence

Swelling will be driven by saturation of the bentonite from either inflow from the rock or redistribution of water from the bentonite near the heater.

The sensors in the pedestal and on the heaters do not show any consistent pattern, with high pressures on the top and bottom surfaces at H2 (no reliable measurements on H1 or H3) and low pressures in the pedestals (Fig. 78).

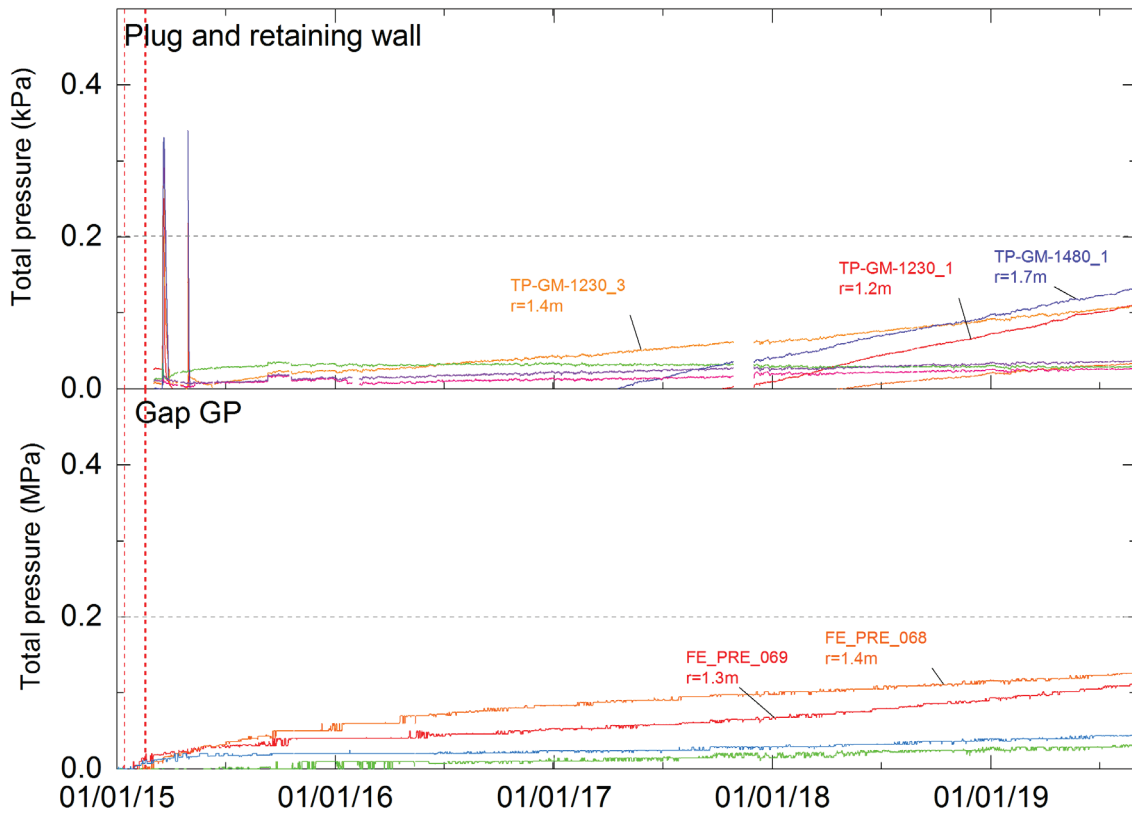


Fig. 74: Time history of total pressure cells at tunnel wall at the Plug and Gap GP sections.

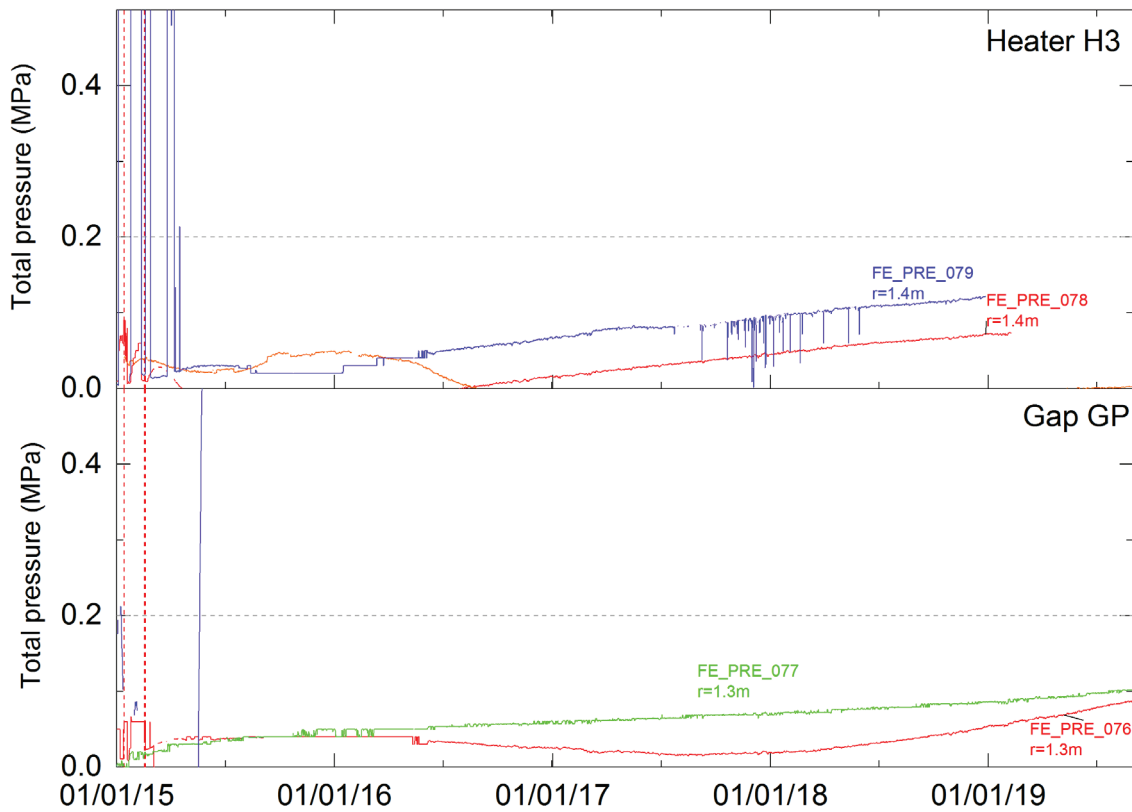


Fig. 75: Time history of total pressure cells on tunnel wall at the H3 and Gap 2-3 sections

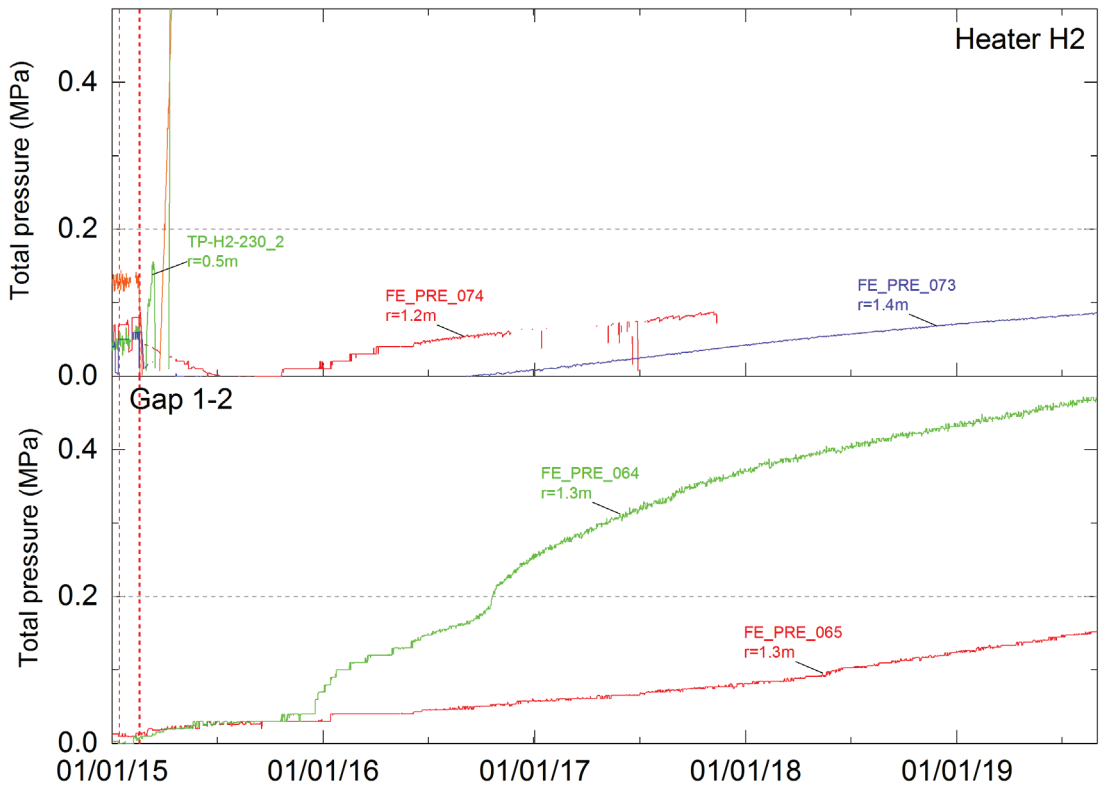


Fig. 76: Time history of total pressure cells at tunnel wall at the H2 and Gap 1-2 sections

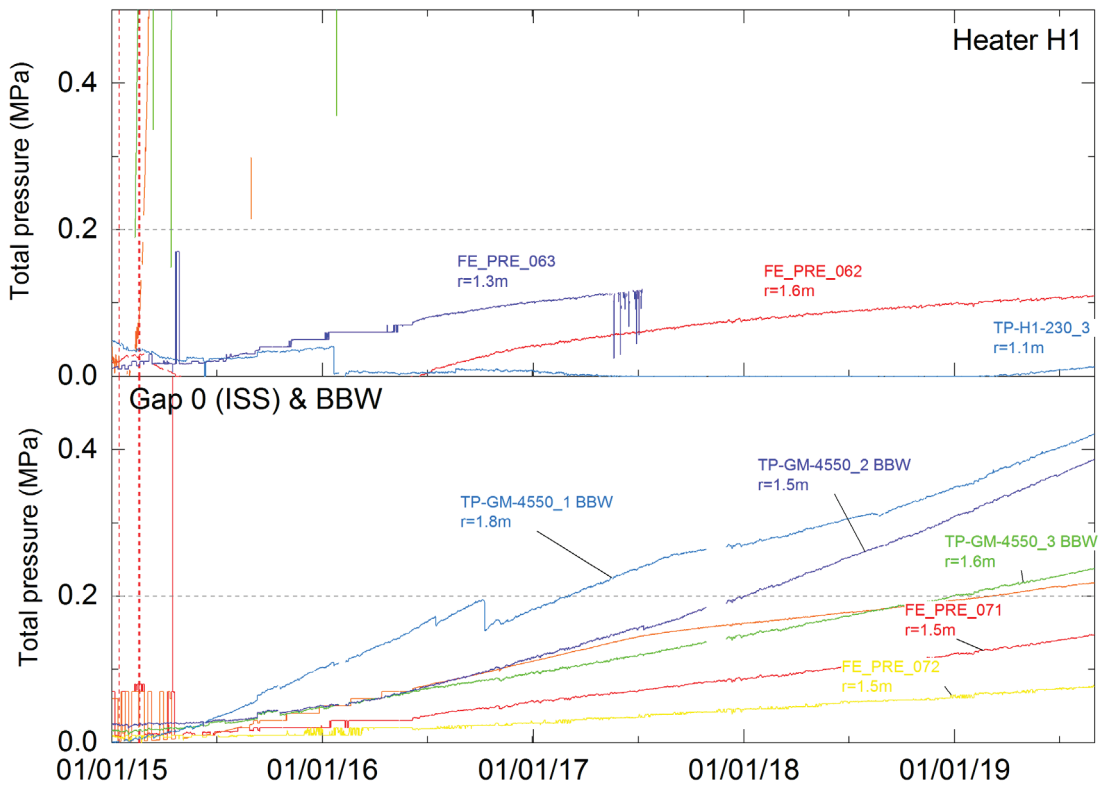


Fig. 77: Time history of total pressure cells at tunnel wall at the H1 and Gap 0 (ISS) and BBW sections

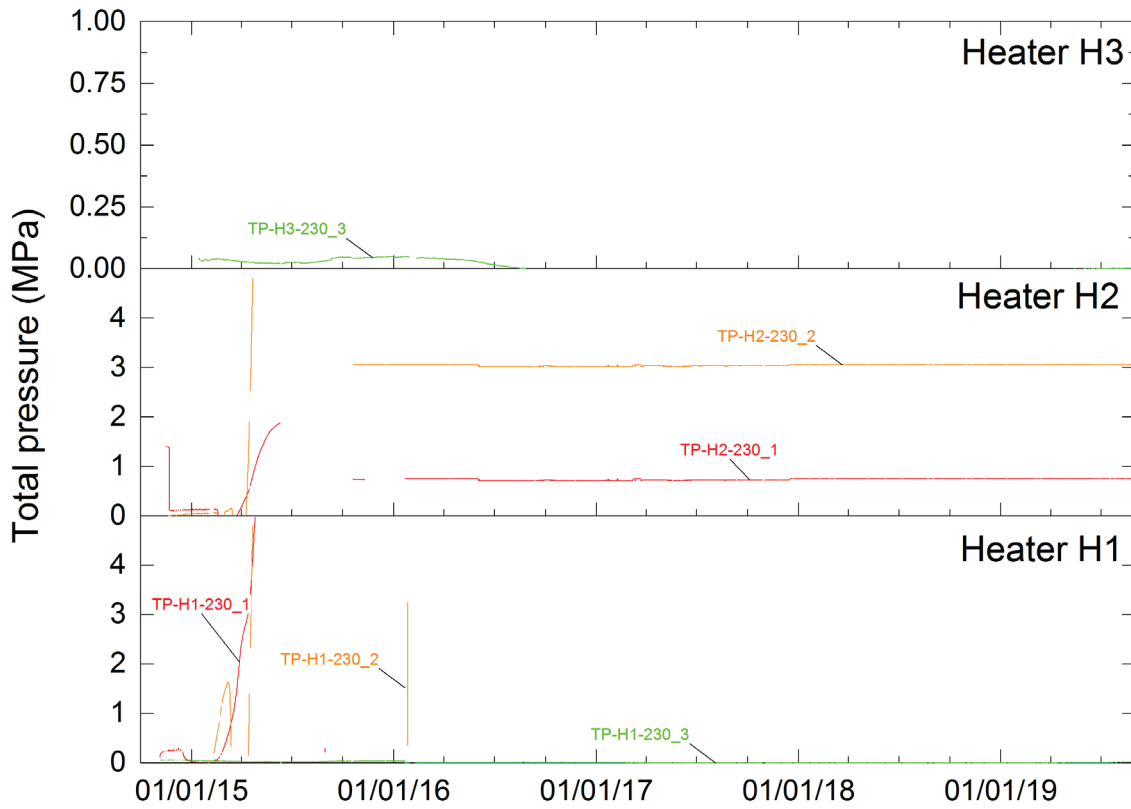


Fig. 78: Time history of total pressure cells on the heater surfaces and in the pedestals

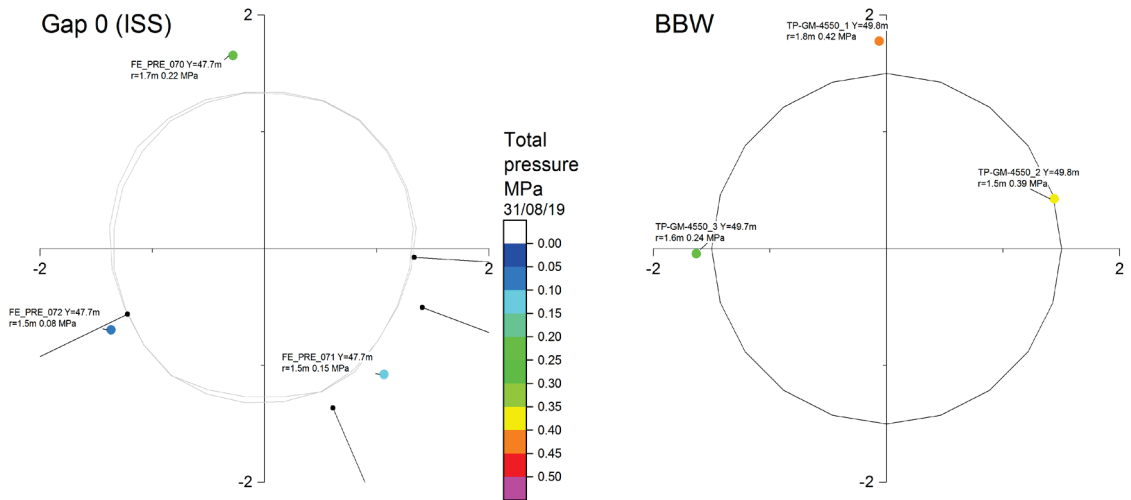


Fig. 79: Time history of total pressure cells at tunnel wall at the H3 and Gap 2-3 sections

### 3.4 Geophysical measurements

Geophysical monitoring of FE has been performed in a series of campaigns from December 2014 onwards. The campaigns are listed in Tab. 19. The data and analyses from the first six campaigns are fully documented in Maurer & Spillman (2018). H3 was switched on at 18.02.2015 12:00 just after the first campaign. Heating at H1 and H2 started on 15.12.2014 17:25 (low power) and 17.02.2015 12:00 respectively.

The geophysical logging is performed in two fibre-glass tubes (GP1 and GP2) inserted into the GBM prior to emplacement of the shotcrete plug. The locations of GP1 and GP2 are shown in Fig. 80, the tubes run through the shotcrete plug into the GBM and then above and slightly beyond H3. The plug extends from 14.51 – 19.57 m, while H3 starts at 22.71 m along the tubes. The measurements performed during the campaigns include:

- single-hole geophysical logging using Gamma-gamma and Neutron tools
- single-hole Ground Penetrating Radar (GPR) and Cross-hole (GP1-GP2) GPR
- cross-hole (GP1-GP2) seismic

The outputs from the different geophysical surveys are summarised in Tab. 20.

Tab. 19: Geophysical campaigns performed in the FE Gallery

	<b>GPR</b>	<b>Seismic</b>	<b>GGD</b>	<b>Neutron</b>	<b>Days since heating H3</b>
			01.12.2014		
1	17.02.2015	18.02.2015	16.02.2015	16.02.2015	0
2	19.05.2015	28.05.2015	27.05.2105	27.05.2015	90/99
3	03.09.2015	27.08.2015	29.08.2105	29.08.2015	197/190
4	03.02.2016	05.02.2016	04.02.2016	03.02.2016	350/352
5	26.08.2016	30.08.2016	25.08.2016	25.08.2016	555/559
6	01.03.2017 17.05.2017	24.02.2017	21.02.2017	21.02.2017	742/737 819-
7	24.05.2018	09.02.2018	25.06.2018	25.06.2018	1'191/1'087
8	26.03.2019 04.04.2019	27.03.2019	23.03.2019	23.03.2019	1'497/1'498/ 1'506

Tab. 20: Outputs from the different geophysical measurements

Measurement	Type	Output	Measurement scale
Gamma-gamma (GGD)	Single-hole	Profiles of Gamma counts and computed density along GP1 and GP2	Shielded 0.2 – 0.3 m sensitivity/penetration depth directed downwards
Neutron-neutron (NN)	Single-hole	Profiles of Neutron counts and "water units" along GP1 and GP2	Not shielded penetration depth is ~ 1 m
Ground Penetrating Radar (GPR)	Single-hole	Profiles of velocity and amplitude along GP1 and GP2	Sensitive to the region around the borehole (probably 10 – 20 cm)
Ground Penetrating Radar (GPR)	Cross-hole	Tomographic inversions of velocity and amplitude on the GP1-GP2 plane	
Seismic	Cross-hole	Tomographic inversions of velocity on the GP1-GP2 plane	

In addition, "semi-continuous" (several measurements per day) seismic measurements are made via transmitter and receivers. emplaced continuous measurements were performed (several measurements per day). Two sources and receivers were placed at the front of the pedestal of H3, and one source and three receivers were installed in the roof of the tunnel. One source was placed in borehole GP1, and eight receivers were distributed along GP2. The locations of the sources and receivers is shown in Fig. 81.

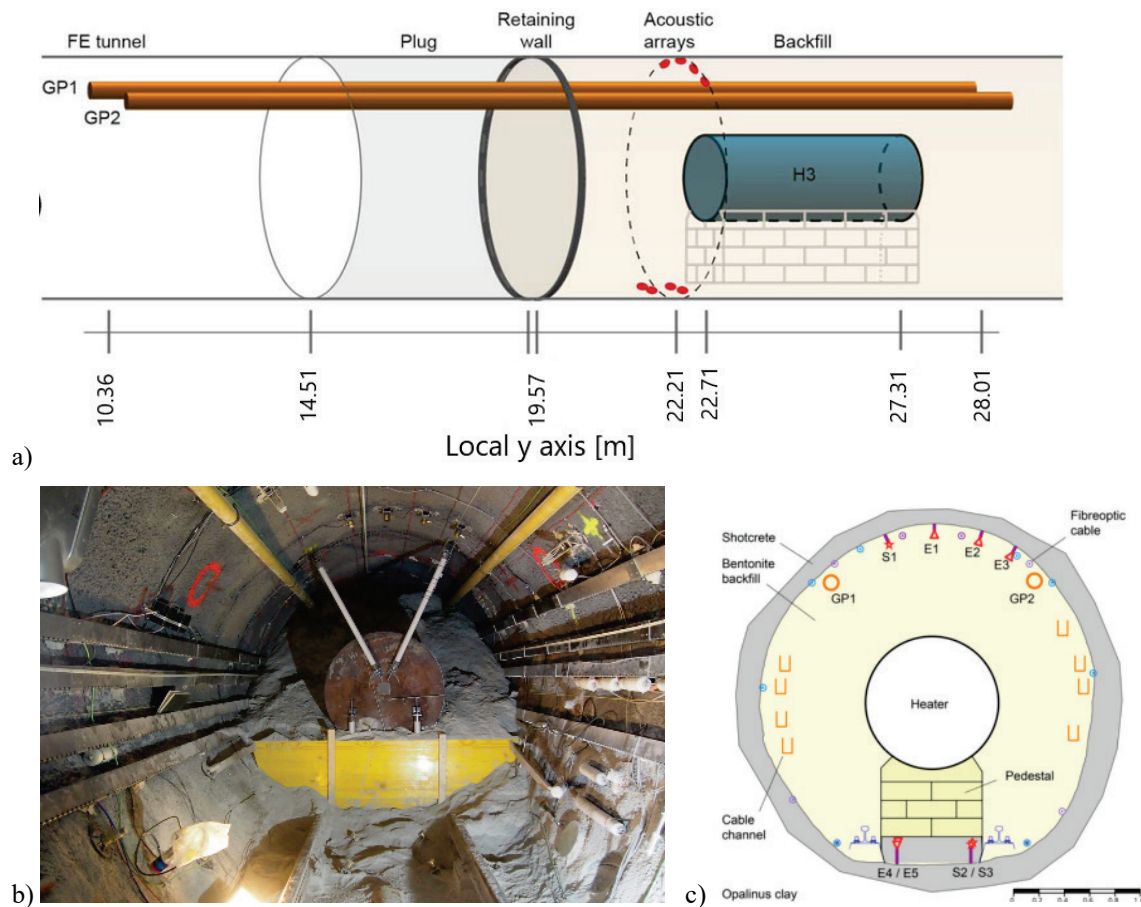


Fig. 80: Location of glass-fibre tubes GP1 and GP2 within FE Gallery  
 a) Schematic showing position of tubes, heater and plug. b) Photograph at installation.  
 c) Vertical cross-section

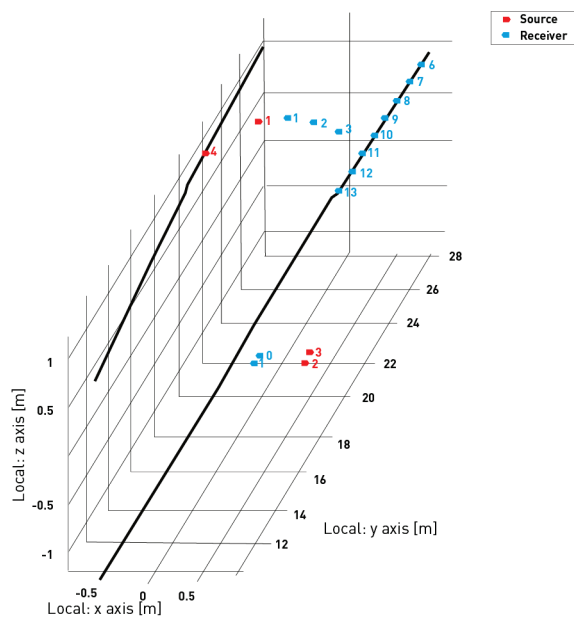


Fig. 81: Location of (semi-)permanently installed seismic sensors

The different logs and cross-hole surveys respond to different properties of the surrounding medium as listed in Tab. 21.

Tab. 21: Geophysical measurement sensitivity

MLog/Survey	Response
GPR	<p>Sensitive to changes of electrical properties. High sensitivity is expected at lower water content. Velocities are governed primarily by the dielectric permittivity. High temperatures cause the dielectric permittivity to increase, and velocities to decrease. Attenuation is largely controlled by the electrical resistivity and air-filled voids cause scattering attenuation.</p> <ul style="list-style-type: none"> <li>• increased water content results in a reduction in velocity and increased attenuation</li> <li>• increased temperature results in a reduction in velocity</li> <li>• air-filled voids will result in lower velocity</li> </ul>
Gamma-gamma	Measures natural and induced gamma radiation and is sensitive to changes in density/porosity
Neutron	Sensitive mainly to the density of hydrogen atoms and hence to changes in density/porosity and water content
Seismic cross-hole and continuous measurements	Sensitive to changes of elastic properties. High sensitivity is expected at high water content. Changes in temperature, density and saturation may influence the seismic velocity

**Semi-continuous seismic data**

Maurer & Spillmann (2018) document all the source-receiver combinations and discuss the results from the semi-continuous seismic data. Only limited analysis of the results is currently possible. It was difficult to identify the first arriving P waves in the individual sections. There were numerous phases visible in the waveform data, and it was unclear whether those phases partially matching predicted arrival times were indeed the first arriving P waves, or had other origins, such as cross-talk or systematic noise. The seismic phases in the waveforms show numerous discontinuities (abrupt time shifts and/or polarity changes), which are unlikely to be caused by changes in the state of the GBM. Results from the semi-continuous data do however suggest that the seismic tomograms of the first two experiments probably overestimate the actual velocities.

**Single hole data**

Gamma-gamma logs show a strong contrast between the shotcrete plug and the GBM at ~ 19 m in GP1 and GP2 (Fig. 82 a). Only relatively minor variations are seen within the two materials or between measurement campaigns suggesting. Maurer and Spillman (2018, 2019) suggest that there is a slight decrease above the heater in the data. The neutron logs (Fig. 82 b) also show a strong contrast between the plug and the GBM, but again there appears to be no clear systematic variation with heating. It is unclear if the gamma-gamma and neutron geophysical log data are currently useful for the interpretation of FE. This may reflect the limited nature of any changes in GBM effective density and moisture content that have occurred.

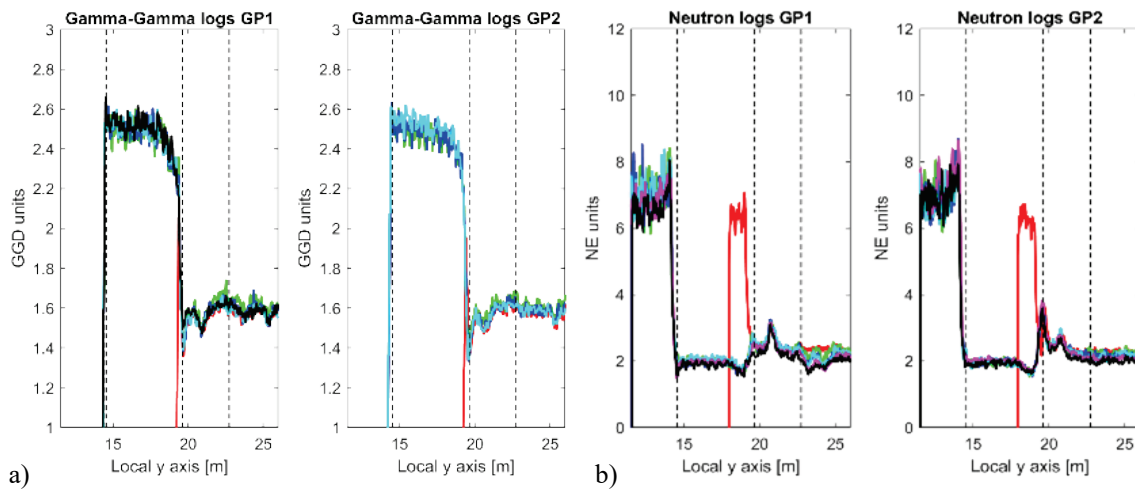


Fig. 82: Singe-hole geophysical logs for GP1 (left) and GP2 (right) for the first 6 campaigns: a) gamma-gamma data, b) neutron data

The vertical dashed lines indicate the plug front (14.51 m), the plug backside (19.57 m) and the front of H3 (22.71 m). From Mauer & Spillmann (2018).

The single-hole GPR data (using the Mala 250 MHz antenna<sup>3</sup>) show consistent pattern in space and time (Fig. 83). Within the plug only small spatial and temporal changes occur. In the GBM the influence of the heater is clearly seen with a reduction in velocity after heating. The change is initial rapid (between campaign 1 and 2) but later changes (campaign 5 – 8) are small. Mauer & Spillmann (2018) suggest that the velocity increase in GP1 is probably due to increased temperature while spatial variability observed along GP2 may be the result of increased moisture.

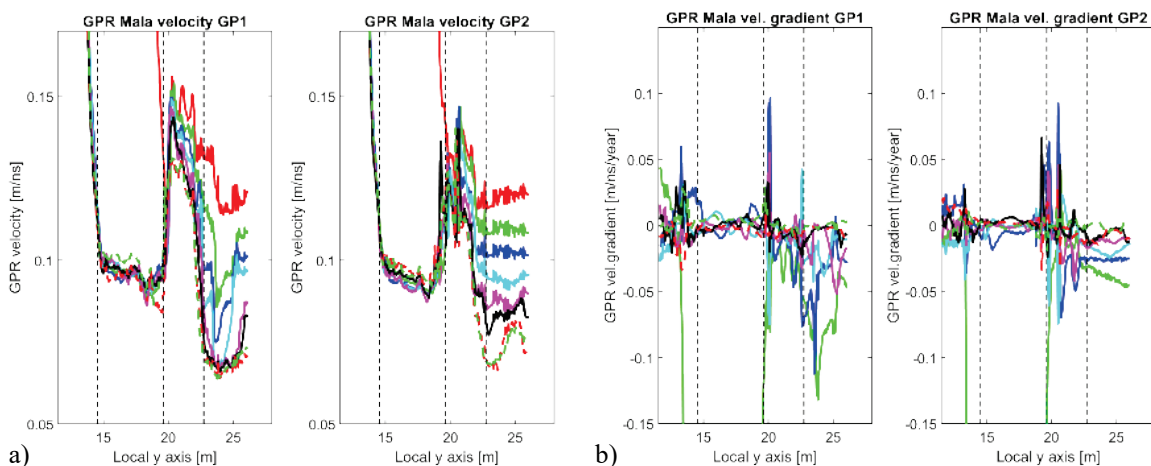


Fig. 83: Mala single-hole velocity logs for GP1 (left) and GP2 (right): a) GPR velocity, b) difference in velocity between campaigns.

<sup>3</sup> The logs using the Mala antenna seemed to offer very useful information. In contrast, the 100 MHz Mala data were less useful. Similarly Mauer & Spillmann (2018) questioned whether the GPR IDS data could be employed to characterize the GBM material in the vicinity of GP1 and GP2.

There are only minor amplitude variations in the plug. Within the GBM there is a small decrease of amplitudes over time between the plug and the heater, and a considerable amplitude decrease above the heater. The differences between GP1 and GP2 are less pronounced in the amplitude data than in the velocity logs.

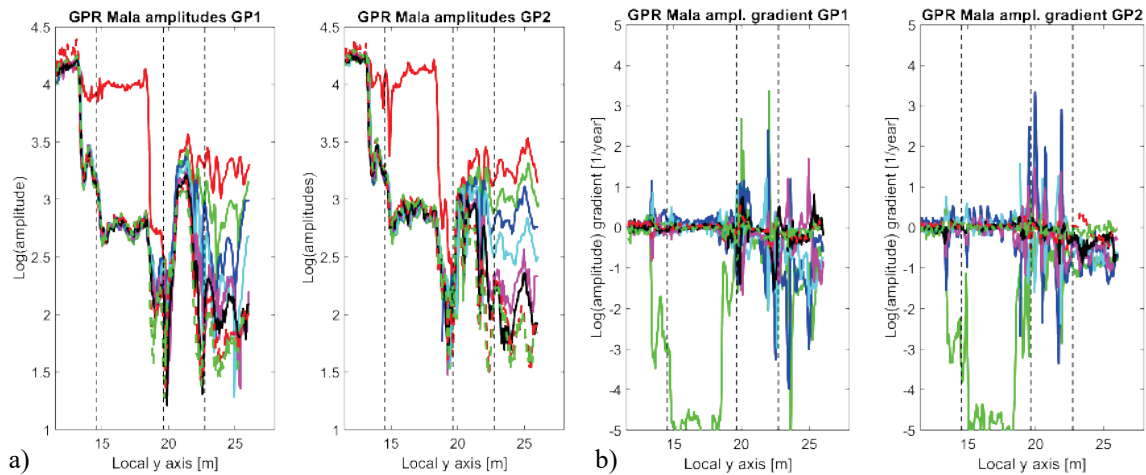


Fig. 84: Mala single-hole amplitude logs for GP1 (left) and GP2 (right): a) GPR amplitude, b) difference in amplitude between campaigns

### Tomographic measurements in the GP1-GP2 plane

The GPR velocity and amplitude tomograms are shown in Fig. 86 and differential tomograms in Fig. 87. A range of inversion approaches were tested on the GPR data (see Maurer & Spillmann, 2018 for details). Joint-inversion of travel time and amplitude provided reliable and consistent images of the electromagnetic properties (Fig. 86). In addition, a novel differential inversion process identified changes between the campaigns (Fig. 87). Analysis showed that full waveform inversion was unlikely to provide useful data.

The GPR velocity (Fig. 86 left) shows a distinct change between the first measurement (immediately prior to heating of H3) and the second 90 days after the start of heating of H3. The velocity drops significantly above the heater and to a lesser extent in the GBM between the heater and the plug. After that there is an ongoing trend for a reduction of velocity in the region between the heater and the plug and some recovery of velocity above the heater (especially locally at ~ 27 m in GP2 in Campaigns 2 – 7). The tomogram from Campaign #8 (~ 1500 days after start of H3 heating) shows more uniform low velocity in the GBM extending towards the plug.

The amplitude (Fig. 86 right) also shows a change in character at 90 days above the heater, but then shows increasing heterogeneity from Campaign #4 onwards (350 days after heating).

The difference tomograms show a similar evolution but provide additional detail. The Campaign #7 - #6 and #8 - #7 tomograms suggest a greater reduction in velocity in the front (nearest plug) of the GBM than in the part above the heater.

Fig. 88 shows the seismic velocity tomograms. The initially very poor data quality improved over time (likely caused by an improved coupling of the sensors to the GBM). Tomographic inversions of the seismic velocity showed progressively increasing velocities probably due to effect of compaction and swelling of the GBM resulting in improved coupling and higher velocity. The

immediate response to heating (Campaign #2) seen in the GPR data is less obvious in the seismic data probably because of the ongoing gradual improvement in coupling. Later seismic velocity tomograms show generally increasing velocity above the heater.

The seismic tomograms show some interesting features, but they are less reliably resolved compared with those found in the GPR tomograms. A higher velocity feature is visible above the heater intersecting GP2 at about 25m in the tomograms from Campaigns #7 and #8.

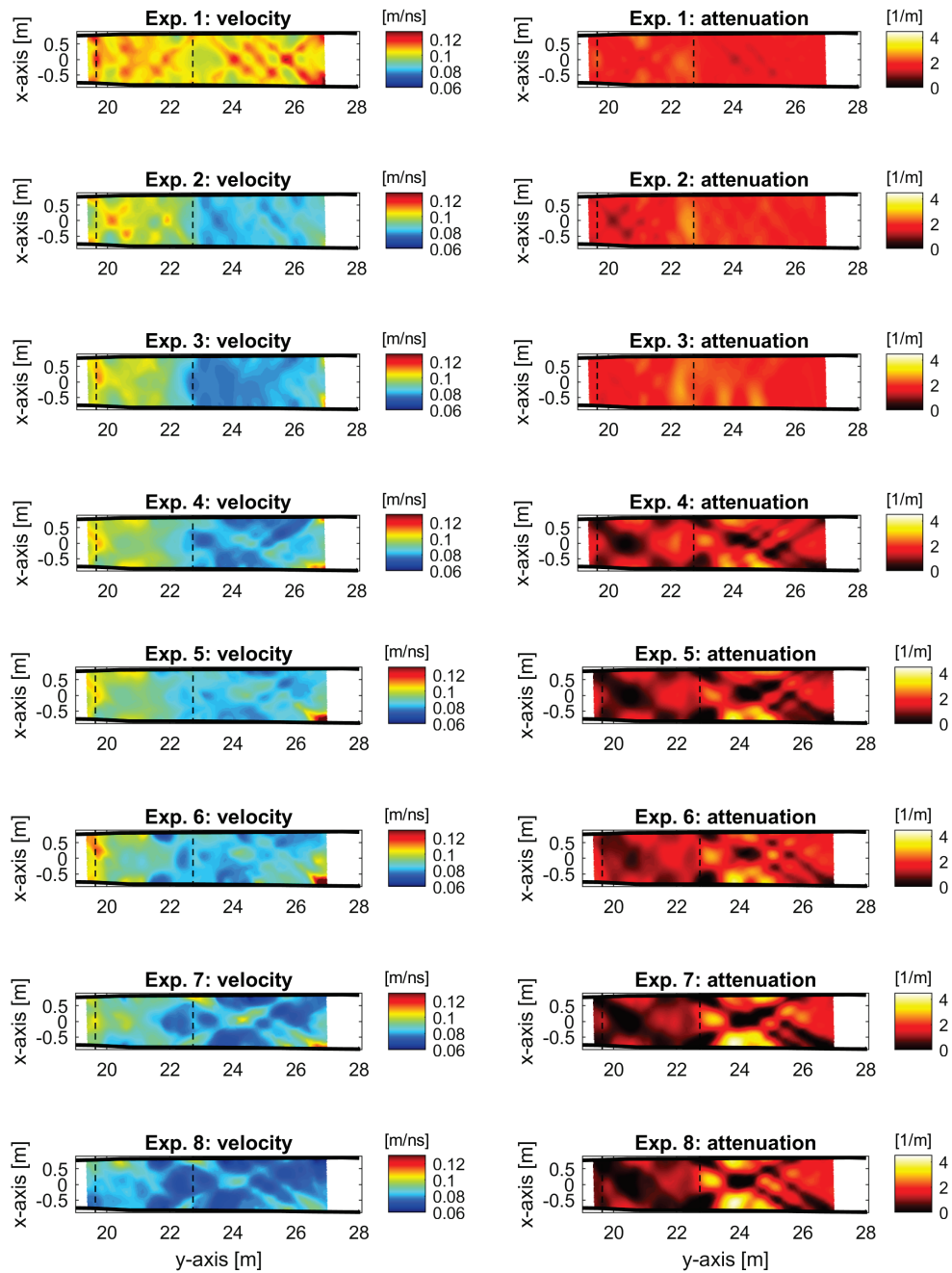


Fig. 85: GPR velocity and attenuation tomograms for the first eight campaigns  
Results from joint inversion of travel time and amplitude

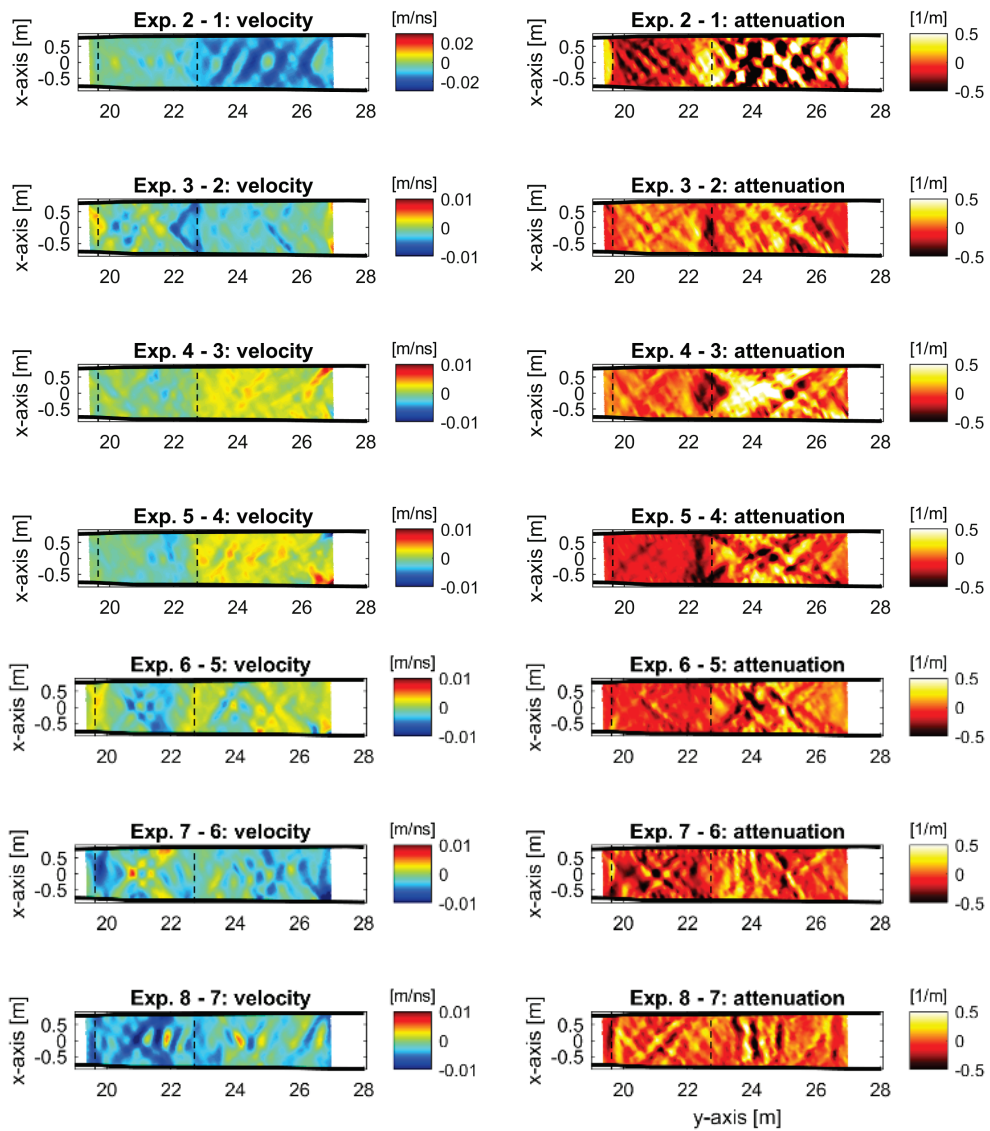


Fig. 86: GPR tomograms for the first eight campaigns

Differential tomograms for velocity and attenuation showing change between measurement campaigns.

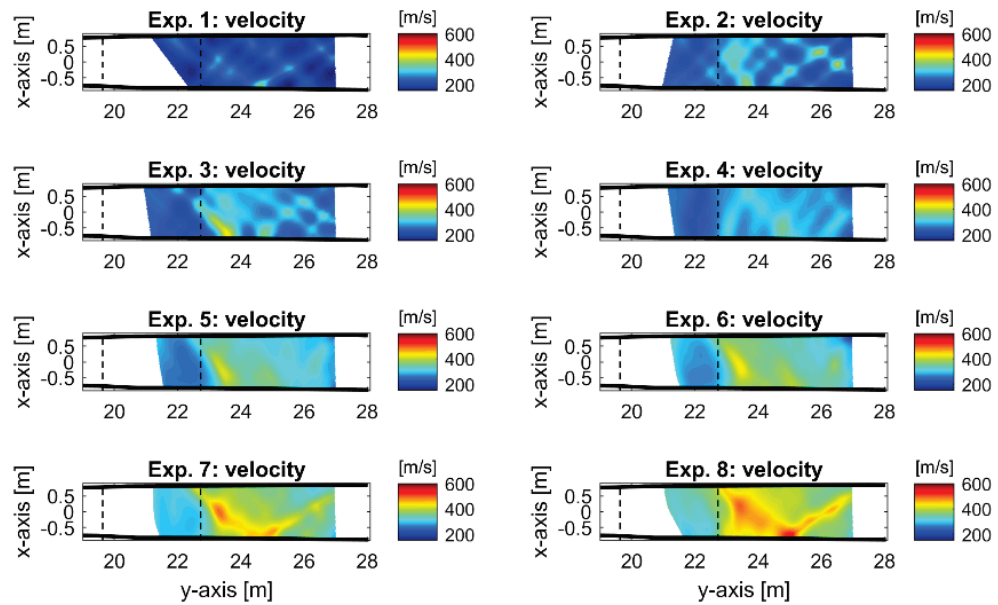


Fig. 87: Seismic and velocity tomograms for the first eight campaigns

### Correlations with moisture and temperature

Maurer & Spillmann (2018) investigate the use of in situ moisture and temperature data for correlation with the geophysical data. They identify the following correlations (Fig. 88):

- approximately linear relationship between GPR log(amplitude) and GPR velocity
- non-linear relationship between temperature and GPR log(amplitude) and GPR velocity
- non-linear relationship between moisture and GPR log(amplitude) and GPR velocity

There were only small variations observed in the gamma-gamma and neutron data and hence no clear correlation with temperature or moisture.

For the tomographic data Maurer & Spillmann (2018) found (Fig. 89):

- a negative correlation between temperature and GPR velocity (not found in experiment 6)
- a negative correlation between moisture and GPR velocity (also not found in experiment 6)
- a negative correlation between seismic and GPR velocities.
- clear positive correlations between temperature and seismic velocity and between moisture and seismic velocity. However, laboratory tests (Tisato & Marelli 2013) with cold pressed bentonite samples showed negative correlation between seismic velocities and temperature, so it is likely that velocity is a function of temperature, pressure, water content

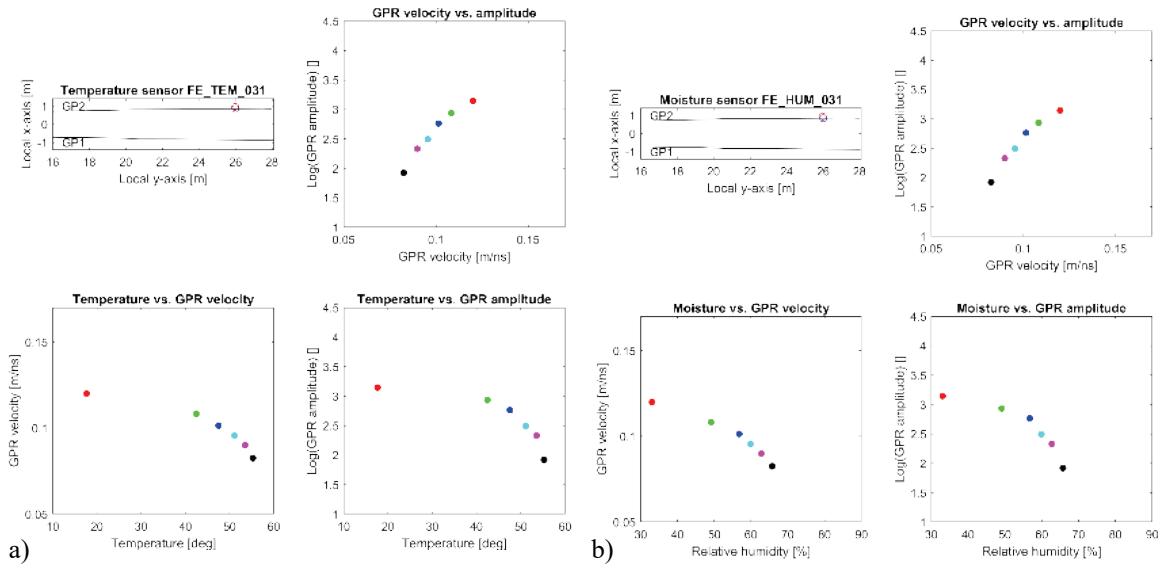


Fig. 88: Comparison of GPR single-hole log data for the first six campaigns with a) temperature measured by FE\_TEM\_031 and b) relative humidity measured by FE\_HUM\_031

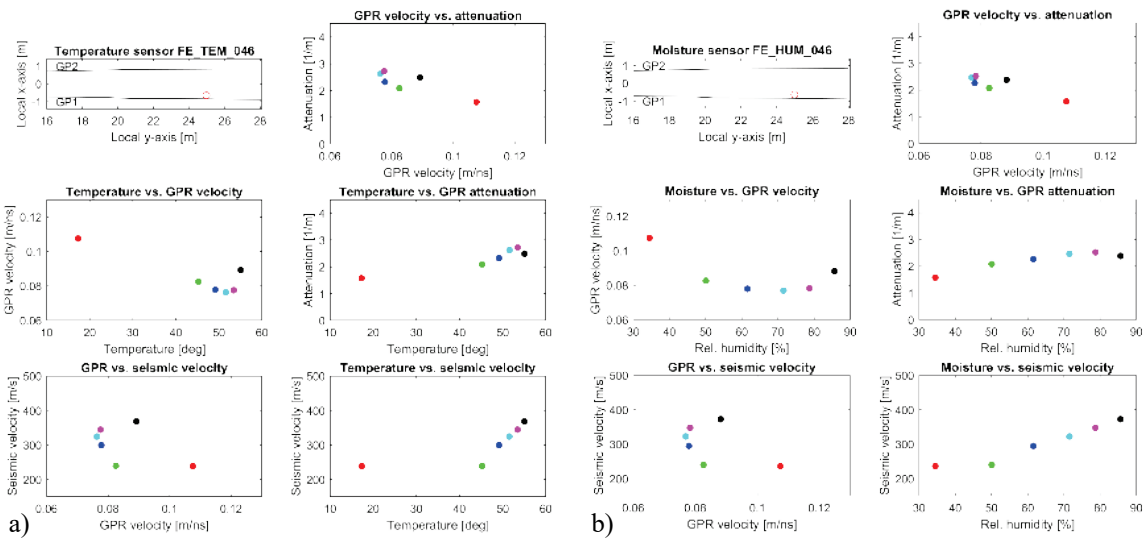


Fig. 89: Comparison of GPR and seismic tomography results for the first six campaigns with a) temperature measured by FE\_TEM\_046 and b) relative humidity measured by FE\_HUM\_046

## Summary

Maurer & Spillmann (2019) summarise the results from the first 8 campaigns as:

- Geophysical measurements indicate **spatial and temporal changes** within the heated GBM backfill.
- **Gamma-gamma logs** resolve spatial variations of **bentonite density** that remained stable over the observation period.
- **Neutron-neutron logs** indicate slightly increasing **water content**, which is attributed to local saturation of the bentonite backfill.
- **GPR velocities** generally decrease over time. This is likely dominated by elevated temperatures from the buried heater element. Tomographic inversions reveal local and **temporal variations of GPR velocities**, which are consistent with the logging results and observed local variations of bentonite saturation.
- **Tomographic seismic velocities** generally increase over time, thereby indicating **bentonite swelling**. Increasing water content in the bentonite backfill may explain the antithetic evolution of GPR and seismic velocities.

## THM Interpretation

Interpretation of the GPR data is complicated by the sensitivity to both temperature and water content. Higher temperature and water content both result in reduced velocity, while amplitude decreases (increased attenuation) with higher water content and scattering due to air-filled voids.

The GPR and seismic data are largely consistent with the in-situ temperature and relative humidity measurements and the expected evolution of the buffer where heating locally dries the GBM close to the heater resulting in moisture redistribution to the outer part of the buffer. This process has been observed in both the FEBEX and HE-E experiments. This will occur most strongly around the heater itself, but moisture will also be transported into the cooler part of the buffer near the plug. The increase in moisture will result in swelling and possible minor additional compaction (pore collapse) of the GBM.

Some moisture may also be transported through the shotcrete from EDZ but this is likely to be slow and gradual whereas the redistribution occurs rapidly on heating. Flow through the shotcrete may be localised at heterogeneities in the shotcrete related to rock bolts, instrumentation or small cracks.

GP1 and GP2 are both located close to the shotcrete in the outer part of the buffer (see Fig. 80) where we might expect moisture increase due to redistribution on heating and temperature increase as possibly shown in the GPR velocity and attenuation in Fig. 85. The improved coupling and increased velocities seen in the seismic tomography (Fig. 87) are consistent with swelling of the GBM due to the increased moisture. We might expect the GBM water content to be heterogeneous in the GP1-GP2 plane because of any heterogeneity in buffer density near the shotcrete and the influence of any localised flow through the shotcrete.

The observed overall reduction in GPR velocity in Campaign 8 may indicate that saturation of the buffer is starting to be influenced by moisture flow through the shotcrete rather than just the initial redistribution of moisture due to heating.

Large changes in buffer porosity or effective density are not expected<sup>4</sup> so the observed lack of major changes in the gamma-gamma and neutron data are also largely consistent with expectation.

---

<sup>4</sup> Although moisture redistribution and subsequent saturation may eventually result in slightly lower density in the outer parts of the buffer.

## 4 Response to Ga18 excavation

### 4.1 Ga18 excavation

Tab. 22 lists the different phases of Ga18 excavation during 2018 and 2019. Fig. 90 shows the main excavation stages. Ga18 is largely within the sandy facies and carbonate-rich sandy facies, with short intervals in the Passwang Formation (Phase 2A) and shaly facies (Phase 2C). The FE Gallery is to the NW of the Ga18 across the Main Fault. The closest excavation points are the start of the gallery (Phase 1), Niche 8 and the final part of the excavation (Phase 2D). At these points the distance is approximately 50 m (Alcolea et al. 2019).

Tab. 22: Ga18 excavation phases

Excavation Phase	Start	Mapping GM	End	Mapping GM
<b><i>Ga18 Phase 1</i></b>	14.03.2018 08:00	314.4	29.03.2018 05:00	297
Niche 7	04.04.2018 15:00	0	20.04.2018 07:00	17.5
Niche 8	24.04.2018 15:00	0	17.05.2018 06:00	17.5
Niche DR	04.06.2018 21:00	0	05.06.2018 13:00	5
Niche 1	14.06.2018 08:00	8	20.06.2018 08:00	18.5
<b><i>Ga18 Phase 2 A</i></b>	03.07.2018 11:30	0	12.09.2018 06:00	67
Niche 2 South	13.09.2018 10:00	6	25.09.2018 06:00	15
<b><i>Ga18 Phase 2 B</i></b>	27.09.2018 08:00	70	30.01.2019 06:00	178
Niche 5	01.02.2019 06:00	2	07.02.2019 06:00	7.5
<b><i>Ga18 Phase 2 C</i></b>	12.02.2019 14:00	182	10.04.2019 06:00	267.7
Niche 5	12.04.2019 06:00	10	03.05.2019 06:00	34
<b><i>Ga18 Phase 2 D</i></b>	07.05.2019 06:00	269.7	27.05.2019 09:00	297

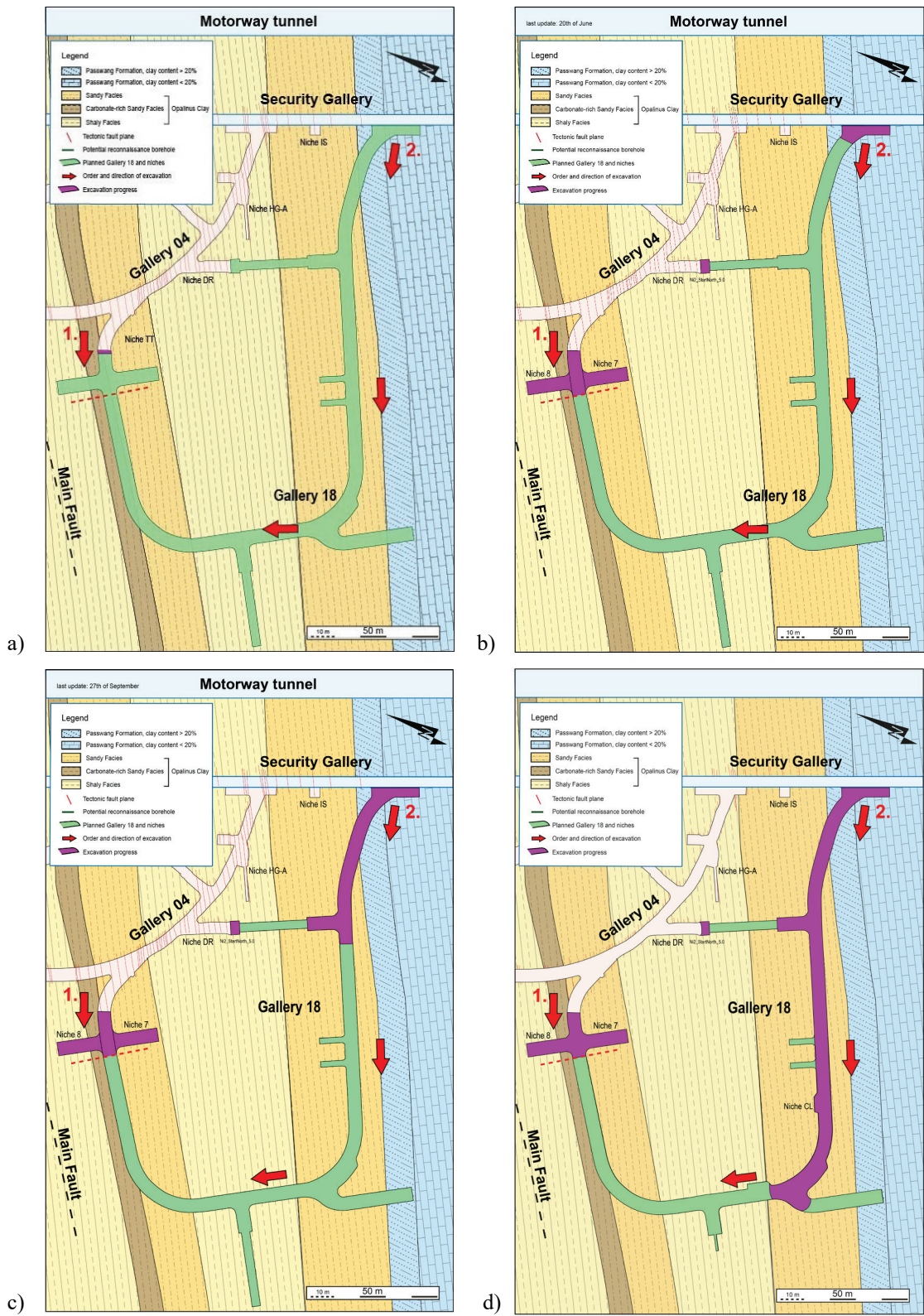
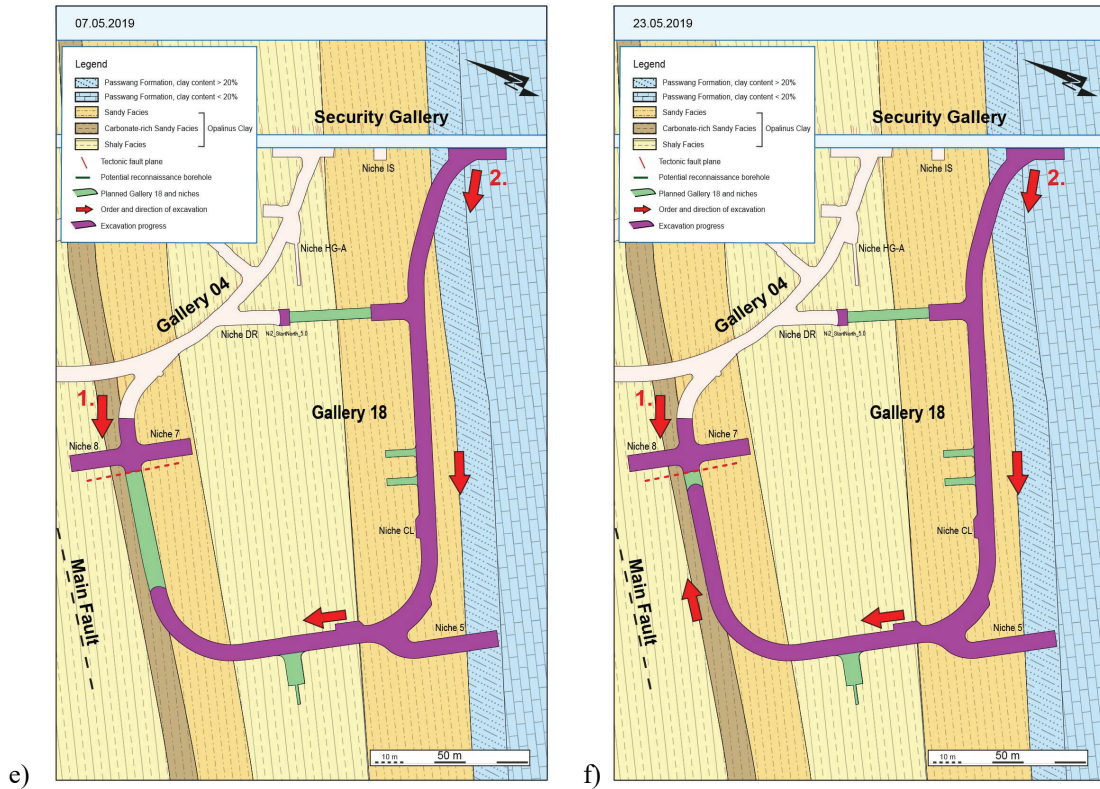


Fig. 90: Stages of Ga18 excavation:

a) Ga18 Phase 1 14.03.2018. b) Ga18 Phase 2A. c) Ga18 Phase 2B 05.07.2018. d) Ga18 Phase 2C 12.02.2019. e) Ga18 Phase 2D 07.05.2019. f) Ga18 on 23.05.2019 as excavation approaches cut-through. Red arrow indicates excavation direction and purple shading indicates completed excavation (compiled from Jaeggi et al. 2018).



e) Fig. 90: Cont.

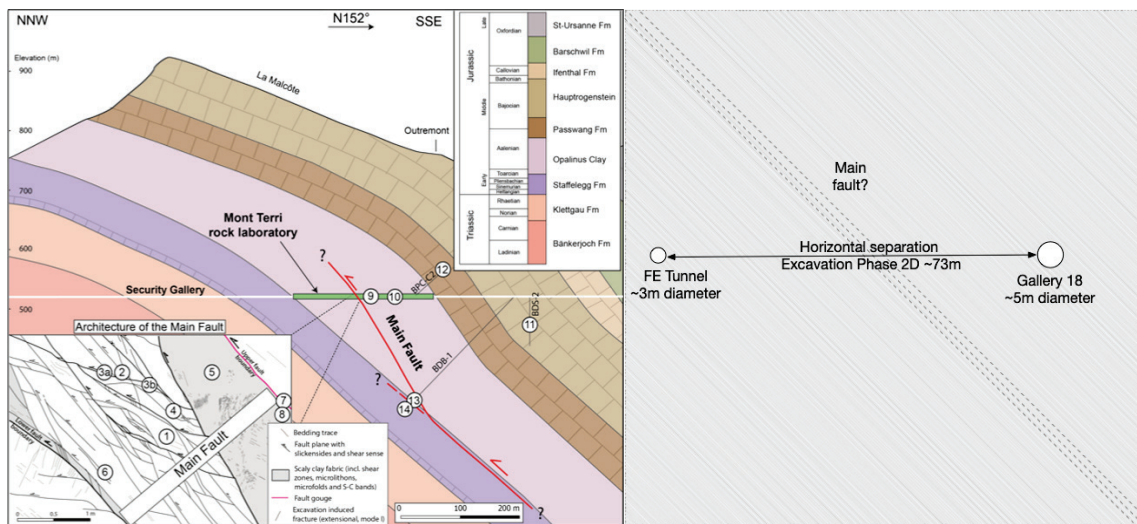


Fig. 91: Vertical geological section and schematic showing FE Tunnel, Ga18 and Main Fault. Numbered locations in geological section relate to geochemical samples analysed by Clauer et al. (2017)

### 4.2 Extensometer and LVDT measurements

Alcolea et al. (2019) present analyses of the extensometer, fibre optic strain (Brugg heatable cable at tunnel crown), LVDT and pore pressure data during Ga18 excavation. They identify possible changes in the LVDT response from the front of H3 to the back of H2, they suggest:

- Front of H3: D\_H3\_000\_1,2 oscillating trend before-during-shortly after excavation; D\_H3\_000\_4 enhanced extension rate
- Back of H3: D\_H3\_460\_2,4 enhanced compression rate
- Gap H3 – H2: FE\_DEF\_003 oscillating trend before-during-after excavation
- Back of H2: enhanced compression rate

The LVDT response (relative to 31.01.2019) is shown in Fig. 92. A small response can be seen at H3 (and possibly H1) to Niche 8 excavation while other small responses can possibly be identified during Ga18 Phase 2D.

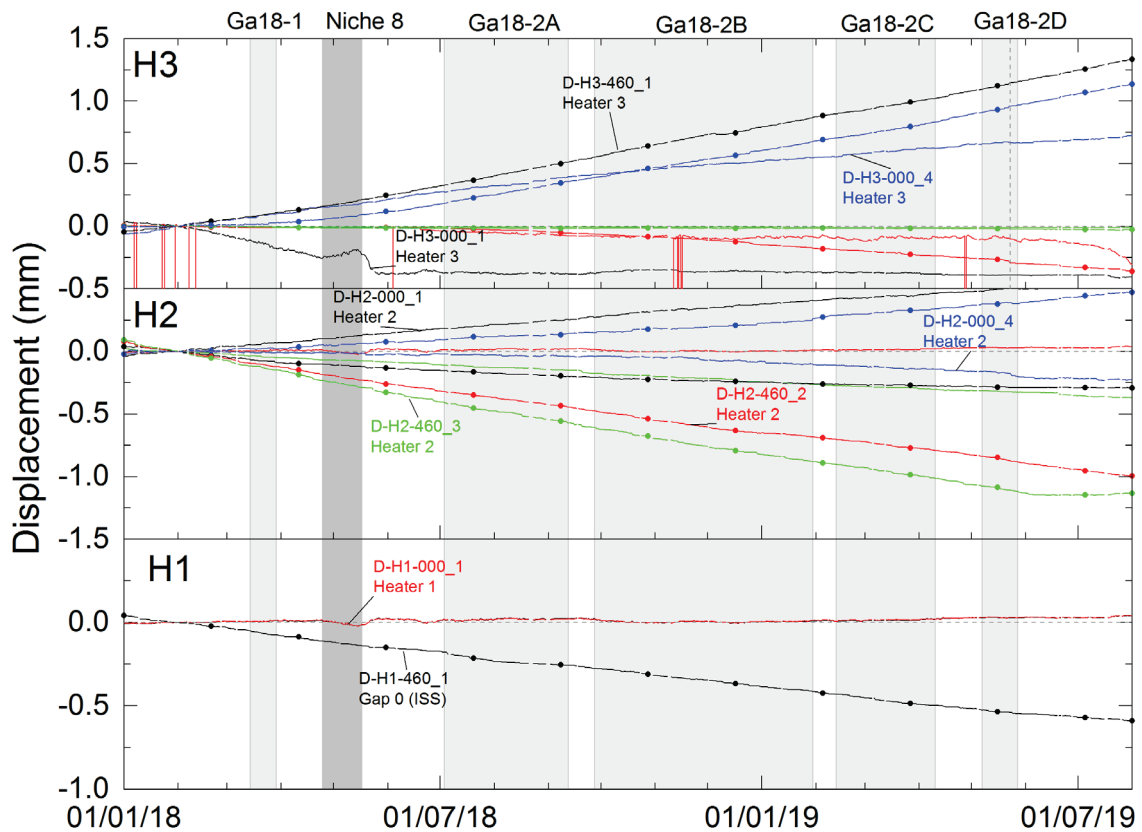


Fig. 92: LVDT response (relative to 31.1.19) at heaters

Alcolea et al. (2019) comment that the measurements from the fibre optic cables installed at the tunnel crown (00:30 and 11:30 o'clock positions) did not show qualitative correlations with the LVDT and extensometer measurements because the LVDT sensors are mostly sensitive to the heater movements, whereas the fibre optic measurements show the deformations around the tunnel wall.

**Inclinometers**

Fig. 93 shows the inclinometer settlement data (relative to 31.01.2019). Changes of ~ 1 mm occur during Ga18 Phase 2A and 2B at the end of the boreholes from  $Y_{FE} = \sim 35$  m in BFE-A11 and from  $Y_{FE} \sim 27$  m in BFEA010.

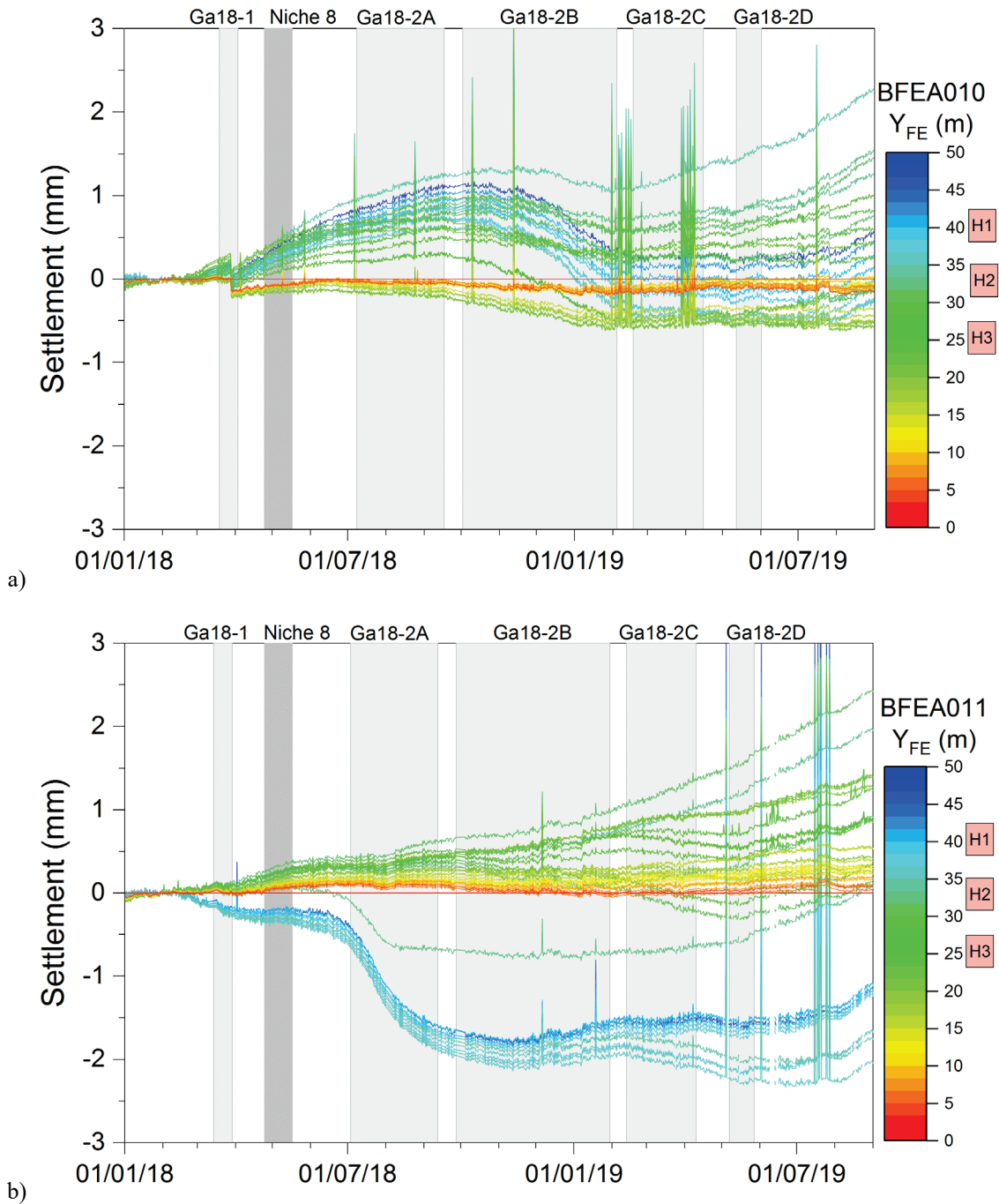


Fig. 93: Inclinometer settlement response (relative to 31.01.2018)

a) BFEA010. b) BFEA011

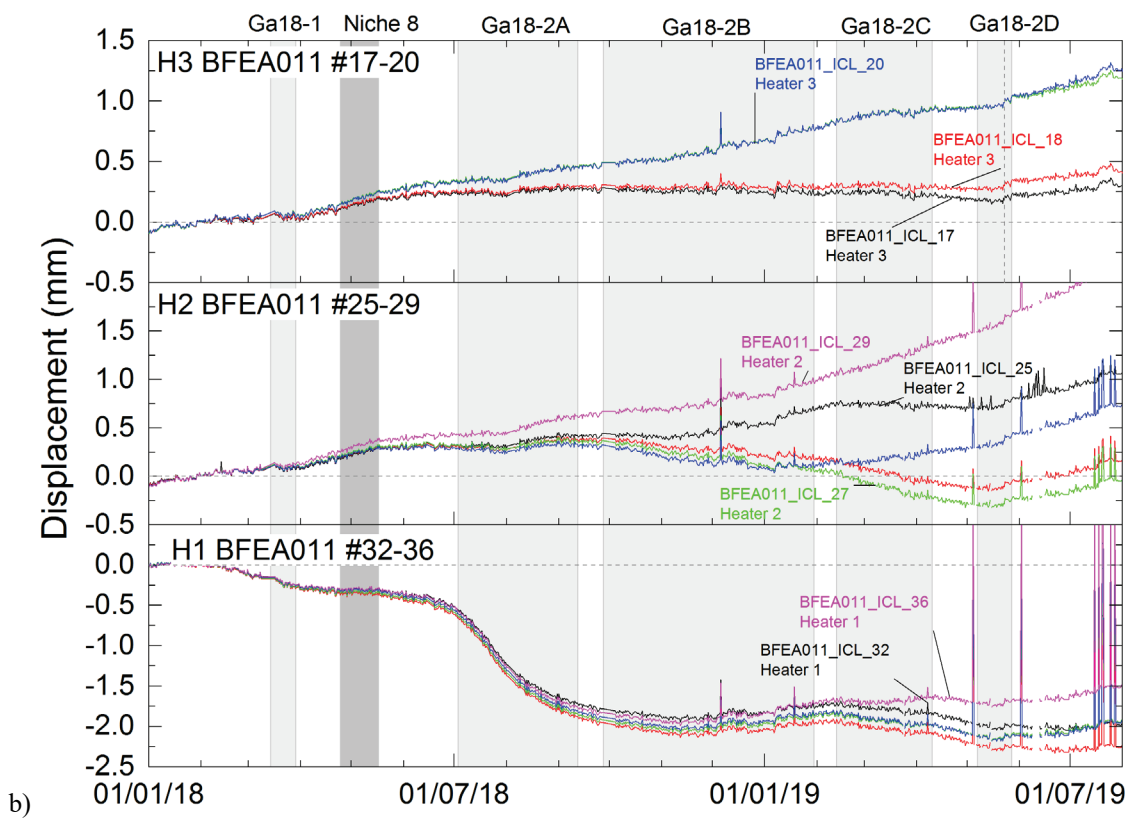
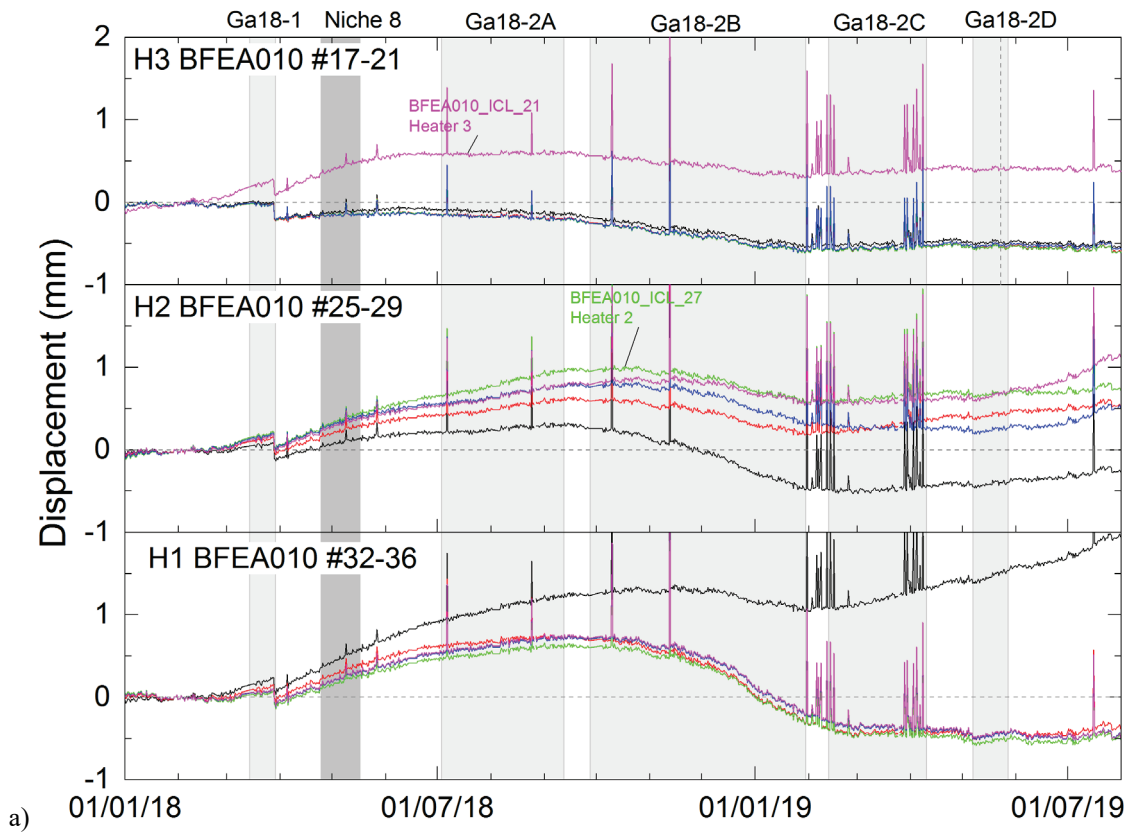


Fig. 94: Inclinator settlement response at heaters (relative to 31.01.2018)  
a) BFEA010. b) BFEA011

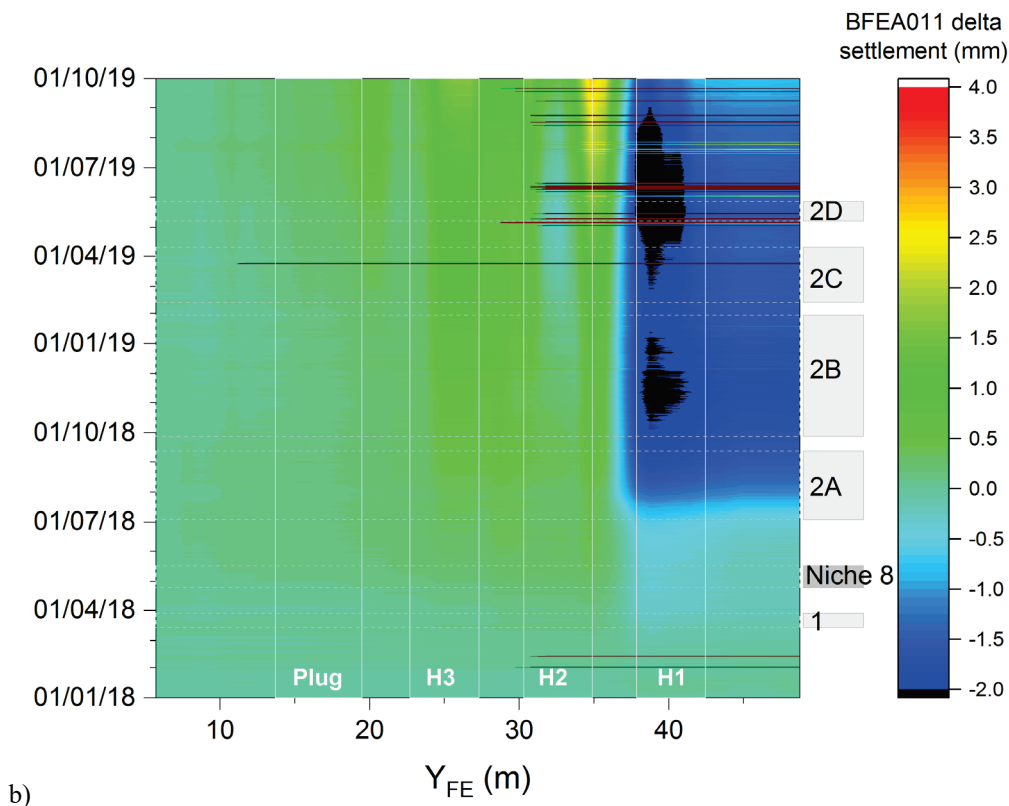
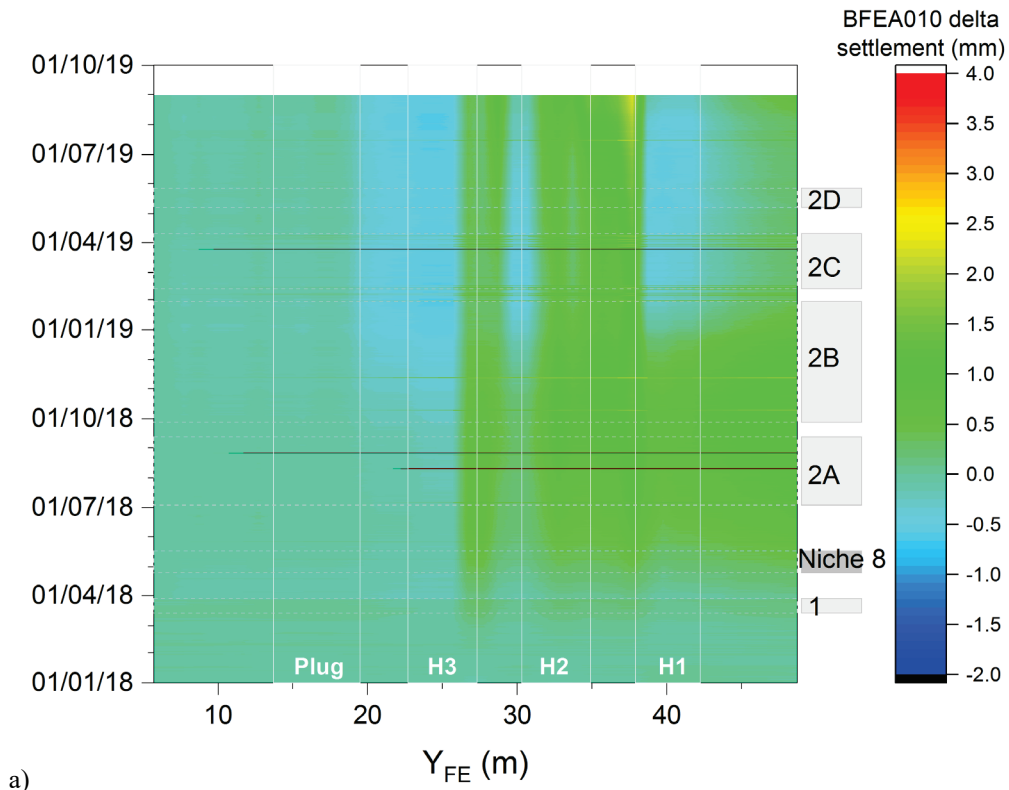


Fig. 95: Inclinator settlement response (relative to 31.01.2018)

a) BFEA010. b) BFEA011

### 4.3 Interval and packer pressures

The interval and packer pressure responses in the multi-packer systems drilled from the FE-A Niche, due to excavation of Ga18 are shown in Fig. 97, Fig. 98 and Fig. 99. During Ga18 excavation pore pressure and stress are changing in the rock as part of the transient response to heating. Typically pore pressures are still increasing during this time in the normal to bedding boreholes and the parallel to bedding intervals furthest from the FE Tunnel. Pressures are decreasing in the BFE002 intervals and some of the BFEA003 intervals. The clearest response to excavation occurs during Ga18 Phase 2D, as Ga18 passed to the SE of the FE Gallery prior to cutting through in May 2019.

Interval i3 in BEFA003 (BFEA003\_PRE\_03) shows a particularly strong response at the start of Phase 2D which is associated with a pressure rise of over 50 kPa in the next month followed by a rapid pressure drop and subsequent recovery. The cause of such a large response is unknown but may indicate some local deformation around the interval. Pressure in packer 2 (BFEA003\_PPK\_02) is very variable throughout the period.

Many of the strongest responses are seen on 23.05.2019 when, between 06:00 – 14:00, Ga18 was excavated from 292 – 294 GM in the Lower Sandy Facies/Carbonate-rich Sandy Facies (bedding orientation of 144/48°). The face mapping on that day (Ga18 Daily Report No. 178) identifies "many EDZ fractures and surfaces on the centre-right part of the tunnel face, that are subparallel to it." The excavation was proceeding to the NE and the right part of the face is that furthest from the FE Gallery.

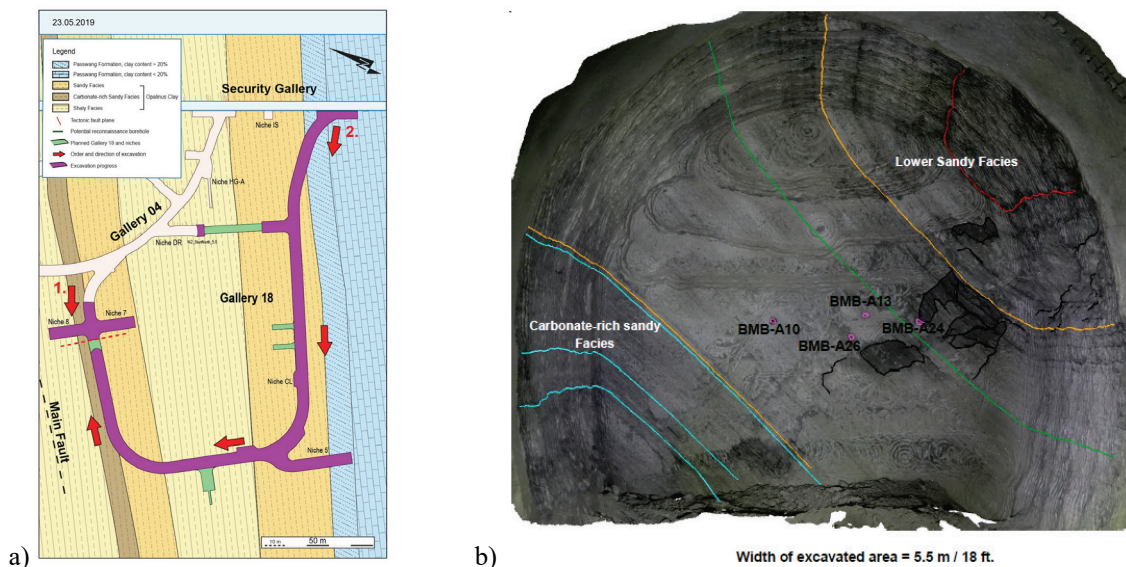


Fig. 96: Ga18 excavation on 23.05.2019 a) Ga18 progress, b) Ga18 face mapping at 294 GM  
From daily report 178

Interval i3 in BFEA007 shows a pressure increase in March 2019 that Alcolea et al. (2019) attribute to a thermally-induced fracture.

Fig. 100 shows the pore pressure responses to Ga18 excavation in radial boreholes drilled from the FE tunnel, where pore pressures are typically dropping strongly during this period. The responses are often larger than those seen in the multi-packer systems and multiple responses can be observed. Intervals in BFEB007 appears to show strong responses during Phase 2C.

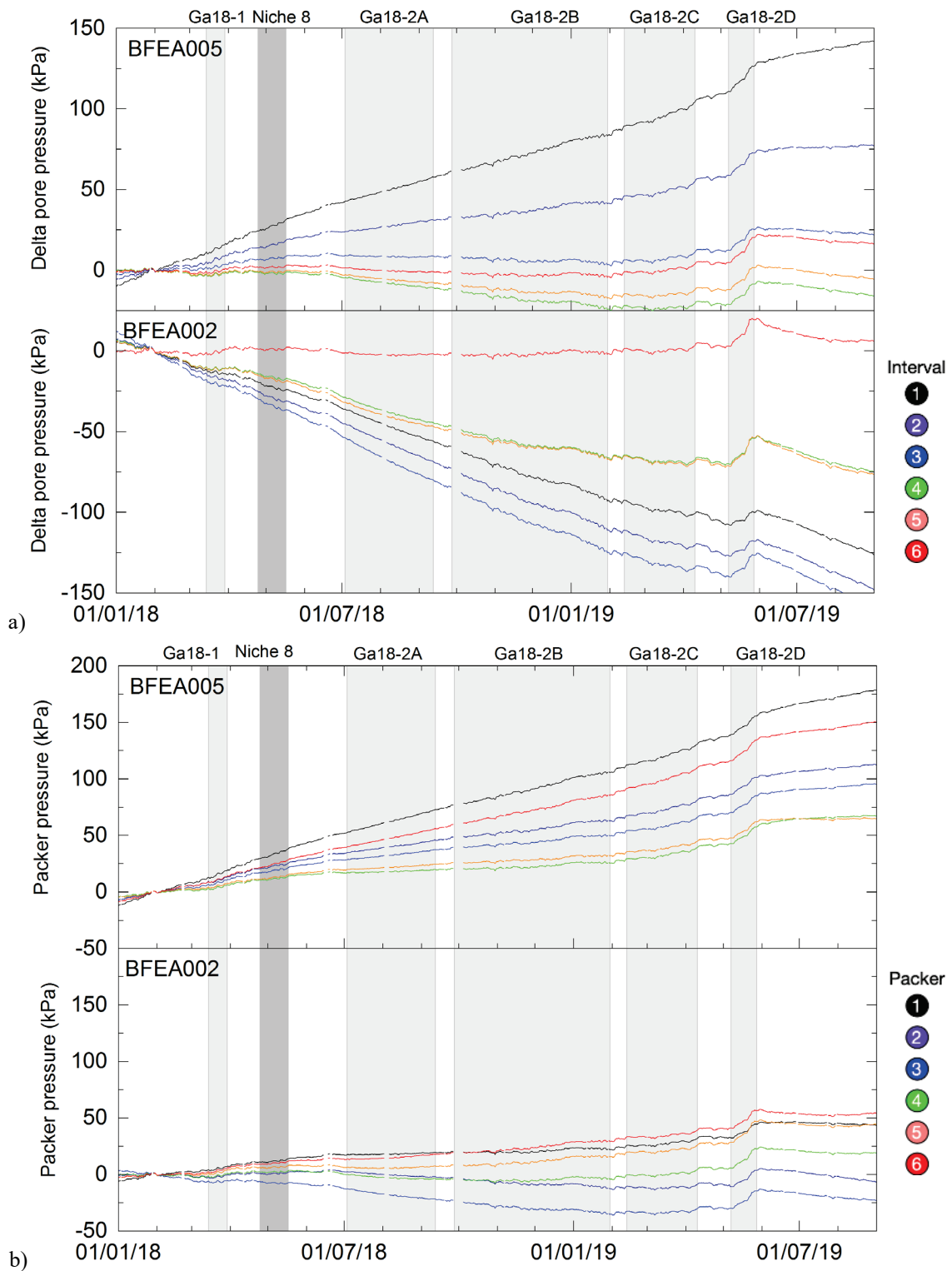


Fig. 97: BFEA002, 5 response to Ga18 excavation  
 a) Change in interval pressure. b) Change in packer pressure

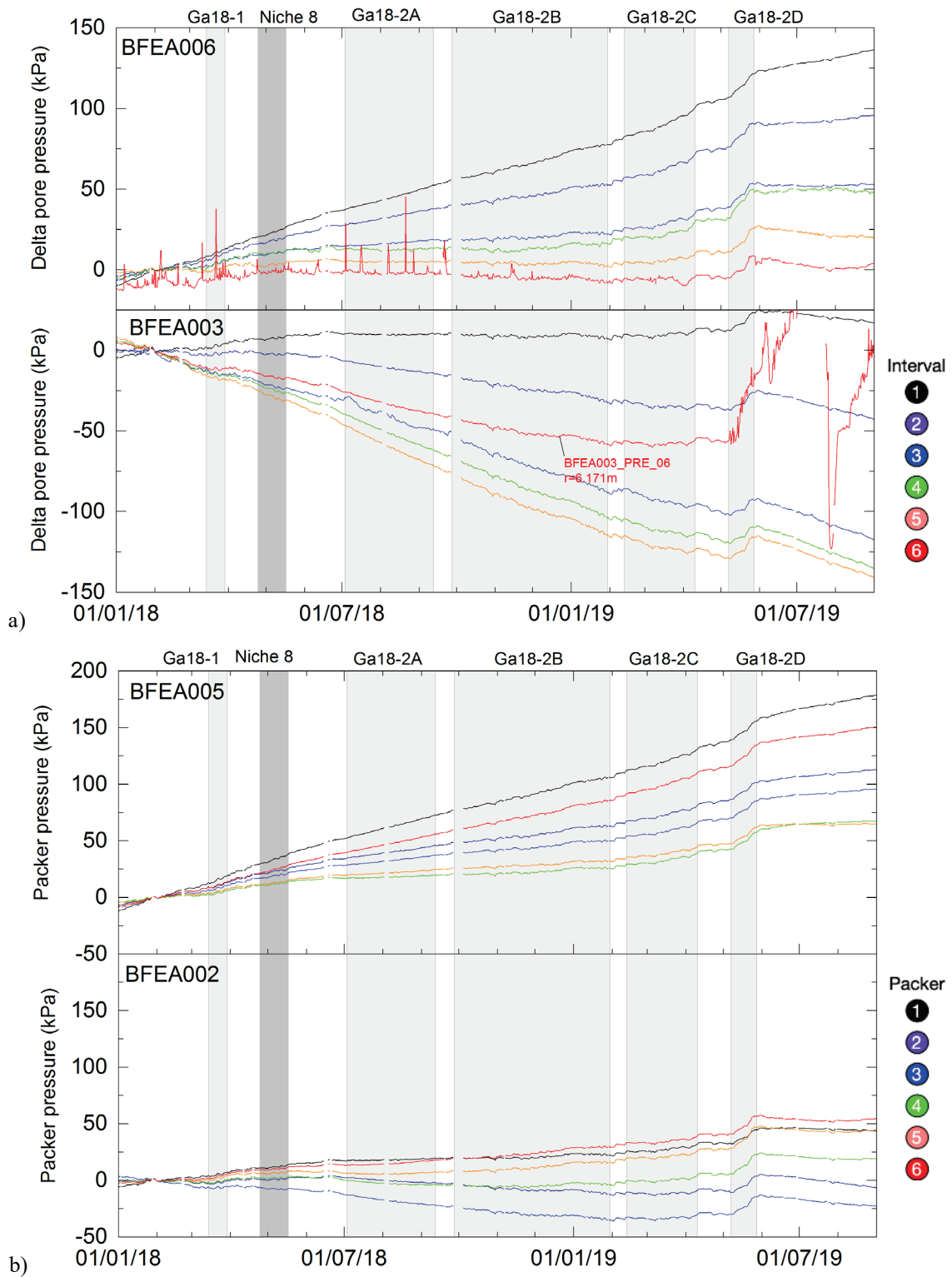


Fig. 98: BFEA003, 6 response to Ga18 excavation  
a) Change in interval pressure. b) Change in packer pressure

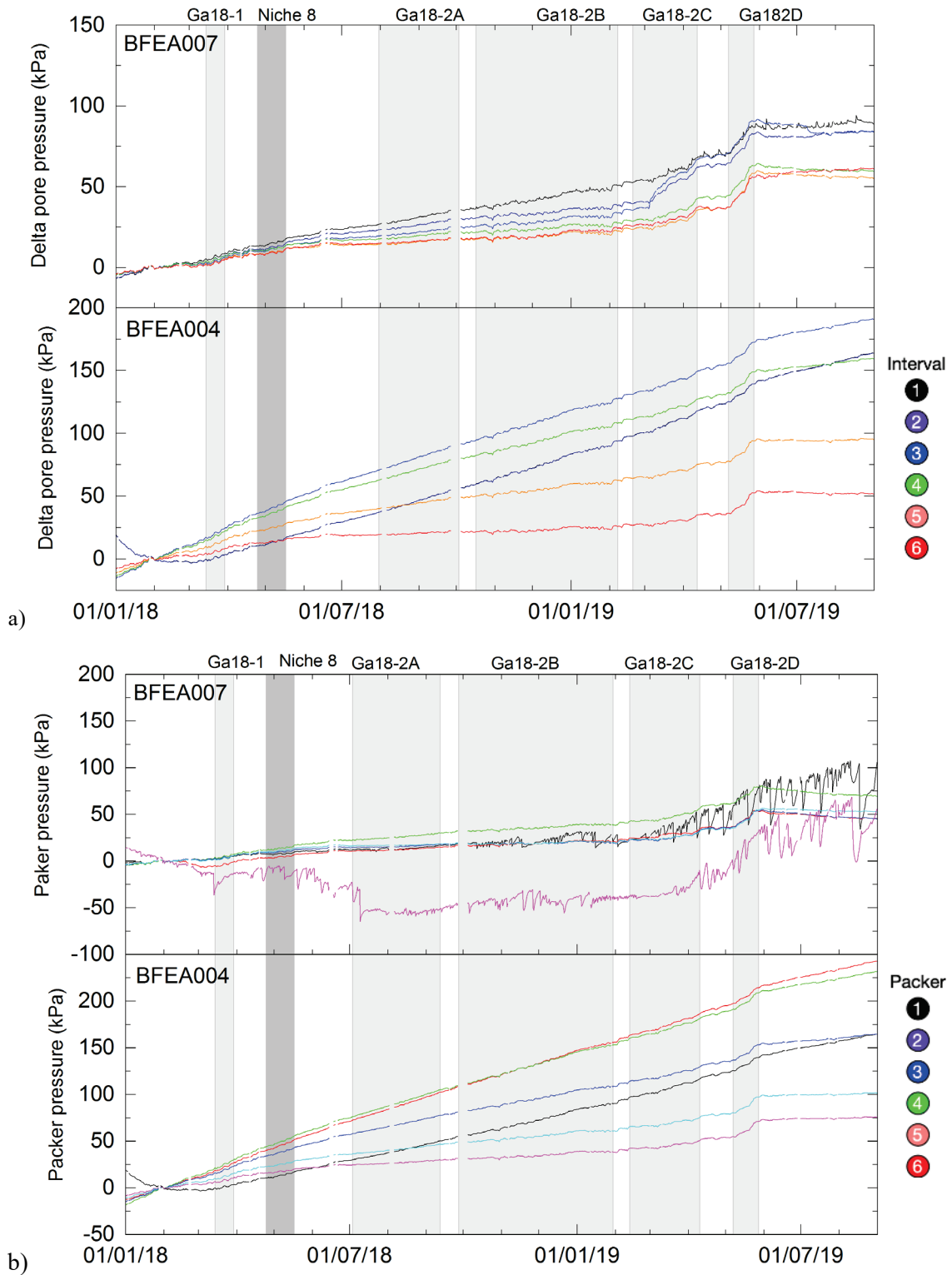


Fig. 99: BFEA003, 6 response to Ga18 excavation  
 a) Change in interval pressure. b) Change in packer pressure

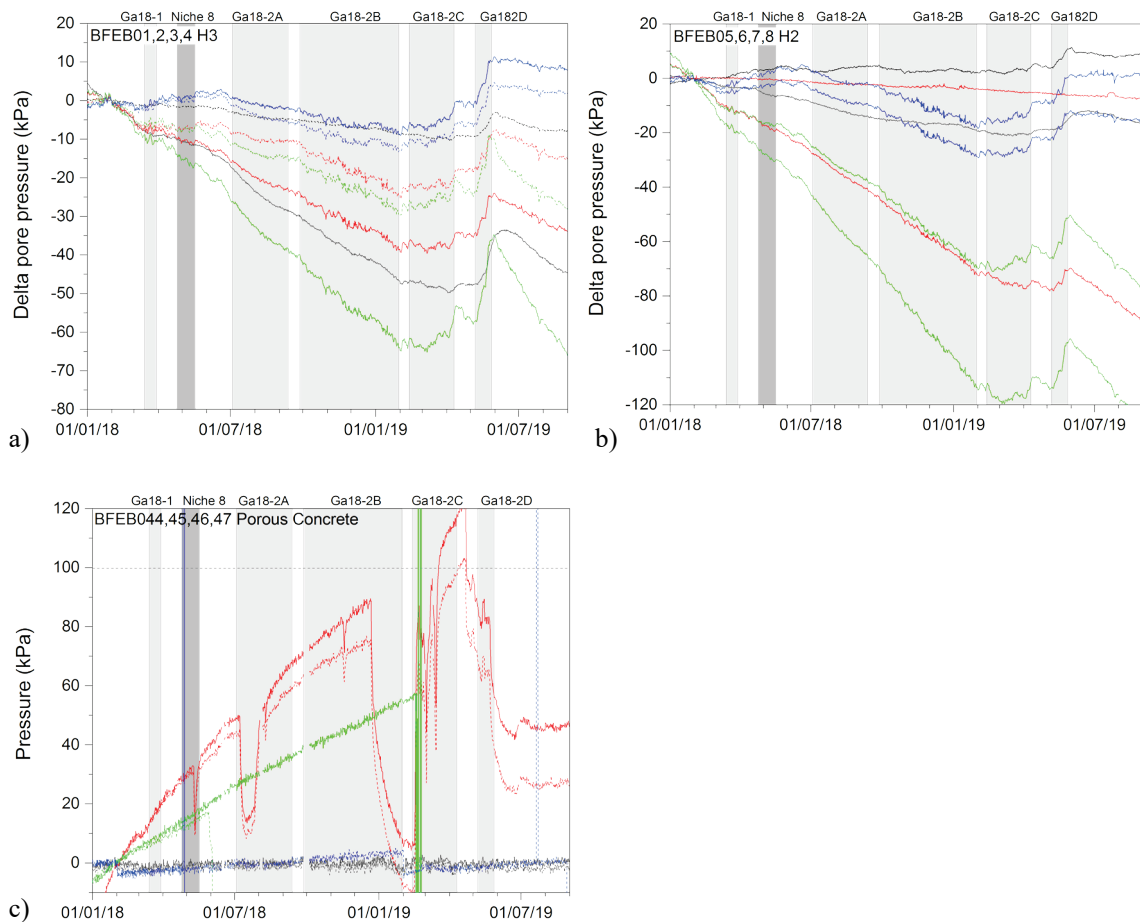


Fig. 100: Radial borehole pressure response to Ga18 excavation  
 a) BFEB01, 2, 3, 4. b) BFEB05, 6, 7, 8. c) BFEB044, 45, 46, 47

Comparable responses were observed in the BMB multi-packer systems installed for the MB experiment (Martin et al. 2015) around the FE-A Niche. At MB the overall pressure response to Ga18 excavation appears to be dominated by thermal pressurisation due to increasing temperature probably related to changes in ventilation in the FE-A Niche. Small pressure responses  $\sim 0.1 - 0.2$  bar (10 – 20 kPa) relate to excavation events during Ga18 Phase 2B and 2C. The response on 23.05.2019 is clearly seen in several packers (see Fig. 101). One monitoring interval shows an early response with a drop  $\sim 0.8$  bar (80 kPa) just prior to the start of Ga18 excavation (but after the start of the increase in temperature).

Overall the responses seen in the MB multi-packer systems are consistent with the change in temperature around the FE-A Niche and the observed response to Ga18 excavation in the FE monitoring systems.

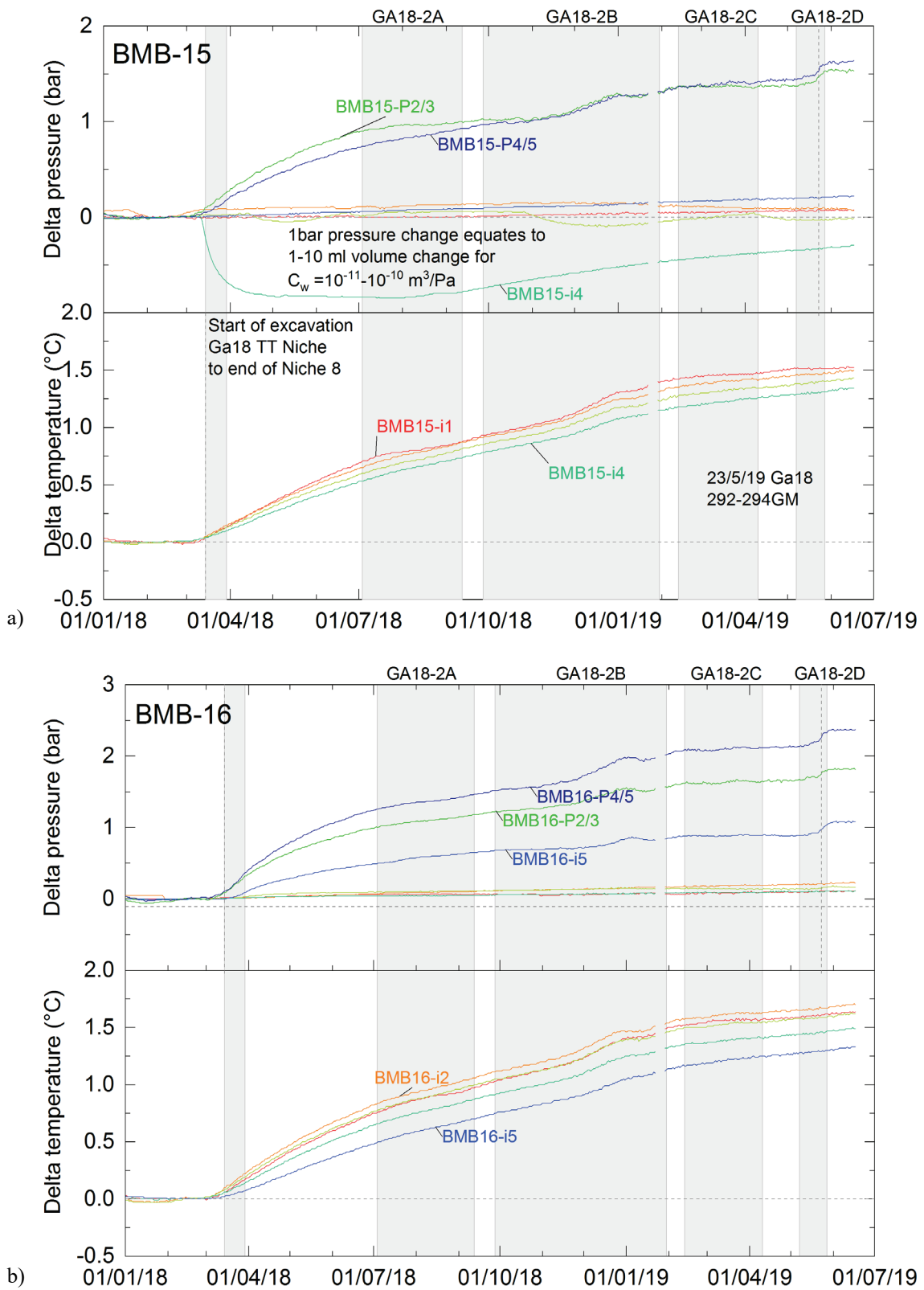


Fig. 101: Interval and packer pressure and temperature responses to Ga18 excavation at the BMB-15, 16 near the FE-A Niche

a) BMB-15. b) BMB-16

### Pressure responses to Ga18 Phase 2D

Higher time resolution data (10 minute) was used to examine the pressure responses observed in Phase 2D, in particular those on 23.05.2019. Fig. 102 shows the relative locations of the Ga18 excavation face during Phase 2D and the FE Tunnel and selected monitoring boreholes.

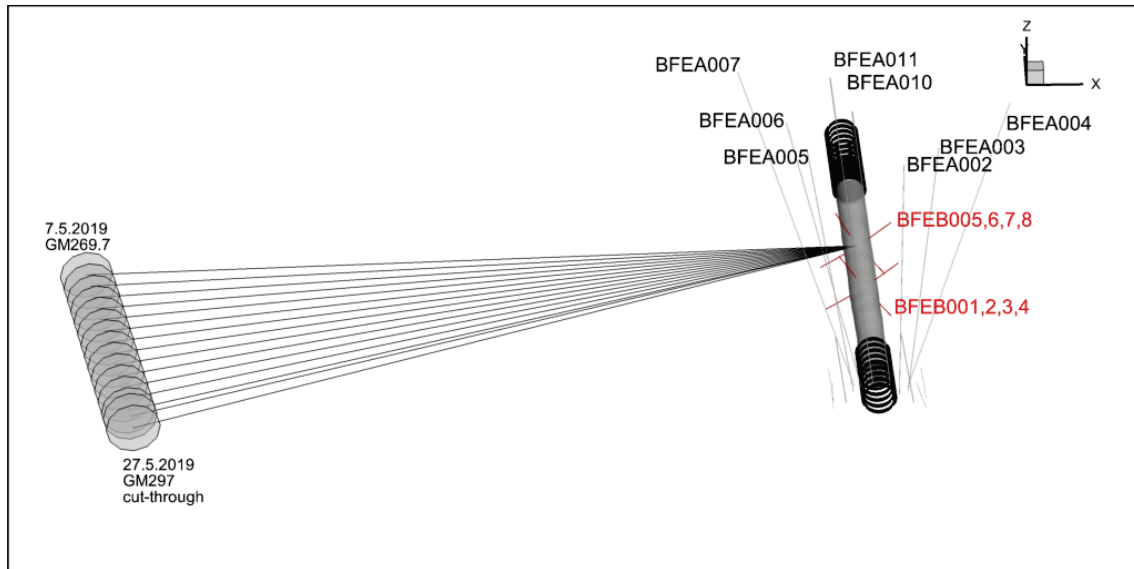


Fig. 102: 3D View of Ga18 excavation Phase 2D and MT FE tunnel and selected boreholes

Fig. 103 shows the change in pressure on 07.05.2019 (start of Ga18 Phase 2D) and 23.05.2019. Pressure is slowly dropping during 07.05.2019 (consistent with the long-term trend) with no clear response to excavation. During 23.05. all intervals show a clear response to excavation with the largest responses in i5 and i6 (nearest the FE Tunnel) in BFEA002. The responses in BFEA002 (far side of FE Tunnel from Ga18) show greater variability than those in BFEA005 (near side of FE Tunnel from Ga18). In BFEA002 there is a trend in response amplitude with distance from the tunnel, while responses vary in BFEA005. There is a minor pressure-drop event ( $\sim 1$  kPa) in BFEA05 i1 perhaps indicating a small volume increase ( $\sim$  ml). Similar responses are seen in BFEA03,4,6 and 7 (see Fig. 104 and Fig. 105).

The only irregular response is in BFEA003 i6 which showed pressure oscillations from earlier in the Ga18 excavation.

Similar pore pressure responses (max  $\sim 4$  kPa) are observed in the other multi-packer systems BFEB001-8 (Fig. 106). The strongest responses are seen in BFEB003 i1 and BFEB007 i1 oriented down parallel to bedding in the side of the FE tunnel closest to Ga18.

The spatial distribution of pore pressure change during Ga18 Phase 2D and during 23.05.2019 are shown in Fig. 107 and Fig. 108.

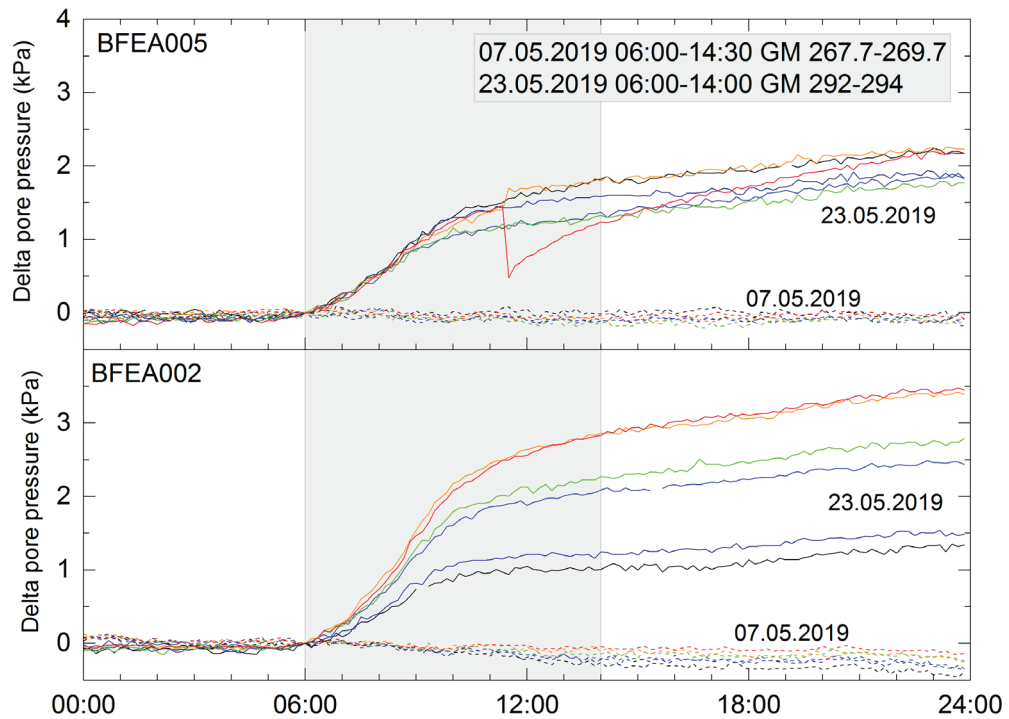


Fig. 103: Interval and responses to Ga18 excavation on 07.05.2019 and 23.05.2019 for BFEA002 and BFEA005

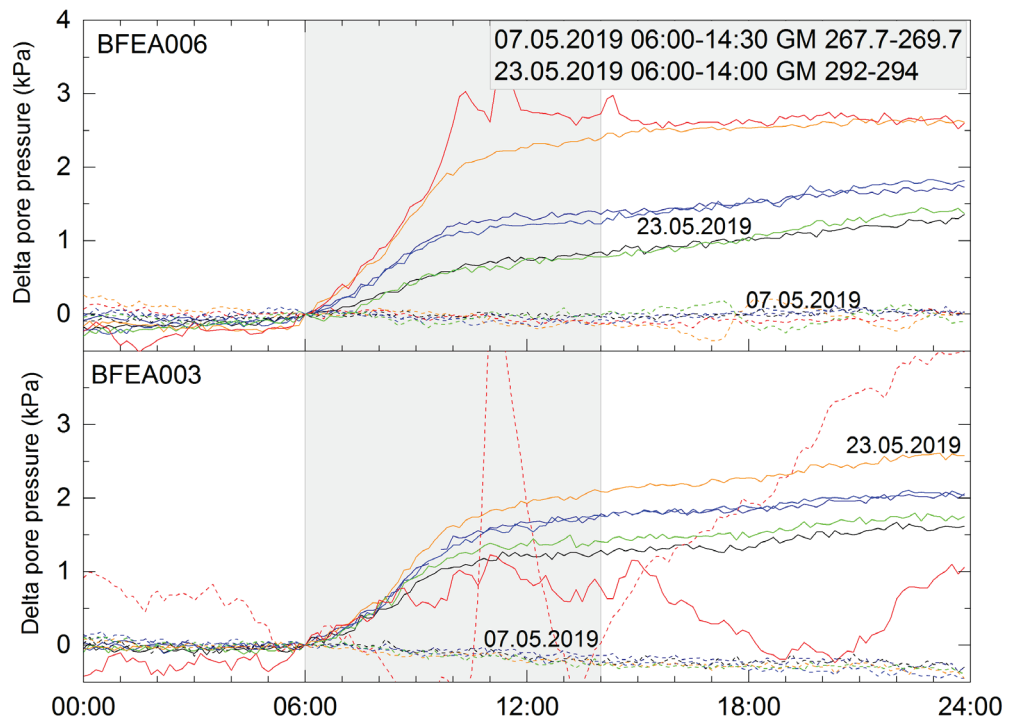


Fig. 104: Interval and responses to Ga18 excavation on 07.05.2019 and 23.05.2019 for BFEA003 and BFEA006

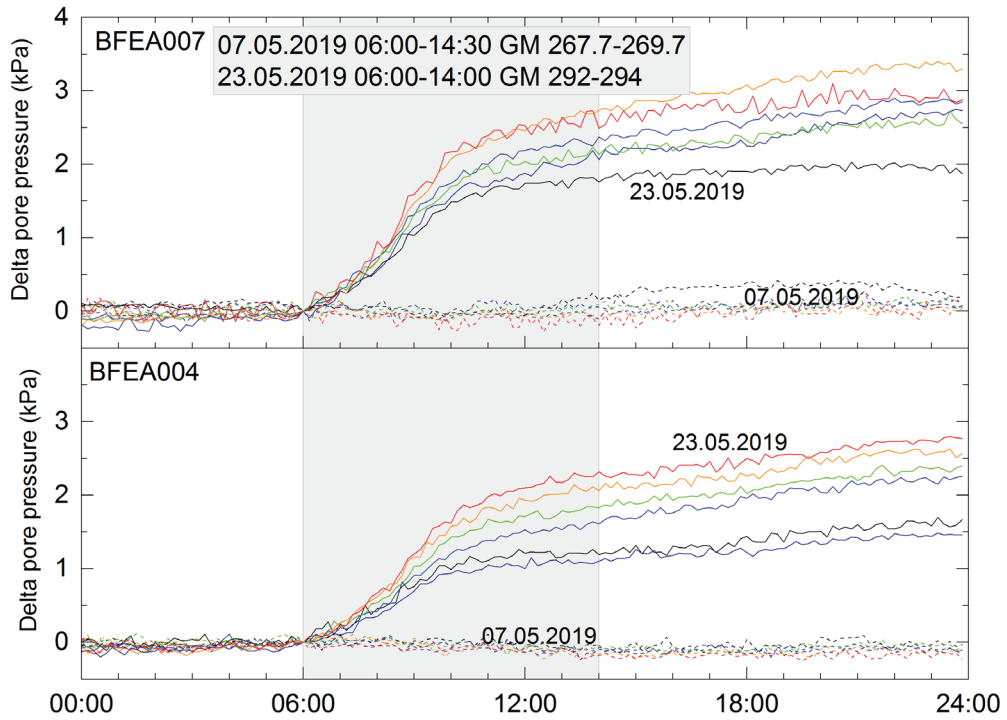


Fig. 105: Interval responses to Ga18 excavation on 07.05.2019 and 23.05.2019 for BFEA003 and BFEA006

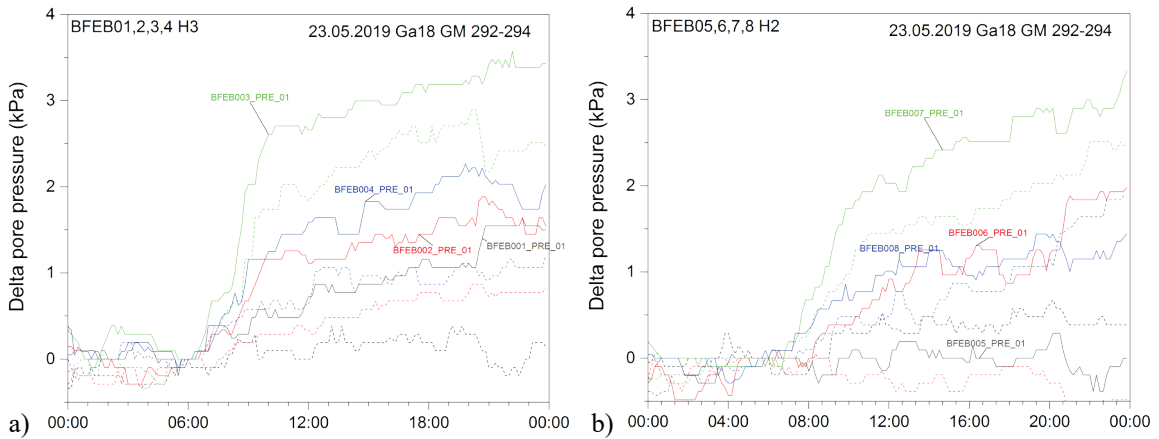


Fig. 106: Interval responses to Ga18 excavation on 23.05.2019 for a) BFEB001,2,3,4 b) BFEB005,6,7,8

The spatial distribution of pressure change around the FE Tunnel is shown in Fig. 107 and Fig. 108. Summary tables of geosphere pressure responses during Ga18 Phase 2D and on 23.05.2019 are given in Appendix F.

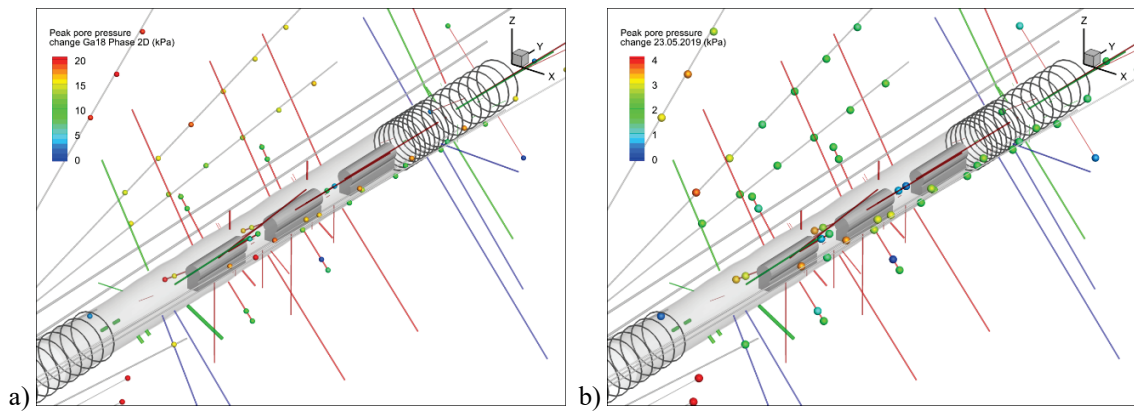


Fig. 107: 3D view showing maximum pressure change during a) Ga18 excavation Phase 2D and b) during 23.05.2019

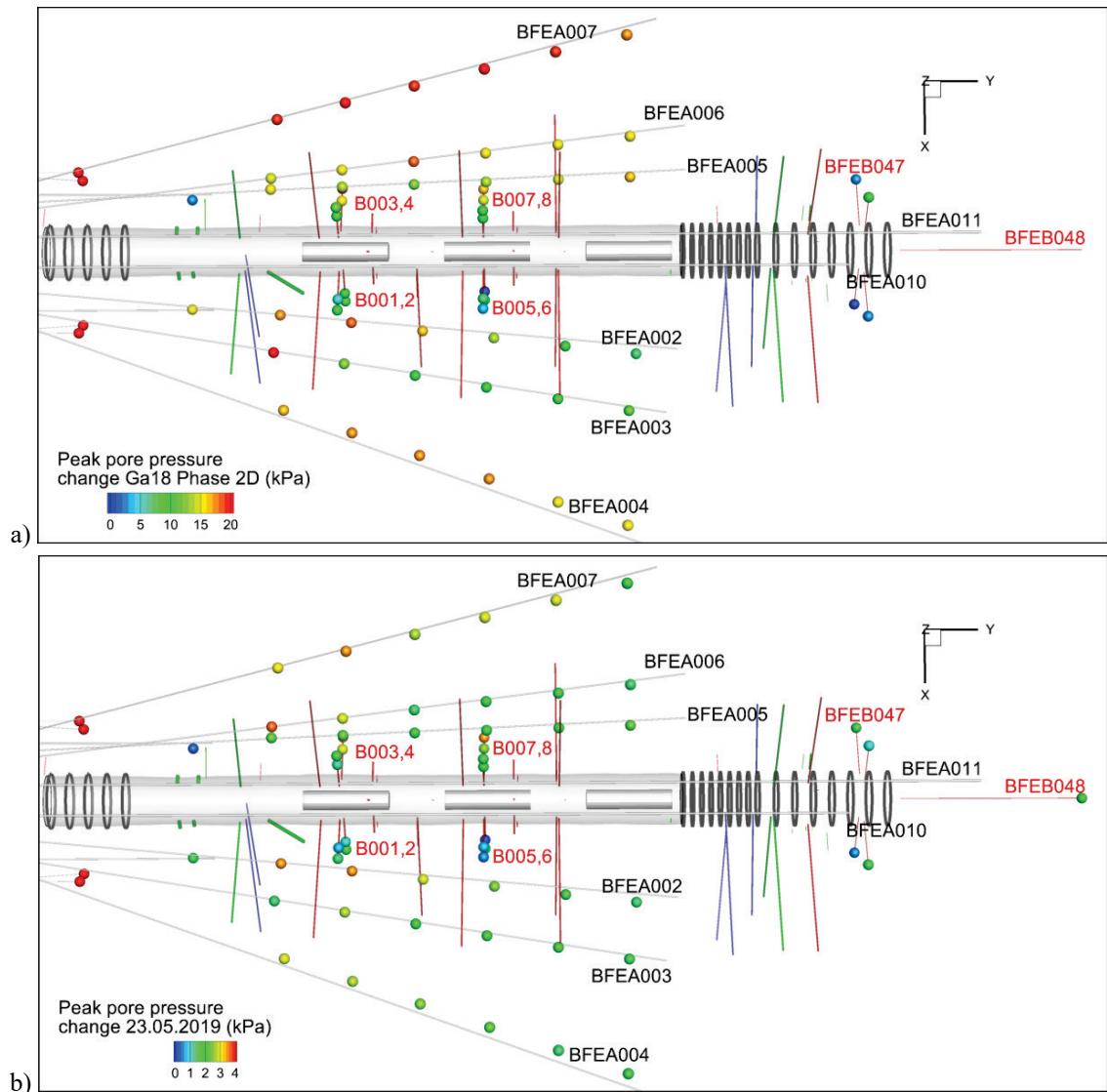


Fig. 108: Plan view showing maximum pressure change during a) Ga18 excavation Phase 2D and b) during 23.05.2019

#### 4.4 Summary of response to Ga18 excavation

Small changes in deformations, pore pressures and packer pressure have been measured in the rock around the FE Gallery and between the rock and the heaters within the tunnel. They correlate to specific excavation steps in Ga18. The clearest responses occur during Excavation Phase 2D on 23.05.2019 as the Ga18 face approached the cut-through (on 27.05.2019 see Fig. 102).

Tab. 23: Summary of Ga18 responses during Phase 2D

Measurement	Summary	Remark
Deformation (mm)	Heater LVDT responses up to ~ 0.2 mm increase (accuracy 0.04 mm) Inclinometer responses ~ 0.1 mm increase (resolution 0.01 mm/m)	LVDT extension +ve Inclinometer settlement +ve (up)
Pore pressure (kPa) Resolution 0.1 kPa	BFEA002-7: 10 – 50 kPa increase BFEB001-8: 0 – 20 kPa increase	Magnitude of response influenced by trends due to heating
Packer pressure (kPa)	BFEA002-7: 10 – 20 kPa increase BFEB001-8: 2 – 4 kPa increase BMB 15,16: 10 – 20 kPa increase	Some interval pressure indicate inelastic response to stress change (BFEA003_PRE_06)

The small magnitude of displacements relative to sensor sensitivity induced by Ga18 excavation limit the analysis possible, but the magnitude of pore pressure response facilitates more detailed analysis. Most sensors indicate an increase in pressure suggesting an increase in stress which is consistent with the measured extension of the LVDT and increase in the settlement. Variations in pressure response between borehole intervals will be influenced by:

- the interval compressibility
- the local saturation and stiffness of the rock around the interval
- the orientation of the interval relative to the induced stress changes
- the drainage to the FE Tunnel
- the location relative to the FE Tunnel

The magnitude of the observed responses is inconsistent with simple homogeneous isotropic 2D models of elastic response (Kirsch 1898) to a cylindrical excavation (see Appendix G) and may indicate either significant elastic anisotropy or a more complex response to excavation. The pattern of response requires further study with responses being focused on particular excavation steps.

The widespread observation of responses to excavation at significant distances (70+m) provides the opportunity to compare responses at individual intervals and packers and potentially derive local compressibility properties (related to saturation and stiffness). A notable aspect of many of the responses is the slow pressure recovery to the induced strain indicating an undrained response.

## 5 Integrated THM interpretation

### 5.1 Expected evolution of EBS and geosphere

The FE Experiment follows on from an extended programme of laboratory and in situ tests at Mont Terri supported by modelling and interpretation. The HE-E experiment (Gaus et al. 2014) is closest in concept to FE and is described in the next section and used for comparison with FE in later sections.

The HE-E experiment forms a key part in the experimental strategy developed by Nagra, although at approximately half-scale. GBM constitutive models and properties from laboratory (Wieczorek et al. 2011, Villar et al. 2012 and Rizzi et al. 2012) and previous in situ tests were calibrated to the early observations from HE-E (Garitte 2013) as input to scoping and design models of the FE Experiment. Key material properties derived from HE-E include the thermal conductivity, water retention curve and intrinsic permeability of the GBM based on the expected as-emplaced conditions (dry density and water content). Since that time further THM characterisation of the GBM has been performed by Seiphoori (2015).

#### 5.1.1 HE-E

HE-E is a 1:2 scale heater experiment with natural resaturation of the EBS and heater temperature  $\sim 140$  °C in the Opalinus Clay at Mont Terri (Gaus et al. 2014). The experiment aims are to:

- investigate the early non-isothermal resaturation period of a heated EBS; and the impact on thermo-hydro-mechanical behaviour
- provide the experimental database required for the calibration and validation of existing THM models of the early resaturation phase
- upscale thermal conductivity of the partially saturated EBS from laboratory to field scale (pure bentonite and sand-bentonite mixtures)

The HE-E experiment is located in the RB micro tunnel excavated by horizontal raise-boring in 1999 in the shaly facies of the Opalinus Clay. The tunnel is 1.3 m in diameter and oriented normal to the local bedding strike. The VE-Experiment - which was performed in the same tunnel section as HE-E - is fully described in Mayor et al. (2007), while the HE-E Experiment setup and initial response is described in Teodori & Gaus (2011) and Gaus et al. (2014).

The HE-E Experiment is in a 10m long section (formerly the VE test section) of the unlined horizontal RB micro tunnel. It was decided to reutilize the instrumentation of the previous VE test for HE-E (see Fig. 109). The existing instrumentation layout played a key role in the determination of the experiment position inside the RB micro tunnel. The SA3 section was selected to be the middle of the HE-E experiment and the location of the plugs was determined from this.

The experiment includes two 4 m-long heater sections isolated by plugs. The heaters are in a central liner with H1 in the sand/bentonite buffer section while H2 is located in the GBM buffer section. The experiment is highly instrumented (Fig. 110) and the instrumentation concept targeted four zones:

1. the heater surface where the temperature is measured
2. the EBS itself and the interface with the Opalinus Clay with very dense measurements of temperature and relative humidity

3. the Opalinus Clay close to the microtunnel which was under the influence of the ventilation before and during construction where temperature, humidity, hydraulic pressure and displacement are monitored
4. the Opalinus Clay at several meters from the microtunnel where hydrostatic conditions were less disturbed by the activities in the microtunnel and where hydraulic pressures are monitored

Data shown in this report covers a period of approximately 2'400 days up to 31.12.2017 and is taken from Kober et al. (2018). Fig. 111 shows the H2 (bentonite pellet section) temperature and power. Other plots in this chapter are used to demonstrate consistency of observations between HE-E and FE and to consider any relevant effects due to scaling up from ½ scale to full-scale. Relevant differences between HE-E and FE are:

- HE-E: 1.3 m diameter unlined and unsupported micro-tunnel, FE 3m diameter tunnel with shotcrete and rock bolts or steel arches (ISS section)
- increased buffer density due to improved emplacement techniques (facilitated by the larger diameter)
- improved and increased quantity of instrumentation at FE
- influence of previous testing at site and typically lower pore pressure (< 1'000 kPa) at start of HE-E.

Heating started on 28.06.2011 and has continued (with only minor interruptions) since then. The outer temperature of the HE-E heaters varies between 122 and 140 °C with a tendency for higher temperatures on the upper surface.

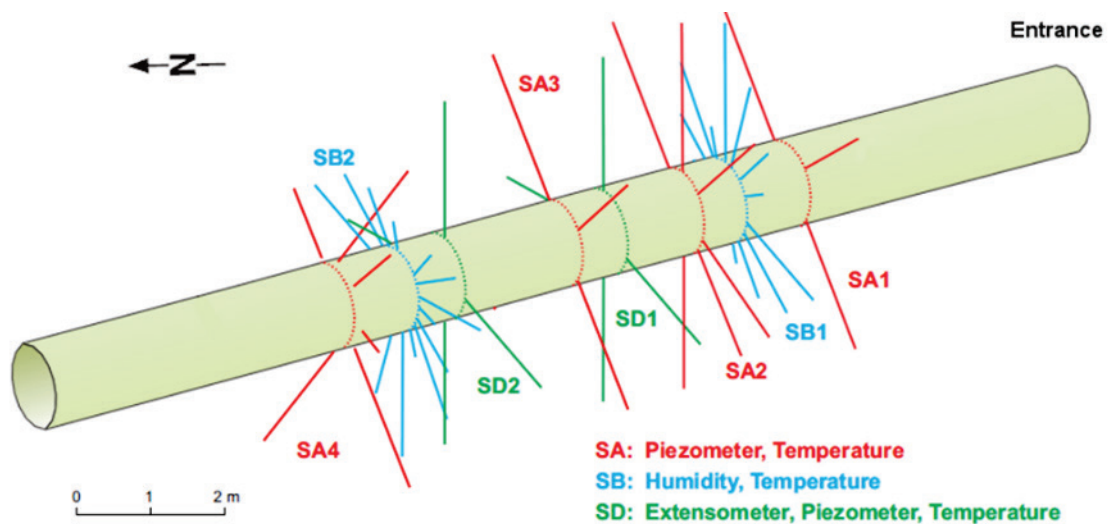


Fig. 109: Geosphere instrumentation around the VE microtunnel at Mont Terri

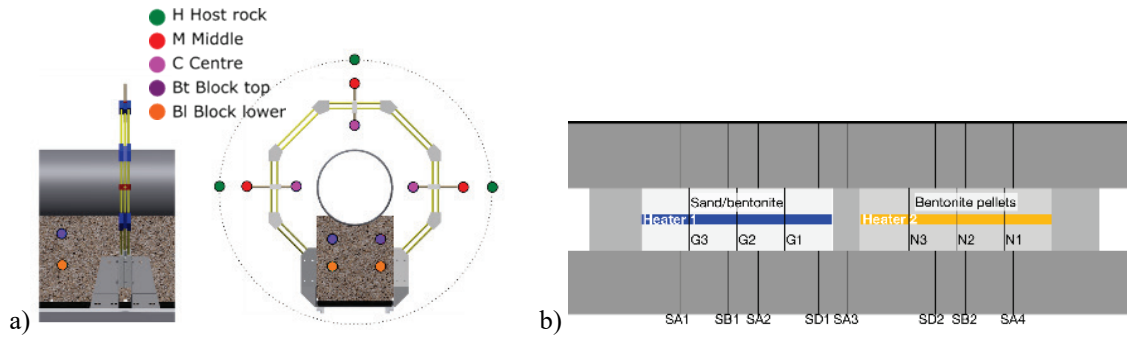


Fig. 110: EBS instrumentation in the VE micro tunnel at Mont Terri  
 a) Cross-section showing sensor carrier, heater and pedestal. b) Geosphere and EBS instrumentation sections

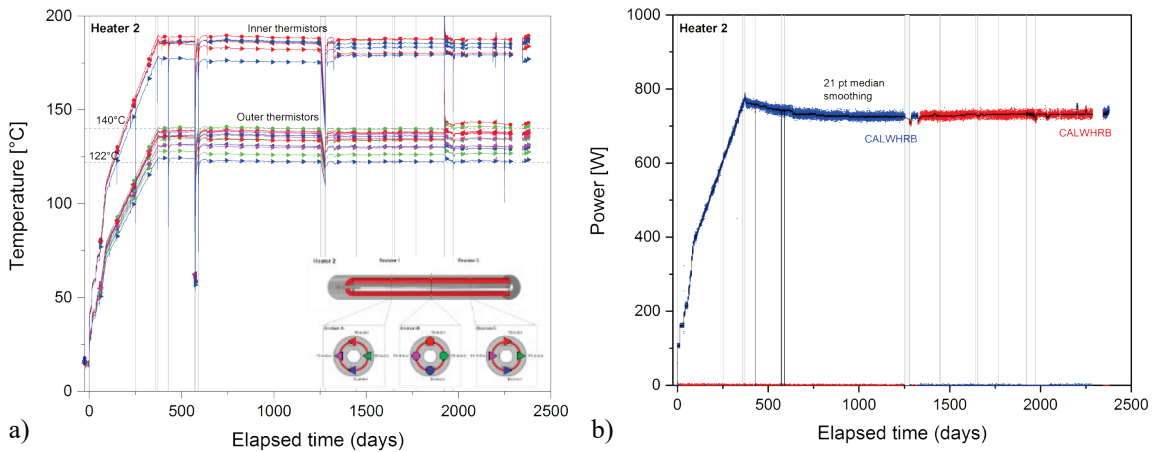


Fig. 111: HE-E H2 a) temperature and b) power  
 Smoothed power estimate calculated by median filter over 21 point (20 hour) window.

### 5.1.2 Modelling and scoping calculations

Design and predictive THM modelling also influenced the understanding of the expected evolution. In particular models were based on those developed from the series of heater experiments previously performed at Mont Terri (HE-B, HE-D and HE-E). Predictive modelling was performed once the detailed design was finalised. These models, together with the understanding developed from other testing at Mont Terri form the basis for the expected evolution of the experiment.

Models and parameters used for the Opalinus Clay in the scoping calculations were largely based on those developed from the previous in situ experiments (see Garitte, 2013). Models of the early response to heating in the HE-E experiment based on the calibrated parameter set (known as "THM\_c") produced reasonable matches to the observed:

- temperature evolution at the heater surface, in the buffer and in the Opalinus Clay
- RH distribution within the buffer
- pore water pressure increase in the Opalinus Clay and overall distribution of pore pressure (extent of partially saturated/low pressure zone).

Garitte (2013) suggests that the saturation of the HE-E buffer is largely controlled by the ability of the Opalinus Clay to provide water to the buffer with buffer properties having only limited influence.

Simple upscaling models (based on the assumption of steady state heat conduction within the buffer) were used to identify the maximum temperature at the rock interface and were used for input to anisotropic models of heat conduction in the tunnel nearfield. An axisymmetric THM model through the central H2 was also developed based on the model parameters calibrated to HE-E (i.e. those that gave the best fit to the first 18 months of data). Predictions from the scoping models are listed in Tab. 24.

Tab. 24: Predictions of FE response to heating from Garitte (2013)

Parameter	Predicted response
Temperature rise in the first few cms of rock.	~ 35 °C after one year and reaches a maximum of 45 °C after about 8 years
Temperature distribution in the buffer at times up to 7'100 days	See Fig. 112
Degree of saturation and relative humidity of the buffer and nearfield rock	Described in terms of 3 zone concept: Zone A: unsaturated (buffer and near field Opalinus Clay) Zone B: saturated and in suction Zone C: saturated and positive pore water pressure
Extent of zone B and saturation/ suction profile	Significant uncertainty on extent of suction (~ 1 – 2 m)
Pore water pressure profile	Pore water pressure peak reach 3 MPa after 2 years of heating at 7 – 8 m. After 8 years, pressure disturbance reaches ~ 15 m and amplitude decreases

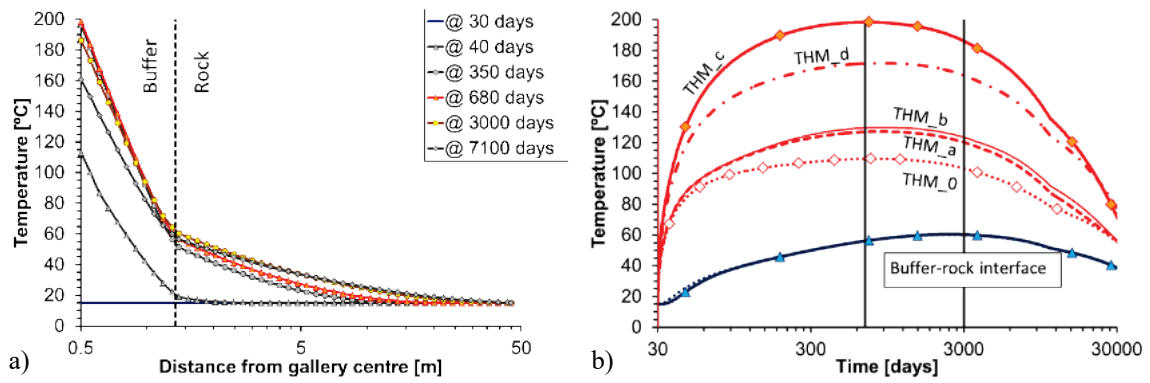


Fig. 112: Predicted temperature a) temperature versus radial distance from the tunnel axis and b) influence of THM parameters on temperature at the heater and at the buffer rock interface

Garitte (2013)

### 5.1.3 Evaluation at 18 months

Nagra (2019) presents a summary of the experiment evolution in a series of schematics reproduced in Fig. 113. The processes considered and descriptions are largely consistent with the interpretations and data presented in this report. Although some discrepancies arise in the description of the pore pressure distribution around the tunnel and the significant THM couplings in the rock including thermal pressurisation and influence of ongoing volumetric strains associated with convergence. Similarly, greater importance is placed on the redistribution of moisture within the GBM from close to the heater towards the shotcrete than is evident in Fig. 113.

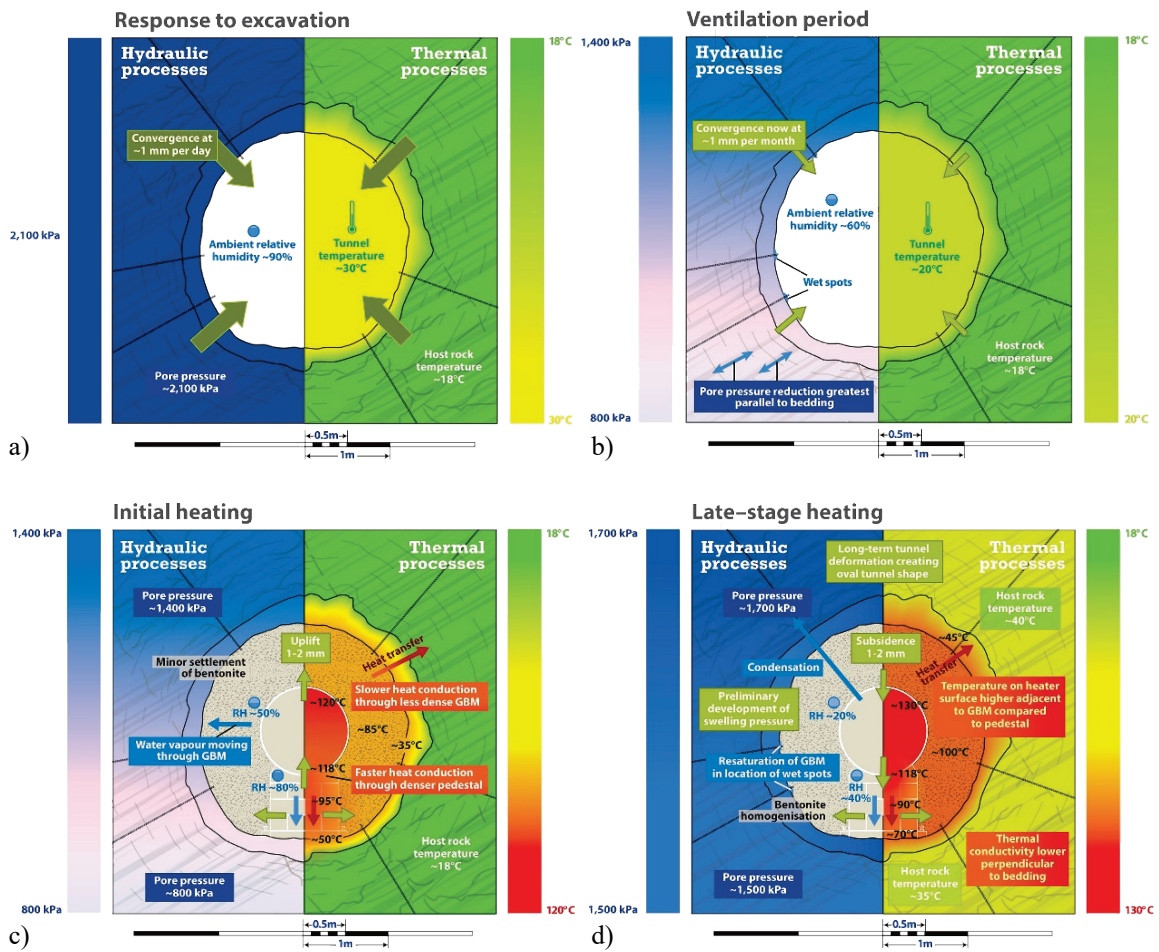


Fig. 113: Illustration of THM processes occurring in the FE Experiment

- a) Following excavation and support installation.
- b) During ventilation.
- c) During the initial heating phase, i.e. approximately the first two months of heater operation.
- d) Late-stage heating, i.e. up to 18 months after heater operation.

Taken from Nagra (2019)

## 5.2 Summary of observed response at FE

The observed evolution of the FE EBS and geosphere as described in Chapter 3 is determined by three main drivers:

- ongoing response to excavation and creation of the tunnel and installation of support
- ongoing response to ventilation of the tunnel
- response to EBS emplacement and heating

The responses to these drivers overlap in time and interact (e.g. via the saturation state of the rock around the tunnel). In addition, some minor perturbations have been caused by the excavation of Ga18 and these have been discussed in the previous chapter.

While most sensors show a relatively smooth evolution from emplacement onwards with long term trends relating to heating, a small number of sensors show short term "events" (other sensors, particularly RH sensors show rather noisy data) for discussion of the behaviour and reliability of particular sensors see Firat Lüthi (2018, 2019).

### 5.2.1 Geosphere response to FE tunnel excavation and ventilation

The short-term excavation response and creation of the EDZ is discussed in Nagra (2019), Lanyon et al. (2014) and briefly presented in Chapter 2 of this report. The longer term response to excavation and ventilation is characterised by:

- ongoing anisotropic convergence (particularly in the ISS)
- drying and desaturation of the shotcrete and Opalinus Clay in the ISS and behind shotcrete
- pore pressure recovery from excavation induced pressures and drainage towards the tunnel
- localised flow into the tunnel associated with features that perforate the shotcrete

The focus in this report is on the response to heating although many of these processes continue to impact the evolution after the start of heating.

### 5.2.2 Response to EBS emplacement and heating

To best represent the disposal system behaviour and responses, heating was started almost immediately after emplacement of the heaters and GBM. It is therefore not possible to separate the response to emplacement from that due to heating. The changes due to emplacement include:

- increased loads due to the weight of the heaters, pedestals and GBM
- reduction and subsequent end of ventilation due to plug emplacement

These result in only relatively minor changes in the rock compared to those due to heating.

The end of ventilation and closure of the tunnel changes the rate of evaporation and removal of water vapour from the shotcrete and rock wall which has created partially saturated zones in the shotcrete and rock. However, the emplacement of the low-water content GBM results in a low relative humidity atmosphere within the tunnel which until the combination of moisture redistribution from around the heater and sufficient water flow from the rock creates saturated conditions at the tunnel wall, may result in ongoing desaturation of the rock.

Longer term swelling of the bentonite may result in internal stresses on the liner and potential recompaction of the EDZ. However swelling pressures based on the measured total pressures are still low < 0.5MPa and so these effects are for the moment small.

**Temperature evolution in EBS and geosphere**

The dominant process is conduction and the speed of propagation of the thermal front is largely controlled by the thermal diffusivity of the bentonite (GBM and blocks), shotcrete and rock. Both thermal conductivity and heat capacity increase with saturation. The coupling between the thermal and hydraulic aspects is relatively weak if the saturation is slow and only limited moisture redistribution occurs (due to the initial low water content of the GBM).

The maximum measured temperature in the rock occurs in BFEB015 (H3): 53 °C and BFEB016 (H2): 58 °C in the intervals closest to tunnel wall ( $r \sim 1.8$  m). this is equivalent to a temperature increase in the range 37 – 42 °C assuming an initial rock temperature of 16 °C. This is consistent with the prediction of maximum temperature change of 45 °C after 8 years (Garitte 2013). Temperature in the far field ( $r \sim 17$  m) show only small changes of temperature  $\sim 1 - 2$  °C parallel to bedding (far sensors BFEA004) and less than this normal to bedding (BFEA007).

The pattern of temperature in the buffer and around the FE tunnel is controlled by the spatial distribution of the heaters. In the heater sections the pattern is largely controlled by radial distance as shown in Fig. 114. The pattern is like that observed at the HE-E experiment as shown in Fig. 115.

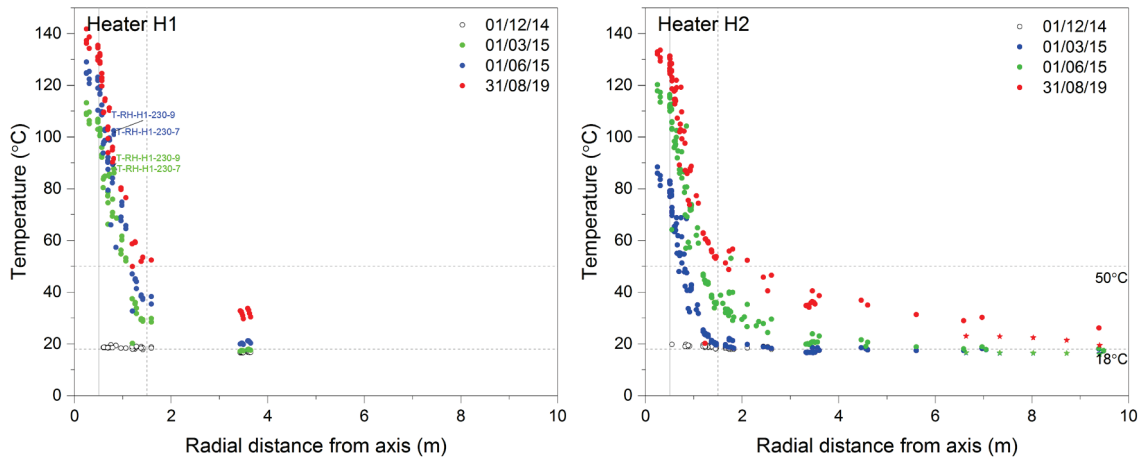


Fig. 114: Radial Distribution of temperature at varying times during heating for a) H1, b) H2  
 31.08.2019 is 1'720 days from the start of heating at H1 and 1656 days for H2.

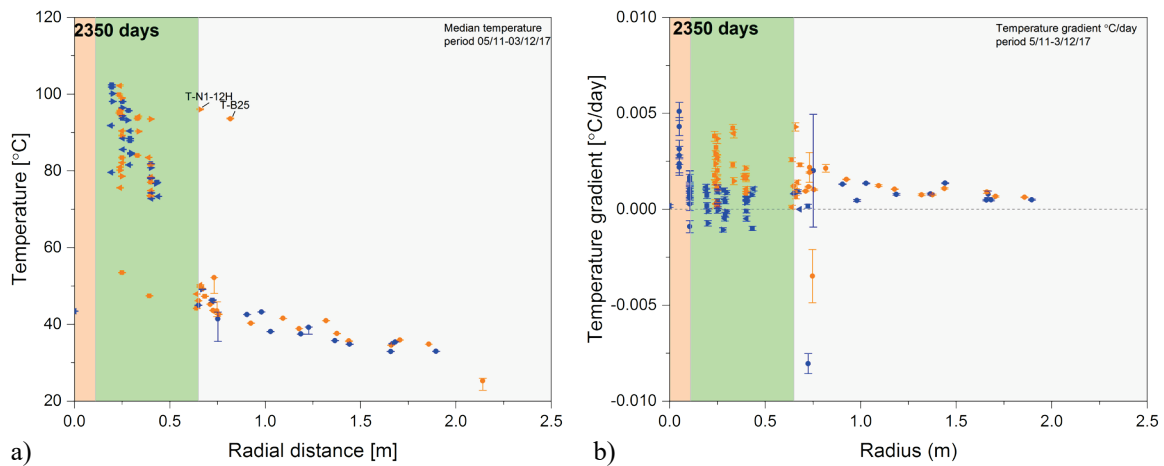


Fig. 115: Distribution of temperature and temperature gradient in HE-E experiment after 2350 days of heating

a) With temperature (°C). b) Temperature gradient (°C/day)

Orange symbols indicate sensors in the GBM buffer section. Blue symbols indicate sensors in the sand/bentonite buffer section. The temperature profiles are similar due to the relatively small differences in thermal conductivity between the two buffer materials.

### EBS coupled responses to heating

The main EBS coupled response to heating is associated with drying of the bentonite near the heater and subsequent moisture transport to the outer parts of the buffer. This process has been recorded in both the FEBEX and HE-E experiments. Moisture redistribution can be observed in the different measurements of saturation listed in Tab. 25. As an example, Fig. 116 shows the RH evolution around H3.

Tab. 25: Measurements related to state of buffer saturation as of 31.08.2019

Measurement	Observations
Thermal conductivity	Increased thermal conductivity at sensors at the shotcrete wall. Near saturated values have been recorded for some sensors near wet spots
Relative humidity	Close to the heaters relative humidity has reduced in both the pedestal (to ~ 40 %) and GBM (to ~ 20 %). At the shotcrete wall relative humidity is heterogenous (perhaps influenced by localised flow from the rock) but has increased to between 60 and 100 %. The increase is typically greater in the centre of the heater sections. In the gaps between the heaters relative humidity is again heterogeneous and varies between 50 to 80 %.
Water content (travel time)	Slow ongoing rise in volumetric water content in the GBM at the shotcrete wall. Estimated volumetric water content is between 14 – 18 % at 31.08.2019 suggesting that saturation is below 50 %.
Seismic and GPR	Seismic and GPR cross-hole measurements in the upper part of the tunnel indicate ongoing increasing saturation.

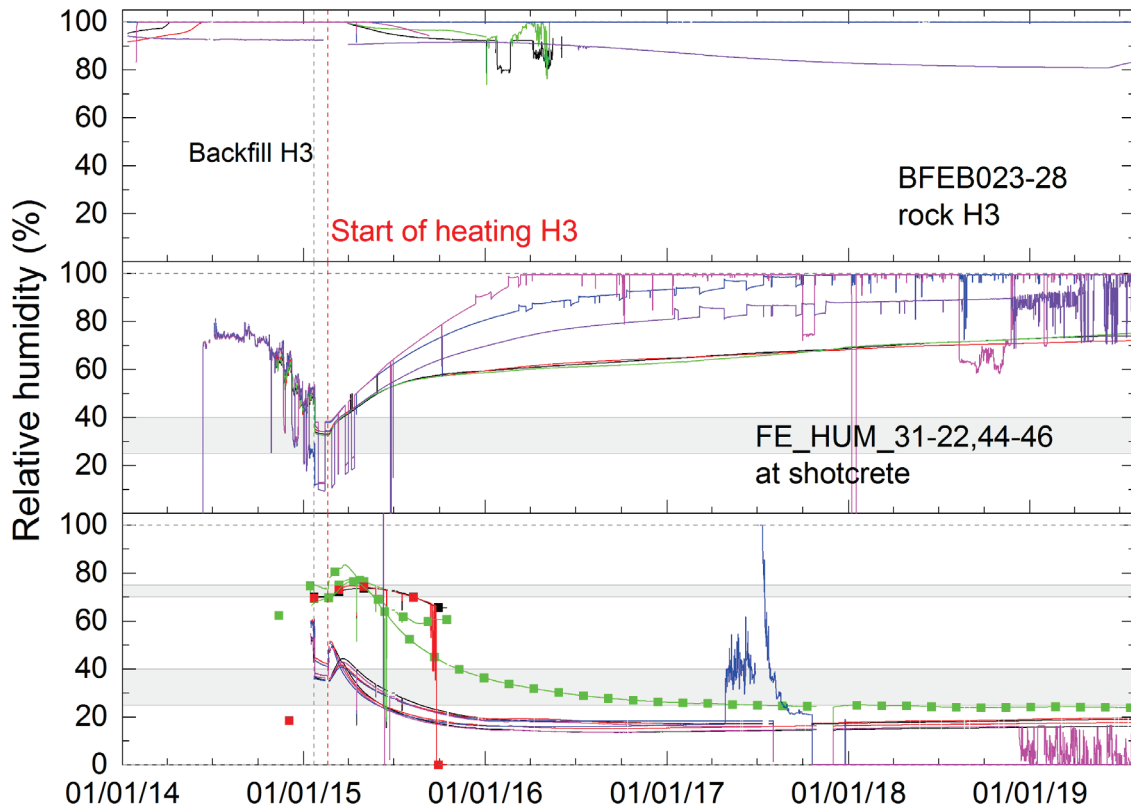


Fig. 116: Relative humidity in H3 sections in rock, at shotcrete wall and around the heater

Assuming an initial gravimetric water content of 5 % and emplaced dry density of  $1.49 \text{ g/cm}^3$  the total water volume within 20 cm of the heater surface is approximately  $0.06 \text{ m}^3/\text{m}$  (not accounting for the difference in water content and dry density of the heater pedestal). The drop in RH near the heater together with the observed rise close to the shotcrete may indicate that a significant fraction of this water has been redistributed to the outer part of the buffer within the first year of heating.

The pattern of moisture redistribution observed at FE is again consistent with observations from HE-E (in both the sand/bentonite and bentonite pellet buffer) and FEBEX (compacted bentonite block buffer). Fig. 115 shows the RH data from the bentonite pellet EBS section with a clear redistribution of moisture from the near heater region to the tunnel wall over the first 500 days.

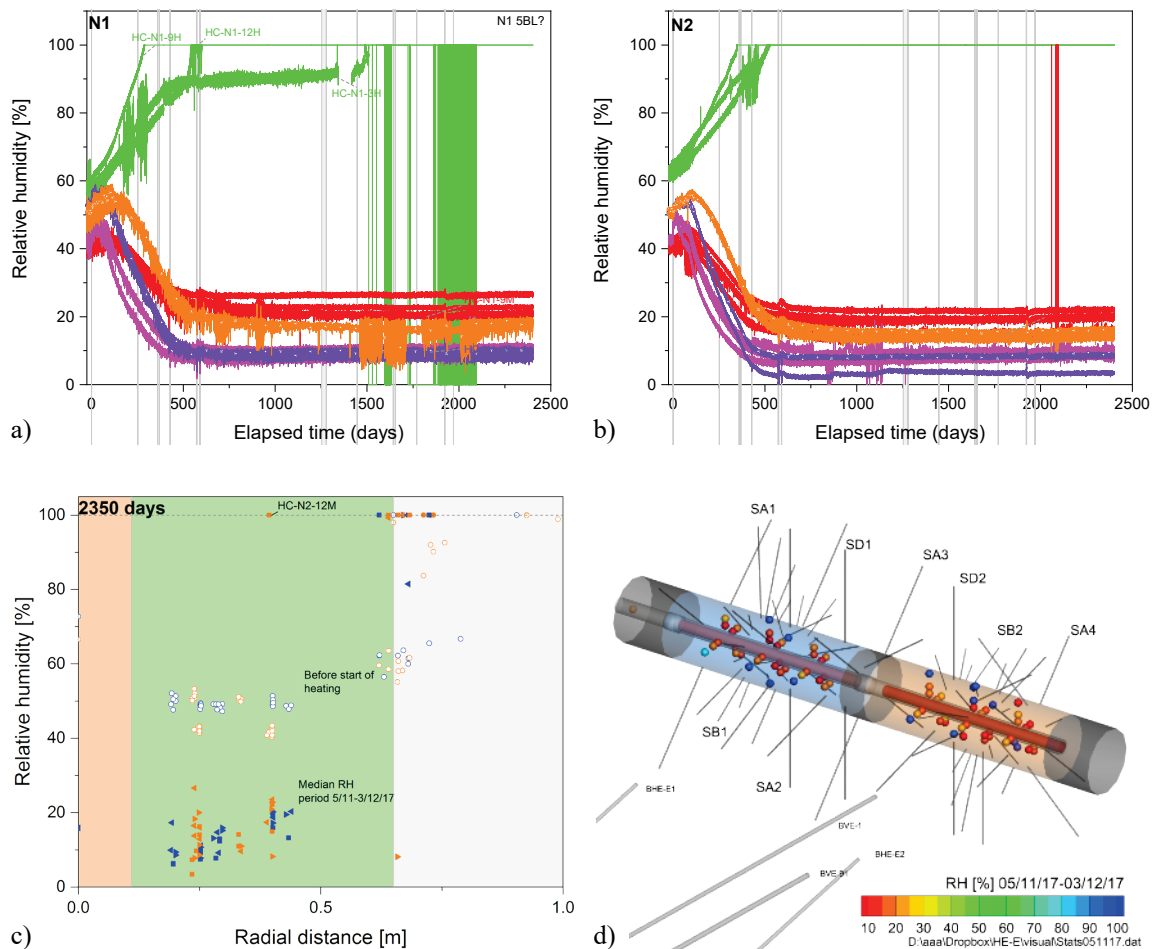


Fig. 117: Relative humidity in HE-E experiment

a) RH evolution at section N1, b) a) RH evolution at section N2, c) distribution with radial distance after 2350 days of heating, d) 3D view at 2350 days

Colour coding in a,b as shown in Fig. 110: green interface with host rock; red 25cm from liner, magenta 10cm from liner, purple top of pedestal, orange base of pedestal.

Other responses observed at FE include some minor upward displacements of the heaters associated with the start of heating (perhaps due to local thermal expansion) and subsequent sinking due to drying and shrinkage of the pedestals. These are observed in the LVDT measurements.

### Geosphere pore pressure response to heating

The observed pressure responses to heating parallel (BFEA002) and normal to bedding (BFEA005) are shown in Fig. 118a, 118b. The induced pressure disturbances have peaked in BFEA002 but are still rising in BFEA005 due to the anisotropy in thermal diffusivity and other rock properties. The responses over the first 5 °C of temperature change are shown in Fig. 118c, 118d. A characteristic small dip in temperature prior to the rise seen parallel to bedding is probably due to the mechanical anisotropy as observed in the ATLAS III in situ heating test in Boom Clay (Chen et al., 2011, Yu et al. 2014). The subsequent increase is typically stiffer with

greater pressure change for unit temperature change but the slope varies for different packers and intervals. The more distinct response parallel to bedding is likely to be influenced by:

- higher thermal diffusivity parallel to bedding
- the greater extent of EDZ and potentially higher hydraulic conductivity in the normal to bedding direction
- the anisotropy in elastic properties of the rock
- ongoing convergence normal to bedding resulting in volumetric strains and pore pressure reduction

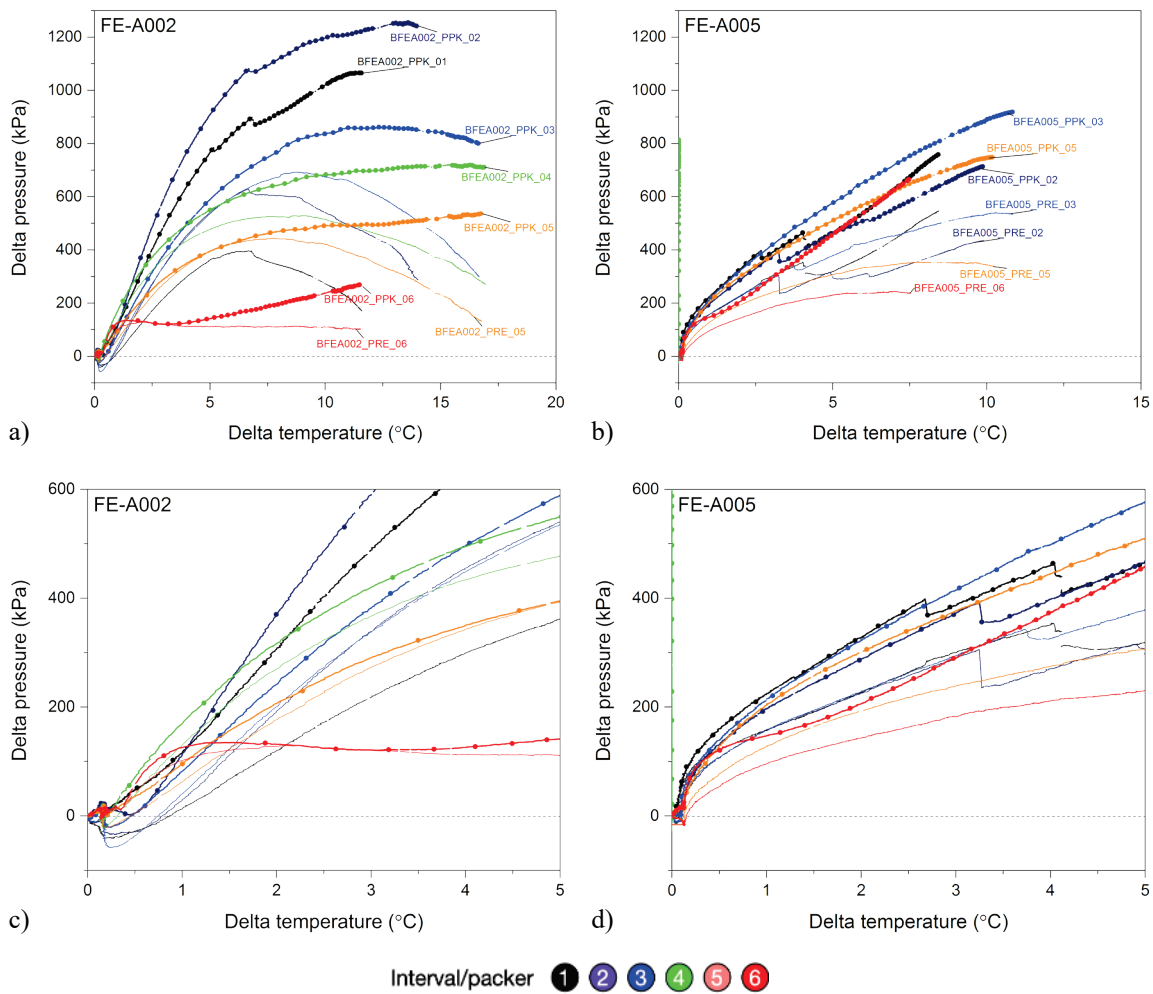


Fig. 118: Pressure change versus temperature change in packers and intervals  
 a) In FE-A002 along-bedding and b) in FE-A005 normal to bedding. Plots c) and d) show only the behaviour over the first 5 °C of temperature change using the same colour conventions as plots a and b.

Further analysis of the induced pore pressure rise can be found in Lanyon (2019a) and is summarised in Tab. 26.

Tab. 26: Summary of BFEA002 to A007 interval and packer response to heating  
From Lanyon (2019a)

Borehole	Orientation	Tunnel radii (a)	Behaviour
BFEA002	Along-bedding	2 – 4 a	Minor peaks in pressure but long-term ongoing quasi-linear response for packers. Interval pressures have peaked and now dropping linearly (i6 nearest the tunnel shows flat response).
BFEA003		4 – 6 a	Multiple pressure drops in p2 when delta pressure exceeds 200 kPa. Packers show long-term quasi-linear response (except p2). Interval pressures have peaked and now dropping linearly.
BFEA004		Beyond 6 a	Irregular pressure pulses in i2 early 2018. Packers show long-term quasi-linear response (i5,i6 flattening). Interval pressures increasing roughly linearly.
BFEA005	Normal to bedding	2 – 4 a	Pressure drops in i1,p1,i2,p2 when delta pressure exceeds 200 kPa.
BFEA006		4 – 6 a	Noisy pressure data small pressure drops in Packer 5 at ~ 200 kPa.
BFEA007		Beyond 6 a	Max temperature change~ 2°C. Noisy irregular data i6.

Increased pore pressure and stress has resulted in minor deformations around the boreholes potentially associated with reactivation of EDZ structures. Increased hydraulic gradients and reduced viscosity will also have resulted in a relatively minor increase in flow to the EDZ and tunnel. However, there is no evidence for any major change in flow or significant changes in the rate of EBS resaturation.

The peak pore pressures observed around FE are shown in Fig. 119. Maximum pressure is highest in the most distant intervals parallel to bedding in BFEA004 at ~ 2'500 kPa. The high pressures in BFEA004 i1 and i2 (2916 and 2915 kPa) relate to a high pressure event in late 2017 perhaps related to packer operations (see Fig. 52 and Fig. 62).

The maximum pore pressures are lower than those suggested by scoping calculations which suggested peak pore water pressures might reach 3 MPa after 2 years of heating at 7 – 8 m, probably indicating the conservative nature of the calculations. The pressure disturbance has also spread somewhat faster than the scoping calculations indicated, with pore pressure disturbances extending to beyond 17m within 3 year of heating in the direction parallel to bedding.

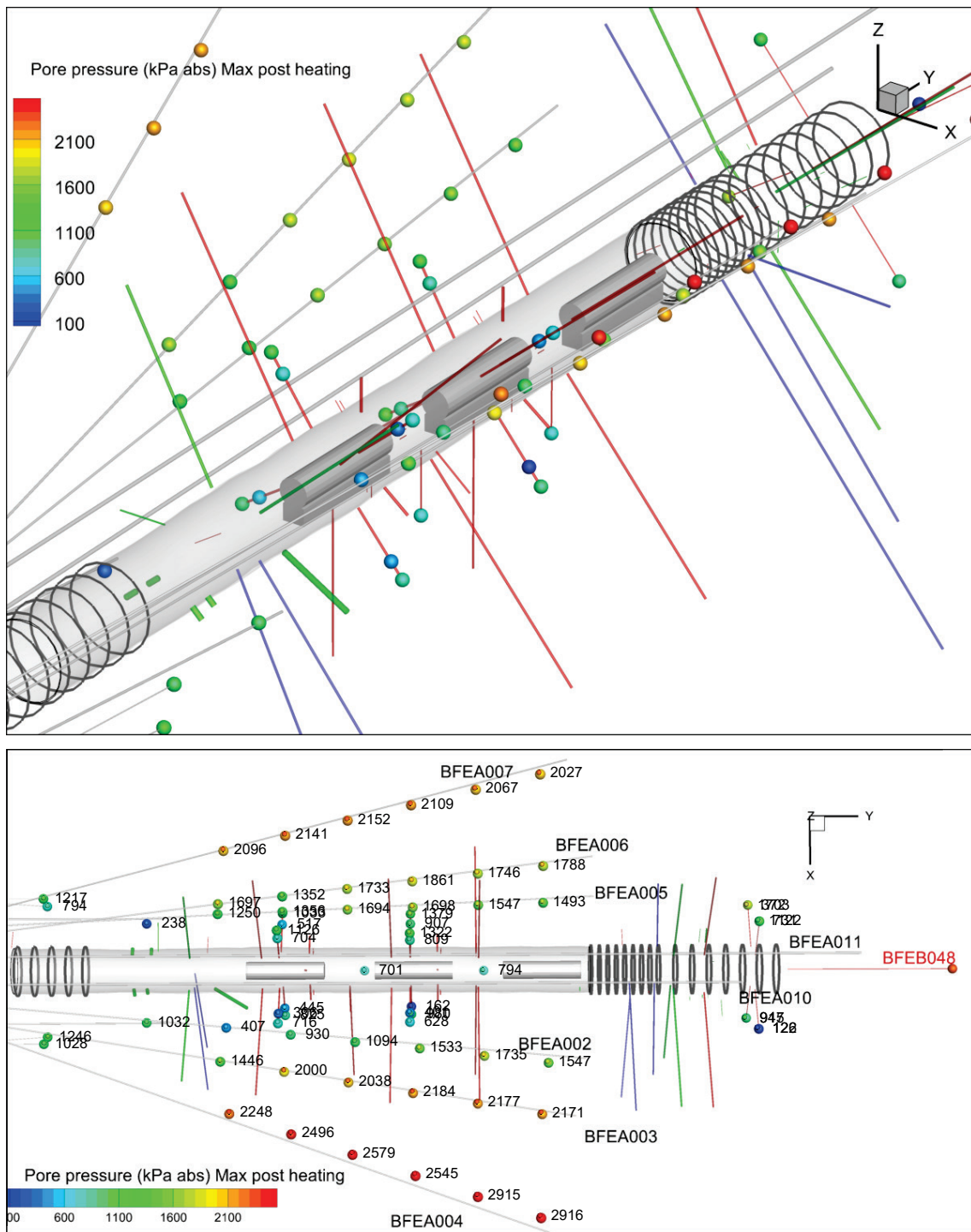


Fig. 119: Maximum post-heating pore pressure  
 a) 3D view. b) Annotaed plan view

## Geosphere deformation response to heating

Heating has influenced the rate and direction of deformations as seen in the inclinometer data (BFEA010, BFEA011) and the extensometers. The response is anisotropic with a clear influence of direction relative to bedding (e.g. see BFEA010 versus BFEA011 responses) and may also indicate greater influence of the observed faulting towards the end of the shotcrete section in BFEA011.

The change in deformation rates is likely be a result of changes in effective stress due to thermal expansion of the rock and the fluid and perhaps an increase in the rate of creep-type processes. It is likely that there has been some fracturing or fracture reactivation in the EDZ due to changes in effective stresses and possibly in saturation (resulting in loss of suction and consequent softening and reduction in apparent strength).

### 5.2.3 Saturation state of the EBS

The saturation state of the EBS is expected to be heterogeneous due to the effects of heating, and variable inflow from the rock (either direct or through the shotcrete). The different measurements (as of 31.08.2019) are summarised in Tab. 27. The RH data is the most extensive set of measurements but conversion to saturation is uncertain and non-linear.

Tab. 27: Summary of saturation related measurements for EBS

	$r < 1 \text{ m}$	$r > 1 \text{ m}$	Comment
Relative humidity sensors	RH 10-30 %	RH 50-100 %	Heterogeneous with possible influence of wetspot see Fig. 45
Volumetric water content		Saturation 40-50 %	Relatively little variation between locations at H2, Gap 2-3 and H3
Thermal conductivity	Saturation 10-20 %	Saturation 20-100 % Mean ~ 50 %	Highest saturation for sensor near known wet spot No regression for sensors in pedestals
Total Pressure cells		Max 0.5 MPa	Indication of wetting at the shotcrete wall
Seismic and GPR	Seismic and GPR cross-hole measurements in the upper part of the tunnel indicate ongoing increasing saturation.		

#### 5.2.4 Saturation of the shotcrete and rock

Shotcrete thickness in radial boreholes varies between 11 and 45 cm with a mean thickness of ~ 22 cm. Ventilation of the FE tunnel will have dried the shotcrete and created partially saturated conditions. Wet spots observed around rock-bolts and other engineered features indicate preferential flow from the geosphere probably influenced by local permeability around the features. These wet spots at the shotcrete wall do not correspond with the wet spots identified during excavation and no wet spots are observed in the ISS section. Ventilation of the tunnel will have locally desaturated the rock in the unlined ISS section and potentially desaturated some rock behind the shotcrete.

Shao et al. (2016) also report water content measurements in radial boreholes:

- BFEC006 in a section with shotcrete. Water content is lower in the first 30 cm of rock but beyond this is close to undisturbed values. There was some seasonal influence especially close to the tunnel wall.
- BFEB050 a section with three layers of shotcrete. Reduced water content (relative to the expected undisturbed levels) is observed from the tunnel wall to 1 m (deepest sensor). Typically, water content drops with time (to about 1.5 years after excavation). The reduction in water content is greatest closest to the tunnel wall but starts to recover after about 0.5 years.

Shao et al. (2016) interpreted the results as indicating a reduction in drying out of the rock in the shotcrete section. In part due to a temporary input of water from the shotcrete but also due to a reduction in the desaturation and EDZ extension.

The observed pressure profile around the tunnel prior to heating suggests a low pressure zone extending to ~ 3 m radius of the tunnel axis (i.e. 1 – 1.5 m in thickness) as shown in Fig. 56. It is not possible to say whether the extent of this zone has reduced during heating. This is consistent with the uncertainty in the extent of the saturated region of suction (Zone B, Garitte 2013) identified in the scoping calculations (estimated at ~ 1 – 2m).

In the shotcrete section RH measurements suggest that there may still be regions of partial saturation while locally saturated regions will exist around preferential flow-paths for drainage from the rock (e.g. poorly sealed rock bolts). While the pore pressure gradient in the rock has increased during heating flow from the Opalinus will still be small (see subsequent sections).

These observations are again consistent with those from the HE-E experiment where a low-pressure zone extends ~ 2 m from the VE micro-tunnel. The thickness of the zone may relate to the previous ventilation experiment in the tunnel and typically low pore pressure around the micro-tunnel (probably related to the presence of other excavations). The extent of the low-pressure zone has not changed significantly in the 6-year period since the start of heating.

Tab. 28: Summary of observations related to rock saturation

Measurement	Observations
Water content	Shao et al. (2016) show ongoing reduction in water content behind the shotcrete with a seasonal response observed in the unlined section during the ventilation period.
Relative humidity	Measurements in radial boreholes show initial RH ~ 100 % but some sensors have shown a reduction in RH since the start of heating to 80 – 90 %  Measurements in BFEB036,37 in Gap 0 (ISS) indicate partially saturated conditions with RH ~ 90 % at
Pore pressure	Pore pressures around the tunnel prior to heating up to ~ 3 m from the tunnel axis are low indicating either partial saturation, saturation but with water under tension or high hydraulic conductivity.  Pore pressure responses to heating are small or non-existent close to the tunnel in a manner consistent with the measured pore pressure.

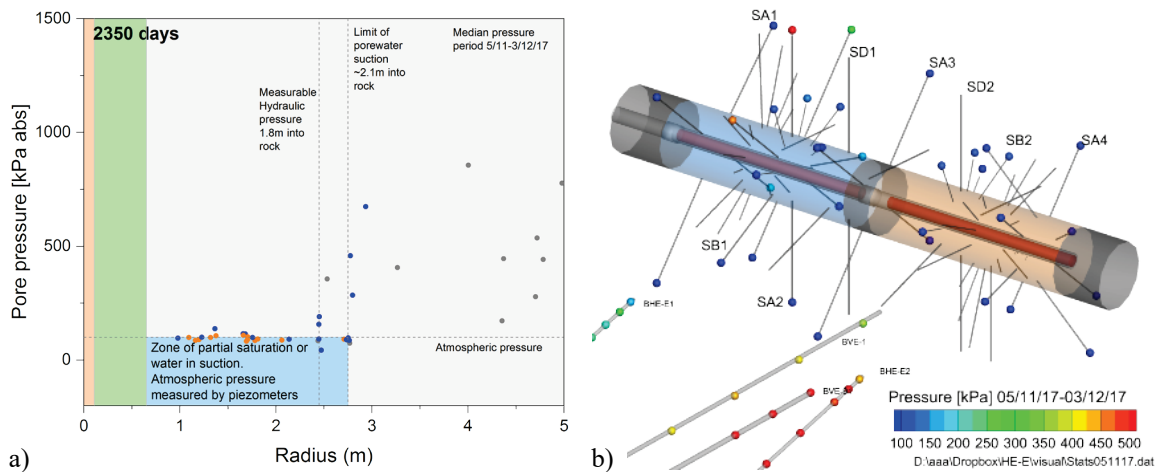


Fig. 120: Distribution of measured pore pressure around VE micro-tunnel in HE-E experiment after 2'350 days of heating

a) With radial distance. b) 3D view

### 5.3 Significant THM Processes during early evolution

#### 5.3.1 THM processes and couplings in the EBS

The main processes and couplings that occur within a bentonite buffer in the early heating period were established within the FEBEX project and related studies since the late 1990s. Although the work at that time focussed on the behaviour of compacted bentonite blocks the processes identified seem to capture much of the TH behaviour observed in FE. The dominant processes associated with moisture redistribution as summarised by Gens (2003) for FEBEX are shown in Fig. 121. The various TH exchange processes are summarised for a heater section and ISS section in Fig. 122.

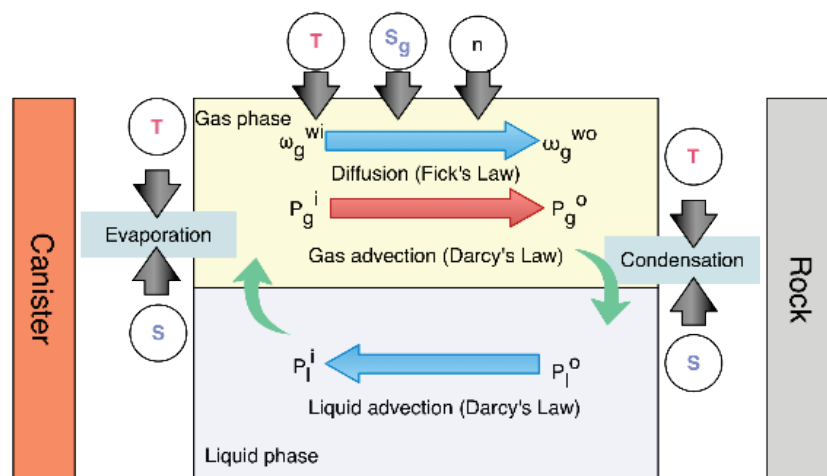


Fig. 121: Schematic of coupled processes associated with moisture redistribution and vapour transport in the buffer  
Gens (2003)

Mechanical process in the EBS during the early heating period appear to be of limited significance. Swelling of the bentonite is slow due to the low overall saturation. At higher saturation some initial pore collapse may proceed the development of swelling and eventual homogenisation of the bentonite (likely to be most significant around the highly compacted bentonite blocks in the pedestals and block walls).

Ongoing anisotropic convergence of the liner and tunnel wall has continued since excavation and support installation. These are affected by heating and changes in the effective stress in the rock which may provide some small additional compaction of the GBM or closure of gaps, while movements of the heaters relate to thermal expansion and drying shrinkage of the pedestals.

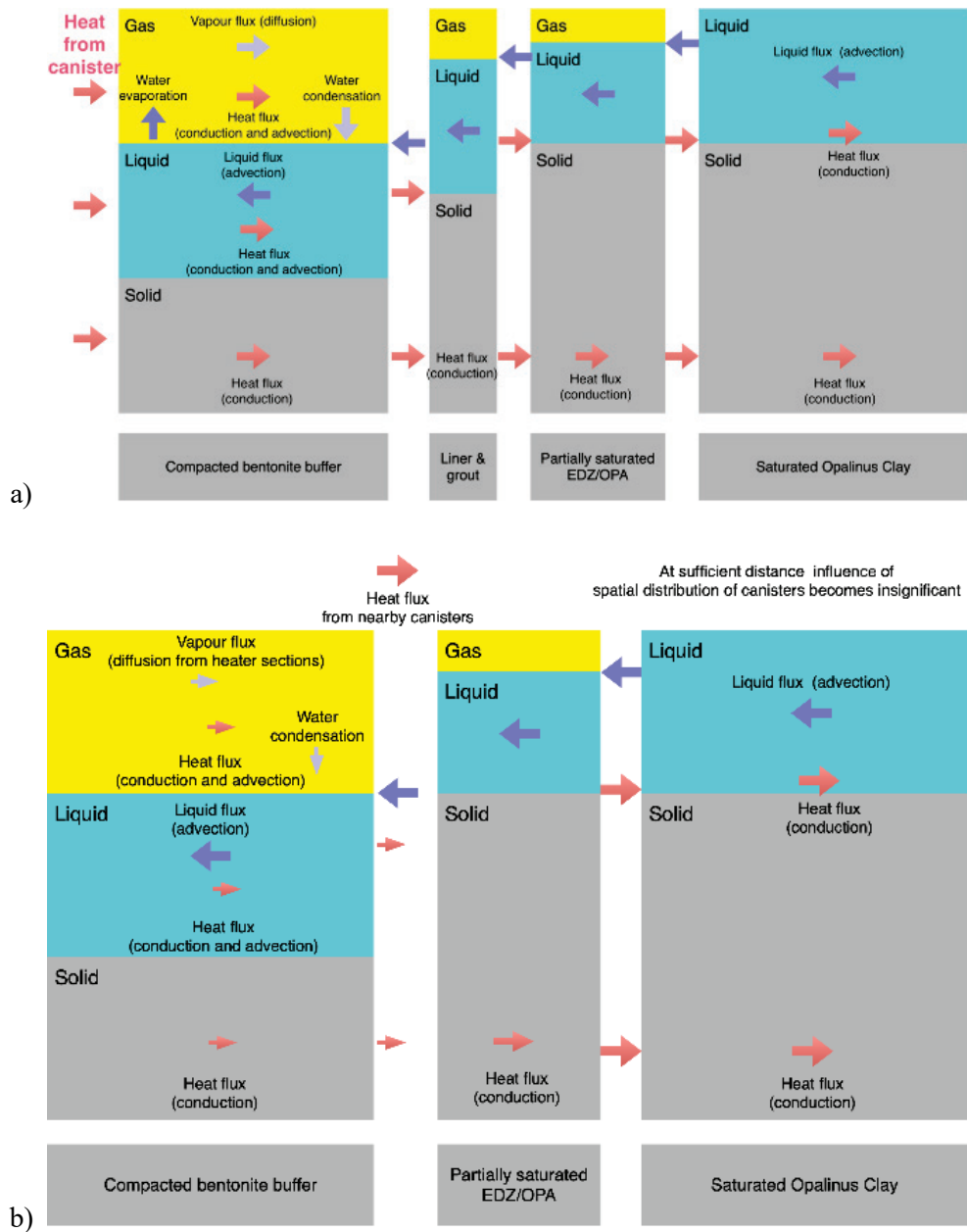


Fig. 122: Schematic of exchange processes in the EBS and rock  
 After Gens (2003). a) Shotcrete heater section. b) ISS section

### 5.3.2 THM processes and couplings in the rock

Again, the main processes and coupling are relatively well known and have been established in numerical codes for some time. Fig. 123 shows the main processes and inter-relationships. The figure is based on the conceptual model behind the CODE\_BRIGHT numerical model (from CODE\_BRIGHT, 2004). But additional swelling and softening mechanisms are relevant to the EDZ creation, development and sealing in the Opalinus Clay.

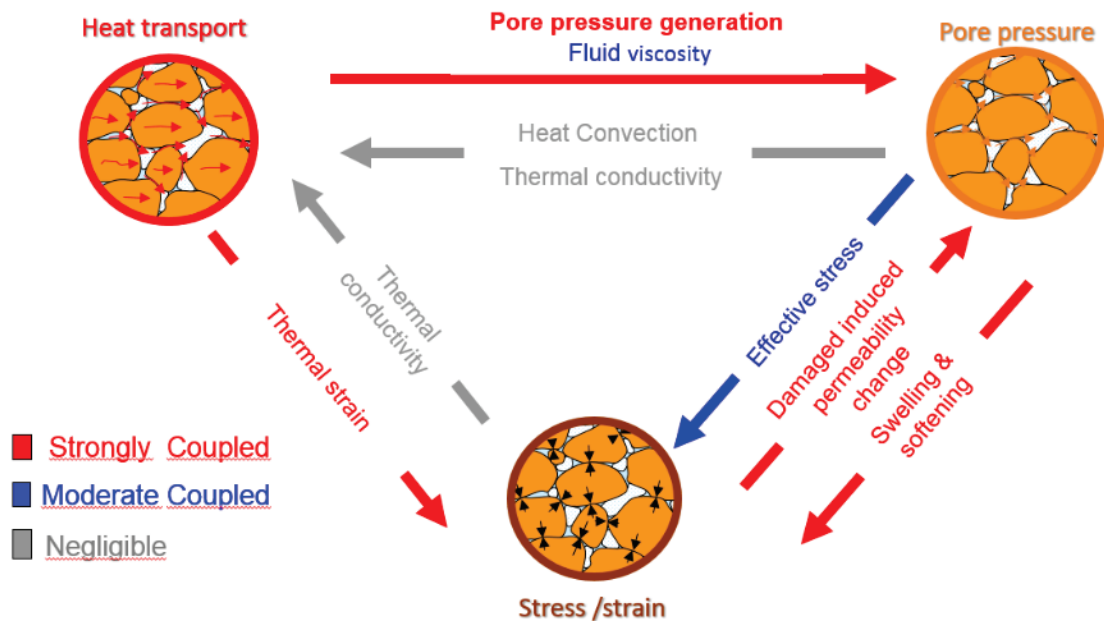


Fig. 123: Schematic of relationships between THM processes in a porous medium  
 After CODE\_BRIGHT 2004, Gens et al. (2007), Armand et al. (2017)

The ongoing response to excavation includes convergence (normal to bedding) and extension (parallel to bedding) and this is most clearly observed in the low temperature arch-supported section (ISS) where the extensometer and inclinometer data indicate ongoing deformations largely unaffected by heating.

In the heater sections there are changes in response at the start of heating with an initial decrease in settlement in BFEA010 and BFEA011 followed by a decrease at later time around H1. The rate of displacements also changes in the boreholes normal to bedding (Fig. 71).

Thermal pressurization due to differential expansion of water and the rock skeleton (Ghabezloo & Sulem, 2009, Delage 2013) dominates the observed pore pressure response after the start of heating. Anisotropy in thermal conductivity is evident in the observed responses. Ongoing drainage to the tunnel is modified by the induced gradients. At FE the observed pore pressure changes are, as yet, relatively small < 1 MPa (Fig. 58). In part this is due to low pressure close to the tunnel and potential drainage to the tunnel.

In addition, induced changes in total and effective stress may result in reactivation or development of the EDZ. There is evidence in the observed interval and packer pressures for minor reactivation

of the EDZ. Resulting pore pressures changes are small <100kPa indicating small changes in volume (high stiffness of the monitoring systems).

Ongoing self-sealing in the EDZ is also likely to be occurring and may have been promoted by heating (increase in water mobility and creep rates). However, no specific measurements (e.g. repeat hydrotesting) have as yet been performed to identify this.

## 5.4 Exchanges between EBS and geosphere

### Water

Within the buffer, water is redistributed due to drying and evaporation near the heater and cooling near the rock wall. This creates a zone of higher saturation at the shotcrete. Transfer of water from the geosphere to the shotcrete and thence to the EBS is driven by the pressure gradients in the rock that are modified by thermally induced pressure rise. The low permeability of the intact Opalinus Clay limits the water flow.

Measurements of permeability at the 10m scale from the VE tunnel suggest an average hydraulic conductivity of  $2 \times 10^{-13}$  m/s (Mayor et al. 2007 and Gautschi 2017) for an interval including several small faults oriented normal to the local bedding strike. At FE the tunnel is oriented along bedding strike such that flow occurs both parallel and perpendicular to bedding, but the rock appears to be more tectonically disturbed with significant faulting being observed in the lower part of the FE tunnel. It may therefore be appropriate to consider a higher hydraulic conductivity for the rock of  $2 \times 10^{-12}$  m/s. Hydrotesting in the tunnel nearfield (Rösli et al. 2016) measured 8 intervals in the range  $1 - 2.3 \times 10^{-12}$  m/s and 2 intervals of higher hydraulic conductivity potentially related to the EDZ around the tunnel.

Assuming pseudo steady state flow, the inflow to a section of the low pressure zone around the FE tunnel can be calculated from the observed radial pressure profile from the Thiem equation.

$$Q = \frac{2\pi LK(h_1 - h_0)}{\ln(r_1/r_0)}$$

Where

- Q is the flow to the low-pressure zone.
- K is the effective (geometric mean) hydraulic conductivity (m/s).
- L is the tunnel section length (m).
- $r_0$  is the inner radius, taken to be 3m where hydraulic head is  $h_0$  (taken as 0 m).
- $r_1$  is the radius of influence of the drawdown where the hydraulic head is undisturbed  $h_1$  (taken as 200 m).

The hydraulic gradient into the tunnel can be estimated from the radial pressure profiles. Fig. 124 shows selected profiles parallel and normal to bedding. The profile is more regular in the parallel to bedding direction which may be due to the greater EDZ extension normal top bedding (and consequent greater pressure heterogeneity). The gradient is higher during heating because of the

thermally induced pore pressures. In addition, hydraulic conductivity will increase (by factor of 50 % from 20 to 40 °C) due to the reduction in water viscosity.

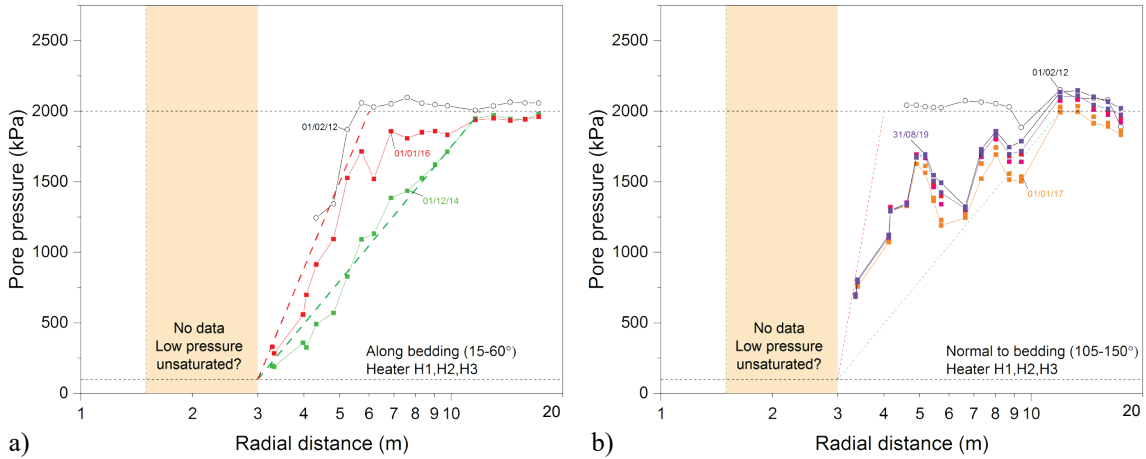


Fig. 124: Radial pressure (log scale) from selected dates together with estimated gradients

a) Parallel to bedding. b) Normal to bedding

Green dashed line indicates gradient prior to heating. Red line indicates gradient during heating.

The estimated flow into 1m of the low pressure zone (assumed to be 3 m radius) is given in Tab. 29. Flow during the heating period is estimated between 64 and 638 ml/day. The approximate water pore volume needed to saturate the EBS (assuming a dry density of 1.49 kg/m<sup>3</sup> and initial water content of 5 %) is 1.4 – 1.6 m<sup>3</sup> per metre of tunnel (dependent on the outer radius and presence of a heater). It should be noted that if the rock is partially saturated much of this flow may go into resaturation of the rock rather than the buffer.

Tab. 29: Estimated flow (ml/day) to 1m of low pressure zone around FE tunnel test section for hydraulic conductivity of  $2 \times 10^{-13}$  and  $2 \times 10^{-12}$  m/s for condition prior to heating and during heating

	$K = 2 \times 10^{-13}$ m/s	$K = 2 \times 10^{-12}$ m/s
Prior to heating $h_l = 200$ m, $r_l = 12$ m	16	157
During heating $h_l = 200$ m, $r_l = 5$ m	64	638
Hydraulic conductivity increase factor 1.5		

These flow rates can be compared with the amount of water available from redistribution of water in the GBM. Assuming an initial gravimetric water content of 5 % and employed dry density of 1.49 g/cm<sup>3</sup> the total water volume within 20 cm of the heater surface is approximately 60 l/m (not accounting for the difference in water content and dry density of the heater pedestal). The drop in RH near the heater together with the rise close to the shotcrete may indicate that a significant fraction of this water has been redistributed to the outer part of the buffer within the first year of heating.

The time for full saturation of the buffer can be estimated from Tab. 29 if we assume that it is largely controlled by the water flow from the Opalinus rather than the buffer properties (see Garitte 2013), but significant uncertainties are associated with:

- the hydraulic conductivity of the Opalinus Clay
- the saturation state of the rock around the tunnel

A discussion of the influence of partial saturation in the rock for the FEBEX experiment can be found in Gens et al. (2009).

The data from the HE-E experiment suggest minimal exchange of water between the rock and the buffer due to the extent of partial saturation in the rock (as influenced by the low pore pressures around the VE micro-tunnel). In FE a more heterogenous pattern has developed<sup>5</sup> with regions of inflow associated with the wet spots in the shotcrete.

## Heat

Heat flow from the EBS to the rock is relatively homogeneous with some influence of the distribution of heaters close to the tunnel wall but a relatively homogeneous increase in temperature even at 5-6 m from the tunnel axis (see Fig. 32) the overall radial distribution of temperature (Fig. 33) is largely controlled by the contrast in thermal conductivity between the EBS and rock and its anisotropy within the geosphere.

Fig. 125 shows a simple 2D isotropic heat conduction model based on homogeneous isotropic properties for the buffer and rock. The model provides a reasonable simulation of the observed temperature evolution at the 3 heater sections shown in the Figure. More complex 2D models might include the anisotropy in the rock mass (Garitte, 2013), while numerical models would be required to provide a detailed simulation of the 3D temperature evolution.

---

<sup>5</sup> This may also be a consequence of the greater instrumentation at FE and consequent ability to identify zones of swelling and change in thermal conductivity that are ascribed to inflow from the rock.

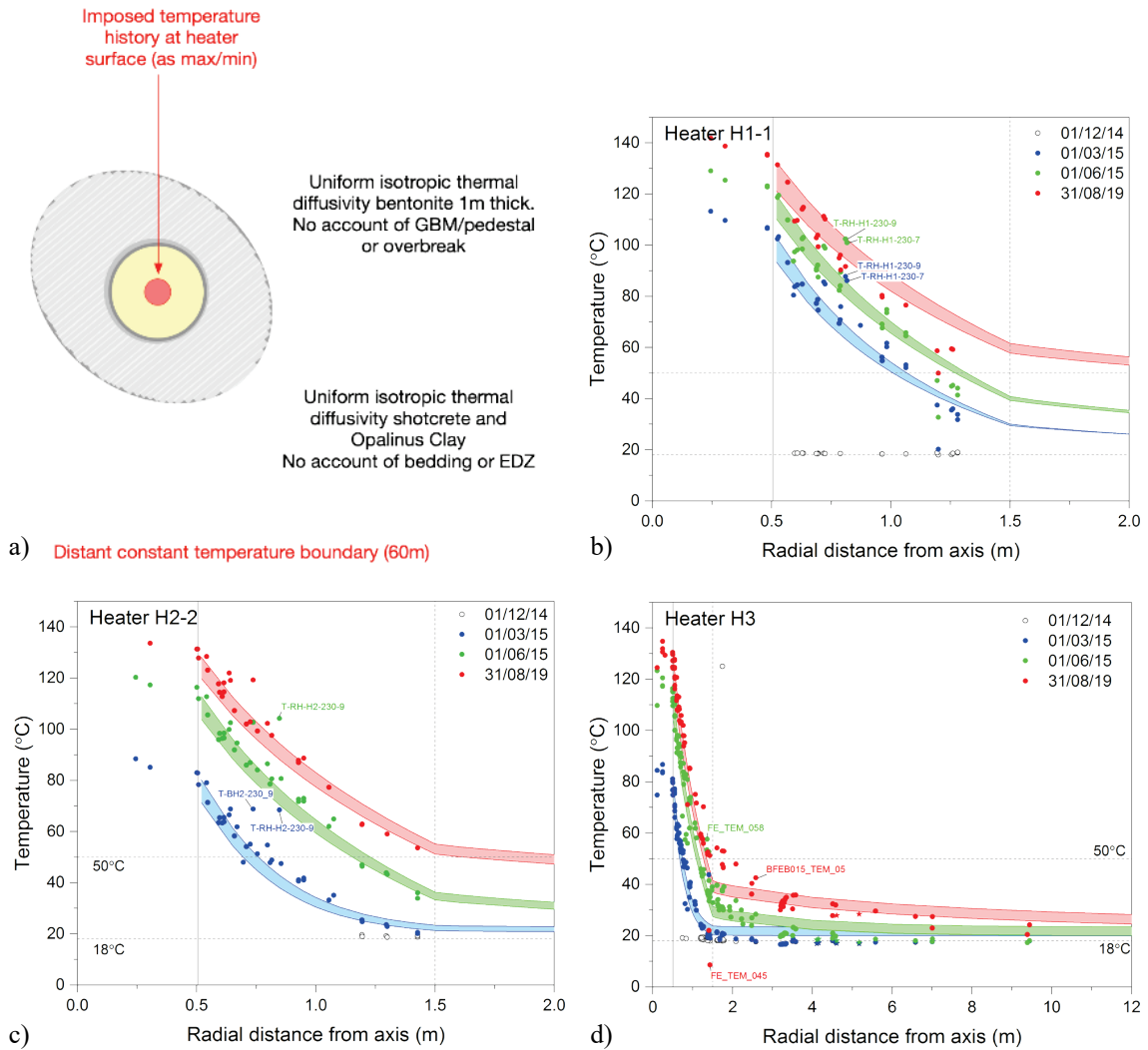


Fig. 125: Simple heat conduction model and computed and measured radial temperature distributions for the 3 heaters

a) Model schematic. b) H1 EBS temperature. c) H2 EBS temperature. d) H3 EBS and geosphere radial temperature distribution.

## 6 Conclusions and recommendations

### 6.1 FE first five years of heating

The overall evolution of the buffer and geosphere is largely as expected based on the extensive laboratory and in situ tests together with design and predictive THM models. The observed response to excavation, emplacement and the first five years of heating are consistent with this understanding in terms of the processes, significant couplings and overall magnitude of effects. The extensive dataset from FE is well-managed and access to the dataset is well supported, although the dataset is now large with over 7 years of data and more than 1'400 sensors.

The results from FE have confirmed:

- Understanding of the main processes and couplings associated with heating and slow saturation of the buffer.
- Understanding of the main processes and couplings associated with heating and resaturation of the EDZ and rock.
- Applicability of calibrated effective thermal and hydraulic properties of the buffer.
- Only small displacements in the rock associated with ongoing trends related to excavation and response to heating.
- No significant movement or deformation of the canister.
- Slow saturation of the EBS largely controlled by the ability of the rock to provide water to the buffer.

Peak thermally-induced pore pressures have already developed within the geosphere close to the tunnel and the thermal disturbance has extended around the tunnel to a significant distance allowing characterisation of the properties parallel and normal to bedding together with any influence of the EDZ.

While simple scoping models of the FE can provide the envelope for performance more detailed interpretation and modelling is complicated by the multiple sources of heterogeneity and anisotropy as listed in Tab. 30. Detailed predictions of the FE Experiment responses are likely to require a coupled 3D models incorporating anisotropy and heterogeneous properties. Validation of such models will require careful management of associated uncertainties and well-defined validation criteria addressing any expected conservatism in the model<sup>6</sup>.

As part of Nagra's FE Modelling Task Force several 3D THM models have been developed. The models incorporate material anisotropy and heterogeneity to some extent and first results are presented in Alcolea et al. (2019). The models will be used to make predictions of the evolution of the FE experiment.

---

<sup>6</sup> It may be considerably easier to validate models that provide conservative estimates of key parameters (e.g. thermally induced pore pressure) than models that seek to make detailed predictions of performance.

Tab. 30: FE Sources of heterogeneity and anisotropy

Type	Heterogeneity	Influence
Buffer/EBS	GBM density Heaters and pedestals	Variability in thermal conductivity and eventual swelling pressure
	Instrumentation	Local variation in GBM dry density and thermal properties.
Support	Shotcrete	Influence of water and local variations in stiffness and cracking
	Rock bolts	Preferential drainage of rock (association with wet spots)
	Steel sets	Localised support limiting deformation to the gaps between the sets
Geosphere	Bedding and fault related anisotropy	Anisotropy in thermal, hydraulic and mechanical properties
	Stress anisotropy	Influence on EDZ
	EDZ	Created by interaction of excavation method, support, stress redistribution, rock properties and structures, creating strong local heterogeneity in tunnel nearfield.
	Wetspots	Localised wetting of buffer (see interaction with rock bolts)

### **Influence of excavation of Gallery 18 (Ga18)**

The excavation has provided information about the response of the tunnel to nearby (~ 70 m) excavations. Only minor changes (see LVDT measurements) occurred within the EBS and these probably relate to deformation of the rock.

In the rock there was evidence of increased stress and pore pressures. Pressure increases were <100 kPa and were essentially undrained due to the large volume of rock influenced by the excavation. There is some possible reactivation of EDZ fractures due to the changes in stress and pore pressure with pressure monitoring intervals showing transient hydraulic behaviour indicating volume/permeability change since Ga18 excavation. Responses seen in the BMB boreholes in the FEA Niche show the influence of changes in ventilation (e.g. installation of dust doors) and warming of the tunnel environment due to the excavation as well as the influence of the excavation itself.

## **6.2 Early evolution of an emplacement drift**

Although the FE aims to be a 1:1 demonstration of the planned disposal system there are inevitable differences in the systems that impact the early evolution: These differences largely result from the boundary conditions associated with performing experiments at Mont Terri and the requirement to instrument the buffer and geosphere to observe the system behaviour.

The use of a shotcrete liner and extensive bolting rather than a pre-formed liner probably resulted in greater convergence and unloading of the rock prior to emplacement than might occur in a deep repository excavated by TBM. Because of experimental requirements related to characterisation,

planning and implementation of the instrumentation and emplacement the FE tunnel was open and ventilated for over two years prior to closure. This may have resulted in a larger zone of desaturation of the rock particularly in the ISS section.

These differences largely affect the early evolution of the geosphere as the buffer will be emplaced under quality control<sup>7</sup> and there is only limited interaction between the geosphere and EBS during this period due to the low permeability of the Opalinus Clay. The increased desaturation due to ventilation and greater convergence probably resulted in a greater zone of low saturation and pressure which will lead to smaller thermally induced pore pressure changes. This in turn may limit the extent of any reactivation or development of the EDZ due to thermal pressurisation.

Other differences relate to the structural context, rock mechanical properties and state variables (stress and pore pressure) between Mont Terri and potential repository sites.

Much of the uncertainty in the early evolution of the disposal system and near-field geosphere relates to the time taken to saturate the rock and EBS. This will be a function of

- the extent of rock desaturation prior to emplacement caused by initial unloading and subsequent ventilation and convergence during the open tunnel period.
- the mass of water required to saturate the EBS which is a function of the as-emplaced dry density and water content.
- the ability of the host rock to provide water, which is a function of the (anisotropic) permeability and storage properties and the pore pressures around the emplacement tunnel.

The results from the FE Experiment provide:

- Confirmation that descriptions of the major THM processes and couplings identified in previous studies are relevant to a full-scale system.
- Confidence in effective parameters derived from laboratory and smaller scale tests.
- Dataset for validation of THM models and further calibration of effective properties.

The contribution of the FE Experiment to understanding of gas phase evolution is discussed in Giroud et al. (2018).

The observed response to Ga18 may be a useful guide to the expected interactions between emplacement tunnels as shown in Fig. 126.

---

<sup>7</sup> There may of course be some influence of the instrumentation, but this has hopefully been minimised by careful design of the experiment.

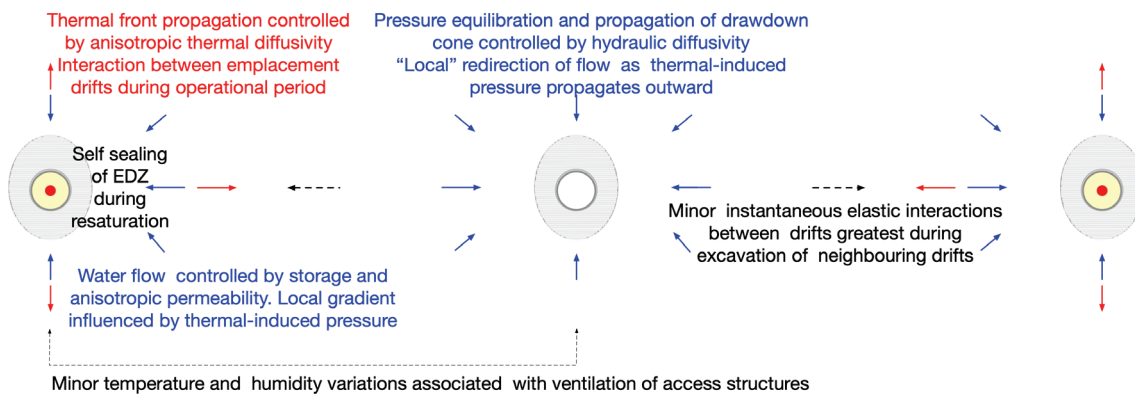


Fig. 126: Interactions between emplacement tunnels in a deep SF/HLW repository

### 6.3 Remaining uncertainties

There is limited knowledge of the hydraulic conditions (pore pressure, saturation and EDZ extent) in the rock immediately around the excavation in the potentially partially saturated zone (thickness  $\sim 1\text{-}2$  m). This zone is likely to be heterogeneous but will also influence the flow from the rock to the buffer. At present the observed pore pressure distribution and expected hydraulic conductivity can be used to estimate the flow to this zone but the extent of any partially saturated pore volumes in this zone and the fraction of the water flowing into this zone that then flows into the tunnel are poorly known. Permeability in the EDZ is also likely to have evolved during the initial heating period with ongoing resaturation (self-sealing) and possible reactivation of EDZ fractures due to stress and pore pressure change.

The dataset of field observations of saturation-related measurements from multiple sensor types shows a qualitatively consistent pattern of saturation but the different measurement require integration to derive a better quantitative estimate of the buffer saturation. This can then be combined with as-built estimates of the water volumes needed for buffer saturation and the potential rate of inflow to the tunnel.

Monitoring of the thermal front is limited to  $\sim 20\text{m}$  from the tunnel axials the front extends consideration could be given to additional far field monitoring of pore pressure and temperature.

The pressure responses to Ga18 excavation demonstrate measurable poro-elastic responses over large distances  $\sim 15$  excavation diameters. At FE these indicate a long-lasting compression of the rock and consequent pore-pressure rise that is likely to be diagnostic of large-scale rock anisotropy (Wild et al. 2015). Observations from previous excavations (see Appendix H) show both positive and negative pressure responses supporting the view that these are essentially poro-elastic response to the opening of the excavation. Further work is needed to integrate these and other responses to Ga 18 excavation (e.g. the MB-A experiment, see Galletti & Jaeggi 2019) and test the ability of models to reproduce the observed pattern of pressure responses.

### 6.4 Recommendations for further work

This report is part of the wider effort to monitor, interpret and model the evolution of the FE Experiment. Regular data trend reports provide updated sensor-by-sensor documentation of the data and on-site activities (Firat Lüthi 2018,2019).

Work within the FE Modelling Task Force is currently focussed on validation of coupled models using the FE dataset (Alcolea et al. 2019) while further interpretation work will include integration of additional monitoring datasets (e.g. distributed temperature measurements<sup>8</sup>) and geophysical measurement campaigns together with updating of the current interpretation on the basis of newly acquired data.

The ongoing slow saturation of the buffer and thermal transient are not expected to show significant changes in the next few years and the main focus of interpretation work is likely to be on:

- Confirming the expected evolution.
- Making quantitative estimates of the effective thermal and hydraulic properties of the buffer and host rock.

At some point the extent of self-sealing in the EDZ can be characterised by performing repeat hydraulic tests in the nearfield monitoring intervals once the response to thermal pressurisation has been characterised.

An integrated approach to developing understanding of the observed interactions with Ga18 is planned. The approach includes:

- Characterisation of the induced changes in stress, pore pressure, deformation, temperature and humidity across the laboratory during Ga18 excavation.
- Development of a lab-scale understanding of the response to excavation.
- Identification of relevant processes and scoping of magnitudes of induced changes.
- Comparison with observed responses from previous excavations at Mont Terri and from other URLs.

---

<sup>8</sup> Additional measurements from the fibre optic systems at the tunnel wall are expected to be largely consistent with the interpretations given here but have yet to be integrated into the interpretation and may provide further information on thermal and mechanical processes.



## 7 References

- Alcolea, A., Firat Lüthi, B. & Garitte, B. (2019): Tunnelwall deformation at FE experiment between January 2018 - April 2019: Analysis of extensometer and LVDT sensor data. Nagra Arbeitsbericht NAB in Vorbereitung.
- Alcolea, A., Marschall, P., Puig Damians, I., Olivella, S., Gens, A., Madaschi, A., Bosch, J., Laloui, L., Shao, H., Wang, W., Kolditz, O., Nagel, T. (2019): FE-Modelling Task Force / Task 1: Validation of thermally induced THM effects in the rock around the FE-tunnel Subtask 1.1: Code and Calculation Verification, Subtask 1.2: Back-analyses. Nagra Arbeitsbericht NAB 19-40.
- Armand, G., Bumbieler, F., Conil, N., de la Vaissière, R., Bosgiraud, J.M. & Vu, M.N. (2017): Main outcomes from in situ thermo-hydro-mechanical experiments programme to demonstrate feasibility of radioactive high-level waste disposal in the Callovo-Oxfordian claystone. *Journal of Rock Mechanics and Geotechnical Engineering*, 9(3), 415-427. <https://doi.org/10.1016/j.jrmge.2017.03.004>.
- Becker, J. & Vogt, T. (2019): WS-I Experiment: Investigation of wet spots. Mont Terri Project Report TR 2012-19.
- Brady B.H.G. & Brown E.T. (1993): *Rock Mechanics for underground mining*. Chapman & Hall London 2nd Edition
- Chen, G.J., Sillen, X., Verstricht, J. & Li, X.L. (2011): ATLAS III in situ heating test in Boom Caly: Field data, observation and interpretation. *Computers and Geotechnics*, 38(5), 683–696. doi:10.1016/j.compgeo.2011.04.001.
- Clauer, N., Techer, I., Nussbaum, C. & Laurich, B. (2017): Geochemical signature of paleofluids in microstructures from Main Fault in the Opalinus Clay of the Mont Terri rock laboratory, Switzerland. *Swiss Journal of Geosciences*, 110(1), 105-128. <https://doi.org/10.1007/s00015-016-0253-0>.
- Delage, P. (2013): On the thermal impact on the excavation damaged zone around deep radioactive waste disposal. *Journal of Rock Mechanics and Geotechnical Engineering*, 5(3), 179–190. <https://doi.org/10.1016/j.jrmge.2013.04.002>.
- Eiholzer, L. (2012): FE-C experiment: Geodetic 3D convergence measurements during the excavation of FE Gallery. Mont Terri Technical Note TN 2012-88.
- Firat Lüthi, B. (2018): Full-Scale Emplacement (FE) Experiment – Data Trend Report. Data from excavation and during 3 first years of heating 01.01.2012 – 31.08.2018. Nagra Arbeitsbericht NAB 18-39.
- Firat Lüthi, B. (2019): Full-Scale Emplacement (FE) Experiment – Data Trend Report. Data from excavation and during 3 first years of heating 01.07.2018 – 31.08.2019. Nagra Arbeitsbericht NAB 19-42.
- Galleti, M. & Jaeggi, D. (2019): MB-A Experiment: Sensor responses caused by excavation activity in MB-A section and Ga18. Mont Terri Technical Note TN 2019-79.

- Garitte, B. (2013): Updated scoping computations for the FE experiment. Nagra Arbeitsbericht NAB 13-99.
- Gaus I. (Ed.) (2011): Long term Performance of Engineered Barrier Systems (PEBS): Mont Terri HE-E experiment: detailed design. Nagra-Arbeitsbericht NAB 11-01.
- Gaus, I., Garitte, B., Senger, R., Gens, A., Vasconcelos, R., Garcia-Sineriz, J.-L., Trick, T., Wieczorek, K., Czaikowski, O., Schuster, K., Mayor, J.C., Velasco, M., Kuhlmann, U. & Villar, M.V. (2014): The HE-E Experiment: Lay-out, Interpretation and THM Modelling Combining D2.2-11: Final Report on the HE-E Experiment and D3.2-2: Modelling and Interpretation of the HE-E Experiment of the PEBS Project. Nagra Arbeitsbericht NAB 14-53 and EU PEBS Project report downloadable from <http://www.pebs-eu.de/>.
- Gautschi, A. (2017): Safety-relevant hydrogeological properties of the claystone barrier of a Swiss radioactive waste repository: An evaluation using multiple lines of evidence, Grundwasser. doi: 10.1007/s00767-017-0364-1.
- Gens, A. (2003): The role of Geotechnical Engineering for nuclear energy utilization. Vanicek et al., editors. Proceedings of the XIII ECSMGE (Prague), Special Lecture 2, vol. 3, Prague, 2003. p. 25-67.
- Gens, A., Sanchez, M., Guimarães, L.D.N., Alonso, E.E., Lloret, A., Olivella, S., Villar, M.V. & Huertas, F. (2009). A full-scale in situ heating test for high-level nuclear waste disposal: observations, analysis and interpretation, (4), 377-399. <https://doi.org/10.1680/geot.2009.59.4.377>
- Gens, A., Vaunat, J., Garitte, B. & Wileveau, Y. (2007): In situ behaviour of a stiff layered clay subject to thermal loading: Observations and interpretation. *Geotechnique*, 57(2), 207-228.
- Ghabezloo, S. & Sulem, J. (2009): Stress dependent thermal pressurization of a fluid-saturated rock. *Rock Mechanics and Rock Engineering*, 42(1), 1-24.
- Giroud, N., Tomonaga, Y., Wersin, P., Briggs, S., King, F., Vogt, T. & Diomidis, N. (2018). On the fate of oxygen in a spent fuel emplacement drift in Opalinus Clay. *Applied geochemistry*, 97, pp.270-278.
- Göbel, I., Alheid, H.-J., Alonso, E., Ammon, Ch., Bossart, P., Bühler, Ch., Emmerich, K., Fernandez, A.M., García-Siñeriz, J.L., Graf, A., Jockwer, N., Kaufhold, St., Kech, M., Klubertanz, G., Lloret, A., Mayor, J.C., Meyer, T., Mieke, R., Muñoz, J.J., Naumann, M., Nussbaum, Ch., Pletsch, Th., Plischke, I., Ploetze, M., Rey, M., Schnier, H., Schuster, K., Sprado, K., Trick, Th., Weber, H., Wieczorek, K. & Zingg A. (2007): Heater Experiment: Rock and bentonite thermohydro-mechanical (THM) processes in the near field of a thermal source for development of deep underground high level radioactive waste repositories.- Mont Terri Project – Heater experiment, engineered barrier emplacement and ventilation experiment, eds. P. Bossart and C. Nussbaum. Reports of the Swiss Geological Survey 1. Swisstopo, Wabern, 7-114.
- Jaeggi, D., Galletti, M., Amacher, F., Dunst, R., Nussbaum, C., Raselli, R., Ringeisen, M., Schefer, S. & Bossart, P. (2018): Gallery 2018: Excavation and geological documentation. Mont Terri Technical Note TN 2018-04.

- Jaeggi, D., Lisjak, A., Gisiger, J. & Becker, J. (2012): FE-C Experiment: Engineering part of full-scale emplacement experiment Geological and structural mapping of the FE-tunnel including a photogrammetric method. Mont Terri Technical Note TN12-82.
- Jaeggi, D., Müller, P., Dolder, F. & Nussbaum, C. (2012): FE-A Experiment: Site preparation for Full-Scale Emplacement Demonstration Experiment Geological and structural mapping of the FE-A niche (start niche). Mont Terri Technical Note TN11-19.
- Kirsch, G. (1898): Die Theorie der Elastizität und die Bedürfnisse der Festigkeitslehre. *Veit. Ver Deut. Ing.* 42 (28), 797-807.
- Kober, F., Lanyon, G.W., Sakaki, T. & HE-E consortia (2018): HE-E heater experiment: first 2400 days of heating. Poster at Mont Terri Annual Meeting FM #36.
- Lanyon, G.W. (2019a): Update of synopsis regarding EDZ development and evolution at the Mont Terri Rock Laboratory. Nagra Arbeitsbericht NAB 18-45.
- Lanyon, G.W. (2019b): Current understanding of self-sealing of clay-rich rocks for deep geological disposal. Nagra Arbeitsbericht NAB 18-46.
- Lanyon, G.W., Martin, C. D., Giger, S. & Marschall, P. (2014): Development and evolution of the Excavation Damaged Zone (EDZ) in the Opalinus Clay – A synopsis of the state of knowledge from Mont Terri. Nagra Arbeitsbericht NAB 14-87.
- Lisjak, A., Garitte, B., Grasselli, G., Müller, H.R. & Vietor, T. (2015): The excavation of a circular tunnel in a bedded argillaceous rock (Opalinus Clay): Short-term rock mass response and FDEM numerical analysis. *Tunnelling and Underground Space Technology*, 45, 227-248.
- Martin, C.D. & Lanyon, G.W. (2003): EDZ in clay shale: Mont Terri. Mont Terri Techn. Rep.2001, 1. With contributions from P. Bossart and P. Blümling.
- Martin, C.D., Maciotta, R., Elwood, D., Lan, H. & Vietor, T. (2015): Evaluation of the Mont Terri Mine-By response: Mont Terri Technical Report TR 2009-02.
- Maurer, H.R. & Spillmann, T. (2018): FE-M:Draft Report on Geophysical monitoring in the FE Experiment. Nagra Arbeitsbericht NAB in Vorbereitung.
- Maurer, H.R. & Spillmann, T. (2019): FE-M Experiment: Ground-penetrating-radar (GPR) and seismic monitoring measurements at the Mont Terri FE experiment - results after Phase 24. Mont Terri Technical Note TN 2019-74.
- Mayor, J.C., García-Siñeriz, J.L., Velasco, M., Gómez- Hernández, J., Lloret, A., Matray, J.-M., Coste, F., Giraud, A., Rothfuchs, T., Marshall, P., Roesli, U. & Mayer, G. (2007): Ventilation Experiment in Opalinus Clay for the disposal of radioactive waste in underground repositories. - In: Bossart, P. & Nussbaum, C. (Eds.): Mont Terri Project – Heater Experiment, Engineered Barrier Emplacement and Ventilation Experiment (p.182-240). - Rep. Swiss Geol. Surv. 1.

- Mazurek, M., Gautschi, A., Marschall, P., Vigneron, G., Lebon, P. & Delay, J. (2008): Transferability of geoscientific information from various sources (study sites, underground rock laboratories, natural analogues) to support safety cases for radioactive waste repositories in argillaceous formations. *Physics and Chemistry of the Earth, Parts A/B/C*, 33, S95-S105. <https://doi.org/10.1016/j.pce.2008.10.046>.
- Müller, H.R., Garitte, B., Vogt, T., Köhler, S., Sakaki, T., Weber, H. & Vietor, T. (2017): Implementation of the full-scale emplacement (FE) experiment at the Mont Terri rock laboratory. *Swiss Journal of Geosciences*, 110(1), 287–306. <https://doi.org/10.1007/s00015-016-0251-2>.
- Nagra (2019): Implementation of the Full-scale Emplacement Experiment in Mont Terri: Design, Construction and Preliminary Results. Nagra Technical Report NTB 15-02.
- Rizzi M., Seiphoori A., Ferrari A., Ceresetti D., Laloui L. & Marschall P. (2012). Analysis of the Behaviour of the Granular MX-80 bentonite in THM-processes. In preparation. Rösli U., Gisiger, J. & Kontar, K. (2016): FE-B Experiment: Hydraulic testing of EDZ and far field around heater 2. Mont Terri Technical Note TN 2014-64.
- Seiphoori, A. (2015): Thermo-hydro-mechanical characterisation and modelling of MX-80 granular bentonite. Nagra Technical Report NTB 15-05.
- Senger, R. (2015): Scoping Calculations in Support of the Design of the Full-Scale Emplacement Experiment at the Mont Terri URL, Evaluation of the Effects and Gas Transport Phenomena. Nagra Arbeitsbericht NAB 13-98.
- Shao, H., Paul, B., Wang, X., Hesser, J., Becker, J., Garitte, B. & Müller, H. (2016): The influence of different supports on the properties of the excavation damaged zone along the FE tunnel in the Mont Terri Underground Rock Laboratory. *Geological Society, London, Special Publications*, 443 (October). <https://doi.org/10.1144/SP443.19>.
- Spillmann, T., Maurer, H.R., Plenkers, K., Montesinos, K., Herrich, M. & Ammann, F. (2018): Geophysical measurements in the FE bentonite. FE-M Project Meeting, St. Ursanne, 8th February 2018.
- Teodori, S.-P. & Gaus, I. (2011): Long Term performance of Engineered Barrier Systems (PEBS), Mont Terri HE-E Experiment: as-built report. Nagra Arbeitsbericht NAB 11-25.
- Tisato, N. & Marelli, S. (2013): Laboratory measurements of the longitudinal and transverse wave velocities of compacted bentonite as a function of water content, temperature, and confining pressure. *Journal of Geophysical Research: Solid Earth*, 118(7), 3380-3393. <https://doi.org/10.1002/jgrb.50252>.
- Trick, T., Gräfe, K. & Rösli, U. (2014): FE Experiment: Data Trend Report 2013 for Multi-Packer-Systems (MPS) installed in BFE-A002, BFE-A003, BFE-A004, BFE-A005, BFE-A006 and BFE-A007. Mont Terri Technical Note TN 2013-110.
- Trick, T., Kontar, K., Rösli, U., Gräfe, K. & Müller, H. (2013): FE-B experiment: Hydraulic testing in borehole BFE-C19. Mont Terri Technical Note TN 2013-100.
- Villar M.V., Martín P.L., Gómez-Espina R., Romero F.J. & Barcala J.M. (2012): THM cells for the HE-E test: setup and first results. PEBS Report D2.2.7a. CIEMAT Technical Report CIEMAT/DMA/2G210/02/2012. Madrid, 34 pp.

- Wieczorek, K., Mieke, R. & Garitte, B. (2011): Measurement of Thermal Parameters of the HE-E Buffer Materials. PEBS Deliverable D2.2-5. Wild, K., Amann, F., & Martin, C. D. (2015). Some fundamental hydro-mechanical processes relevant for understanding the pore pressure response around excavations in low permeable clay rocks. ISRM Congress 2015 Proceedings - 13th International Congress on Rock Mechanics, 10-13 May 2015, Montreal, Canada, (March 2016), Paper 505.
- Yu, L., Weetjens, E., Sillen, X., Vietor, T., Li, X., Delage, P., Labiouse, V. & Charlier, R. (2014): Consequences of the thermal transient on the evolution of the damaged zone around a repository for heat-emitting high-level radioactive waste in a clay formation: A performance assessment perspective. *Rock Mechanics and Rock Engineering*, 47(1), 3-19. <https://doi.org/10.1007/s00603-013-0409-4>.
- Zhang, C.-L., Rothfuchs, T., Jockwer, N., Wieczorek, K., Dittrich, J., Müller, J., Hartwig, L. & Komischke, M. (2007): Thermal Effects on the Opalinus Clay. A Joint Heating Experiment of ANDRA and GRS at the Mont Terri URL (HE-D Project). Final Report. Mont Terri Project Technical Report TR 2007-02 and GRS Report 224, ISBN 3-931995-98-4. [https://www.grs.de/sites/default/files/fue/grs\\_224\\_thermeff\\_clay.pdf](https://www.grs.de/sites/default/files/fue/grs_224_thermeff_clay.pdf).



## Appendix A: Instrumentation

Tab. A-1: Number of sensors used in THM interpretation split by location

Location	Temperature	Relative Humidity	Total Pressure	Displacement	Interval Temperature	Interval Pressure
Niche	2	2	0	0	0	0
Tunnel Entrance	23	3	0	2	0	4
Plug	18	0	5	4	2	2
Retaining wall	1	0	2	3	0	0
Gap GP	46	10	4	1	6	6
Heater 3	136	34	6	16	10	14
Gap 2-3	33	9	3	7	6	7
Heater 2	133	35	6	16	10	14
Gap 1-2	28	6	2	17	6	7
Heater 1	77	21	6	2	6	6
Gap 0 (ISS)	37	10	3	19	0	0
Bentonite Block Wall	21	5	3	8	0	0
Porouse Concrete Backfilling	7	1	0	0	0	8
<b>Total</b>	<b>563</b>	<b>136</b>	<b>40</b>	<b>95</b>	<b>46</b>	<b>70</b>

The EBS instrumentation considered within this study is described in greater detail within Firat Lüthi (2018, 2019).



## Appendix B: Borehole instrumentation

Tab. B-1: BFEA boreholes drilled from FE-A Niche sub-parallel to FE Gallery

<b>Borehole</b>	<b><i>Start section</i></b>	<b><i>End section</i></b>	<b>Instrumentation</b>
BFEA002	<i>Niche</i>	<i>Gap 0 (ISS)</i>	6 intervals: temperature, pressure and packer pressure
BFEA003	<i>Niche</i>	<i>Heater 1</i>	6 intervals: temperature, pressure and packer pressure
BFEA004	<i>Niche</i>	<i>Heater 1</i>	6 intervals: temperature, pressure and packer pressure
BFEA005	<i>Niche</i>	<i>Gap 0 (ISS)</i>	6 intervals: temperature, pressure and packer pressure
BFEA006	<i>Niche</i>	<i>Gap 0 (ISS)</i>	6 intervals: temperature, pressure and packer pressure
BFEA007	<i>Niche</i>	<i>Heater 1</i>	6 intervals: temperature, pressure and packer pressure
BFEA008	<i>Niche</i>	<i>Plug</i>	1 interval: temperature, pressure and packer pressure
BFEA009	<i>Niche</i>	<i>Plug</i>	1 interval: temperature, pressure and packer pressure
BFEA010	<i>Niche</i>	<i>Porous Concrete Backfilling</i>	Inclination 80 sections, 40 temperature sensors
BFEA011	<i>Niche</i>	<i>Rock</i>	Inclination 80 sections, 40 temperature sensors
BFEA012	<i>Tunnel Entrance</i>		1 interval: temperature and pressure
BFEA013	<i>Tunnel Entrance</i>		1 interval: temperature and pressure
BFEA014	<i>Niche</i>	<i>Tunnel Entrance</i>	1 interval: temperature and pressure
BFEA015	<i>Niche</i>	<i>Tunnel Entrance</i>	1 interval: temperature and pressure

Tab. B-2: BFEB boreholes drilled radially out from FE Gallery (except BFEB048)

Borehole	Start section	GM	Length (m)	Instrumentation
BFEB001	Heater 3	20.01	2.85	2 intervals: pressure (x2), temperature and packer pressure
BFEB002	Heater 3	20.11	2.70	2 intervals: pressure (x2), temperature and packer pressure
BFEB003	Heater 3	20.01	2.80	2 intervals: pressure (x2), temperature and packer pressure
BFEB004	Heater 3	20.01	2.89	2 intervals: pressure (x2), temperature and packer pressure
BFEB005	Heater 2	27.70	2.75	2 intervals: pressure (x2), temperature and packer pressure
BFEB006	Heater 2	27.72	2.80	2 intervals: pressure (x2), temperature and packer pressure
BFEB007	Heater 2	27.68	2.76	2 intervals: pressure (x2), temperature and packer pressure
BFEB008	Heater 2	27.72	2.88	2 intervals: pressure (x2), temperature and packer pressure
BFEB009	Heater 3	19.01	8.55	Displacement 4 sections and temperature (x5)
BFEB010	Heater 3	18.98	8.50	Displacement 4 sections and temperature (x5)
BFEB011	Heater 2	26.60	8.55	Displacement 4 sections and temperature (x5)
BFEB012	Heater 2	26.60	8.60	Displacement 4 sections and temperature (x5)
BFEB013	Bentonite Block Wall	45.01	8.54	Displacement 4 sections and temperature (x5)
BFEB014	Bentonite Block Wall	45.00	8.55	Displacement 4 sections and temperature (x5)
BFEB015	Heater 3	20.10	5.33	Temperature (x7)
BFEB016	Heater 2	27.70	5.40	Temperature (x7)
BFEB017	Heater 3	21.60	1.20	Temperature (x6), water content/travel time (x4)
BFEB018	Heater 3	21.72	1.15	Temperature (x7), water content/travel time (x4)
BFEB019	Heater 3	21.68	1.20	Temperature (x7), water content/travel time (x4)
BFEB020	Heater 2	29.32	1.20	Temperature (x7), water content/travel time (x4)
BFEB021	Heater 2	29.31	1.21	Temperature (x7), water content/travel time (x4)
BFEB022	Heater 2	29.29	1.19	Temperature (x7), water content/travel time (x4)
BFEB023	Heater 3	22.01	0.31	Temperature (x2) and relative humidity
BFEB024	Heater 3	22.00	0.41	Temperature (x2) and relative humidity
BFEB025	Heater 3	21.99	0.38	Temperature (x2) and relative humidity
BFEB026	Heater 3	21.99	0.50	Temperature (x2) and relative humidity
BFEB027	Heater 3	22.00	0.31	Temperature (x2) and relative humidity
BFEB028	Heater 3	22.01	0.43	Temperature (x2) and relative humidity
BFEB029	Heater 2	29.50	0.31	Temperature (x2) and relative humidity
BFEB030	Heater 2	29.46	0.42	Temperature and relative humidity
BFEB031	Heater 2	29.48	0.41	Temperature (x2) and relative humidity
BFEB032	Heater 2	29.48	0.46	Temperature and relative humidity
BFEB033	Heater 2	29.52	0.31	Temperature (x2) and relative humidity
BFEB034	Heater 2	29.51	0.41	Temperature and relative humidity

Tab. B-2: Cont.

<b>Borehole</b>	<b>Start section</b>	<b>GM</b>	<b>Length (m)</b>	<b>Instrumentation</b>
BFEB035	Gap 0 (ISS)	41.75	0.20	Temperature (x2) and relative humidity
BFEB036	Gap 0 (ISS)	41.77	0.21	Temperature (x2) and relative humidity
BFEB037	Gap 0 (ISS)	41.73	0.21	Temperature (x2) and relative humidity
BFEB038	Gap 2-3	24.09	8.45	Temperature (x2) and displacement (x4)
BFEB040	Gap 1-2	31.71	8.45	Temperature (x2) and displacement (x4)
BFEB041	Gap 1-2	31.60	8.46	Temperature (x2) and displacement (x4)
BFEB042	Gap 1-2	31.61	8.52	Temperature (x2) and displacement (x4)
BFEB043	Gap 1-2	31.73	8.46	Temperature (x2) and displacement (x4)
BFEB044	Porous Concrete Backfilling	48.03	3.00	Temperature and pressure (x2)
BFEB045	Porous Concrete Backfilling	47.99	3.00	Temperature and pressure (x2)
BFEB046	Porous Concrete Backfilling	47.99	3.00	Temperature and pressure (x2)
BFEB047	Porous Concrete Backfilling	48.01	3.00	Temperature and pressure (x2)
BFEB048	Porous Concrete Backfilling	50.08	10.00	Temperature and pressure (x2)
BFEB049	Tunnel Entrance	4.13	1.18	
BFEB050	Gap GP	15.63	1.18	Water content (x6)
BFEB051	Gap 0 (ISS)	40.31	1.18	Water content (x6)
BFEB052	Gap 2-3	24.08	1.70	Temperature and displacement
BFEB053	Gap 1-2	31.60	1.70	Temperature and displacement
BFEB054	Gap 2-3	24.88	2.48	Temperature and pressure
BFEB055	Gap 1-2	32.09	2.46	Temperature and pressure

Tab. B-3: BFEC boreholes drilled radially out from FE Gallery (except BFEC054)

Borehole	Start Section	GM	Length (m)	Instrumentation
BFEC001	Plug	14.71	6.90	Displacement 4 sections
BFEC002	Plug	14.77	6.80	Displacement 4 sections
BFEC003	Gap 0 (ISS)	43.21	8.75	Displacement 4 sections
BFEC004	Gap 0 (ISS)	43.21	6.93	Displacement 4 sections
BFEC005	Gap 0 (ISS)	43.21	7.40	Displacement 4 sections
BFEC006	Bentonite Block Wall	46.10	1.18	Water content (x6)
BFEC007	Bentonite Block Wall	45.86	1.18	Water content (x6)
BFEC008	Bentonite Block Wall	44.81	1.18	Water content (x6)
BFEC009	Heater 1	37.69	0.30	Suction
BFEC010	Bentonite Block Wall	44.92	0.21	Suction
BFEC011	Bentonite Block Wall	45.25	0.20	Temperature and relative humidity
BFEC012	Bentonite Block Wall	45.01	0.20	Temperature and relative humidity
BFEC013	Gap 0 (ISS)	44.23	0.31	Gravimetric water content
BFEC014	Gap 0 (ISS)	44.26	0.30	Water content
BFEC015	Bentonite Block Wall	45.21	1.17	
BFEC019	Plug	12.87	1.70	Pressure (x5)
BFEC054	Gap GP	16.07	3.20	
BFEC055	Plug	11.27	0.49	
BFEC056	Plug	12.05	0.35	
BFEC057	Plug	11.17	0.48	
BFEC058	Plug	12.29	0.47	

Tab. B-4: BFEE boreholes drilled radially out from FE Gallery

<b>Borehole</b>	<b>Start Section</b>	<b>GM</b>	<b>Length (m)</b>	<b>Instrumentation</b>
BFEE001	Plug	14.86	10.21	
BFEE002	Plug	14.84	10.30	
BFEE004	Gap 0 (ISS)	40.72	5.87	
BFEE005	Gap 0 (ISS)	40.75	14.22	
BFEE007	Gap 0 (ISS)	42.26	9.77	
BFEE008	Gap 0 (ISS)	42.27	6.05	



## Appendix C: FE multi-packer system interval and packer systems

### FE-A borehole completions and hydrotests

The boreholes BFE-A002-7 were drilled from the FE-A Niche prior to excavation and are equipped with multi-packer systems with pore pressure, packer pressure and temperature sensors. The pressure monitoring intervals are 1'950 mm long (Fig. C-1). The intervals contain a central stainless-steel tube with an outer diameter of 60.3 mm. A helical groove of 1 mm depth was cut into the central tube to facilitate proper mixing of the pore water within the measuring sections. Each interval is equipped with two stainless steel lines (OD 4 mm, ID 2.4 mm). A sintered stainless-steel screen with a porosity of 36 % was placed along the entire interval length (OD 70 mm, ID 64 mm) to ensure borehole stability and to avoid clogging of line ports. The temperature probe (PT1000) was mounted inside the central tube without contact with the fluid in the interval. The intervals were saturated with uranine (Na-Fluorescein, C<sub>20</sub>H<sub>10</sub>Na<sub>2</sub>O<sub>5</sub>) doped Pearson water using the 4/2.4 mm stainless steel injection line. Suggested range of properties of the intervals and packer systems are given in Tab. C-1.

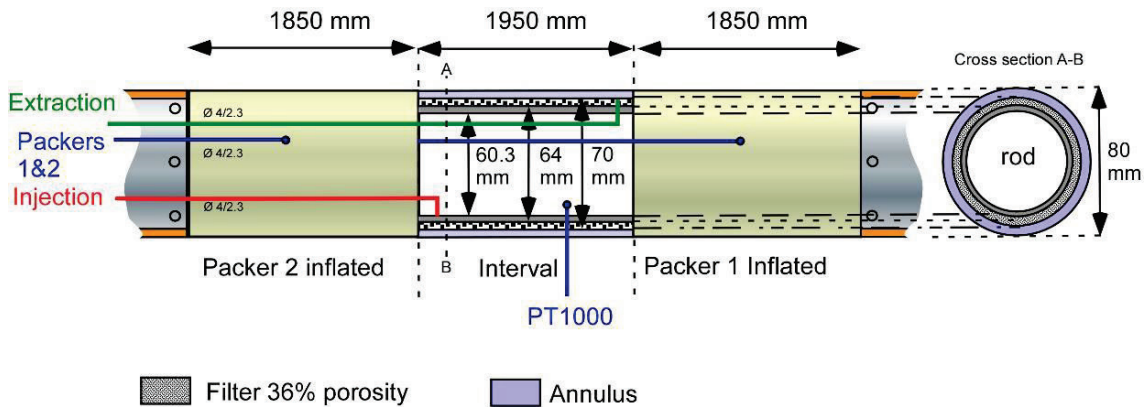


Fig. C-1: FEA multi-packer system interval layout (BFEA002-7)

Tab. C-1: Parameter ranges

Property	Description	Range
Cint Interval compressibility (m <sup>3</sup> /Pa)	Fluid volume and compressibility including lines and surface equipment, compressibility of BDZ (if present) and packer system	1-10 × 10 <sup>-11</sup> Rösli et al. 2016 2-6 × 10 <sup>-11</sup>
Vint	Fluid volume in interval	4'400 ml BFE-A002-7 saturation volume 786 × 5'477 ml
Packer compressibility (m <sup>3</sup> /Pa)	Compressibility of packer materials and fluid volume including any lines	No data found for this

The 6 sliding end packers have a sealing length of 1'850 mm (the packers are fixed at the upper end) and the 7<sup>th</sup> packer for the resin injection section has a sealing length of 500 mm. The outer diameter is 72 mm (deflated). The packer sleeve is manufactured using natural rubber reinforced with steel wires. The metal parts are of stainless steel (1.4301 DIN) and packer working pressure is up to 80 bar in an 80 mm borehole. Each packer was inflated with eosine Y (C20H6Br4Na2O5) doped water using a 4/2.4 mm stainless steel line.

Full scale experiment					Date	19.01.2012	Responsible / version	RA //Vinst																																																			
Borehole	BFE-A11.002	Direction	43.8	Reference point	Borehole head	JOB Nr	1944-2	Location	(M) Term URL																																																		
Borehole Depth	38.420 m	Stickup	0.198 m	Borehole diameter	80.00 mm	Pressure Packer	80 bar	System	MPS																																																		
<small>Note: All depths shown are not corrected for borehole deviation</small>																																																											
<table border="0"> <tr> <td>Packer, inox (42.4 mm)</td> <td>Lines</td> <td>Qty</td> <td>L<sub>used</sub> m</td> <td>L<sub>total</sub> m</td> <td>Depth (m)</td> <td>OD (mm)</td> <td>ID (mm)</td> <td colspan="2">Comments:</td> </tr> <tr> <td>Circulation, inox (42.4 mm)</td> <td></td> <td>1</td> <td>7.12</td> <td>0.712</td> <td></td> <td></td> <td></td> <td></td> <td>Stickup &lt; 0 means out of borehole</td> </tr> <tr> <td>Pressure, inox (42.4 mm)</td> <td></td> <td>0</td> <td>0</td> <td>0.00</td> <td></td> <td></td> <td></td> <td></td> <td>Reference at concrete wall</td> </tr> <tr> <td>Resin inj., polyamid (6/4 mm)</td> <td></td> <td></td> <td></td> <td></td> <td></td> <td></td> <td></td> <td></td> <td></td> </tr> <tr> <td>Resin ext., polyamid (4/2 mm)</td> <td></td> <td></td> <td></td> <td></td> <td></td> <td></td> <td></td> <td></td> <td></td> </tr> </table>										Packer, inox (42.4 mm)	Lines	Qty	L <sub>used</sub> m	L <sub>total</sub> m	Depth (m)	OD (mm)	ID (mm)	Comments:		Circulation, inox (42.4 mm)		1	7.12	0.712					Stickup < 0 means out of borehole	Pressure, inox (42.4 mm)		0	0	0.00					Reference at concrete wall	Resin inj., polyamid (6/4 mm)										Resin ext., polyamid (4/2 mm)									
Packer, inox (42.4 mm)	Lines	Qty	L <sub>used</sub> m	L <sub>total</sub> m	Depth (m)	OD (mm)	ID (mm)	Comments:																																																			
Circulation, inox (42.4 mm)		1	7.12	0.712					Stickup < 0 means out of borehole																																																		
Pressure, inox (42.4 mm)		0	0	0.00					Reference at concrete wall																																																		
Resin inj., polyamid (6/4 mm)																																																											
Resin ext., polyamid (4/2 mm)																																																											
Stickup	0.198 m bgl																																																										
Reference																																																											
RODS																																																											
PACKER 7																																																											
RESIN																																																											
PACKER 6	Pa6																																																										
INTERVAL 6	Q6																																																										
PACKER 5	Pa5																																																										
INTERVAL 5	Q5																																																										
PACKER 4	Pa4																																																										
INTERVAL 4	Q4																																																										
PACKER 3	Pa3																																																										
INTERVAL 3	Q3																																																										
PACKER 2	Pa2																																																										
INTERVAL 2	Q2																																																										
PACKER 1	Pa1																																																										
INTERVAL 1	Q1																																																										
End cap																																																											
End Borehole																																																											

Qty	L <sub>used</sub> m	L <sub>total</sub> m	Depth (m)	OD (mm)	ID (mm)	Comments
<b>VOLUMES measured:</b>						
Filter inner tube OD: 64 mm						
1	7.12	0.712				
0	0	0.00				
1	500	0.50	1.41			
0	0	0.00				
1	3000	12.00	14.47			34.0 L
1	1060	1.06	14.47			
1	1850	1.85	16.32	72		
0	0	0.00	18.27	70		5.48 L
1	1850	1.85	20.12	72		
0	0	0.00	22.07	70		4.11 L
1	1850	1.85	23.92	72		
0	0	0.00	25.87	70		4.59 L
1	1850	1.85	27.72	72		
0	0	0.00	29.67	70		6.02 L
1	1850	1.85	31.52	72		
0	0	0.00	33.47	70		3.67 L
1	1850	1.85	35.32	72		
0	0	0.00	37.19	70		11.74 L

Fig. C-2: FE multi-packer system schematic for BFE-A002 (BFE-A003-A007 are similarly equipped)

Tab. C-2: Multi-packer monitoring system interval locations

Borehole	Int.	Start (m)	End (m)	Length (m)	Y <sub>FE</sub>	R <sub>FE</sub>	Y <sub>FE</sub>	R <sub>FE</sub>	Section
BFEA002	i1	35.32	38.42	3.1	39.53	6.07	42.56	6.44	Heater 1
BFEA002	i2	31.52	33.47	1.95	35.77	5.60	37.69	5.85	Gap 1-2
BFEA002	i3	27.72	29.67	1.95	31.99	5.13	33.93	5.35	Heater 2
BFEA002	i4	23.92	25.87	1.95	28.21	4.68	30.16	4.92	Gap 2-3
BFEA002	i5	20.12	22.07	1.95	24.45	4.20	26.39	4.43	Heater 3
BFEA002	i6	16.32	18.27	1.95	20.67	3.76	22.61	3.96	Gap GP
BFEA003	i1	35.37	38.25	2.88	39.09	9.58	41.90	10.11	Heater 1
BFEA003	i2	31.57	33.52	1.95	35.36	8.87	37.27	9.22	Gap 1-2
BFEA003	i3	27.77	29.72	1.95	31.62	8.14	33.54	8.51	Heater 2
BFEA003	i4	23.97	25.92	1.95	27.89	7.41	29.81	7.79	Gap 2-3
BFEA003	i5	20.17	22.12	1.95	24.16	6.69	26.08	7.06	Heater 3
BFEA003	i6	16.37	18.32	1.95	20.42	5.99	22.35	6.35	Gap GP
BFEA004	i1	37.38	40.21	2.83	38.91	16.88	41.55	17.93	Heater 1
BFEA004	i2	33.58	35.53	1.95	35.36	15.47	37.17	16.19	Gap 1-2
BFEA004	i3	29.78	31.73	1.95	31.85	14.08	33.67	14.80	Heater 2
BFEA004	i4	25.98	27.93	1.95	28.29	12.66	30.11	13.38	Gap 2-3
BFEA004	i5	22.18	24.13	1.95	24.80	11.26	26.60	11.98	Heater 3
BFEA004	i6	18.38	20.33	1.95	21.29	9.86	23.10	10.59	Gap GP
BFEA005	i1	34.99	38.85	3.86	39.20	5.64	43.05	5.92	Heater 1
BFEA005	i2	31.19	33.14	1.95	35.41	5.38	37.36	5.52	Gap 1-2
BFEA005	i3	27.39	29.34	1.95	31.62	5.10	33.56	5.25	Heater 2
BFEA005	i4	23.59	25.54	1.95	27.83	4.82	29.78	4.97	Gap 2-3
BFEA005	i5	19.79	21.74	1.95	24.05	4.54	25.99	4.68	Heater 3
BFEA005	i6	15.99	17.94	1.95	20.26	4.24	22.21	4.40	Gap GP
BFEA006	i1	35.67	39.46	3.79	39.12	9.23	42.86	9.91	Heater 1
BFEA006	i2	31.87	33.82	1.95	35.38	8.54	37.30	8.90	Gap 1-2
BFEA006	i3	28.07	30.02	1.95	31.65	7.85	33.57	8.20	Heater 2
BFEA006	i4	24.27	26.22	1.95	27.91	7.15	29.83	7.51	Gap 2-3
BFEA006	i5	20.47	22.42	1.95	24.18	6.46	26.10	6.81	Heater 3
BFEA006	i6	16.67	18.62	1.95	20.45	5.76	22.36	6.12	Gap GP
BFEA007	i1	37.53	40.08	2.55	38.82	17.13	41.19	18.04	Heater 1
BFEA007	i2	33.73	35.68	1.95	35.27	15.76	37.09	16.46	Gap 1-2
BFEA007	i3	29.93	31.88	1.95	31.73	14.38	33.55	15.09	Heater 2

Tab. C-2: Cont.

Borehole	Int.	Start (m)	End (m)	Length (m)	Y <sub>FE</sub>	R <sub>FE</sub>	Y <sub>FE</sub>	R <sub>FE</sub>	Section
BFEA007	i4	26.13	28.08	1.95	28.19	13.00	30.01	13.71	Gap 2-3
BFEA007	i5	22.33	24.28	1.95	24.65	11.61	26.46	12.33	Heater 3
BFEA007	i6	18.53	20.48	1.95	21.12	10.23	22.94	10.94	Gap GP

Tab. C-3: Multi-packer monitoring system packer locations

Borehole	Int.	Start (m)	End (m)	Length (m)	Y <sub>FE</sub>	R <sub>FE</sub>	Y <sub>FE</sub>	R <sub>FE</sub>	Section
BFEA002	P1	33.47	35.32	1.85	37.69	5.85	39.53	6.07	Heater 1
BFEA002	P2	29.67	31.52	1.85	33.93	5.35	35.77	5.60	Heater 2
BFEA002	P3	25.87	27.72	1.85	30.16	4.92	31.99	5.13	Heater 2
BFEA002	P4	22.07	23.92	1.85	26.39	4.43	28.21	4.68	Gap 2-3
BFEA002	P5	18.27	20.12	1.85	22.61	3.96	24.45	4.20	Heater 3
BFEA002	P6	14.47	16.32	1.85	18.83	3.57	20.67	3.76	Gap GP
BFEA003	P1	33.52	35.37	1.85	37.27	9.22	39.09	9.58	Heater 1
BFEA003	P2	29.72	31.57	1.85	33.54	8.51	35.36	8.87	Heater 2
BFEA003	P3	25.92	27.77	1.85	29.81	7.79	31.62	8.14	Heater 2
BFEA003	P4	22.12	23.97	1.85	26.08	7.06	27.89	7.41	Heater 3
BFEA003	P5	18.32	20.17	1.85	22.35	6.35	24.16	6.69	Heater 3
BFEA003	P6	14.52	16.37	1.85	18.60	5.65	20.42	5.99	Retaining wall
BFEA004	P1	35.53	37.38	1.85	37.17	16.19	38.91	16.88	Heater 1
BFEA004	P2	31.73	33.58	1.85	33.67	14.80	35.36	15.47	Heater 2
BFEA004	P3	27.93	29.78	1.85	30.11	13.38	31.85	14.08	Heater 2
BFEA004	P4	24.13	25.98	1.85	26.60	11.98	28.29	12.66	Gap 2-3
BFEA004	P5	20.33	22.18	1.85	23.10	10.59	24.80	11.26	Heater 3
BFEA004	P6	16.53	18.38	1.85	19.56	9.17	21.29	9.86	Gap GP
BFEA005	P1	33.14	34.99	1.85	37.36	5.52	39.20	5.64	Heater 1
BFEA005	P2	29.34	31.19	1.85	33.56	5.25	35.41	5.38	Heater 2
BFEA005	P3	25.54	27.39	1.85	29.78	4.97	31.62	5.10	Heater 2
BFEA005	P4	21.74	23.59	1.85	25.99	4.68	27.83	4.82	Heater 3
BFEA005	P5	17.94	19.79	1.85	22.21	4.40	24.05	4.54	Heater 3
BFEA005	P6	14.14	15.99	1.85	18.41	4.10	20.26	4.24	Plug
BFEA006	P1	33.82	35.67	1.85	37.30	8.90	39.12	9.23	Heater 1

Tab. C-3: Cont.

Borehole	Int.	Start (m)	End (m)	Length (m)	Y <sub>FE</sub>	R <sub>FE</sub>	Y <sub>FE</sub>	R <sub>FE</sub>	Section
BFEA006	P2	30.02	31.87	1.85	33.57	8.20	35.38	8.54	Heater 2
BFEA006	P3	26.22	28.07	1.85	29.83	7.51	31.65	7.85	Heater 2
BFEA006	P4	22.42	24.27	1.85	26.10	6.81	27.91	7.15	Heater 3
BFEA006	P5	18.62	20.47	1.85	22.36	6.12	24.18	6.46	Heater 3
BFEA006	P6	14.82	16.67	1.85	18.63	5.41	20.45	5.76	Retaining wall
BFEA007	P1	35.68	37.53	1.85	37.09	16.46	38.82	17.13	Heater 1
BFEA007	P2	31.88	33.73	1.85	33.55	15.09	35.27	15.76	Heater 2
BFEA007	P3	28.08	29.93	1.85	30.01	13.71	31.73	14.38	Heater 2
BFEA007	P4	24.28	26.13	1.85	26.46	12.33	28.19	13.00	Gap 2-3
BFEA007	P5	20.48	22.33	1.85	22.94	10.94	24.65	11.61	Heater 3
BFEA007	P6	16.68	18.53	1.85	19.40	9.55	21.12	10.23	Gap GP

Tab. C-4: Hydrotesting in FEA multi-packer systems around FE Gallery

Borehole interval	Radial distance		Relationship to bedding*	Type	Compressibility (m <sup>3</sup> /Pa)	Hydraulic conductivity (m/s)
	(m)	Tunnel radii (-)				
BFEA002i3	5.2	3.5	AB	HI		1.0E-13
BFEA003i3	8.3	5.6	AB	PI	2.9E-11	6.8E-13
BFEA004i3	14.4	9.6	AB	PW	1.7E-11	2.5E-13
BFEA005i3	5.2	3.4	XB	HI		2.9E-13
BFEA006i5	6.6	4.4	XB	PI	6.3E-11	8.4E-12
BFEA007i5	12.0	8.0	XB	PW	3.2E-11	2.3E-12
BFEB004i1	4.1	2.7	XB	HI		2.2E-13
BFEB004i2	3.4	2.2	XB	HI		7.6E-13
BFEB005i1	4.0	2.7	AB	HI		1.8E-12
BFEB005i2	3.3	2.2	AB	HI		6.8E-11

\* AB parallel to bedding, XB normal to bedding



## Appendix D: Relationship between relative humidity and saturation/volumetric water content and thermal conductivity and saturation for GBM

### Relative humidity and saturation

Saturation can theoretically be calculated from measured relative humidity via the capillary pressure curve. The capillary pressure  $P_c$  (Pa) is related to RH (-) by:

$$P_c = \ln(RH)\rho_w \frac{RT}{M_w}$$

where T (°K) is the temperature,  $\rho_w$  is the water density,  $M_w$  is the molecular weight  $N_2$  (0.018 kg/mol) and R is the universal gas constant (8.315 J K<sup>-1</sup> mol<sup>-1</sup>). TOUGH2 and other two-phase flow models have described the capillary pressure curve for granular bentonite using a van Genuchten model. The van Genuchten capillary pressure curve is given by:

$$P_c = P_0 \left( S_e^{n/1-n} - 1 \right)^{1/n}; P_c = P_0 \left( S_e^{\frac{-1}{m}} - 1 \right)^{1-m}$$

where  $S_e$  is the effective saturation,  $n$  is the shape factor (-) and  $P_0$  (alternatively  $l/\alpha$ ) is the pressure scaling factor. The shape factor  $n$  is related to  $m$  by:

$$m = 1 - \frac{1}{n} = \frac{n-1}{n}; \frac{1}{n} = 1 - m; \frac{n}{1-n} = \frac{-1}{m}$$

and the effective saturation is a function of the saturation  $S$  (-) and the irreducible liquid saturation  $S_{lr}$  (-):

$$S_e = \frac{S_l - S_{lr}}{1 - S_{lr}}; S_l = S_e(1 - S_{lr}) + S_{lr}$$

The effective saturation can therefore be derived from  $P_c$  as:

$$S_e = \left( 1 + \left( \frac{P_c}{P_0} \right)^n \right)^{-m}$$

Parameter values used in relevant modelling for GAST and the HAA repository are summarised in Tab. D-1. The resulting RH versus saturation curve is shown in Fig. D-1 using the design model parameters together with cases where the capillary pressure is scaled by factors of 0.1 and 10.

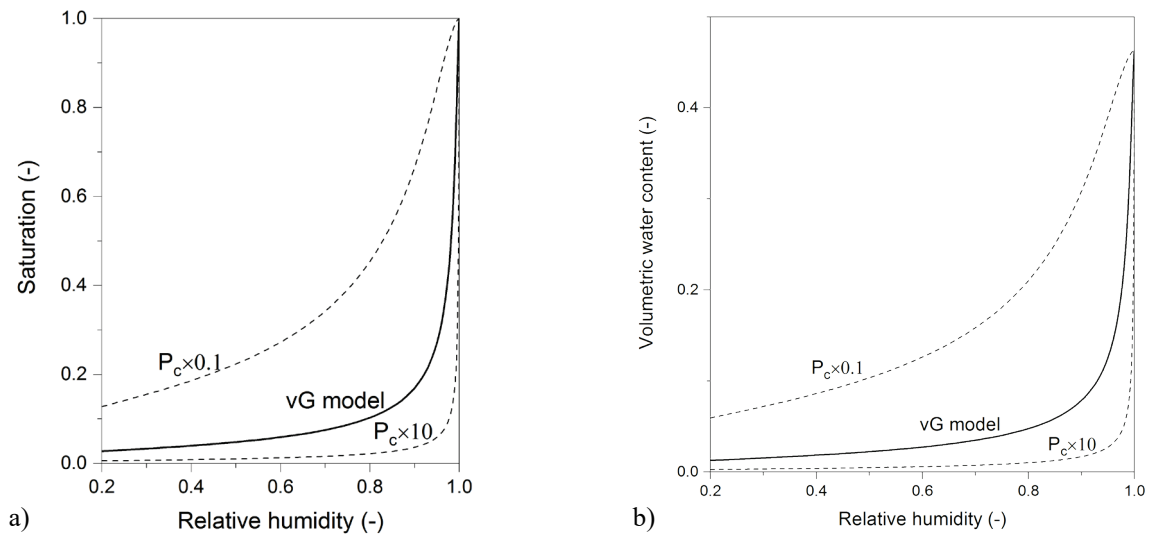


Fig. D-1: Relative humidity versus a) saturation and b) volumetric water content based on van Genuchten model with uncertainty given by factor of 0.1,10 in capillary pressure

Tab. D-1: Granular bentonite properties and van Genuchten model parameters from Nagra (2019), Garitte (2013)

	As-emplaced values	FE design case (THM_c)	Repository models	Remarks
Dry density Mg/m <sup>3</sup>	1.49		1.49	Mean as-emplaced dry density (Nagra, 2019)
Porosity	0.46		0.45/0.46	Calculated assuming grain density 2.7 g/cm <sup>3</sup>
Initial saturation	0.17		0.2	Based on gravimetric water content 5 %
Vg P <sub>0</sub> (Pa)	-	10 <sup>7</sup>	10 <sup>7</sup>	Seiphoori (2015) measured air-entry pressure for S <sub>r</sub> = 0.95 for granular bentonite ( void ratio ~ 0.82, dry density 1.51 Mg/m <sup>3</sup> )
VG n (-)	-		1.67	
VG m(-)	-	0.4	0.4	
S <sub>lr</sub> (-):	-	0	0 – 0.01	

### Thermal conductivity and saturation

Garitte (2013) present data and fitted regressions for the GBM (Fig. D-2) as part of the scoping calculations for FE. The adopted curves (case THM\_c) uses a function of the form:

$$\lambda = \lambda_{sat}^{S_i} \cdot \lambda_{dry}^{1-S_i}$$

So that saturation can be calculated from the measured thermal conductivity using:

$$S = \frac{\log \lambda - \log \lambda_{sat}}{\log \lambda_{sat} - \log \lambda_{dry}}$$

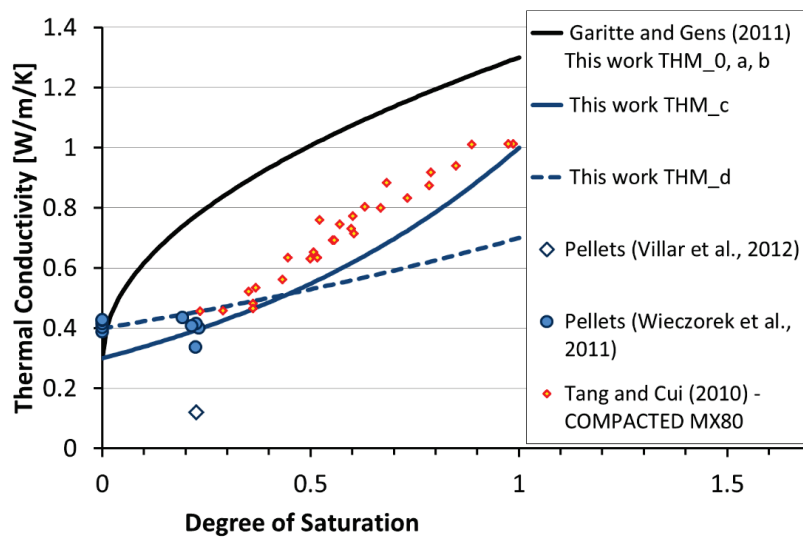


Fig. D-2: Thermal conductivity as a function of the saturation measured in the lab for MX-80 bentonite pellets (blue dots) and MX80 bentonite blocks (red dots)

From Garitte (2013)



### Appendix E: Water Content Measurements (non-engineering units)

Water content data from FDRs in the rock in BFEC006-8 and BFEB050,51 were not available as calibrated volumetric water content within FEISDB. The data are presented here as the values in mV.

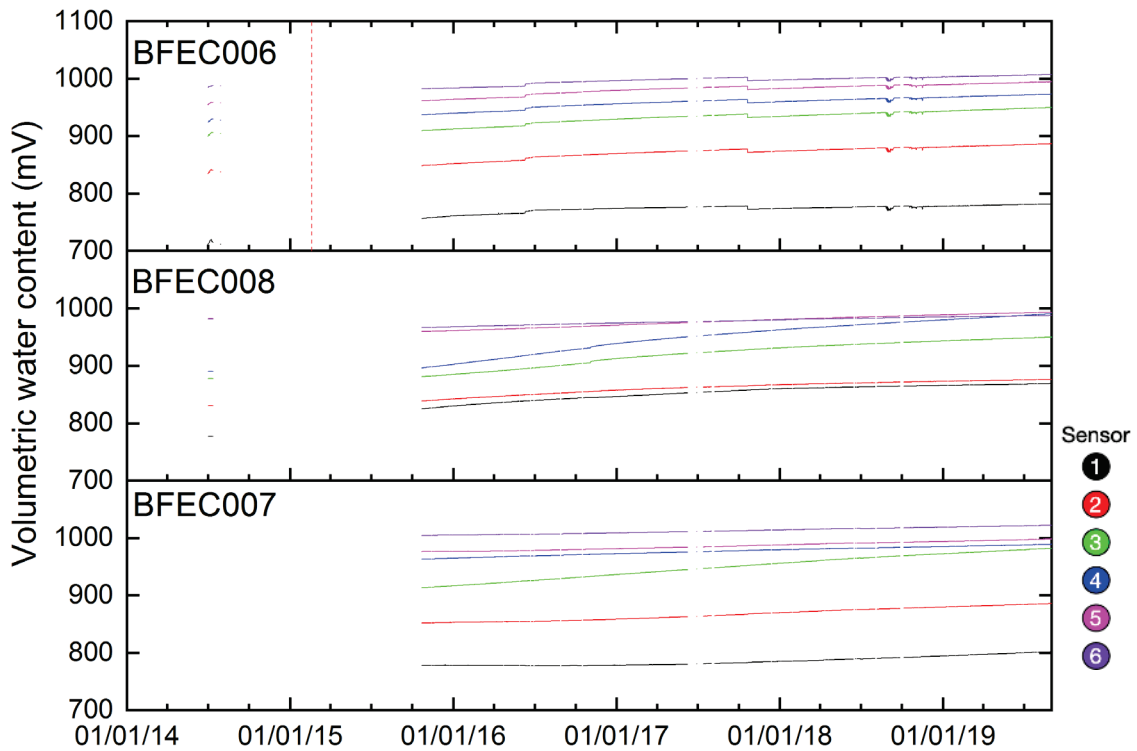


Fig. E-1: Volumetric water content measurements (mV) from BFEC006-8

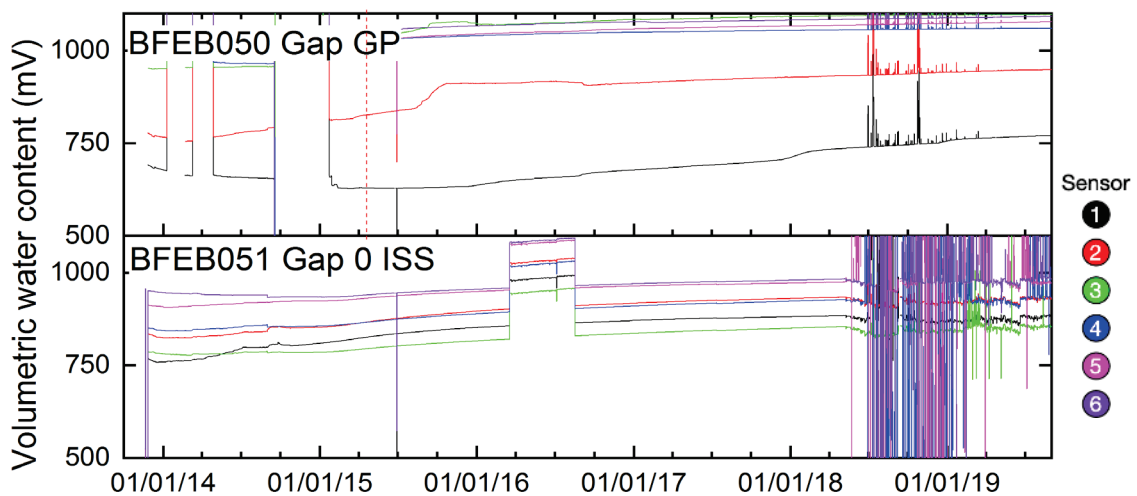


Fig. E-2: Volumetric water content measurements (mV) from BFEB050,51



## Appendix F: Pressure change in response to Ga18 excavation

Tab. F-1: Pore pressure peak and change during Ga18 excavation Phase 2D. Change calculated as peak pressure minus average pressure from 02. – 07.05.2019

Monitoring interval	Average pressure prior to Phase 2D	Peak pressure during Phase 2D	Difference between	ExpDelta	R
BFEA002-i1	1'291.3	1'298.8	7.6	-2.2	-0.6
BFEA002-i2	1'361.2	1'370.4	9.2	-2.2	-0.4
BFEA002-i3	1'107.4	1'120.6	13.2	-2.2	-0.4
BFEA002-i4	825.2	841.4	16.2	-2.2	0.3
BFEA002-i5	607.4	625.5	18.0	-2.2	0.4
BFEA002-i6	385.7	403.3	17.6	-2.2	0.7
BFEA003-i1	2'158.5	2'169.8	11.3	-2.2	0.7
BFEA003-i2	2'138.1	2'148.9	10.7	-2.2	0.4
BFEA003-i3	2'059.5	2'068.6	9.1	-2.2	-0.5
BFEA003-i4	1'868.3	1'877.9	9.6	-2.2	-0.4
BFEA003-i5	1'787.2	1'800.1	12.9	-2.2	-0.3
BFEA003-i6	1'175.7	1'229.3	53.6	-2.2	0.5
BFEA004-i1	2'358.5	2'374.1	15.6	-2.2	0.9
BFEA004-i2	2'358.3	2'373.7	15.4	-2.2	1.0
BFEA004-i3	2'508.4	2'525.9	17.6	-2.2	1.0
BFEA004-i4	2'550.3	2'568.1	17.8	-2.2	0.9
BFEA004-i5	2'477.3	2'494.4	17.1	-2.2	0.9
BFEA004-i6	2'229.5	2'246.6	17.0	-2.2	0.8
BFEA005-i1	1'460.7	1'477.7	16.9	-2.2	1.0
BFEA005-i2	1'527.0	1'541.8	14.8	-2.2	0.9
BFEA005-i3	1'683.8	1'697.3	13.6	-2.2	0.8
BFEA005-i4	1'670.7	1'683.6	12.9	-2.2	0.6
BFEA005-i5	1'340.6	1'354.6	14.0	-2.2	0.7
BFEA005-i6	1'231.8	1'247.7	15.9	-2.2	0.8
BFEA006-i1	1'758.0	1'773.6	15.5	-2.2	0.9
BFEA006-i2	1'725.5	1'741.2	15.7	-2.2	0.9
BFEA006-i3	1'845.3	1'860.7	15.5	-2.2	0.9
BFEA006-i4	1'713.1	1'731.8	18.7	-2.2	0.8
BFEA006-i5	1'315.2	1'330.3	15.1	-2.2	0.7
BFEA006-i6	1'249.0	1'263.2	14.2	-2.2	0.7

Tab. F-1: Cont.

Monitoring interval	Average pressure prior to Phase 2D	Peak pressure during Phase 2D	Difference between	ExpDelta	R
BFEA007-i1	2'002.6	2'020.4	17.8	-2.2	0.5
BFEA007-i2	2'046.7	2'065.8	19.1	-2.2	0.9
BFEA007-i3	2'087.7	2'108.7	21.0	-2.2	0.9
BFEA007-i4	2'131.1	2'150.4	19.3	-2.2	0.8
BFEA007-i5	2'117.8	2'139.6	21.8	-2.2	0.8
BFEA007-i6	2'071.1	2'090.5	19.4	-2.2	0.9
BFEA008-i1	563.7	578.9	15.2	-2.2	0.7
BFEA009-i1	204.8	207.2	2.5	-2.2	-0.1
BFEA012-i1			Noisy pressure data no clear response		
BFEA013-i1			Noisy pressure data no clear response		
BFEA014-i1			Noisy pressure data no clear response		
BFEA015-i1			Noisy pressure data no clear response		
BFEB001-i1	473.2	482.9	9.7	-2.2	0.1
BFEB001-i2	237.1	242.4	5.3	-2.2	-0.2
BFEB002-i1	774.2	785.2	11.0	-2.2	0.7
BFEB002-i2	402.6	412.0	9.5	-2.2	0.7
BFEB003-i1	722.1	743.6	21.4	-2.2	0.3
BFEB003-i2	334.1	349.8	15.7	-2.2	0.6
BFEB004-i1	1'113.8	1125.4	11.6	-2.2	0.6
BFEB004-i2	692.8	703.1	10.3	-2.2	0.5
BFEB005-i1	598.5	602.2	3.7	-2.2	0.4
BFEB005-i2	393.4	400.6	7.1	-2.2	0.2
BFEB006-i1	828.7	836.4	7.7	-2.2	0.2
BFEB006-i2	120.0	120.3	0.3	-2.2	0.0
BFEB007-i1	868.9	886.0	17.0	-2.2	-0.4
BFEB007-i2	459.2	474.2	15.0	-2.2	-0.4
BFEB008-i1	1'291.4	1301.1	9.7	-2.2	0.7
BFEB008-i2	794.9	804.9	10.0	-2.2	0.7
BFEB044-i1	123.1	126.3	3.2	-2.2	0.1
BFEB044-i2	114.5	118.1	3.6	-2.2	0.1
BFEB045-i1	912.3	913.9	1.6	-2.2	-0.8
BFEB045-i2	885.5	886.8	1.3	-2.2	-0.8

Tab. F-1: Cont.

<b>Monitoring interval</b>	<b>Average pressure prior to Phase 2D</b>	<b>Peak pressure during Phase 2D</b>	<b>Difference between</b>	<b>ExpDelta</b>	<b>R</b>
BFEB046-i1	-445.9	-443.8	<b>2.1</b>	-2.2	0.0
BFEB046-i2	-450.7	-448.3	<b>2.4</b>	-2.2	0.1
BFEB047-i1	-443.8	-441.7	<b>2.1</b>	-2.2	0.0
BFEB047-i2	139.1	142.3	<b>3.2</b>	-2.2	0.0
BFEB048-i1	-444.5	-442.0	<b>2.5</b>	-2.2	-0.2

Tab. F-2: Pore pressure change during excavation days Ga18 Phase 2D. Change calculated as maximum pressure after 06:00 minus average pressure from 00:00 – 06:00

GM Mapping	269.7	271.8	273.9	275.9	277.9	280.0	282.0	284.0	286.0	288.0	290.0	292.0	294.0	295.0	297.0
Day in 05.2019	07	08	09	10	13	14	15	16	17	20	21	22	23	25	27
BFEA002-i1	0.1	0.2	1.0	0.6	0.3	0.3	0.4	0.4	0.5	1.3	1.3	0.8	1.4	0.7	0.1
BFEA002-i2	0.1	0.3	1.2	0.7	0.4	0.4	0.5	0.5	0.6	1.4	1.5	1.0	1.6	0.7	0.1
BFEA002-i3	0.0	0.4	1.3	0.8	0.5	0.5	0.7	0.7	0.8	1.7	1.8	1.3	2.5	1.1	0.1
BFEA002-i4	0.1	0.5	1.5	0.9	0.6	0.6	0.8	0.9	1.0	1.8	2.1	1.3	2.9	1.2	0.1
BFEA002-i5	0.0	0.5	1.5	1.0	0.6	0.7	0.9	0.9	1.1	2.0	2.2	1.6	3.5	1.2	0.2
BFEA002-i6	0.0	0.5	1.5	1.0	0.6	0.7	0.8	0.9	1.1	2.0	2.3	1.5	3.5	1.0	0.1
BFEA003-i1	0.1	0.4	1.1	0.7	0.4	0.4	0.5	0.4	0.7	1.4	1.5	1.0	1.7	0.9	0.1
BFEA003-i2	0.1	0.3	1.1	0.6	0.4	0.4	0.5	0.5	0.7	1.5	1.5	1.0	2.1	1.0	0.1
BFEA003-i3	0.0	0.2	1.1	0.6	0.4	0.4	0.5	0.5	0.6	1.5	1.5	0.9	2.1	0.8	0.1
BFEA003-i4	0.1	0.4	1.1	0.7	0.4	0.4	0.5	0.5	0.6	1.5	1.6	1.0	1.9	0.7	0.1
BFEA003-i5	0.0	0.3	1.2	0.7	0.5	0.5	0.6	0.7	0.8	1.7	1.8	1.2	2.6	1.0	0.1
BFEA003-i6	4.4	9.9	6.2	5.5	4.1	13.5	8.6	7.2	10.3	5.2	15.1	7.0	1.5	18.2	10.4
BFEA004-i1	0.1	0.4	1.3	0.8	0.5	0.4	0.6	0.5	0.8	1.6	1.5	1.0	1.7	0.9	0.2
BFEA004-i2	0.1	0.4	1.2	0.9	0.5	0.4	0.6	0.5	0.8	1.6	1.5	1.0	1.6	0.9	0.2
BFEA004-i3	0.1	0.4	1.4	0.8	0.6	0.5	0.7	0.6	0.9	1.6	1.8	1.2	2.3	1.1	0.3
BFEA004-i4	0.0	0.5	1.3	0.9	0.5	0.5	0.6	0.7	0.9	1.9	1.8	1.4	2.4	1.0	0.2
BFEA004-i5	0.1	0.4	1.3	0.9	0.5	0.6	0.7	0.7	1.0	1.8	2.0	1.4	2.7	1.2	0.2
BFEA004-i6	0.1	0.4	1.3	0.9	0.5	0.5	0.7	0.7	1.0	1.8	1.9	1.4	2.8	1.2	0.2
BFEA005-i1	0.1	0.7	1.6	0.8	0.6	0.5	1.0	0.8	0.9	1.7	1.7	1.1	2.3	1.2	0.3
BFEA005-i2	0.1	0.6	1.5	0.8	0.6	0.6	0.7	0.7	0.7	1.6	1.7	1.0	2.0	0.8	0.1
BFEA005-i3	0.1	0.5	1.3	0.9	0.5	0.6	0.6	0.6	0.7	1.8	1.5	1.0	2.0	0.7	0.1
BFEA005-i4	0.1	0.5	1.2	0.9	0.5	0.5	0.6	0.8	0.8	1.3	1.6	1.0	1.9	0.7	0.1
BFEA005-i5	0.0	0.5	1.3	0.7	0.5	0.6	0.7	0.7	0.8	1.4	1.7	1.1	2.3	0.9	0.1
BFEA005-i6	0.0	0.5	1.3	0.9	0.5	0.6	0.7	0.8	0.9	1.6	1.8	1.2	2.3	1.1	0.2
BFEA006-i1	0.1	0.4	1.0	0.9	0.6	0.5	0.6	0.6	0.7	1.1	1.3	1.0	1.5	0.8	0.2
BFEA006-i2	0.1	0.7	1.6	0.9	0.6	0.7	0.7	0.8	0.8	1.6	1.7	1.0	1.8	0.6	0.1
BFEA006-i3	0.1	0.7	1.5	1.0	0.5	0.7	0.8	0.8	0.8	1.6	1.6	1.0	2.0	0.6	0.1
BFEA006-i4	0.2	0.9	2.5	1.1	0.9	0.8	0.9	1.0	0.9	1.5	1.5	1.1	1.6	0.3	-0.1
BFEA006-i5	0.2	0.5	0.8	0.9	0.7	0.8	0.9	0.7	1.1	1.6	2.2	1.2	2.9	1.2	1.4
BFEA006-i6	0.1	0.5	1.3	0.8	0.5	0.7	0.2	0.6	0.9	1.8	2.1	1.3	3.7	1.1	0.5
BFEA007-i1	0.3	0.5	1.6	1.0	0.5	1.0	2.8	0.4	0.6	1.2	1.6	0.9	2.0	1.5	0.6
BFEA007-i2	0.2	0.7	1.7	1.1	0.8	0.8	1.0	1.0	1.0	1.9	2.0	1.3	2.9	1.0	0.2
BFEA007-i3	0.2	0.8	1.7	1.1	0.9	1.0	1.1	1.0	1.2	2.0	2.2	1.5	3.0	1.0	0.1
BFEA007-i4	0.2	0.8	1.8	1.2	0.8	0.8	1.1	1.0	1.1	1.9	2.1	1.4	2.8	1.0	0.2
BFEA007-i5	0.1	0.8	1.7	1.2	0.8	0.9	1.0	1.0	1.2	2.0	2.4	1.6	3.5	1.4	0.4
BFEA007-i6	0.3	0.9	1.8	1.2	0.9	1.0	1.3	1.2	0.9	1.9	2.3	1.6	3.1	1.2	0.4
BFEA008-i1	0.5	1.1	1.2	1.2	0.9	1.5	0.7	0.8	1.3	1.5	2.6	1.4	1.7	1.7	0.6
BFEA009-i1	0.0	0.0	0.1	0.1	0.2	0.1	0.1	0.2	0.2	0.2	0.2	0.2	0.3	0.2	0.1
BFEA012-i1	Noisy pressure data no clear response														

Tab. F-2: Pore pressure change during excavation days Ga18 Phase 2D. Change calculated as maximum pressure after 06:00 minus average pressure from 00:00 – 06:00

GM Mapping	269. 7	271. 8	273. 9	275. 9	277. 9	280. 0	282. 0	284. 0	286. 0	288. 0	290. 0	292. 0	294. 0	295. 0	297. 0
BFEA013-i1	Noisy pressure data no clear response														
BFEA014-i1	Noisy pressure data no clear response														
BFEA015-i1	Noisy pressure data no clear response														
BFEB001-i1	0.2	0.3	0.5	0.5	0.5	0.4	0.7	0.3	0.4	0.8	0.6	1.1	1.6	0.5	0.6
BFEB001-i2	0.4	0.2	0.4	0.4	0.3	0.4	0.5	0.3	0.3	0.5	0.4	0.3	0.6	0.7	0.2
BFEB002-i1	0.3	0.0	0.9	0.9	1.0	0.7	0.7	0.4	0.4	1.6	1.7	1.5	2.0	0.9	0.2
BFEB002-i2	0.5	0.0	0.7	0.8	1.0	1.2	0.7	0.1	0.4	1.2	1.1	1.0	1.0	0.6	0.3
BFEB003-i1	0.4	0.4	1.8	1.2	1.2	1.4	1.1	1.3	1.1	2.7	3.0	2.1	3.4	1.5	0.5
BFEB003-i2	0.3	0.2	1.7	1.1	1.0	1.4	1.0	0.5	0.6	2.1	2.2	1.8	3.0	0.9	0.2
BFEB004-i1	0.2	0.6	1.2	0.9	0.6	0.7	0.7	0.7	0.5	1.5	1.4	1.4	2.2	0.9	0.2
BFEB004-i2	0.2	0.4	1.0	1.0	0.9	0.9	0.5	0.7	0.5	1.4	1.3	1.2	1.4	0.6	0.5
BFEB005-i1	0.5	0.3	0.4	0.3	0.4	0.2	0.2	0.4	0.5	0.3	0.6	0.7	0.4	0.4	0.4
BFEB005-i2	0.3	0.3	0.2	0.7	0.5	0.5	0.4	0.3	0.4	0.4	0.6	0.8	0.6	0.5	0.2
BFEB006-i1	0.1	0.5	0.8	0.9	0.7	0.8	0.7	0.4	0.6	1.0	1.4	1.2	2.2	0.5	0.5
BFEB006-i2	0.4	0.2	0.2	0.4	0.2	0.2	0.1	0.2	0.2	0.3	0.3	0.3	0.1	0.2	0.3
BFEB007-i1	0.4	0.2	1.5	0.7	1.4	1.3	1.1	0.6	0.8	2.2	2.4	2.0	3.5	1.4	0.4
BFEB007-i2	0.4	0.1	1.1	1.0	1.1	1.3	0.9	0.7	0.8	1.9	1.9	1.7	2.6	1.2	0.2
BFEB008-i1	0.4	0.3	1.3	0.6	0.8	1.1	0.5	0.3	0.5	1.4	1.2	1.2	1.7	0.7	0.5
BFEB008-i2	0.6	-0.1	1.1	1.0	1.0	1.1	0.5	0.3	0.4	1.4	1.5	1.2	2.0	1.2	0.6
BFEB044-i1	1.9	1.6	1.5	1.7	1.8	1.2	1.9	2.6	1.1	1.5	1.6	2.2	1.7	1.8	1.7
BFEB044-i2	1.7	1.7	1.3	1.5	1.3	2.2	1.9	1.9	1.9	2.2	3.0	1.3	2.1	2.0	1.6
BFEB045-i1	-0.5	0.3	0.9	1.1	5.9	2.9	0.6	3.1	1.9	2.3	1.2	0.2	-0.3	0.8	2.0
BFEB045-i2	1.6	1.5	1.2	1.4	5.0	3.0	1.7	2.3	0.9	2.3	2.3	-0.1	0.5	1.0	1.6
BFEB046-i1	1.5	2.5	1.8	2.0	1.7	0.8	2.4	1.5	1.8	1.2	1.2	2.1	1.8	1.3	2.5
BFEB046-i2	1.8	1.5	2.4	1.8	2.2	1.4	1.9	0.9	1.5	0.7	1.0	1.8	1.5	1.9	1.7
BFEB047-i1	1.9	1.2	1.9	1.7	1.4	1.3	1.0	1.2	1.8	1.2	1.5	1.8	1.0	1.0	1.8
BFEB047-i2	1.4	2.7	2.4	1.4	1.9	1.4	1.9	1.6	2.4	2.2	2.2	1.5	3.0	1.4	2.1
BFEB048-i1	1.8	2.2	1.5	1.5	1.4	1.1	1.7	1.1	1.2	1.9	2.7	0.9	1.9	0.9	1.8



## Appendix G: Kirsch equations

The calculation of local stresses is performed by use of an analytical solution to stress around an infinite cylinder in a continuous, homogeneous, isotropic, linear elastic medium (Kirsch 1898, Leeman Hayes 1966). The 2D version (Kirsch *op cit*) as given by Brady & Brown (1993):

$$\sigma_r = \frac{p}{2} \left\{ (1+k) \left( 1 - \frac{a^2}{r^2} \right) - (1-k) \left( 1 - 4 \frac{a^2}{r^2} + 3 \frac{a^4}{r^4} \right) \cos 2\theta \right\}$$

$$\sigma_\theta = \frac{p}{2} \left\{ (1+k) \left( 1 + \frac{a^2}{r^2} \right) + (1-k) \left( 1 + 3 \frac{a^4}{r^4} \right) \cos 2\theta \right\}$$

$$\tau_{r\theta} = \frac{p}{2} \left\{ (1-k) \left( 1 + 2 \frac{a^2}{r^2} - 3 \frac{a^4}{r^4} \right) \sin 2\theta \right\}$$

where  $a$  is the tunnel radius,  $r$  is the radial distance from the tunnel axis,  $p$  the vertical stress and  $kp$  the horizontal stress as shown in Fig. 3-3.

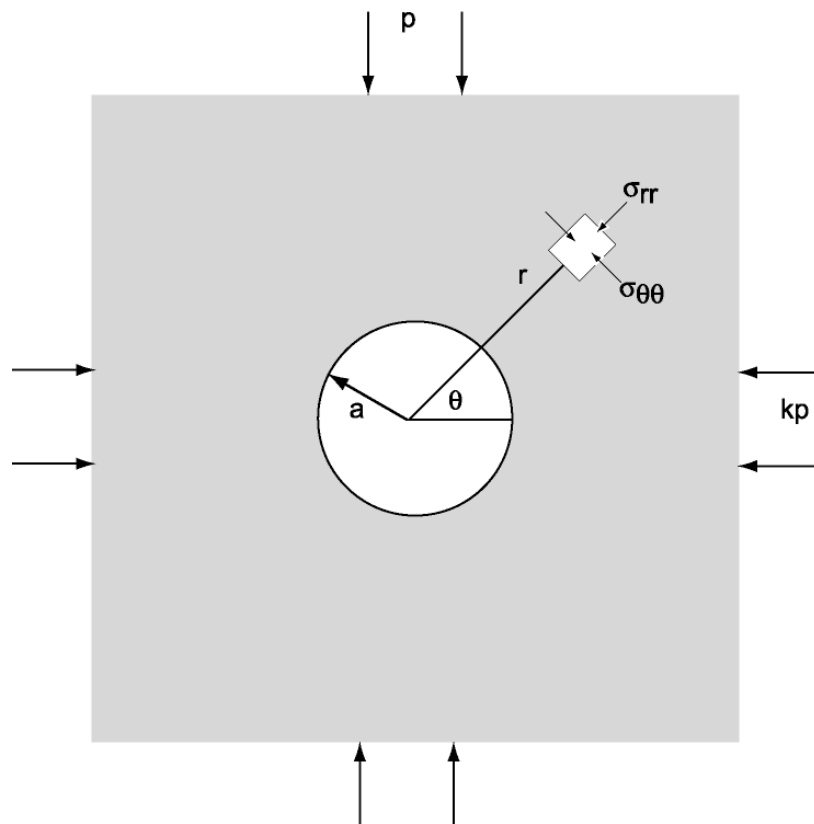


Fig. G-1: Geometry and co-ordinate system for Kirsch solution  
From Brady & Brown (1993)

The estimated change in vertical total stress as a function of horizontal distance ( $r/a$ ) for  $\sigma_V = 6.5$  MPa and  $\sigma_H = 4$  MPa is shown in Fig. G-2.

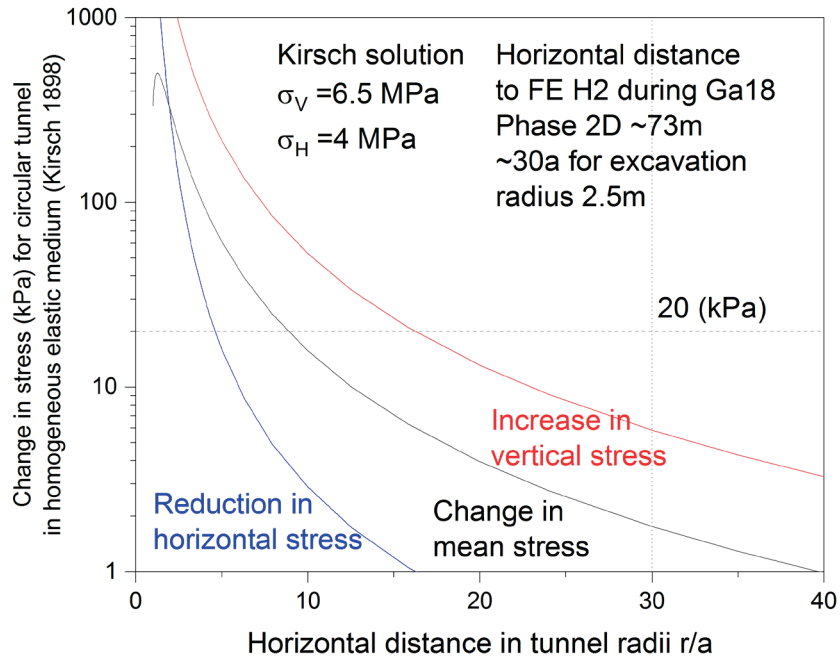


Fig. G-2: Estimated change in vertical, horizontal and mean total stress as a function of horizontal distance ( $r/a$ ) in homogeneous elastic meadium under plan strain conditions

$\sigma_V = 6.5$ MPa and  $\sigma_H = 4$ MPa.

## Appendix H: Pore pressure disturbances during excavation of Gallery 98 (New Gallery)

Martin & Lanyon (2003) present pore pressure data from the excavation of the ED-B section and other parts of Gallery 98 (then known as the) New Gallery. Fig. H-1a shows the measured pressure in BPP-1 during excavation of the DI Niche. There is a clear correspondence between individual blasting sequences and the measured pressure in both the test intervals and packers. The instantaneous pressure increase in the packers and test intervals is very similar. In the test intervals large pressure increases (~ 50 kPa) appear to leak off while later smaller increases are held. The packer pressures decline more slowly. This suggests that some mechanical relaxation occurs due to the increased packer pressures while fluid may leak off from the borehole intervals more rapidly.

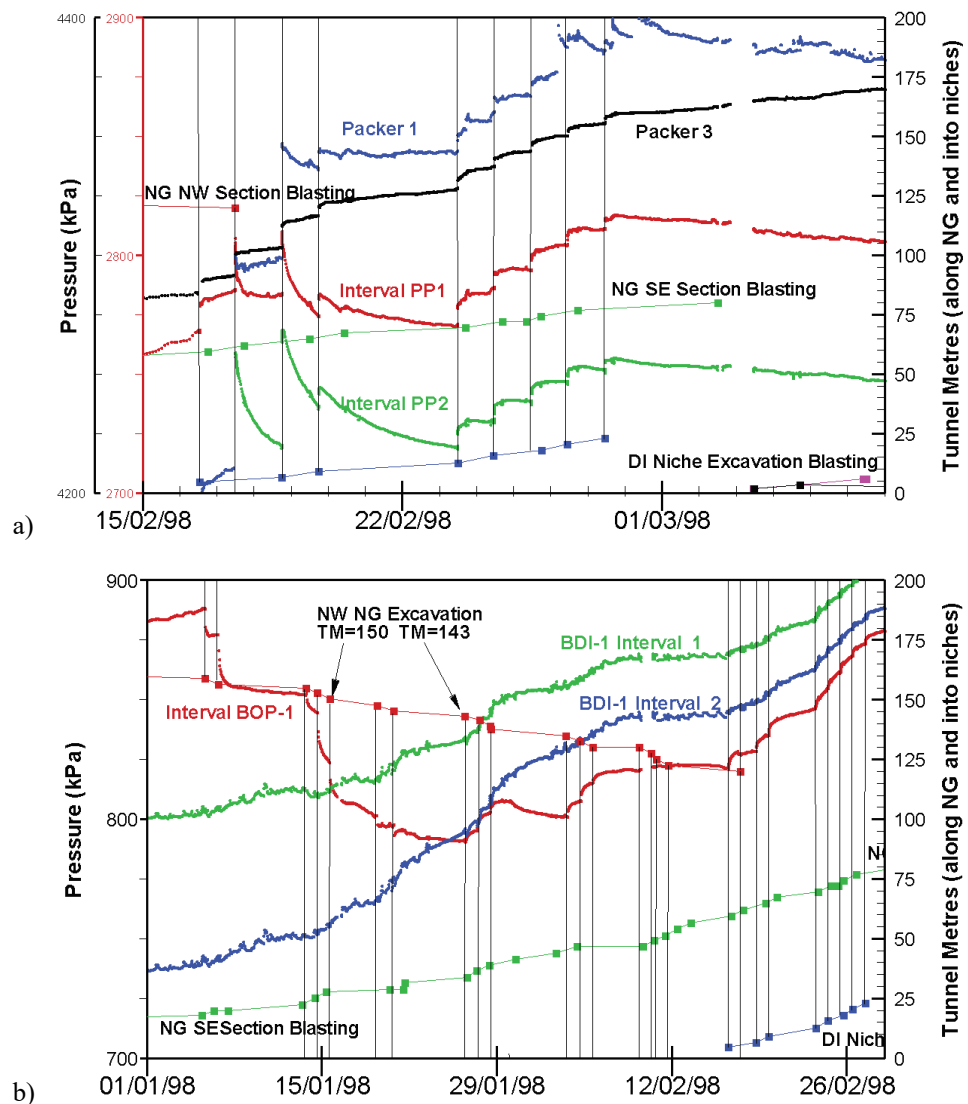


Fig. H-1: BOP-1 and BDI-1 interval pressures during New Gallery excavation  
From Lanyon & Martin (2003)

While most pressure responses to blasting or mechanical excavation are positive, responses in borehole BOP-1 a vertical hole 8m deep drilled from the OP Niche were initially negative (i.e. pressure drops with each blast) but then change to positive as the face approaches. Fig. H-1b shows the pressures in BOP-1 and BDI-1 as the face advances. It is noteworthy that as the New Gallery changes direction from approximately  $192^\circ$  at NG 150 towards  $152^\circ$  in the ED-B section of the gallery the sign of the induced pore pressure changes. This suggests that the effect is related to stress redistribution rather than any blast-induced phenomena.

Martin & Lanyon (2003) compared the observed nearfield pore pressures ahead of the face (before nonelastic rock mass response is induced and drainage to the tunnel becomes significant) in the ED-B section to demonstrate qualitative agreement with a simple elastic model based on mean stress change.